ADVANCING PROCESS UNDERSTANDING OF OZONE DRY DEPOSITION ACROSS SCALES

AUKE J. VISSER

Propositions

1. The contribution of agricultural soil NO_x sources to European ozone formation is more important than previously assumed.
   (this thesis)

2. Ignoring variability in non-stomatal ozone deposition leads to biased predictions of ozone damage to vegetation.
   (this thesis)

3. The importance assigned to scholarly metrics is an indicator of organizational distrust.

4. The environmental benefits of reducing Dutch intensive livestock farming outweigh its cost.

5. Democracies are undermined by information illiteracy of their citizens.

6. The Dutch culinary culture is richer than its everyday dishes suggest.

Propositions belonging to the thesis, entitled

Advancing process understanding of ozone dry deposition across scales

Auke Visser

Wageningen, 31 October 2022

Advancing process understanding of ozone dry deposition across scales

Auke J. Visser

Thesis committee

Promotors:
Dr K.F. Boersma
Associate Professor, Meteorology and Air Quality
Wageningen University & Research
Research Scientist, R&D Satellite Observations
Royal Netherlands Meteorological Institute (KNMI), De Bilt

Prof. Dr M.C. Krol
Professor of Air Quality and Atmospheric Chemistry
Wageningen University & Research

Co-promotor:
Dr L.N. Ganzeveld
Assistant Professor, Meteorology and Air Quality
Wageningen University & Research

Other members:
Prof. Dr G.J.M. Velders, Utrecht University
Prof. Dr W. de Vries, Wageningen University & Research
Prof. Dr L. Emberson, York University, United Kingdom
Dr K. Ashworth, Lancaster University, United Kingdom

Advancing process understanding of ozone dry deposition across scales

Auke. J. Visser

Summary

Ozone is a harmful air pollutant in the surface atmosphere that affects human health and ecosystems. Ozone is formed in the troposphere as a result of chemical reactions involving two precursor groups, nitrogen oxides (NO_x) and volatile organic compounds (VOCs), under the influence of sunlight. Ozone dry deposition, when vertical transport brings ozone in contact with the Earth surface leading to ozone removal, is an important ozone sink. Deposition to vegetation is a particularly efficient ozone sink, consisting of various pathways, including uptake by plant stomata, deposition to other surfaces in the canopy (e.g., to leaves and to the soil) and chemical removal inside the vegetation canopy. Stomatal ozone uptake can negatively impact photosynthesis, which reduces ecosystem carbon uptake and affects the terrestrial water cycle.

The central aim of this thesis is to improve process understanding of ozone dry deposition using atmospheric chemistry models at different spatial and temporal scales, combined with remote sensing and in situ observations. First, this thesis focuses on ozone air quality simulations with a regional atmospheric chemistry model covering Europe. Model simulations tend to underestimate observed peak daytime surface ozone concentrations. This underestimation also affects model simulations of the ozone dry deposition flux, since ozone concentrations partly determine the dry deposition sink. A mis-representation of NO_x emissions may contribute to the underestimated model-simulated surface ozone concentrations. Second, this thesis focuses on point-scale, observation-driven modelling dry deposition to vegetation, with the aim to understand temporal variability in stomatal ozone uptake (responsible for vegetation ozone damage) and various non-stomatal deposition pathways, with the aim to improve understanding of temporal variability in ozone deposition on diurnal to seasonal timescales. Third, this thesis presents ozone dry deposition simulations with a high-resolution Large Eddy Simulation model, helping to address the gap in spatial scales between the coarse-scale European air quality simulations and the point-scale dry deposition simulations.

Chapter 2 explores the dependence of summertime ozone formation in Europe on surface NO_x emissions. This chapter presents simulations with the regional air quality model WRF-Chem. A comparison with surface in situ observations and NO_2 column measurements from the OMI satellite shows that WRF-Chem underestimates simulated NO_2, and also

peak ozone simulations. A mass balance approach is used to derive updated surface NO_x emissions based on the difference between WRF-Chem-simulated and OMI-observed NO_2 columns, which results in an average emission increase by 56% over the model domain. The emission increase is strongest in rural regions, which could be due to substantially underestimated NO_x emissions from agricultural soils in WRF-Chem. A WRF-Chem simulation with the updated surface NO_x emissions results in an improved agreement with independent surface NO_2 observations, and also improved simulations of peak daytime ozone concentrations. This chapter concludes that a comprehensive description of anthropogenic as well as biogenic NO_x sources is required in atmospheric chemistry models for accurate simulations surface ozone concentrations.

Chapter 3 investigates how ozone dry deposition simulations depend on the model representation of the dry deposition process. To address this research question, simulations are performed with a commonly used big leaf parameterization and a multi-layer canopy exchange model, driven by canopy-top observations of micro-meteorology and ozone concentrations at two measurement sites in European forests with long-term ozone flux data records. The multi-layer model reproduces temporal variability in stomatal and bulk non-stomatal ozone dry deposition on diurnal timescales, but the simulated diurnal cycles of stomatal and non-stomatal removal by the big leaf parameterization systematically deviate from observations. The multi-layer model performs better compared to the big leaf parameterization because of a better representation of stomatal ozone deposition and a better response of non-stomatal deposition to micro-meteorological drivers of non-stomatal ozone removal (temperature, relative humidity). As a result, the multi-layer model better simulates cumulative stomatal ozone uptake over the growing season compared to the big leaf parameterization.

Chapter 4 considers the contribution of two non-stomatal processes (canopy-atmosphere turbulent exchange and chemical removal by soil-emitted NO) to ozone deposition in a temperate deciduous forest. In this chapter, detailed campaign observations of NO_x and ozone exchange are interpreted using a multi-layer canopy exchange model. Canopy-atmosphere exchange is overestimated by two tested representations of in-canopy vertical transport in the model, leading to overestimated dry deposition velocity simulations by 10–19%. A simulation applying observation-derived vertical exchange results in an improved model-observation agreement for the dry deposition velocity. Soil NO emissions are substantial in this forest canopy, and are an important ozone sink in the bottom half of the forest canopy. However, sensitivity simulations indicate that the magnitude of the canopy-top ozone flux is not affected by the high soil NO emissions. This is because the lower canopy ozone sink remains constant regardless of the soil NO emission strength: the enhanced chemical ozone sink is offset by increased vertical ozone transport from the upper canopy, and by suppressed dry deposition. This chapter highlights the need for improved observational constraints on non-stomatal deposition processes and ozone dry deposition simulations using models that resolve turbulence in forest canopies.

Chapter 5 examines the effects of heterogeneity in land surface properties on ozone via its effects on turbulent mixing and the dry deposition velocity. To address this, a big leaf dry deposition parameterization is implemented in a Large Eddy Simulation model. This model setup is used to investigate covariance of the dry deposition flux, occurring in case of coinciding fluctuations in the concentration and dry deposition velocity, resulting in a change in the domain-wide deposition flux. Covariance between dry deposition velocity and ozone concentration are negative and very small (<0.1%). Sensitivity simulations demonstrate that the magnitude of this covariance is affected by the strength and variability of the dry deposition velocity, and by the vertical profile of the depositing tracer. If concentrations increase with height, downward vertical transport of air with high concentrations can compensate for the negative deposition flux covariance resulting from the negative effect of dry deposition on the surface concentration. The covariances are stronger in a simulation of a NO_x plume emitted by a power plant. Inside the plume, the normalized dry deposition covariance is +2%, since ozone increases strongly with height due to in-plume ozone titration. For NO and NO_2, in-plume deposition is lower by 9–22%, since their vertical profiles strongly peak at the surface. This chapter indicates that the covariance between the dry deposition velocity and the surface concentration can be important and affects domain-integrated deposition fluxes, especially in case of strong gradients in the vertical profile of the depositing species.

The results of this thesis contribute to improved understanding of the ozone dry deposition sink to the land surface, which can benefit air quality predictions and assessments of the ozone impact on the land carbon sink. Moving forward, we suggest that a scale-bridging modelling approach is a fruitful method to further advance ozone deposition process understanding, consisting of three model setups. First, coarse-scale ($\pm 10 \times 10$ km^2) simulations can be used for ozone air quality simulations at the regional to global scale. These models cover large spatial scales, do not resolve small-scale surface heterogeneity. Second, simulations at a spatial resolution of 100×100 m^2 can therefore be used to quantify the effects of resolving small-scale effects of land cover heterogeneity on turbulent mixing and dry deposition. Third, detailed simulations for forest canopies at a $1 \times 1 \times 1$ m^3 resolution can be used to explicitly resolve in-canopy turbulence, stomatal removal, soil and leaf uptake and chemical removal. The outcomes of the second and the third modelling steps can be used to develop parameterizations for unresolved processes in coarser-resolution models.

Contents

Chapter 1

Introduction

Ozone (O_3) is an important trace gas in the Earth's atmosphere. Ozone takes up only a small part of the atmosphere (typically 0.000002% near the surface and roughly 0.0004% at 20 km altitude), yet it has profound climatic impacts. The majority of atmospheric ozone, around 90%, is present in the stratosphere (an air layer at 10-50 km above the Earth surface) in the so-called ozone layer, where it absorbs harmful ultraviolet radiation and prevents this radiation from reaching the surface. Thereby, the ozone layer contributes to maintaining habitable living conditions on Earth. At the same time, ozone is also a greenhouse gas in the troposphere (an air layer at 0-10 km above the Earth surface). Anthropogenic activities contribute to ozone formation, and as a result, tropospheric ozone is the third most important anthropogenic greenhouse gas contributing to climate change (IPCC, 2021). Besides, ozone is a hazardous air pollutant linked to prevalence of respiratory diseases in humans (Nuvolone et al., 2018). Additionally, ozone is harmful for vegetation, leading to reduced crop growth and vegetation carbon uptake (Ainsworth et al., 2012; Emberson et al., 2018; Mills et al., 2018). The resulting reduction in the land carbon sink leads to an increase in atmospheric CO_2, which is thought to have a similar contribution to global warming by ozone in its role as a greenhouse gas (Sitch et al., 2007).

In the troposphere, ozone is formed chemically when pollutants, so-called ozone precursors, react under the influence of sunlight. Overall, tropospheric ozone concentrations have increased by 30-70% in the past century (Tarasick et al., 2019) due to increases in anthropogenic emissions of ozone precursors. Surface ozone concentrations exhibit large variability depending on season and location. Ozone formation is dependent on temperature and sunlight, and therefore ozone concentrations peak during summer in most regions. In remote regions unaffected by anthropogenic pollution, surface ozone concentrations can be as low as 10-20 parts per billion or ppb (i.e., out of every billion air molecules, 10-20 are ozone). Ozone smog can form downwind of anthropogenic pollution hotspots, and surface ozone concentrations typically exceeds 100 ppb under these circumstances (i.e., a factor 5-10 difference).

Ozone loss processes in the troposphere include removal by chemistry and removal at the Earth surface, a process termed dry deposition (Fowler et al., 2008). This thesis is concerned with strategies to obtain a better understanding of the dry deposition removal processes of ozone in the lowermost part of the Earth's atmosphere. To better understand the sources and sinks of ozone, it is insightful to consider the budget equation of ozone, which expresses the changes in the ozone concentration over time in an atmospheric volume in contact with the Earth surface as a function of its source and sink processes (Jacob, 1999):

$$\frac{d[O_3]}{dt} = (P + T) - (L + D) \tag{1.1}$$

This equation expresses that the amount of ozone (unit: ppb) changes over time because of the effects of chemical production (P) and loss (L), transport (T) and loss processes at the land surface, or dry deposition (D) (the units of the four terms on the right-hand side of Equation 1.1 are ppb per second). The net effect of transport can be positive or negative, which means that transport can act to increase or decrease the ozone levels at a given location and time (e.g., transport from an upwind region where it is chemically produced).

In Section 1.1, we introduce the chemical formation of ozone (P) in the lower troposphere, mainly focusing on the planetary boundary layer (the lowermost 1-2 kilometers of the troposphere in direct contact with the Earth surface). Section 1.2 considers dry deposition of ozone (D). Section 1.3 is concerned with surface observations of ozone, while Section 1.4 focuses on the application of modelling tools to enhance our understanding and quantification of ozone formation and deposition to land surfaces, building on Equation 1.1. Section 1.5, summarizes the theoretical framework underlying this thesis and introduces the research questions.

1.1 Chemical ozone formation and removal

The formation of ozone in the troposphere is a complex chemical process that depends non-linearly on two groups of ozone precursor species and sunlight (Fowler et al., 2008). The first group is volatile organic compounds (VOCs), a group consisting of reactive hydrocarbon species. These undergo a chain of reactions, whose outcome depends on the presence of a second group of precursor species, nitrogen oxides (NO_x, consisting of NO and NO_2). NO reacts with ozone to form NO_2:

$$NO + O_3 \longrightarrow NO_2 + O_2 \tag{R1.1}$$
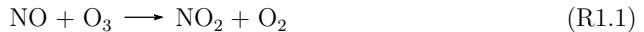
NO_2 reacts back to NO and ozone under the influence of sunlight:

$$NO_2 + h\nu \xrightarrow{\ O_2\ } NO + O_3 \tag{R1.2}$$
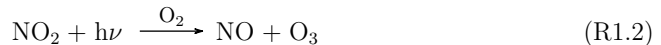
Since these two reactions combined do not result in production or loss of NO_x and ozone under typical daytime circumstances, this is considered a chemical null-cycle called the photo-stationary state. Production of ozone follows a different pathway, which involves VOCs. Consider the following reaction chain for a generic hydrocarbon RH, consisting of a chain of carbon atoms bound to hydrogen atoms (Jacob, 1999):
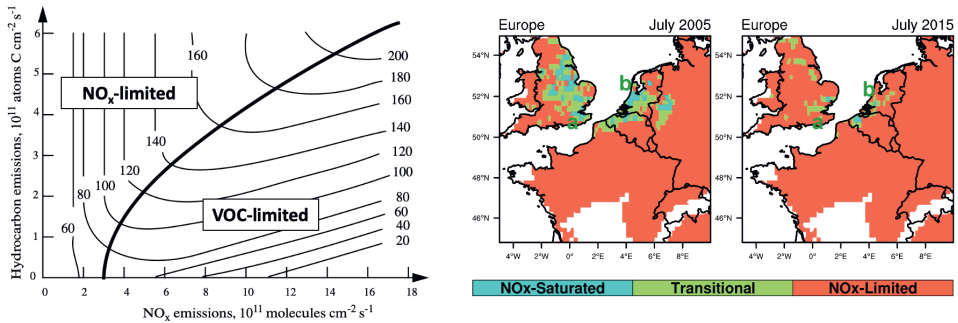
Figure 1.1: Left panel: contour lines of model-simulated ozone concentrations (in parts per billion) as a function of NO_x emissions (x axis) and hydrocarbon (or VOC) emissions (y axis). The thick black line separates the NO_x-limited and VOC-limited ozone preduction regimes (source: Jacob, 1999, modified). Right panel: Ozone production regimes in Western Europe in summer 2005 (left) and 2015 (right), categorized as NO_x-saturated (i.e., VOC-limited), NO_x-limited, or transitional. Ozone production regimes are derived as the ratio of NO_2 and formaldehyde tropospheric columns, obtained from OMI satellite observations (source: Jin et al., 2017).

$$RH + OH \xrightarrow{O_2} RO_2 + H_2O \tag{R1.3}$$

$$RO_2 + NO \longrightarrow RO + NO_2 \tag{R1.4}$$

$$RO + O_2 \longrightarrow R'CHO + HO_2 \tag{R1.5}$$

$$HO_2 + NO \longrightarrow OH + NO_2 \tag{R1.6}$$
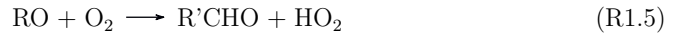
Reaction R1.3 initiates the reaction cycle that leads to the formation of ozone, in presence of VOCs and OH. Reactions R1.5 and R1.6 form an alternative pathway for reaction R1.1 to produce NO_2 from NO without consuming ozone, and these reactions are followed by Reaction R1.2, thus disrupting the photo-stationary state. The net reaction of reactions R1.3-R1.6 reads (note that R'CHO has two hydrogen atoms less than RH due to Reactions R1.3-R1.6):

$$RH + 2\,O_2 \longrightarrow R'CHO + H_2O + 2\,O_3 \tag{R1.7}$$

The left panel of Figure 1.1 shows how ozone production is dependent on NO_x and VOC emissions. In case of sufficient availability of VOCs and NO_x, this cycle will continue to proceed and ozone will continuously be produced until this reaction chain (Reactions R1.3-R1.6) is terminated by loss of hydrogen oxides (shortly HO_x, OH or HO_2). HO_x loss

generally proceeds in two different pathways. On the one hand, Reaction R1.6 cannot proceed if NO is not sufficiently available, which allows the self-reaction of HO_2 to hydrogen peroxide (H_2O_2) and termination of the reaction chain. These conditions are referred to as the NO_x-limited ozone production regime (Sillman, 1999, see Fig. 1.1, left panel), where the production of ozone depends only on NO_x concentrations and not on the availability of hydrocarbons.

On the other hand, Reaction R1.3 cannot proceed if the availability of hydrocarbons is insufficient. In this case, HO_x will be lost by the following three-body reaction to form nitric acid (HNO_3):

$$NO_2 + OH + M \longrightarrow HNO_3 + M \qquad\qquad (R1.8)$$
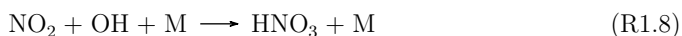
HNO_3 is removed efficiently by wet and dry deposition in the lower troposphere (Jacob, 1999). This regime is referred to as the VOC-limited ozone production regime (Sillman, 1999, see Fig. 1.1, left panel). In this regime, ozone production depends on the availability of hydrocarbons. However, ozone production depends inversely on NO_x in this regime: freshly emitted NO_x - mostly in the form of NO – reacts with ozone via Reaction R1.1 in a process called ozone titration. This regime is typical for high-NO_x regions such as urban areas, or downwind of point source NO_x emissions such as smokestacks. It is characterized by local minima in ozone levels in the vicinity of these NO_x sources. The occurrence of these regimes changes seasonally, and depends on the abundance of hydrocarbons and NO_x. We will now discuss recent trends in European ozone precursor emissions, and how they have affected the ozone production regime.

Trends in ozone and its precursors

VOCs have a predominantly biogenic origin, being emitted by vegetation. The global total biogenic VOC source is estimated at 760 Tg C yr^{-1}, and the most important species emitted are isoprene and monoterpenes, which together comprise more than 80% of the global biogenic VOC emissions (Sindelarova et al., 2014). Anthropogenic sources are only responsible for some 15% of total VOC emissions (Curci et al., 2010), and in Europe the dominant anthropogenic VOC sources are industrial processes, agriculture, commercial and domestic processes, energy generation and road transport (European Environment Agency, 2020).

In contrast, the sources of NO_x are primarily anthropogenic. NO_x is a by-product of combustion reactions, and as such its dominant sources are road transport, energy generation and industry. Present-day global anthropogenic NO_x emissions are estimated at ± 37 Tg N yr^{-1} (Crippa et al., 2018). Besides anthropogenic sources, NO_x has considerable

(semi-)natural sources, from biomass burning (8.9 Tg N yr^{-1}; Andreae, 2019), lightning (5 Tg N yr^{-1}; Schumann and Huntrieser, 2007) and (agricultural) soils (11 Tg N yr^{-1}; Vinken et al., 2014b). These sources are especially important for determining the NO$_x$ burden in remote and rural regions, where anthropogenic emissions are smaller. It must be noted that these emission estimates carry substantial uncertainties. For example, uncertainties in country-level anthropogenic emissions vary between 10-60% in Europe (Kuenen et al., 2022), and uncertainty margins on natural emission sources are often even higher (Vinken et al., 2014b).

In Europe, the past decades have seen substantial declines in anthropogenic ozone precursor emissions. Anthropogenic NO$_x$ emissions have dropped by 39% between 2000 and 2017 (Kuenen et al., 2022) as a result of emission control measures. NO$_x$ emissions from natural and agricultural soils have also decreased in the past 30 years, albeit at a slower rate (Skiba et al., 2021). Coincidently with anthropogenic NO$_x$ emission reductions, anthropogenic VOC emissions have declined by 38% over 2000-2017 (Kuenen et al., 2022). On the other hand, modelling experiments suggest that biogenic VOC emissions may have increased by 12-13% over the period 2000-2019 (Sindelarova et al., 2022).

The changes in ozone precursor emissions outlined above have also affected ozone production regimes in Europe. An example of this shift to NO$_x$-limited ozone production conditions is shown in Figure 1.1 (right panel). During summer, ozone production regimes in large parts of western Europe have shifted from a VOC-limited regime to a NO$_x$-limited regime between 2005 and 2015 as a result of declining NO$_x$ emissions (Jin et al., 2017). This facilitates targeting ozone air pollution via controls on NO$_x$ emissions. However, detecting a uniform decreasing trend in European ozone levels is more challenging. In background regions, ozone formation conditions are generally NO$_x$-limited, and ozone levels in these regions have decreased significantly following the decreasing NO$_x$ emissions (Chang et al., 2017). In contrast, ozone levels in European urban areas have actually increased as a result of decreasing NO$_x$ emissions, due to a shift in the ozone production regime (Yan et al., 2018). For example, average summer ozone concentrations in the Netherlands have increased by 6 ppb as a result of decreasing availability of NO for ozone titration via Reaction R1.1 (Zara et al., 2021). However, peak ozone concentrations show a stronger decreasing trend in Europe, even in urban areas (Chang et al., 2017; Yan et al., 2018), which is also attributable to downward trends in anthropogenic emissions (ETC/ACM, 2016).

This indicates that we need a good understanding of the other drivers of surface ozone for air quality predictions and for assessments of air pollution impacts on human health and vegetation.
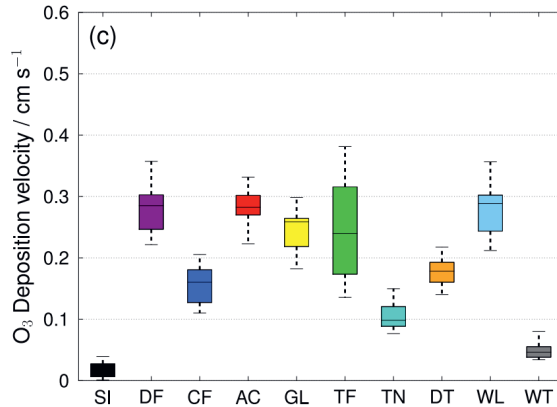
Figure 1.2: Yearly averaged ozone dry deposition velocity per land cover type. Land cover types are: snow and ice (SI), deciduous forest (DF), coniferous forest (CF), agricultural land (AC), grassland (GL), tropical forest (TF), tundra (TN), desert (DT), wetland (WL), and water (WT) (source: Hardacre et al., 2015).

1.2 Ozone dry deposition

An important ozone loss term in Equation 1.1 is removal near the Earth surface, termed dry deposition (D; see Eqn 1.1). This occurs when ozone-containing air masses are transported downward in the atmosphere, and come in contact with the ocean and the land surface where it quickly reacts. These surfaces can then remove ozone via a range of processes. Ozone deposition constitutes some 15-25% of the global annual tropospheric ozone sink (Bates and Jacob, 2020; Hu et al., 2017; Lelieveld and Dentener, 2000; Young et al., 2018) .

Ozone can deposit to a wide range of land surface types, such as water bodies, snow, soils, and vegetation (Clifton et al., 2020b). The rate of ozone uptake is often expressed by the deposition velocity, which can be derived from observations by normalizing the land surface ozone flux by the local surface ozone concentration:

$$V_d(O_3) = -\frac{F_{O_3}}{[O_3]} \tag{1.2}$$

where $V_d(O_3)$ is the dry deposition velocity (unit: m s^{-1}), $[O_3]$ is the ozone concentration (unit: ppb), and F_{O_3} is the ozone flux to the land surface (unit: ppb m s^{-1}). The rate of uptake by the land surface varies strongly depending on the land cover type. Figure 1.2 shows the estimated global average dry deposition velocity per land cover class. According to this model-based analysis, wetlands are particularly effective at removing

In-canopy ozone sink pathways
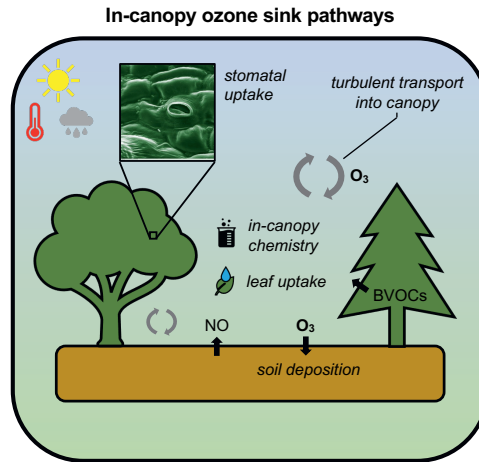
Figure 1.3: Schematic representation of dry deposition pathways in vegetation canopies (image showing a stomate retrieved from: `https://en.wikipedia.org/wiki/Stoma#/media/File:Tomato_leaf_stomate_1-color.jpg`).

ozone, although the global coverage of this land cover class is small. Deposition to water, snow and ice surfaces is typically less efficient (Clifton et al., 2020b). Vegetated land surfaces, including forests, are among the most efficient ozone deposition sinks (Hardacre et al., 2015).

There are several pathways of ozone deposition to vegetation, which are depicted in Figure 1.3. For ozone to be removed by vegetation, the gas must first be transported into the vegetation canopy by turbulent motions. Once inside a vegetation canopy, ozone may be removed via several pathways. First, ozone can diffuse into in plant stomata, small openings on leaves where gas exchange of CO_2 and water vapor takes place as part of the photosynthesis process. Upon stomatal uptake, ozone can react with plant tissue in the plant's interior which leads to tissue injury (Ainsworth et al., 2012). As a result, plant eco-physiology is affected, which can lead to reductions in stomatal conductance and photosynthesis (Lombardozzi et al., 2013). This accelerates senescence and reduces ecosystem productivity (Ainsworth et al., 2012; Wittig et al., 2009). On larger scales, the damaging effects of ozone on plant growth reduce agricultural yields of ozone-sensitive crops (Mills et al., 2011a; Tai et al., 2014; Van Dingenen et al., 2009), leading to substantial economic losses (Avnery et al., 2011). Additionally, vegetation ozone damage reduces the land carbon sink (Oliver et al., 2018; Wittig et al., 2009), leading to increased atmospheric CO_2 and thereby affecting climate (Sitch et al., 2007).

Second, ozone can also deposit onto external surfaces in the canopy such as leaf cuticula (Altimir et al., 2006; Potier et al., 2015). A third pathway of ozone removal is soil deposition, for which ozone must first be transported downward by turbulent motions from the top of the canopy to the soil surface. Fourth, ozone may be removed chemically by removal by NO (via Reaction R1.1) or VOCs. This is formally not recognized as a mechanism of dry deposition, but included as an additional contribution to the overall vegetation sink whose magnitude is reflected by a flux measured above the canopy. This flux is referred to as the ozone dry deposition flux, which includes a contribution by in-canopy chemical removal. Typically, the stomatal pathway is responsible for 40-90% of total ozone deposition to vegetation during the growing season (Fowler et al., 2009), but stomatal and non-stomatal ozone deposition exhibit spatio-temporal variability that is incompletely understood (Clifton et al., 2020b; Wu et al., 2018).

1.2.1   Spatial and temporal variability in ozone deposition

Understanding spatio-temporal variability in ozone deposition is essential to better quantify effects of ozone on ecosystem carbon uptake as a function of stomatal uptake (Visser et al., 2021, see Chapter 3). Additionally, temporal variability in dry deposition affects surface ozone concentrations (e.g., Kavassalis and Murphy, 2017; Lin et al., 2019; Travis and Jacob, 2019). Ozone deposition to ecosystems exhibits temporal variability on inter-annual to sub-daily timescales that is only partially understood (Clifton et al., 2020b). This inhibits our ability to assess ecosystem damage incurred by stomatal ozone uptake. Seasonal variability in vegetation ozone uptake is largely controlled by the seasonal cycles in leaf area index, radiation and temperatures which drive stomatal uptake of ozone (Fowler et al., 2009; Val Martin et al., 2014).

Clifton et al. (2017) found strong interannual variability of non-stomatal ozone dry deposition in a US midlatitude deciduous forest, which could be partly attributed to variability in forest soil uptake in dry versus wet years (Clifton et al., 2019). On diurnal timescales, variability in ozone uptake is largely controlled by stomatal uptake which peaks during daytime as a function of solar radiation and temperature (Fowler et al., 2009). During dry conditions typical for summer afternoons, plants tend to close their stomata to minimize water loss, which also suppresses ozone deposition (e.g., Kavassalis and Murphy, 2017). Additional sources of diurnal variability are deposition to wet leaves, which typically peaks in the morning as leaves are wetted by dew (Altimir et al., 2006; Potier et al., 2015). In some cases, the degree of turbulent mixing above the vegetation canopy explains part of the observed temporal variability in ozone dry deposition (Fares et al., 2014; Neirynck et al., 2012). On even faster timescales, fast ambient chemistry with VOCs or NO may explain part of the ozone deposition signal (e.g., Fares et al., 2010; Finco et al., 2018; Goldstein et al., 2004; Vermeuel et al., 2021). The spatio-temporal variability in ozone dry deposition during extreme climatic events, such as droughts and

heatwaves, is largely unexplored. For example, ozone dry deposition during droughts is strongly reduced as the stomatal sink is shut off (Lin et al., 2020). However, Wong et al. (2022) recently found observational evidence for increased non-stomatal ozone removal under hot and dry conditions, partly offsetting the reduced stomatal sink.

Overall, temporal variability in ozone dry deposition and the contribution of stomatal and non-stomatal dry deposition processes are incompletely understood, limiting the quantification of the ozone dry deposition sink to land surfaces. As a result, model estimates of this sink display a large spread (700-1500 Tg O_3 yr^{-1}) around the mean of 1000 Tg O_3 yr^{-1} (Young et al., 2018). This thesis (Chapters 3, 4) aims to advance our understanding of the drivers of temporal variability in ozone deposition to vegetation. To improve the understanding of ozone deposition to vegetated surfaces, scientists employ numerical models in combination with observations to evaluate and/or improve the model performance. In the next sections, we outline the different observations and modelling tools that are used in this thesis.

1.2.2 Metrics of ozone damage to vegetation

Policy applications to quantify the risk of ozone air pollution to crops and forests require a quantitative estimate of stomatal uptake of ozone. An often-applied metric to assess risks of ozone damage to vegetation is based on the growing season-accumulated exposure to ozone over a threshold of 40 ppb (AOT40; e.g., EEA, 2020). This metric assumes that ozone is toxic to vegetation above the threshold exposure concentration, and that the surface ozone concentration is indicative of the stomatal ozone flux into the plant. To address these assumptions, an alternative ozone impact metric can be applied: the cumulative stomatal uptake of ozone (CUO; Matyssek et al., 2004; Musselman et al., 2006). This metric recognizes that ozone damages plants upon stomatal uptake. Additionally, ozone damage to plants also depends on a species-specific detoxification level, which is the plant's capacity to counteract ozone's negative effects on plant growth (Mills et al., 2011b; Musselman et al., 2006), for example by releasing compounds that scavenge ozone inside the leaf before it can damage cell tissue.

The AOT40 metric remains commonly used in many policy applications in Europe, since validating the CUO metric with observations is challenging, and since the uncertainties associated with estimates of stomatal conductance and the detoxification threshold are large (Mills et al., 2011b; Otu-Larbi et al., 2021). However, intercomparison studies between both metrics find that these metrics often display distinctly different spatial patters. An example is shown in Figure 1.4, which displays the AOT40 and CUO for 2005 in Europe. The AOT40 map suggests the highest impact of ozone on vegetation in Italy and other Mediterranean regions, following the distribution of ozone concentrations which also peak in these regions. In contrast, the CUO-based map shows much lower
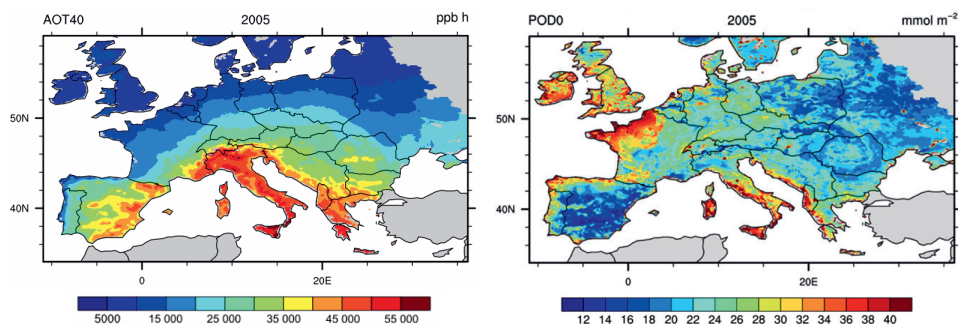
Figure 1.4: Comparison between an exposure-based (AOT40) and flux-based (POD0, analogous to CUO with a detoxification threshold of 0 nmol m^{-2} s^{-1}) metrics of ozone impact to vegetation. Note that the data underlying these calculations, derived from on 12×12 km^2 simulations of meteorological variables and surface ozone concentrations, are identical for both maps (source: Anav et al., 2016, modified).

effects of ozone in these regions, and higher impacts in other regions such as western France and the United Kingdom. Additionally, flux-based ozone impact metrics tend to correspond better with observed impacts of ozone on crops (Mills et al., 2011a). The CUO metric has been linked to independent reductions in stomatal conductance and photosynthesis (Lombardozzi et al., 2013), which is the basis for model-based estimates of the effects of vegetation ozone damage on global climate (Arnold et al., 2018), and the feedback between vegetation ozone damage and atmospheric ozone concentrations (Sadiq et al., 2017). Chapter 3 considers cumulative ozone uptake and how it depends on the representation of dry deposition in different types of models to simulate ozone deposition (see Section 1.4.3).

1.3   Observations

1.3.1   Surface concentration measurements

Surface concentration measurements are the most common type of ozone observations. These measurements are representative for surface ozone concentrations, which is important information from an air quality perspective. Additionally, the surface ozone concentration partly determines how much ozone is removed at the surface by dry deposition. Measurements can provide information about ozone air quality in cities, which is important for assessments of human exposure to air pollution. Since the photochemical ozone formation regime is often distinctly different in cities compared to remote regions, monitoring ozone in so-called rural background stations is important as well (Tarasick et al., 2019). These

are more indicative of ozone levels for a larger domain, and are governed by local ozone production and larger-scale processes such as long-range transport. The downside of surface observations is that they are only representative for a limited region. Maintaining a dense enough observational network to have good coverage in larger regions is costly and labor-intensive. Current surface ozone monitoring networks therefore compromise between representativeness and operability. In this thesis, surface concentration measurements are used in Chapter 2 for a comparison against air quality model simulations, and to evaluate our understanding of the surface NO_x emission budget.

1.3.2 Surface flux measurements

Measurements of surface ozone concentrations alone are not indicative of ozone removal at the land surface. A different observational method, the eddy covariance technique, can be used to assess ozone dry deposition. This method relies on high temporal frequency measurements (typically 5-40 measurements per second) of vertical wind speed and the ozone concentration, usually performed at a height of several meters above the surface (Aubinet et al., 2012; Clifton et al., 2020b). The wind speed measurements detect small-scale changes in the vertical wind speed and direction (upward or downward) as a result of turbulent motions in the lower atmosphere. The high-frequency ozone concentration measurements display small concentration divergences: air parcels moving upward from the surface (where ozone is removed by deposition) will typically have a slightly lower ozone concentration than air parcels moving downward. From these coincident fluctuations in vertical wind speed and ozone concentrations, the ozone deposition flux can be derived as the time-average (typically over a 10-30 minute period) of the product of the high-frequency vertical wind speed and ozone concentration fluctuation measurements over this time period. Surface ozone flux measurements are used in Chapters 3 and 4 to evaluate the performance of a canopy-atmosphere exchange model (introduced in Section 1.4.3).

1.3.3 Satellite remote sensing observations

The abundance of air pollutants can also be monitored from space. An important advantage of this measurement technique is that modern satellite sensors, such as the Ozone Monitoring Instrument (OMI; Levelt et al., 2006) and the TROPOspheric Monitoring Instrument (TROPOMI; Veefkind et al., 2012) have a daily global coverage. Satellites such as OMI and TROPOMI measure differences in radiation spectra between direct solar radiation and solar radiation that has been reflected by the Earth to the satellite. Since gases present in the atmosphere absorb radiation in a specific wavelength region, the difference between these two spectra at each wavelength can be related to the abundance of specific gases in the atmosphere.

Monitoring surface ozone with satellites is challenging, since a considerable part of the ozone column is present in the stratosphere, and ozone displays relatively little vertical variation in the troposphere. However, ozone precursor gases can be better monitored from space. Satellite observations of formaldehyde (HCHO), an intermediate product in the oxidation chain of many VOCs, can be used to infer emission patterns from sources at the surface (Bauwens et al., 2016). NO_2 can also be observed with satellites, which provides information about NO_x emissions from cities (Beirle et al., 2011), ships (Riess et al., 2022; Vinken et al., 2014a), soils (Vinken et al., 2014b) and lightning (Boersma et al., 2005). In Chapter 2, remote sensing observations of NO_2 are used to derive updated surface NO_x emission estimates.

1.4 Modelling the sources and sinks of boundary layer ozone

Often, atmospheric scientists cannot answer their questions by using only observations. This is because measurements alone have a limited spatial and temporal coverage and do not contain unique information on the processes contributing to the observed concentrations. For example, only ozone flux measurements above a forest do not inform us about the contribution by individual deposition processes to total deposition by the canopy. Therefore, some form of modelling is needed to interpret observations and how they are affected by these processes. To address questions related to this thesis, such as 'how much does stomatal ozone uptake contribute to ozone deposition?' or 'how much ozone measured at point X is produced from nearby NO_x emissions?', we need to adopt a (numerical) representation of the processes involved. Models come in many forms and degrees of complexity.

The research presented in this thesis considers a range of temporal and spatial scales. Ozone formation from NO_x emissions is a larger-scale process on spatial scales that range from several kilometers to hundreds of kilometers. In contrast, ozone deposition to forest canopies depends on forest properties such as canopy height, which is on the order of several tens of meters. Likewise, turbulent motions in the atmosphere happen on a timescale of several minutes, while the average lifetime of an ozone molecule in the troposphere is several weeks. Integrating these spatial and temporal scales in a single model is not possible given the current computational constraints. Therefore, we apply a range of different models that resolve the relevant processes at different spatial and temporal scales. The underlying principles of these models are introduced in this section. These models are in a so-called Eulerian form, meaning that the three-dimensional model domain is subdivided into fixed grid cells of a smaller size, through which air flows.

1.4.1 Fundamentals of Eulerian models

Eulerian models provide an approximate numerical solution for differential equations such as Equation 1.1. This equation can be rewritten such that it expresses the ozone concentration at a given point in space and time as a function of its driving processes (Jacob, 1999). In this rewritten form, the temporal evolution of the concentration of species i can be expressed as follows:

$$\frac{\partial c_i}{\partial t} = \left[\frac{\partial c_i}{\partial t}\right]_{advection} + \left[\frac{\partial c_i}{\partial t}\right]_{turbulence} + \left[\frac{\partial c_i}{\partial t}\right]_{emissions} + \left[\frac{\partial c_i}{\partial t}\right]_{chemistry} + \left[\frac{\partial c_i}{\partial t}\right]_{deposition} \quad (1.3)$$

This equation expresses that the concentration of species i at time t and location X depends on advective and turbulent transport, chemistry and deposition. A modeler should choose a time step such that the processes in Equation 1.3 can be numerically separated. For example, a too large time step may result in chemistry affecting the concentration before it is transported to location X. Additionally, the choice of the horizontal resolution (i.e., the size of the cells in the model grid) may affect model outcomes (an example will be given below). To solve Equation 1.3, we also need information on the initial distribution of c (the initial conditions) and the model boundaries (such as inflow at the model top).

The representation of atmospheric chemistry in these models includes NO_x-VOC-ozone chemistry (including Reactions R1.1-R1.6) at different degrees of detail regarding the number of reactive compounds and reactions. The representation of dry deposition is the subject of Section 1.4.3. Advective transport here means transport along the general, average flow fields in the horizontal and vertical directions. Turbulent transport represents motions not resolved by the model resolution and that need to be parameterized. Most global and regional models have a spatial resolution too coarse to explicitly represent turbulent motions. This is because turbulence causes small-scale gradients in the three-dimensional concentration field of species c, which cannot be resolved at these scales. These models therefore use statistical averages of turbulent motion in the atmosphere, using the notion that instantaneous effects of turbulence are chaotic, but its effects averaged over a time window can be predicted. In these models, the effect of turbulent transport is approximated (or 'parameterized') by means of the product of the turbulent diffusion coefficient and the vertical concentration gradient (Jacob, 1999):

$$\overline{F_T} = -K_z \frac{\delta \overline{c}}{\delta z} \quad (1.4)$$

In this equation, $\overline{F_T}$ is the flux, and K_z is a vertical diffusion coefficient that expresses how efficiently a tracer (or scalar) is transported along a vertical gradient.

1.4.2   Regional air quality models

Regional air quality models are one particular type of Eulerian models that can be used to simulate ozone concentrations in a specific region of interest. These models typically cover a continent or an even smaller model domain. These models usually have a spatial resolution on the order of 5-50 km. Since these models are set up over a specific region, they need additional information about inflow of pollutants along the lateral domain boundaries, which typically comes from global chemistry transport models.

Regional air quality models can satisfactorily reproduce the spatial distribution of ozone concentrations (e.g., Mar et al., 2016). A problem with these models is, however, that they tend to consistently underestimate high observed ozone concentrations (Im et al., 2015; Solazzo et al., 2012; Tuccella et al., 2012), which limits their applicability to develop and evaluate ozone pollution abatement strategies and to estimate dry deposition fluxes. One potential reason for this underestimation relates to underestimated NO_x emissions. Regional models also tend to underestimate summer NO_x concentrations (e.g., Mar et al., 2016) and vertical NO_2 columns (e.g., Huijnen et al., 2010) compared to observations in background regions without strong anthropogenic NO_x sources. Since these regions typically have a NO_x-limited ozone formation regime, a hypothesis is that the mis-representation of NO_x in these models may contribute to the underestimated ozone in these models. Chapter 2 explores the dependence of regional air quality model simulations of surface ozone concentrations on surface NO_x emissions.

1.4.3   Modelling dry deposition

In Equation 1.2, we discussed how the dry deposition velocity can be calculated from the observed ozone flux and concentration. In atmospheric models, this dry deposition velocity is estimated based on local atmospheric, vegetation and soil properties, and then multiplied by the surface concentration to obtain the flux to the land surface. The most common way to represent dry deposition to the land surface in atmospheric models is via a resistance approach (Wesely and Hicks, 1977):

$$V_d(O_3) = \frac{1}{r_a + r_b + r_c} \tag{1.5}$$

Where r_a is the aerodynamic resistance (the resistance to turbulent transport to the land surface), r_b is the quasi-laminar layer resistance (reflecting the resistance against diffusive transport to the surface where uptake takes place), and r_c is the surface resistance (the resistance to uptake via different pathways, see Section 1.2).

Equation 1.5 is a so-called 'big leaf' representation of ozone deposition, since this model assumes that the surface sink to a vegetation canopy can be represented by an individual
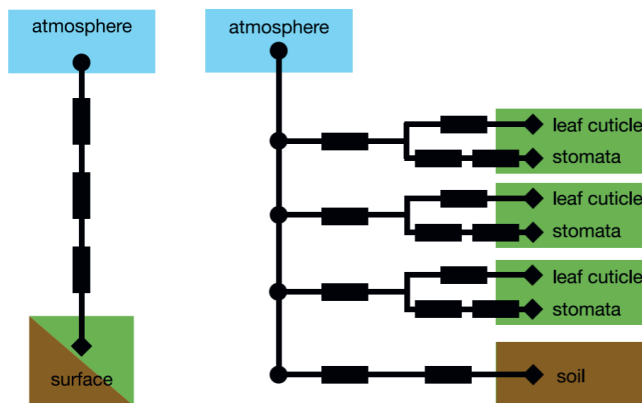
Figure 1.5: Schematic depiction of big leaf (left) and multi-layer canopy representation of ozone deposition to vegetation canopies. Green and brown rectangles reflect the uptake pathways, and uptake resistances are shown as black rectangles (source: Clifton et al., 2020b, modified)

leaf scaled up to the entire canopy using the leaf area index (LAI; Hicks et al., 1987). The resistance framework of the big leaf parameterization is shown in Figure 1.5. In this approach, the vertical concentration profile inside the canopy and the contribution of in-canopy processes, such as gas-phase chemical removal, are not explicitly considered. This approach works well for surfaces such as bare soils and water bodies. For vegetation canopies, this scheme is useful to relate inferred leaf-level uptake rates to the canopy-scale deposition velocity. The model has a representation of seasonality and represents differences between daytime and nighttime uptake and some simplified dependencies on micro-meteorology (Wesely, 1989). Although there have been several improvements to the initial big leaf dry deposition parameterization (e.g., Ganzeveld and Lelieveld, 1995; Zhang et al., 2002), and particularly in the representation of stomatal ozone uptake (e.g. Val Martin et al., 2014), the original scheme remains commonly used in large-scale atmospheric chemistry models, including the one used in Chapter 2.

However, a major shortcoming is that big leaf parameterizations do not account for vertical gradients of ozone uptake inside vegetation canopies. An additional class of models, multi-layer canopy models, divides the canopy into several layers and calculates the processes acting on the concentration in each layer following Equation 1.3. A schematic representation of a multi-layer canopy model is shown in Figure 1.5. The dry deposition velocity is calculated per model layer. A big advantage of such approaches is that they can account for vertical gradients in leaf area, shading of leaves inside the canopy (which affects stomatal uptake, Makar et al., 2017), vertical mixing inside the canopy (i.e., incorporating canopy effects in Equation 1.4; e.g., Bryan et al., 2012), in-canopy chemistry (Ashworth

et al., 2015; Wolfe et al., 2011) and the soil sink at the bottom of the canopy. Additionally, these models can account for the distinct photo-chemical regime inside the canopy, which is affected by low-radiation conditions, biogenic VOC emissions, and NO emissions from the forest floor. These models have mostly been applied to interpret above-canopy flux observations in a single-point application (e.g., Ashworth et al., 2015; Duyzer et al., 2004; Fares et al., 2019; Wolfe et al., 2011; Zhou et al., 2017), an approach we follow in Chapters 3 and 4. However, application of such approaches is also possible in larger-scale atmospheric chemistry models (e.g., Ganzeveld et al., 2010; Ganzeveld et al., 2002b).

1.4.4   Turbulence-resolving models

Another class of models are Large-Eddy Simulation (LES) models, used in Chapter 5 of this thesis. These models operate on much higher horizontal and temporal resolutions compared to regional air quality models (typically on the order of 10-100 m, and $\pm$1-10s) and are capable of resolving turbulent motions in the atmosphere of $> \pm 10$ m (e.g., Heus et al., 2010). Therefore, part of the parameterized turbulent motions in Equation 1.3 are resolved in this class of models, which is ideal for investigating interactions between the land surface and the overlying atmosphere (Bou-Zeid et al., 2020). Given their high computational cost associated with the high spatial and temporal resolution, these models typically have a domain size up to several tens of kilometers.

As explained before, larger-scale models typically average the effect of turbulence on concentrations over a time window. In doing so, they assume that the air contained in a model pixel is well-mixed. This assumption is questionable, particularly when there are large gradients in land use and, as a result, land surface energy fluxes, and emissions. This results in inhomogeneous mixing of pollutants, and can for example lead to separation between two species that react with one another (e.g., Auger and Legras, 2007; Ouwersloot et al., 2011). On a domain average basis, this can slow down or accelerate the reaction rate compared to a situation where the species are well mixed. This process is called segregation, which can be quantified as a reduction (or enhancement) in a model-simulated process (e.g., a chemical reaction) as a result of inhomogeneous mixing conditions within the model domain. Segregation of chemical reactions has been quantified particularly for inhomogeneous turbulent mixing conditions (Vila-Guerau De Arellano et al., 1993) and inhomogeneous emission sources (e.g., Auger and Legras, 2007; Krol et al., 2000; Ouwersloot et al., 2011). If the segregation intensity is substantial (e.g., higher than a few percent), this effect must be parameterized in larger-scale atmospheric chemistry models.

The dry deposition process also has the potential to introduce small-scale fluctuations in surface concentrations, since it can result in coincident variations in dry deposition velocities and surface ozone concentrations. Because dry deposition is an ozone sink term,

a locally high dry deposition velocity could coincide with a low concentration of ozone. This mechanism has received less attention until recently. Clifton and Patton (2021) recently investigated covariance between ozone concentration and its dry deposition sink of ozone dry deposition using LES simulations over homogeneous land cover conditions representative for temperate midlatitude forests. They found that this effect is typically very small. However, their simulations are representative for homogeneous conditions. In reality, land cover is often heterogeneous over the size of a model domain. An open question remains if segregation of dry deposition associated with land cover heterogeneity is an important process for heterogeneous land surfaces. This question is the subject of Chapter 5.

1.5   Research questions and thesis outline

The previous sections have introduced the concepts, tools, spatio-temporal scales and research challenges under consideration in this work. Figure 1.6 schematically depicts the objectives of Chapters 2-5. Here, we further build on these concepts and formulate a set of research questions that are addressed in this thesis.

In Chapter 2, we first zoom in on simulations of surface ozone in a European summer month. We have seen in Section 1.1 how ozone formation has increasingly become NO_x-limited in the past decade. At the same time, in Section 1.4 we discussed how regional air quality models tend to underpredict high-ozone conditions over Europe. In chapter 2, we investigate the potential improvement of using satellite NO_2 observations to improve NO_x emission estimates, and resultingly, simulations of surface ozone using a regional meteorology-atmospheric chemistry model (Fig. 1.6, left panel). The research questions addressed in Chapter 2 are:

- How well do we understand the anthropogenic and natural sources of nitrogen oxides?

- What is the sensitivity of surface ozone formation to the representation of emissions of nitrogen oxides?

In Chapters 3 and 4, we zoom in on the representation of forest ozone deposition processes in atmospheric models (Fig. 1.6, center panel). Ozone deposition in forests is a complex combination of sink pathways, whose temporal variability and contribution to the total ozone deposition sink are incompletely understood (Section 1.2). We have also seen that the degree of empiricism varies greatly between dry deposition parameterizations in atmospheric models (Section 1.4). Therefore, in Chapter 3 we confront two of those parameterizations with ozone flux observations above two European forests (Section 1.3), and ask:
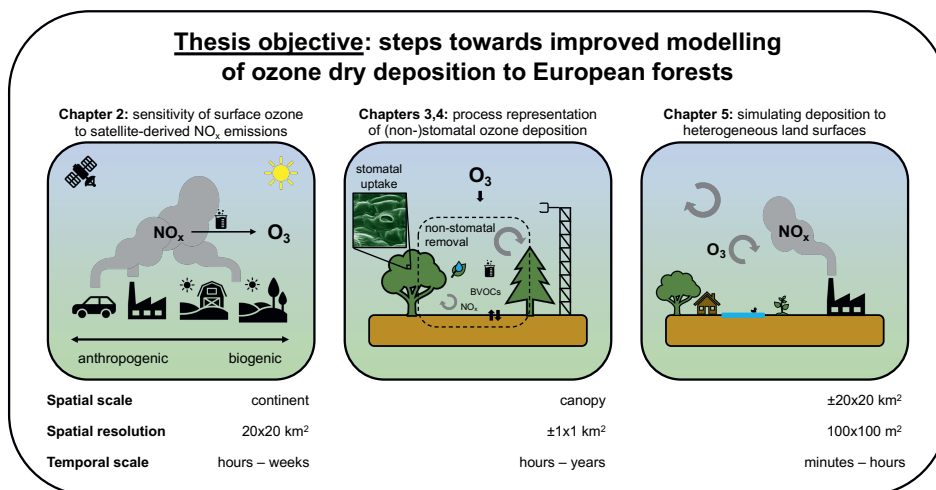
Figure 1.6: Schematic of the research objectives ans spatio-temporal scales under consideration in Chapters 2-5 (image showing a stomate retrieved from: `https://en.wikipedia.org/wiki/Stoma#/media/File:Tomato_leaf_stomate_1-color.jpg`).

- How well do a simple and a more complex dry deposition representation perform at simulating ozone dry deposition to forests?

- What is the sensitivity of a flux-based ozone impact metric to the representation of dry deposition?

Chapter 3 is mostly concerned with the contribution of stomatal ozone deposition to total deposition as stomatal ozone impacts vegetation. Since stomatal and non-stomatal sinks act in parallel, non-stomatal ozone removal can indirectly also affect the ozone impact. In Chapter 4, we zoom in on two non-stomatal processes affecting ozone deposition, namely turbulent transport from the atmosphere into the canopy, and chemical ozone removal by NO. Here, we use campaign observations of the ozone flux along a vertical profile inside and above the canopy, which enables us to separate different ozone sinks at different heights within the canopy. The research questions addressed in Chapter 4 are:

- What is the effect of canopy-atmosphere vertical exchange on forest ozone deposition?

- What is the contribution of chemical ozone removal by reaction with NO to total ozone deposition?

The models or parameterizations discussed in Chapters 2-4 typically assume that the land surface has homogeneous characteristics, such as vegetation cover, over grid cells that typically span 5-100 km. This assumption is invalid in most regions, where forests,

agricultural fields and urban areas can all be present within a 20 km × 20 km area (the resolution of the model applied in Chapter 2). In chapter 5, we therefore implement a dry deposition parameterization in a turbulence-resolving model (see Section 1.4) accounting for realistic surface heterogeneity at a much higher spatial resolution (100 m × 100 m, Fig. 1.6, right panel).

We apply this model to investigate whether small-scale variations in land cover affect the total deposition of ozone. The hypothesis is that dry deposition affects surface ozone mixing ratios, leading to locally lower surface ozone where dry deposition velocities high. Since the ozone deposition flux is calculated as the product of the dry deposition velocity and the surface ozone mixing ratio, coincident anomalies of high deposition velocities and lower mixing ratios (or vice versa) are expected to lead to a lower domain-average flux compared to a situation where a uniform dry deposition velocity is applied across the domain. We address the following research questions in chapter 5:

- What is the effect of resolving land cover and chemical plumes at a high spatial resolution on simulated dry deposition?

- Does heterogeneity in dry deposition introduce co-variability between dry deposition and surface mixing ratios, affecting the domain-integrated deposition flux?

Chapter 2

European NO$_x$ emissions in WRF-Chem derived from OMI: impacts on summertime surface ozone

Abstract

Ozone (O_3) is a secondary air pollutant that negatively affects human and ecosystem health. Ozone simulations with regional air quality models suffer from unexplained biases over Europe, and uncertainties in the emissions of ozone precursor group nitrogen oxides (NO_x = NO + NO_2) contribute to these biases. The goal of this study is to use NO_2 column observations from the OMI satellite sensor to infer top-down NO_x emissions in the regional meteorology-chemistry model WRF-Chem, and to evaluate the impact on simulated surface O_3 with in situ observations. We first perform a simulation for July 2015 over Europe and evaluate its performance against in situ observations from the AirBase network. The spatial distribution of mean ozone concenctrations is reproduced satisfactorily. However, the simulated maximum daily 8-hour ozone concentration (MDA8 O_3) is underestimated (mean bias error (MBE) = -14.2 µg m^{-3}), and its spread is too low. We subsequently derive satellite-constrained surface NO_x emissions using a mass balance approach based on the relative difference between OMI and WRF-Chem NO_2 columns. The method accounts for feedbacks through OH, NO_2's dominant daytime oxidant. Our optimized European NO_x emissions amount to 0.50 Tg N (for July 2015), 0.18 Tg N higher than the bottom-up emissions (which lacked agricultural soil NO_x emissions). Much of the increases occur across Europe in regions where agricultural soil NO_x emissions dominate. Our best estimate of soil NO_x emissions in July 2015 is 0.1 Tg N, much higher than the bottom-up 0.02 Tg N natural soil NO_x emissions from the MEGAN model. A simulation with satellite-updated NO_x emissions reduces the systematic bias between WRF-Chem and OMI NO_2 (slope = 0.98, r^2 = 0.84), and reduces the low bias against independent surface NO_2 measurements by 1.1 µg m^{-3} (-56%). Following these NO_x emission changes, daytime ozone is strongly affected, since NO_x emission changes particularly affect daytime ozone formation. Monthly averaged simulated daytime ozone increases by 6.0 µg m^{-3}, and increases of >10 µg m^{-3} are seen in regions with large emission increases. With respect to the initial simulation, MDA8 O_3 has an improved spatial distribution, expressed by an increase in r^2 from 0.40 to 0.53, and a decrease of the mean bias by 7.4 µg m^{-3} (48%). Overall, our results highlight the dependence of surface ozone on its precursor NO_x and demonstrate that simulations of surface ozone benefit from constraining surface NO_x emissions by satellite NO_2 column observations.

2.1 Introduction

Ozone (O_3) is an air pollutant that affects human and ecosystem health (Ainsworth et al., 2012; Lelieveld et al., 2015). It also affects radiative forcing directly as a greenhouse gas (IPCC, 2013), and indirectly by impacting ecosystem carbon uptake via deposition (Sitch et al., 2007). Despite decreases in ozone concentrations in Europe since 2000 (Chang et al., 2017), peak ozone concentrations still exceed the WHO air quality guideline of 100 µg m^{-3} and the European long-term objective of 120 µg m^{-3} (EMEP/CCC, 2016). For example, 87% of European air quality stations did not meet this long-term objective (EEA, 2017) in 2015, and vegetation exposure thresholds were exceeded in large parts of the continent during this year, particularly in Southern and Central Europe (Rouïl and Meleux, 2018).

The formation of ozone in the lower troposphere is a photochemical process that depends nonlinearly on concentrations of its precursor species nitrogen oxides (NO_x = NO + NO_2) and volatile organic compounds (VOCs) (e.g. Sillman et al., 1990). In NO_x-limited conditions, ozone production increases with NO_x emissions and is less sensitive to VOC emissions. However, ozone production under NO_x-saturated conditions increases with VOC emissions, but decreases with increasing NO_x emissions. European NO_x emissions are dominated by the anthropogenic contribution from fossil fuel combustion for transportation, electricity generation and industry. In summer, there are additional contributions from soils and lightning, which together comprise 40% of the total European NO_x emission budget (Jaeglé et al., 2005). Soil NO_x emissions in turn have an anthropogenic component, since nitrogen-containing fertilizers are partly re-emitted to the atmosphere as NO_x (Steinkamp and Lawrence, 2011).

Anthropogenic emissions in Europe have decreased due to air pollution abatement measures and the economic crisis that started in 2008 (Castellanos and Boersma, 2012). Bottom-up anthropogenic emission inventories suggest a continued reduction of NO_x emissions in more recent years. This is consistent with the ongoing tendency of European air quality conditions towards the NO_x-limited regime (Jin et al., 2017), which is projected to continue in the future (Beekmann and Vautard, 2010). Downward anthropogenic emission trends have been suggested as an important driver of the decreasing trend in peak ozone concentrations in Europe (ETC/ACM, 2016).

Regional air quality (AQ) models are important tools for studying and forecasting ozone pollution. These models simulate processes relevant for ozone pollution at a resolution that can better capture observed spatial gradients compared to coarser global models. Regional AQ models can therefore be applied to simulate polluted conditions in or surrounding urban areas, or for air quality impact assessments. Coupled (or "online") meteorology-chemistry models resolve meteorology, transport, chemical transformation and removal of pollutants at the same spatial and temporal resolution. The coupled treatment of meteorology

and chemistry is mandatory, because ozone concentrations depend on feedbacks between meteorological and chemical processes: 1) O_3 sources such as chemical formation depend on radiation, temperature and water vapour (Coates et al., 2016; Pusede et al., 2015), and 2) O_3 sinks, such as dry deposition, also largely depend on meteorological drivers (Clifton et al., 2017; Kavassalis and Murphy, 2017). However, coupled regional air quality models are subject to several sources of uncertainties. These uncertainties are related to the limited knowledge on ozone precursor emissoins (Kuenen et al., 2014; Pouliot et al., 2015), the representation of boundary conditions (Giordano et al., 2015), tropospheric chemistry in the chemical mechanism (Knote et al., 2015), and the land surface and its feedbacks with tropospheric chemistry (Baklanov et al., 2014).

Many regional AQ models have been applied to simulate NO_x and O_3 in European summers, for research and forecasting purposes. Models tend to underestimate summertime NO_x compared to rural background in situ observations (Mar et al., 2016; Terrenoire et al., 2015). Comparison against satellite NO_2 column observations also revealed underestimations at regional scales (Aidaoui et al., 2015; Huijnen et al., 2010). Another study found both positive as well as negative biases, which were attributed to the coarse resolution of the emission inventories (Pope et al., 2015). AQ models satisfactorily reproduce the spatial distribution in summer O_3. However, mean O_3 can be under- or overestimated depending on the model and chemical mechanism (Mar et al., 2016; Terrenoire et al., 2015). In addition, many models consistently underestimate peak ozone values that typically occur in the afternoon (Im et al., 2015; Marécal et al., 2015; Solazzo et al., 2012; Tuccella et al., 2012). This is problematic for air pollution impact assessments, since the peak ozone values are important for determining the detrimental effects on human health and ecosystems.

The sensitivity of O_3 to its precursor NO_x, which is particularly pronounced in summer (e.g. Jin et al., 2017), suggests that there is good potential to improve O_3 simulations by constraining simulated NO_x with observations. The past 20 years have seen the development of methods to estimate NO_x emissions with satellite-based NO_2 columns in a mass balance approach, where biases in the model-simulated and satellite-observed NO_2 columns are used to update NO_x emissions. The technique has been applied in global models (Lamsal et al., 2008; Martin et al., 2003; Vinken et al., 2014b), and more recently also in regional models (e.g. Ghude et al., 2013). Applications of the technique include emission trend analysis (e.g. Lamsal et al., 2011) and source-specific constraints on NO_x emissions (e.g. Ghude et al., 2013; Verstraeten et al., 2015; Vinken et al., 2014a; Vinken et al., 2014b). Changes in NO_x emissions impact tropospheric chemistry, and therefore changes in O_3 are expected. This was shown by Ghude et al. (2013), who found local changes in surface O_3 mole fractions up to 10 ppb over India after satellite-based NO_x emission scaling. Verstraeten et al. (2015) reported ozone increases up to 8 ppb at 800 hPa (±1.5 km) in China after scaling local NO_x emissions with OMI observations, and found that simulated free-tropospheric ozone between 3-9 km was in better agreement

with tropospheric O_3 columns observed by the Tropospheric Emission Sounder. However, ozone changes at the surface after constraining NO_x emissions with satellite observations have thus far not been evaluated with in situ data to our knowledge.

Considering the importance of NO_x for simulations of ozone and the previously reported ozone changes after applying satellite-based NO_x emissions, we here investigate the potential improvement in simulated surface ozone concentrations over Europe due to the application of satellite observations of NO_2 to adjust NO_x emissions. To this end, we use the WRF-Chem meteorology-chemistry model (Grell et al., 2005) to simulate surface ozone in Europe in July 2015, at the approximate peak of the ozone season. We first perform a model evaluation with AirBase in situ NO_2 and O_3 observations (EEA, 2018) and OMI NO_2 column measurements from the recently released QA4ECV dataset (Boersma et al., 2017b). We subsequently derive a new, OMI-based ("top-down") NO_x emission inventory, and evaluate its effects on WRF-Chem simulations of surface NO_2 and O_3 with the independent AirBase observations.

The structure of the paper is as follows. We describe the model set-up and observations in section 2. Section 3 presents the method to calculate OMI-derived NO_x emissions. In section 4, we evaluate a WRF-Chem set-up with bottom-up emissions in situ and column observations, and in section 5 we describe the derived modified surface NO_x emissions. We evaluate the impacts on surface NO_x and O_3 with independent in situ observations in section 6. We conclude with a discussion (section 7) and summarize our conclusions in section 8.

2.2   Model and data description

2.2.1   WRF-Chem

We perform simulations with the coupled meteorology-chemistry model WRF-Chem, version 3.7.1 (Grell et al., 2005). The model domain consists of 170 by 170 cells at 20×20 km^2 horizontal resolution covering Europe, centered at 51.98°N and 5.66°E. Vertically, the domain extends from the Earth's surface up to 50hPa, and consists of 27 layers with 13 layers in the lowermost 1500m. Chemistry simulations of O_3 and its precursor groups NO_x and VOCs are performed with the CBM-Z gas-phase chemical mechanism (Zaveri and Peters, 1999). Simulations of atmospheric chemistry with this mechanism compare well with the European multi-model mean for summer O_3 in a gas-phase mechanism comparison study (Knote et al., 2015). A complete list of parameterization options adopted in our WRF-Chem setup can be found in Table A2.1. Our simulations were performed with a time stepping of 180 s for a period of 38 days (24 June - 31 July 2015), allowing a 1-week

spin-up to analyze the model output for July. An evaluation of large-scale meteorological performance with ERA-Interim reanalysis fields can be found in Section A2.2.

We used anthropogenic emissions from the TNO-MACC-III inventory (Kuenen et al., 2014) for 2011, the most recent inventory available when the model experiments were performed. TNO-MACC-III contains anthropogenic emissions for lumped species groups NO_x and VOCs. NO_x emissions were partitioned assuming that 97% is emitted as NO and 3% as NO_2. VOC emissions were divided over 15 emission categories in CBM-Z, following the VOC speciation by Archer-Nicholls et al. (2014). This speciation procedure is further described in Table A2.3. Point source emissions were distributed over the five lowermost model layers following sector-specific emission altitude profiles (Bieser et al., 2011).

Biogenic emissions of VOCs and soil NO_x were calculated online with the MEGAN model implementation within WRF-Chem (Guenther et al., 2006; Guenther et al., 2012). The domain-total biogenic isoprene emissions are 1.82 Tg of isoprene, which is slightly lower than the 9-year spread of 2-4.5 Tg isoprene for July, based on an inverse modeling study using OMI HCHO column measurements for 2005-2013 (Bauwens et al., 2016). We simulate lightning NO_x emissions using a parameterization based on cloud-top height (Price and Rind, 1993; Wong et al., 2013), using a flash rate of 80 mol flash^{-1} based on a recent satellite-based estimate (Pickering et al., 2016). Simulations with higher flash rates of 500 mol flash^{-1} (Ott et al., 2010) and 310 mol flash^{-1} (Miyazaki et al., 2014) resulted in overestimated upper-tropospheric contributions to the NO_2 columns relative to OMI.

Anthropogenic emissions are the dominant NO_x source over Europe in July with a total monthly emission strength of 304 Gg N (76%). Minor contributions are associated with lightning (81.4 Gg N; 20%) and soils (15.0 Gg N; 4%). We note that especially soil NO_x emissions are low compared to previous studies, in which soils, including agricultural areas, have been estimated to contribute 40% to the total European NO_x emission budget (Ganzeveld et al., 2010; Jaeglé et al., 2005).

Meteorological initial and boundary conditions were taken from ERA-Interim reanalysis data (Dee et al., 2011). Chemical boundary conditions for O_3, NO, NO_2, CO and peroxyacetyl nitrate (PAN) are taken from the CAMS chemical reanalysis product for Europe (Inness et al., 2015, retrieved at: `http://apps.ecmwf.int/datasets/data/cams-nrealtime/levtype=sfc/`). Upper boundary conditions for ozone were prescribed with climatological values (retrieved at: `https://www2.acom.ucar.edu/wrf-chem/wrf-chem-tools-community`).

2.2.2   AirBase NO_2 and O_3 in situ measurements

Surface measurements are taken from the European Air Quality Data Portal operated by the European Environment Agency, hereafter referred to as AirBase (EEA, 2018). We used all data at rural background stations from the validated E1a data stream. The

large availability of the data allows us to make a strict selection on data availability. For monthly averages, we discard stations if data is missing for more than 24 hours. Stations used for the evaluation of monthly averages at 12:00 h UTC may have a maximum data gap of 1 data point. This resulted in a final selection of 184-397 stations, depending on the performance metric (see Table 2.1). In our analysis of O_3 and NO_2 we evaluate monthly time series and mid-day (12:00 h UTC) concentrations (denoted as $[O_3]^{12h}$ and $[NO_2]^{12h}$, respectively). We additionally calculate the maximum daily 8-hour mean ozone concentration (MDA8 O_3), a widely applied metric for O_3 health impacts.

2.2.3 OMI NO_2 column measurements

We use tropospheric NO_2 columns from the Ozone Monitoring Instrument (OMI) onboard NASA's EOS Aura mission (Levelt et al., 2006). The polar-orbiting instrument detects radiation backscattered from the Earth's atmosphere. Retrieval of tropospheric vertical column densities (VCDs) from space follows a three-step procedure (Boersma et al., 2018b). First, total slant columns (SCDs; i.e., columns along the average light path through the atmosphere) are obtained from a spectral fit to the OMI-measured reflectance spectra in the visible wavelength range using the Differential Optical Absorption Spectroscopy (DOAS) method. Then, the stratospheric contribution component is separated from the total NO_2 column via data assimilation into the TM5 global Chemistry Transport Model (Dirksen et al., 2011). The final step is to obtain tropospheric VCDs by dividing the SCDs by a tropospheric Air Mass Factor (AMF) that describes the vertical sensitivity of the instrument to atmospheric NO_2 (Eskes and Boersma, 2003). This is a function of satellite viewing geometry, surface albedo, terrain height, cloud properties, and a priori NO_2 profile.

The recent EU FP7 project Quality Assurance for Essential Climate Variables (QA4ECV) has led to the development of a new OMI NO_2 data product (Boersma et al., 2017b). The underlying consortium retrieval algorithm is based on the NO_2 column retrieval principles described in Boersma et al. (2007), but with improvements in the three aforementioned steps (Boersma et al., 2018b). Zara et al. (2018) described how better wavelength calibration, and inclusion of liquid water absorption and an intensity offset-correction reduced uncertainties in NO_2 SCDs to $0.7 - 0.8 \times 10^{15}$ molec. cm^{-2} (up to ± 35 %). Lorente et al. (2017) improved the AMF calculation method via the extension of the AMF look-up table with more reference points, and a correction for the sphericity of the atmosphere. The ancillary data for the AMF calcultion has also improved relative to earlier algorithms such as DOMINO v2 (Boersma et al., 2011): surface albedo from the 5-year OMI albedo climatology (Kleipool et al., 2008), cloud information from the improved OMI O_2-O_2 algorithm (Veefkind et al., 2016), and a priori NO_2 profiles from TM5-MP at $1° \times 1°$ (Williams et al., 2017). The study by Lorente et al. (2017) also showed that substantial differences between AMFs arise when different a priori NO_2 profiles (as

well as surface albedo and cloud properties) are used in the retrieval. This underlines that a re-calculation of the tropospheric AMFs based on simulated WRF-Chem 20×20 km^2, replacing the coarse TM5-MP $1° \times 1°$ NO$_2$ profiles, may help to reduce model-satellite differences (Lamsal et al., 2010; Vinken et al., 2014a), and we will explore this further below.

2.2.4   AMF re-calculation

We take care to remove inconsistencies in the model-satellite comparison introduced by different assumptions about the vertical NO$_2$ profile in the satellite product compared to the model. The AMF calculation requires assumptions about the vertical profile of NO$_2$ to convert slant columns into vertical columns. We replace the a priori TM5-MP NO$_2$ profiles (at $1° \times 1°$) by WRF-Chem NO$_2$ profiles at a 20×20 km^2 resolution. This has two advantages: 1) model-satellite comparisons are no longer affected by differences in model assumptions between WRF-Chem and TM5-MP that lead to different vertical NO$_2$ profiles, and 2) the higher resolution WRF-Chem setup resolves spatial gradients in the a priori profile that are not appropriately captured in TM5-MP due to the coarser model resolution. Single-orbit results indicate that re-calculation of the AMFs leads to retrieved columns that are 1×10^{15} molec. cm^{-2} higher in densely populated areas, and lower or unaffected in surrounding non-urban regions. This effect has been seen before in earlier studies (Heckel et al., 2011; Huijnen et al., 2010; Maasakkers, 2013; Russell et al., 2011; Vinken et al., 2014a).

We apply the method described by Lamsal et al. (2010) and Boersma et al. (2016) to replace the TM5-MP vertical NO$_2$ profile by the WRF-Chem profile in the calculation of the air mass factor (AMF):

$$M_{trop,WRF-Chem} = M_{trop,TM5} \times \frac{\sum_{l=1}^{L} A_{trop,l} x_{l,WRF-Chem}}{\sum_{l=1}^{L} x_{l,WRF-Chem}} \qquad (2.1)$$

where M_{trop} is the tropospheric AMF based on an assumed profile from WRF-Chem or TM5, $A_{trop,l}$ is the tropospheric averaging kernel element for layer l, $x_{l,WRF-Chem}$ is the NO$_2$ column density in model layer l, and L is the uppermost TM5-MP layer in the troposphere. The tropospheric averaging kernel in Eq. 2.1 is defined as follows (Boersma et al., 2017a): $A_{trop} = A \times \frac{M}{M_{trop}}$, where M and M_{trop} refer to the AMF and the tropospheric AMF, respectively. Note that the WRF-Chem vertical NO$_2$ profile has been sampled at the TM5-MP vertical layer structure, so l refers to TM5-MP model layers.

2.3 Top-down NO$_x$ emissions: methods

Satellite-detected NO$_2$ columns are sensitive to NO$_x$ emissions at the surface. We exploit this dependence to derive satellite-based surface NO$_x$ emissions using local OMI NO$_2$ columns. We apply an improved version of the mass balance procedure (Lamsal et al., 2011; Martin et al., 2003; Vinken et al., 2014a), which accounts for non-linear feedback from NO$_x$ emission changes on NO$_2$ concentrations via OH:

$$E_{td} = E_{bu} \left(1 + \beta(1+\gamma)\frac{C_{OMI,bu} - C_{WC,bu}}{C_{WC,bu}} \right) \qquad (2.2)$$

where E_{bu} and E_{td} represent NO$_x$ emissions from the bottom-up inventory (bu) and the satellite-based top-down estimate (td), respectively. $C_{WC,bu}$ represents the monthly-averaged NO$_2$ vertical column density (VCD) simulated by WRF-Chem, and $C_{OMI,bu}$ is the monthly averaged modified QA4ECV OMI NO$_2$ VCD using air mass factors based on the original WRF-Chem NO$_2$ vertical profile ($C_{WC,bu}$, see Section 2.2.4). WRF-Chem NO$_2$ VCDs are co-sampled with valid OMI observations. We only use OMI and WRF-Chem data for pixels with valid satellite observations for at least 4 days in July 2015 to minimize the random error in the satellite retrieval.

We account for the nonlinear NO$_x$-OH chemistry feedback via a dimensionless scaling factor β, for which we performed a perturbation simulation with surface emissions increased by 20%:

$$\beta = \frac{\Delta E_{bu,1.2}/E_{bu}}{\Delta C_{bu,1.2}/C_{bu}} = \frac{0.2 C_{bu}}{\Delta C_{bu,1.2}} \qquad (2.3)$$

where C_{bu} are the NO$_2$ columns after a WRF-Chem simulation with bottom-up NO$_x$ emissions, and $\Delta C_{bu,1.2}$ is the change in NO$_2$ columns after perturbing bottom-up NO$_x$ emissions by +20%. In low-NO$_x$ environments, this perturbation leads to higher OH levels and thus to more efficient NO$_x$ loss to HNO$_3$, so that a $\beta > 1$ is needed to achieve column agreement. In NO$_x$-rich environments, however, OH levels are suppressed by enhanced NO$_x$ emissions so that the relative increase in NO$_2$ columns is larger than 20%, resulting in a $\beta < 1$. The use of β to account for the sensitivity of the NO$_2$ column to local emissions is essentially a linearization step of non-linear effects due to chemistry.

Application of Equations 2.2 and 2.3 would lead to updated NO$_x$ emissions, and consequently also to modifications in the WRF-Chem NO$_2$ profile shapes in response to the updates (e.g. Vinken et al., 2014a). This is accounted for via γ, which we also obtain from the simulation with +20% perturbed emissions:

$$\gamma = \frac{(C_{OMI,1.2} - C_{OMI,bu})/C_{OMI,bu}}{(C_{WC,1.2} - C_{WC,bu})/C_{WC,bu}} \tag{2.4}$$

where C_{WC} represents the WRF-Chem NO$_2$ vertical column density (VCD), and C_{OMI} represent the OMI NO$_2$ VCD retrieved using WRF-Chem NO$_2$ vertical profiles from the bottom-up simulation (C_{WC}), for the bottom-up (subscript bu) and emission perturbation simulation (subscript 1.2), respectively. Our approach to calculate γ differs from Vinken et al. (2014a), who derived γ from a separate simulation after accounting for β. Our approach requires one less forward simulation and is thus computationally more efficient, with little impact ($<3\%$) on total derived emissions compared to the approach by Vinken et al. (2014a).

We calculate the scaling factors β and γ for all land-based and shipping lane WRF-Chem cells based on monthly mean NO$_2$ columns (i.e., ocean-based pixels with emissions above a threshold value of 1 mol km^{-2} h^{-1}). These pixels thus also include shipping lanes and offshore oil platforms. OMI-inferred emission changes are calculated locally, i.e. for each individual model cell for which the aforementioned data availability criteria are fulfilled. This differs from previous work where these factors were calculated for regions containing multiple model cells (Vinken et al., 2014a; Vinken et al., 2014b) or for individual pixels in global models with a coarse resolution (e.g. Lamsal et al., 2011).

We discard the effect of transport of NO$_2$ away from the source region ('smearing'). In July, solar intensity in Europe is close to its annual peak, which means that the NO$_2$ lifetime is short due to efficient oxidation. Therefore, the clear-sky monthly mean NO$_2$ column difference between model and satellite is indicative of local NO$_x$ emission updates. Previous studies showed that this method reduces the model-satellite NO$_2$ column difference but does not resolve it completely (e.g. Ghude et al., 2013; Vinken et al., 2014a) as a result of the linearization that is applied in the perturbation calculation. Nonetheless, we will show in this study that the systematic bias between WRF-Chem and OMI NO$_2$ columns is largely removed after application of Eqns. 2.2-2.4.

Table 2.1: Performance statistics of WRF-Chem bottom-up and top-down simulations for July 2015 for several conventionally applied performance metrics (MBE, RMSE, slope and intercept of a linear regression fit of simulations against observations, and r^2 from orthogonal distance regression), as well as the index of agreement (d = 1 - $\frac{\sum_{i=1}^{N}(P_i - O_i)^2}{\sum_{i=1}^{N}(|P_i'|+|O_i'|)^2}$, Willmott, 1982), where P_i and O_i represent simulations and observations, respectively. MBE, RMSE and intercept have unit µg m^{-3}, slope, r^2 and d are unitless.

	n	Bottom-up						Top-down					
		MBE	RMSE	slope	intercept	r^2	d	MBE	RMSE	slope	intercept	r^2	d
$\overline{[O_3]}$	289	-2.37	2.50	0.26	54.27	0.32	0.60	2.18	17.03	0.34	53.23	0.41	0.68
$\overline{[O_3]}^{12h}$	397	-15.07	24.68	0.33	51.63	0.43	0.63	-7.56	19.09	0.41	51.13	0.58	0.74
MDA8 O$_3$	289	-14.24	24.79	0.28	55.98	0.40	0.61	-7.38	19.99	0.36	55.72	0.53	0.70
$\overline{[NO_2]}$	184	-2.49	3.86	0.73	-0.28	0.42	0.70	-1.09	3.09	0.89	-0.12	0.46	0.80
$\overline{[NO_2]}^{12h}$	250	-2.96	3.56	0.30	-0.03	0.25	0.51	-2.59	3.28	0.33	0.04	0.23	0.53

2.4   Bottom-up model evaluation

2.4.1   Surface O_3

We start our evaluation of O_3 chemistry in WRF-Chem (with bottom-up NO_x emissions, i.e. not yet based on the OMI-inferred NO_x emissions) by a comparison of monthly-averaged, 24-hour mean surface ozone simulations with AirBase observations (Fig. 2.1, panels a and b, and Table 2.1). WRF-Chem reproduces the spatial distribution of surface ozone satisfactorily, with an increase in surface O_3 concentrations from north to south, as reported elsewhere (e.g. Mar et al., 2016). Highest concentrations are found around the Mediterranean basin. O_3 concentrations over Central and Southern Europe are underestimated in WRF-Chem. Simulated monthly-averaged concentrations do not exceed 110 µg m^{-3}, while higher concentrations were observed at several stations in the southern part of the domain. Most notably, WRF-Chem does not capture observed high concentrations of $\pm$130 µg m^{-3} in northern Italy. The good agreement between WRF-Chem and in situ data in the western part of the domain close to the model boundaries with a prevailing westerly circulation indicates that the model boundary conditions describe inflow of long-lived compounds such as O_3 from the western boundary well.

Monthly averaged ozone concentrations are an important and widely used metric to evaluate model skill, but are not necessarily indicative of the peak ozone concentrations that typically occur in the afternoon. These monthly averages include the nocturnal conditions with generally the presence of stable boundary layers, in which the titration of ozone in the NO_x-saturated regions is difficult to model (e.g. Im et al., 2015). The simulated and observed monthly averaged ozone concentrations at 12:00 h UTC (Fig. 2.1, panels c and d) demonstrate a similar geographical distribution compared to the monthly average, but with higher values because photochemical ozone production generally peaks during daytime. This figure demonstrates that peak ozone values occur around the Mediterranean basin, most prominently in North Italy and Spain, where the levels of sunlight and ozone precursor concentrations are high. WRF-Chem shows elevated ozone with respect to adjacent areas, but maximum simulated ozone levels do not exceed 120 µg m^{-3}. This underestimation of peak ozone concentrations is also apparent from in Fig. 2.8b (discussed in more detail in Sect. 2.6), which shows the simulated versus the observed 12:00 h UTC ozone concentrations.

Our results are in agreement with previous regional chemistry model evaluations for Europe. Such studies typically focus on seasonal variability; we compare our results with the results for European summer (JJA) from those studies. Im et al. (2015) found that a model ensemble underestimates the daytime maximum O_3 concentration for sites where observed O_3 concentrations exceed 120-140 µg m^{-3}, which agrees with our results. In that study, the ensemble mean model bias tends to become more negative for observed
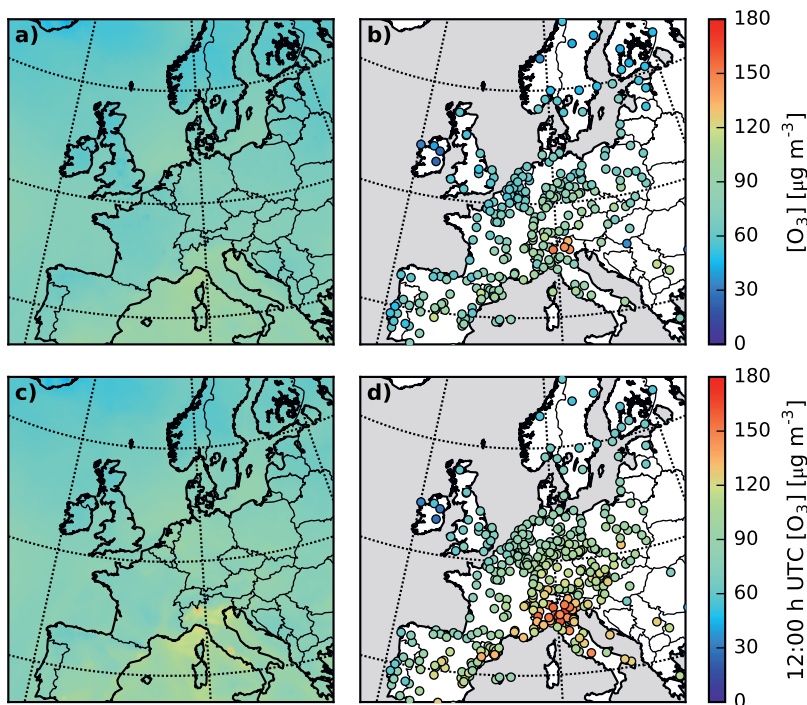
Figure 2.1: Monthly averaged surface O_3 and simulated by WRF-Chem with bottom-up NO_x emissions (a & c) and observed at AirBase stations (b & d). Panels a) and b) are monthly averages, and c) and d) are sampled at 12:00 h UTC.

concentrations above 80 µg m^{-3} (Im et al., 2015). The two ensemble members that use CBM-Z chemistry, similar to our WRF-Chem model set-up, are qualitatively in line with the ensemble mean, lending support to the use of CBM-Z in this study. Mar et al. (2016) compared two chemical mechanisms in a WRF-Chem evaluation study over Europe and reported large differences in the representation of peak summer (JJA) ozone: one chemistry model (MOZART) overestimates mean and MDA8 ozone, while simulations with the other chemistry scheme (RADM2) shows underestimations of peak ozone that are in line with our findings. We will discuss the dependence of ozone simulation on the chemical mechanism choice in detail in Sect. 2.7. The ensemble model mean daytime ozone concentration in Solazzo et al. (2012) is underestimated by 10-30 µg m^{-3} in four sub-regions of the European continent. Tuccella et al. (2012) analyzed WRF-Chem O_3 concentrations for 2007 and found that yearly-averaged mid-day ozone is underestimated by approximately 10 µg m^{-3}. The model performance in the aforementioned studies is qualitatively similar to our findings and the magnitude compares well. Overall, most studies consistently show underestimated daytime O_3, regardless of the chemical mechanism, model resolution and other model

assumptions. To further explore the potential role of a model misrepresentation of NO$_2$ concentrations in explaining this model O$_3$ bias, the next sections will focus on a model comparison with in situ and remote sensing data for NO$_2$.

2.4.2   Surface NO$_2$

Fig. 2.2 a and b present a comparison of monthly-averaged surface concentrations of NO$_2$ between WRF-Chem and AirBase (note the logarithmic scale). Performance statistics are shown in Table 2.1. We find that WRF-Chem reproduces the spatial distribution well, with peak NO$_2$ occurring in Northwest Europe and North Italy. In these regions with high NO$_x$ emissions, average WRF-Chem-simulated concentrations are however underestimated by up to 10 µg m^{-3} compared to observations. AirBase concentrations show a region with elevated NO$_2$ concentrations in Southwest Germany. WRF-Chem also shows elevated NO$_2$ concentrations in this region, but does not reach such elevated concentrations. Overall, WRF-Chem shows more spatial heterogeneity in surface NO$_2$ concentrations than is apparent from the observations. Observed NO$_2$ concentrations in background areas in Spain, France and Eastern Europe are 2-5 µg m^{-3} or higher, while the model consistently simulates values <2 µg m^{-3} in these regions. This overall underestimation is also seen in Fig. 2.8, where the simulated daily mean NO$_2$ concentration is shown against AirBase observations. The model performance of our WRF-Chem setup is in line with previous WRF-Chem studies. Mar et al. (2016) found small overestimations (0.67-2.96 µg m^{-3}) in mean NO$_2$. Another study found an annual average mean bias of -0.9 µg m^{-3}, caused by underestimations of peak NO$_2$ in WRF-Chem (Tuccella et al., 2012).

A comparison between WRF-Chem and AirBase monthly-averaged 12:00 h UTC NO$_2$ concentrations is presented in Figure 2.2c and d and Table 2.1. We find that WRF-Chem on average strongly underestimates mid-day NO$_2$ concentrations by 2.96 µg m^{-3} (38.5%).

2.4.3   NO$_2$ VCD

Before we perform a comparison between NO$_2$ VCDs from WRF-Chem and OMI, we first discuss the effect of the NO$_2$ profile shape on the OMI-retrieved columns. Figure 2.3 shows the change in the monthly-averaged OMI NO$_2$ column density after replacing TM5-MP NO$_2$ profiles by WRF-Chem profiles using the procedure described in Sect. 2.2.4. The OMI NO$_2$ VCDs change most prominently over urban/industrial areas such as the Netherlands, Paris, Berlin, Madrid, Milano and Rome. The background areas are largely unaffected, or show small (± 0.2 ×10^{15} molec. cm^{-2}) NO$_2$ VCD increases (e.g. Spain) or decreases (regions in France, Germany, Poland, Ukraine and Romania). The vertical NO$_2$ profile over sea regions in western Europe strongly peaks at the surface, because shipping
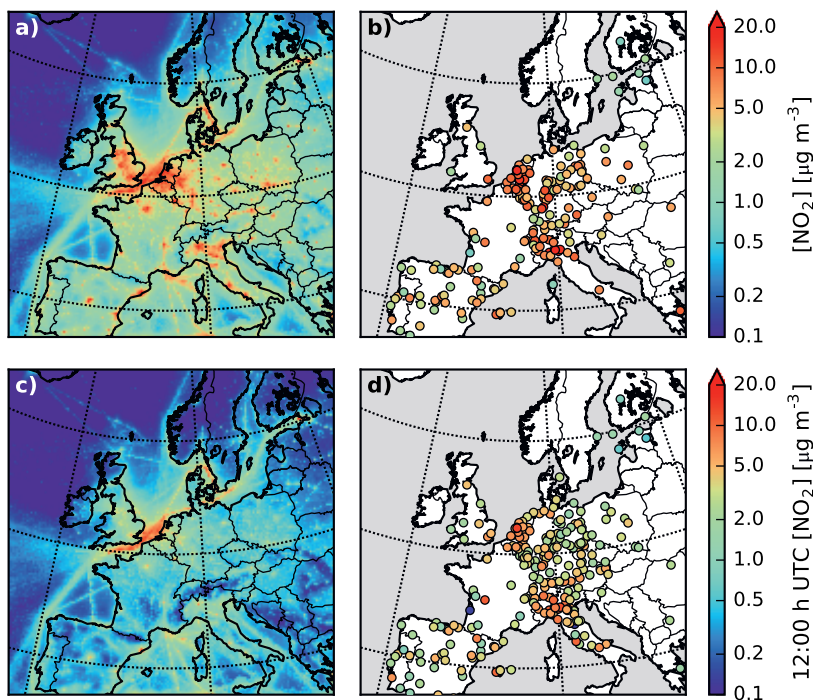
Figure 2.2: As Fig. 2.1, but for NO$_2$.

NO$_x$ in WRF-Chem is emitted in the lowermost model layer. Overall, the average NO$_2$ column change over non-land regions is small (<2%).

We subsequently compare WRF-Chem to this modified OMI product. The monthly-averaged NO$_2$ vertical column densities from WRF-Chem and OMI are displayed in Fig. 2.4. The model is sampled at 12:00 h UTC, close to the OMI overpass time of ±13:30 h LT, and is co-sampled with valid satellite observations. There is good agreement in the spatial distribution of monthly-averaged NO$_2$ VCDs (r^2 = 0.68). NO$_2$ columns are underestimated by 0.3×10^{15} molec. cm^{-2} on average, with strong underestimations of up to 2×10^{15} molec. cm^{-2} in urban and industrial northwestern Europe. WRF-Chem overestimates NO$_2$ columns in some isolated urban areas with high NO$_x$ emissions such as London, Madrid, Rome, and in parts of Eastern Europe.

We note that Fig. 2.4 shows small underestimations of the simulated NO$_2$ VCD compared to OMI ($\pm 0.2 \times 10^{15}$ molec. cm^{-2}) in background regions (e.g. the Alps, rural Spain and France, Scandinavia) and over the oceans. Simulated NO$_2$ columns therefore show stronger spatial gradients than OMI-retrieved columns, which is in line with Huijnen et al. (2010). Other distinct underestimations in the simulated NO$_2$ columns compared to OMI
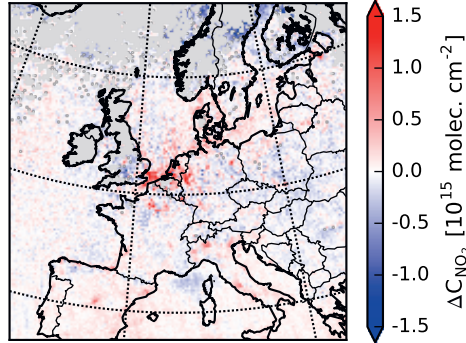
Figure 2.3: Change in monthly-averaged OMI-retrieved NO_2 columns after using WRF-Chem vertical NO_2 profiles to calculate the Air Mass Factors (AMFs) in the OMI retrieval, as described in Sect. 2.2.4.
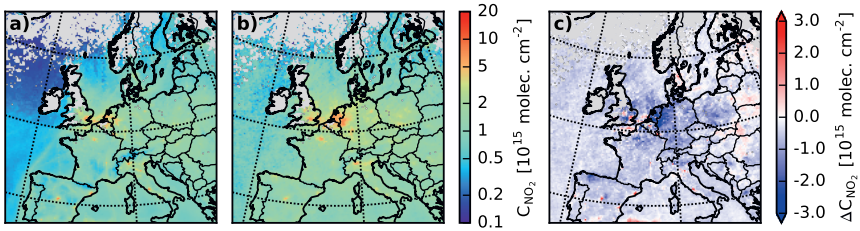
Figure 2.4: Monthly-averaged tropospheric NO_2 vertical column densities from a) WRF-Chem with bottom-up NO_x emissions, b) OMI and c) their difference (WRF-Chem - OMI). WRF-Chem NO_2 columns have been co-sampled with OMI, and pixels are shown when $n_{obs} \geq 4$.

indicate a misrepresentation of emissions. For example, the simulated NO_2 column in northwestern Spain is underestimated by 2×10^{15} molec. cm^{-2} compared to OMI. The enhanced NO_2 columns in this region mainly reflect the contribution to atmospheric NO_x by power plant emissions. Although emissions from power plants should have decreased in recent years in this region (Zhou et al., 2012), these emissions seem to be underestimated in WRF-Chem. However, since these results are only representative or July 2015, a more dedicated analysis is needed to further corroborate this hypothesis.

We have shown that our WRF-Chem set-up with bottom-up emissions underestimates NO_2 with respect to both surface and column measurements. To combine these model comparisons against different data sources, we already discuss parts of Fig. 2.9, which compares the agreement between simulations with bottom-up and top-down emissions. Fig. 2.9a shows the relative difference of WRF-Chem against AirBase and OMI NO_2
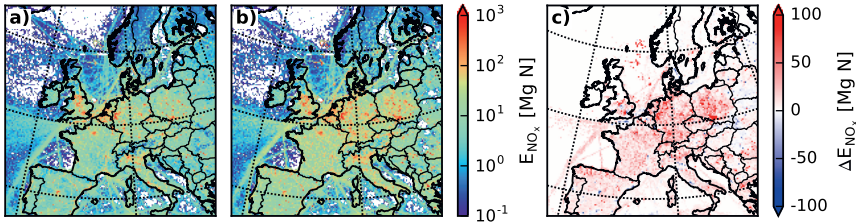
Figure 2.5: Surface NO$_x$ emissions for a) the a bottom-up simulation (TNO-MACC-III anthropogenic + MEGAN soil NO$_x$), and b) the top-down simulation; c) depicts the change in surface NO$_x$ emissions after the recalculation procedure.

binned as a function of bottom-up anthropogenic emission strength. This shows an overall underestimation of WRF-Chem at the surface and in the troposphere, except for regions with strongest emissions. There is a relatively larger model underestimation of surface NO$_2$ than of the NO$_2$ VCD in regions with comparatively low emissions. Given that the surface NO$_2$ mixing ratios are more sensitive to surface emissions than the NO$_2$ column (Li and Wang, 2019), this suggests that emissions are generally too low in WRF-Chem, but especially that emissions in rural background regions, are underestimated. This, in turn, suggests that the representation of surface NO$_x$ emissions in WRF-Chem (anthropogenic emissions for 2011 and on-line calculated natural soil emissions) are too low to explain the observations in July 2015. In the following section, we will derive satellite-constrained NO$_x$ emissions and discuss potential reasons for this mismatch.

2.5 Satellite-derived NO$_x$ emissions

2.5.1 Top-down emissions

We derive top-down NO$_x$ emissions using the method described in Section 2.3. Fig. 2.5 shows the July total bottom-up and top-down surface NO$_x$ emissions and their difference. Top-down NO$_x$ emissions amount to 498 Gg N, which is 56% higher than the bottom-up inventory, and increases occur across the domain (Fig. 2.5c). NO$_x$ emissions are reduced in several isolated grid cells that generally correspond to urban areas. The difference between top-down and bottom-up emissions is larger than the 16% increase reported by Miyazaki et al. (2017), although that study found strong (40-67%) local increases in areas with high NO$_x$ emissions such as Belgium, western Germany and northern Italy.

Our top-down emissions are much higher than the bottom-up emissions over Germany and Poland. Over Belgium and the Netherlands, the difference between top-down and bottom-up emissions is also substantial, but notably smaller despite larger differences
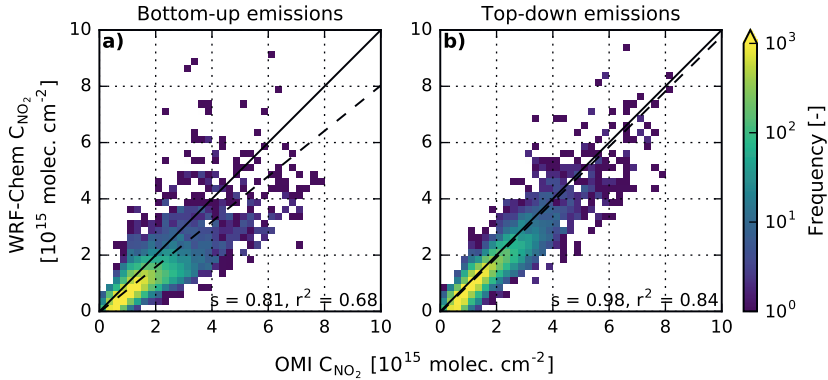
Figure 2.6: NO$_2$ vertical column density scatter plots of WRF-Chem against OMI, presented as a heat map with a bin size of 0.25×10^{15} molec. cm^{-2}, for WRF-Chem with bottom-up emissions (a), and WRF-Chem with OMI-derived top-down surface NO$_x$ emissions (b).The OMI NO$_2$ VCDs in panels a) and b) are calculated with AMFs based on NO$_2$ vertical profiles of the WRF-Chem simulations against which they are compared, to ensure a consistent model-satellite comparison. The solid black lines represent the 1:1 line, and the dashed lines display the orthogonal distance regression fits.

between OMI and WRF-Chem NO$_2$ columns over the low-countries (Fig. 2.4c). This reflects the chemical regime with very high bottom-up NO$_x$ emissions in this region, resulting in suppressed mid-day OH concentrations, and consequently, longer NO$_2$ lifetimes (as diagnosed by low beta values over northwestern Europe in Fig. A2.1).

We subsequently replace bottom-up emissions with our observation-constrained top-down NO$_x$ emissions and perform a new WRF-Chem simulation. As expected, the new NO$_2$ columns agree much better with the OMI NO$_2$ columns than those from the simulation with bottom-up emissions (Fig. 2.6). WRF-Chem with bottom-up emissions generally underestimates OMI NO$_2$ columns by 23.4%. As expected, the simulations with the top-down emissions agree better with OMI, and the slope of 0.98 between the new WRF-Chem and OMI NO$_2$ columns (Fig. 2.6b) suggests that the systematic underestimation in the model is effectively resolved by applying the top-down emissions. The mean relative error is reduced to -7.5%, and the spatial correlation coefficient between WRF-Chem and OMI NO$_2$ also improves considerably (from 0.68 to 0.84).

2.5.2 Attribution to emission sources

Fig. 2.7 shows the bottom-up and top-down NO$_x$ emissions as a function of the bottom-up anthropogenic emission strength. This comparison demonstrates that top-down NO$_x$ emissions are higher than bottom-up emissions regardless of the emission strength. However,
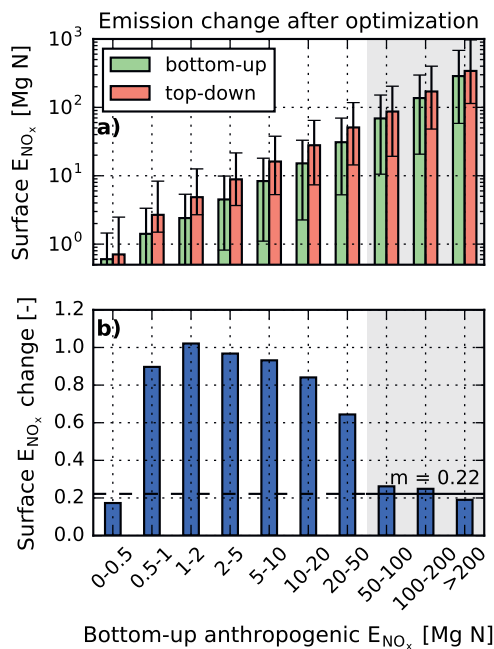
Figure 2.7: Difference between bottom-up and top-down surface NO$_x$ emissions, expressed as a) a bar plot (note the logarithmic scale) of median emissions binned by bottom-up anthropogenic NO$_x$ emissions (error bars indicate the inter-quartile range), and b) a bar plot of relative emission differences $\left(\frac{posterior-prior}{prior}\right)$ between the bars in panel a). In panel b) we define the relative anthropogenic emission difference to be the median of the relative change between top-down and bottom-up emissions in anthropogenic-dominated regions (shaded, with bottom-up emissions >50 Mg N month^{-1} cell^{-1}.

top-down emissions are 50-100% higher than bottom-up estimates for relatively weak emissions between 0.5-50 Mg N month^{-1} cell^{-1}, and only up to 20% higher for some urban and industrial hotspots (Fig. 2.7b). This 0.5-50 Mg N month^{-1} range is dominated by WRF-Chem grid cells located in the rural areas of Europe, excluding the largest urban agglomerations as well as low-emission regions such as mountainous areas. Our substantially larger top-down emissions partly reflect a required increase in NO$_x$ emissions in areas where soil NO emissions are expected to be a dominant NO$_x$ source. Soil NO emissions are simulated in WRF-Chem using an implementation of the MEGAN biogenic emission model. The observed discrepancy between the WRF-Chem-simulated and OMI-observed NO$_2$ VCD triggers to assess how much of this discrepancy can be attributed to this model's representation of soil NO emissions.

To separate the soil NO$_x$ contribution from the anthropogenic emission updates, we perform a simple budget calculation as a first-order constraint on the partitioning of the top-down emissions between their anthropogenic and soil-based sources. We assume that the relative difference in anthropogenic sources is uniform over the emission bins in Fig. 2.7. This factor is calculated as the median of the relative change in emissions for the three highest bins (>50 Mg N cell^{-1} for July, see Fig. 2.7), and amounts to 0.22. This allows us to attribute the remaining emission difference to soils. Based on this crude first estimate, we derive top-down soil NO$_x$ emissions to be 112 Gg N month^{-1}, versus WRF-Chem/MEGAN-simulated bottom-up soil NO emissions of only 15 Gg N month^{-1}. The anthropogenic enhancement factor is relatively uncertain, but does not strongly impact our derived posterior soil NO$_x$ emission estimate: if, instead of the median (m = 0.22), we use the mean relative change in emissions for the three highest bins ($\mu = 0.41$), our soil contribution is still a factor >4 larger (69.0 Gg N month $^{-1}$) compared to WRF-Chem's simulated bottom-up soil NO source. Therefore, this first-order estimation suggests that a substantial fraction (43-69%) of the NO$_x$ emission increment after optimization can be attributed to soils.

To evaluate the derived total soil NO$_x$ emissions, we perform a comparison with literature-based estimates in Table 2.2. We find that bottom-up soil NO$_x$ emissions are under-estimated by a factor 5-7 compared to previous studies. In some of those studies (e.g. Ganzeveld et al., 2010), land use management practices (fertilizer and manure application) provide a substantial contribution to European soil NO emissions, a feature that appears to be missing in the representation of soil NO emissions in WRF-Chem. This supports our hypothesis that a substantial fraction of the increase in surface NO$_x$ emissions may be attributed to soils. We will discuss this further in Sect. 2.7.

Table 2.2: Comparison of WRF-Chem surface NO$_x$ emissions in July (in Tg N month^{-1}, unless indicated otherwise) with literature-reported values.

	Year	Region	Surface	Anthropogenic	Soils	Soils (%)
This study, bottom-up	2015	Maps in this study	0.32	0.30	0.015	4.7
This study, top down, after bias attribution (see Sect. 2.5.2)	2015	Maps in this study	0.50	0.39-0.43	0.07-0.11	14-22
Stohl et al. (1996)	1994	-24.6-41.9°E, 34.9-72.1°N	-	-	-	17.6[1]
Ganzeveld et al. (2010)	2000	-16-41°E, 34-64°N	-	-	0.14	-
Jaeglé et al. (2005)	2000	-15-45°E, 35-60°N	0.59	0.35	0.25	42.3
Miyazaki et al. (2017)	2005-2014	-10-30°E, 35-60°N	0.33-0.38	-	-	-
Dammers (2013)	2005-2007	-15-35°E, 35-70°N	-	-	0.09	-
Lathière et al. (2005) referenced in Dammers (2013)	1983-1995	-15-35°E, 35-70°N	-	-	0.13	-

[1] This estimate is based on summer (JJA) estimates.

2.6   Emission scaling impacts on surface NO_2 and O_3

2.6.1   Nitrogen dioxide

Table 2.1 summarizes the model performance of our bottom-up and top-down WRF-Chem simulations against a large number of AirBase NO_2 observations throughout Europe in July 2015. The simulation with top-down emissions improves upon the a priori run in all metrics. Most notably, the model index of agreement (d) improves by 0.10 (14%). The modified model set-up still slightly underestimates the monthly averaged observed NO_2 observations, as indicated by a slope of 0.89. However, the low bias in WRF-Chem surface NO_2 concentrations with respect to AirBase improves from -2.5 to -1.1 µg m^{-3}.

Compared to the monthly average, we find little improvement in WRF-Chem's skill to predict surface NO_2 at 12:00 h UTC. The model's low bias in NO_2 reduces from -3.0 to -2.6 µg m^{-3} and the index of agreement improves by only 0.02 (4%). This more modest improvement in performance can be understood from mid-day surface NO_2 concentrations being more strongly driven by photochemical removal processes and boundary layer development than the 24-hour mean NO_2 levels, that are more sensitive to NO_x emissions due to strongly reduced mixing and photochemistry at night. Fig. 2.8 displays WRF-Chem monthly, 24-hour mean NO_2 concentrations against AirBase observations, for the bottom-up (black) and top-down (red) simulations. The model orthogonal distance regression (ODR) slope improves considerably, while the explained variance of the model improves slightly to 0.46.

Fig. 2.9 shows the relative biases between WRF-Chem and observed NO_2 as a function of (binned) bottom-up anthropogenic NO emission strength. Both the WRF-Chem simulations with bottom-up emissions (Fig. 2.9a) as well as the simulation with top-down emissions (Fig. 2.9b) show a low bias against OMI and AirBase for regions with low emissions, and a positive relative bias in regions with stronger emissions. The relative bias is however considerably reduced in the simulation with top-down NO_x emissions, both at the surface and in the column. However, WRF-Chem still displays a stronger relative bias compared to AirBase than compared to OMI. This feature can likely be attributed to a difference in spatial scales between the 20×20 km^2-resolution model versus the footprint area of local AirBase measurements, which can be easily influenced by a nearby NO_x source that is less well captured in the model, due to instantaneous mixing over a larger volume. Another potential explanation for the stronger relative bias of WRF-Chem compared to AirBase than compared to OMI is interference of in situ measurements with molybdenum converters (see Sect. 2.2.2). This is in line with our previous finding that the slope of the top-down NO_2 column regression fit approaches 1, while the slope of the fit for in situ NO_2 observations is still below 1. We also note that the spread in the relative bias
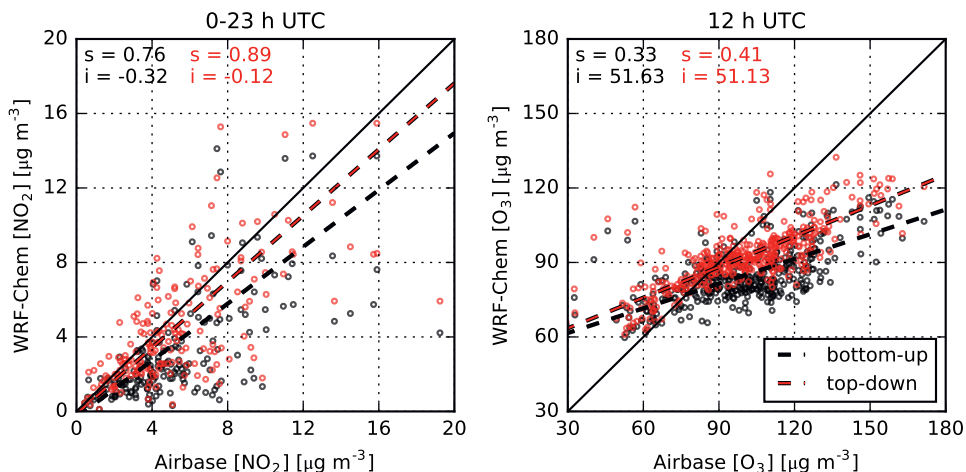
Figure 2.8: Scatter plots of monthly averaged simulated concentrations of a) NO$_2$ and b) O$_3$ against AirBase observations. Panel a) shows monthly averages for 0-23 h UTC, while panel b) is sampled at 12 h UTC. The black solid lines represent the 1:1 line.

compared to AirBase increased for the top-down simulation, with more positive relative bias values for all bins. Nonetheless, the results shown in Fig. 2.9 provide confidence regarding application of the model as a tool to reconcile local-scale bottom-up emissions and concentrations with larger-scale remote sensing-based NO$_2$ measurements.

2.6.2   Ozone

Next, we address our main question whether the improved simulation of NO$_2$ leads to better model performance for surface ozone simulations. We find that WRF-Chem with top-down emissions improves upon the bottom-up simulation for both the 24-hour mean, as well as the 12:00 h UTC and MDA8 ozone metrics. The model index of agreement improves by 0.08-0.11 (13-17 %, Table 2.1). However, the top-down model still simulates too low surface O$_3$, especially over southern, eastern and central Europe, where observed surface O$_3$ exceeds 80 µg m^{-3} at 12:00 h UTC (see Fig. 2.11).

A comparison between monthly averaged mid-day O$_3$ concentrations from the bottom-up and top-down simulation (Fig. 2.11, panels a and b, respectively) shows that ozone increases across the model domain. This particularly improves the WRF-Chem-AirBase agreement in large parts of western and Central Europe. The simulated ozone values in northern Italy remain underestimated.
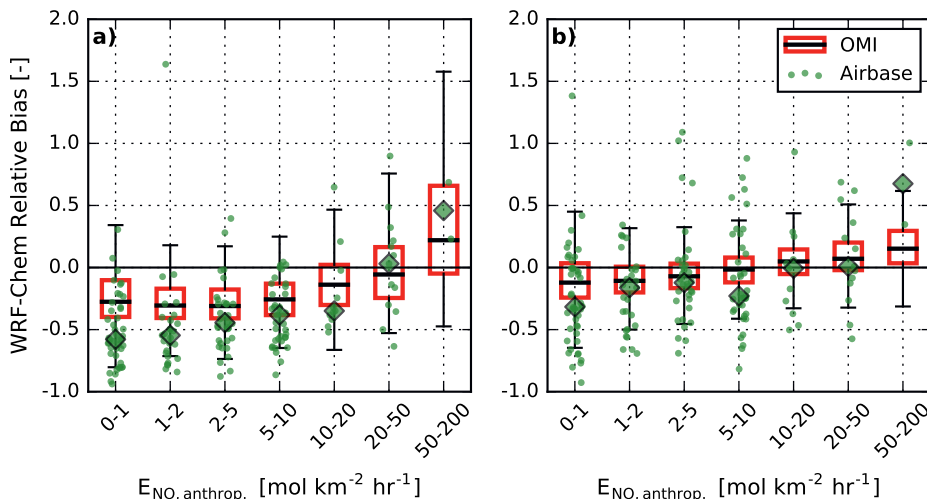
Figure 2.9: Relative bias $\left(\text{RB} = \frac{\text{model - observations}}{\text{observations}}\right)$ of WRF-Chem against land-based OMI NO_2 vertical column densities (box plots) and AirBase in situ NO_2 measurements (green scatter), binned by bottom-up anthropogenic NO emission strength, for the bottom-up (a) and top-down WRF-Chem simulation (b). Green diamonds indicate the median WRF-Chem RB against AirBase observations for pixels within every emissions bin.

Surface ozone concentrations display a strong increase due to the use of top-down NO_x emissions (Fig. 2.11). The areas where ozone concentrations increase by >10 µg m^{-3} largely coincide with regions where top-down NO_x emissions are much higher than the bottom-up emissions (Fig. 2.5c), such as in northern Spain, southern Germany, southern Poland, Croatia, Serbia, western Greece and southern Romania. There are also strong simulated ozone increases in central France and over the Adriatic Sea. These regions are all characterized as (rural) background areas, where ozone formation is strongly sensitive to the increases introduced in the NO_x emissions for the relatively low bottom-up anthropogenic and soil emissions. We find decreases in ozone around the main shipping lanes, where the higher NO_x emissions further enhance ozone titration. The enhanced titration also reduced simulated surface ozone around urban regions such as Barcelona, Rome, and Paris. The increases in surface NO_x emissions in the BeNeLux and western Germany slightly increase simulated mid-day surface ozone. Ozone production is less sensitive to NO_x emissions in these high NO_x-emitting regions compared to the unpolluted background (Beekmann and Vautard, 2010; Jin et al., 2017; Mar et al., 2016).

Fig. 2.8 shows that O_3 simulations with the higher top-down NO_x emissions lead to a somewhat better match between modeled and observed surface O_3, with an improvement in spatial correlation coefficient from 0.43 to 0.57, and an increase in slope from 0.33 to

0.41. Overall, the model low bias has reduced from -15 to -8 µg m^{-3}, which indicates that the use of OMI NO$_2$ VCD data to constrain WRF-Chem surface NO$_x$ emissions results in a considerable improvement regarding simulation of surface layer O$_3$ concentrations.

We additionally analyzed changes in the temporal evolution of ozone concentrations resulting from NO$_x$ emission changes (Fig. 2.10). Daytime median O$_3$ concentrations are better captured in the Po Valley, Central Spain and Poland. The NO$_x$ emission changes lead to a model overestimation of surface O$_3$ concentrations for Central France and South Germany, while concentrations change only slightly in the BeNeLux and Ruhr areas. In those regions, the mean bias error increases, while the hourly correlation coefficient and RMSE values improve for all regions (Table A2.4). In all areas, changes in NO$_x$ emissions lead to increased ozone concentrations particularly during daytime. Enhancements in simulated night-time concentrations are only observed in Central Spain. In other areas, night-time O$_3$ concentrations are overestimated in both simulations. Peak daytime O$_3$ concentrations are better captured in all areas, as evidenced by the increase of the 75th percentile of simulated O$_3$ concentrations with top-down emissions. However, peak O$_3$ concentrations remain underestimated in the Po Valley, Central Spain and South Germany. Additionally, nighttime O$_3$ concentration overestimations remain, likely due to issues related to model resolution and vertical mixing. Overall, the NO$_x$ emission changes most effectively increase O$_3$ concentrations during periods with elevated ozone (Fig. A2.3), which coincide with high solar radiation and temperatures and thus have a strongly NO$_x$-dependent O$_3$ formation.

2.7   Discussion

In this study we demonstrate the added value of deriving satellite-based NO$_x$ emissions in (regional) air pollution models for simulations of summertime ozone, focusing on July 2015 over Europe. We use a modified version of the mass balance approach introduced by Martin et al. (2003), with further improvements by Lamsal et al. (2011) and Vinken et al. (2014a). Although many studies report differences in simulated (surface) ozone concentrations after applying this mass balance approach (e.g. Ghude et al., 2013), we are aware of only one other study that used observations to validate subsequent ozone changes. Verstraeten et al. (2015) used TES O$_3$ observations in the global chemistry model TM5 in a study on trans-continental transport of Asian air pollution, and found an improved model-satellite agreement in lower-tropospheric ozone. However, their approach did not allow for an evaluation of model performance closer to the surface.

The mass balance approach that we used to derive observation-constrained European NO$_x$ emissions has several important advantages over more formal inversion methods that are applied in the literature (e.g. Miyazaki et al., 2014; Miyazaki et al., 2017). The method is highly traceable due to the simple calculation of scaling parameters from model output
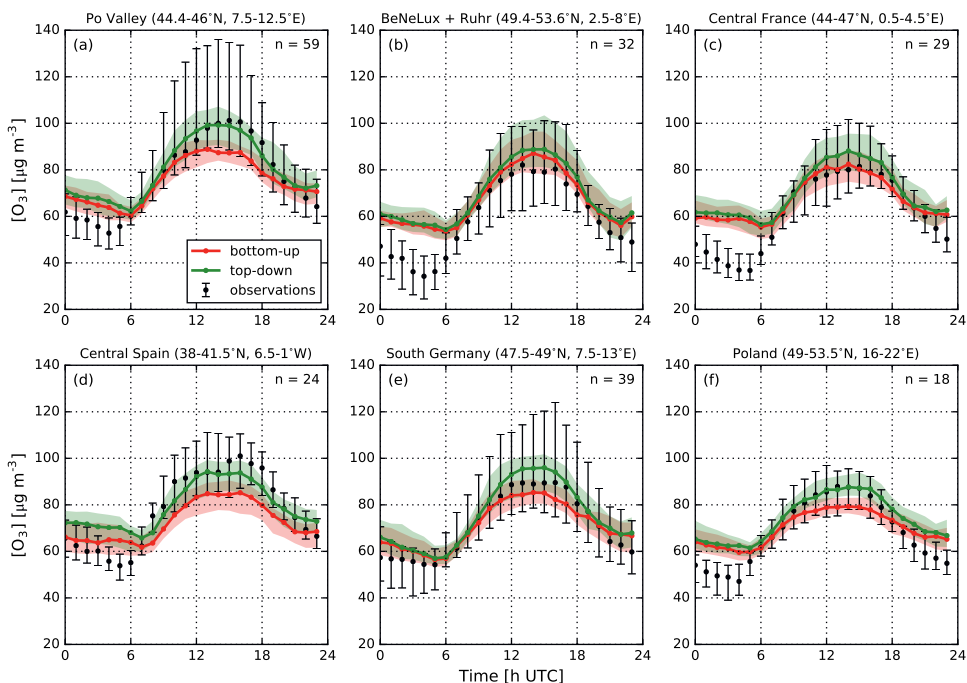
Figure 2.10: July 2015 monthly median diurnal ozone concentrations for six representative regions in Europe, as simulated by WRF-Chem with bottom-up NO_x emissions (green line) and top-down NO_x emissions (red line), and as observed at AirBase stations in these regions. Shaded areas and whiskers indicate the inter-quartile range. Results represent the median over all model-observation comparisons per region. The sample size for the comparison is displayed on the top right of each subplot.

for a baseline and perturbation simulation, and column NO_2 measurements. However, the linearization (see Sect. 2.3) oversimplifies the nonlinearity of the NO_x-O_3 chemistry, which means that the model-satellite discrepancy is not resolved completely after one iteration. Additionally, the approach is only applicable on a pixel-basis when the NO_x lifetime is sufficiently short to discard the contribution of transport from adjacent model NO_2 columns. The model-satellite difference for a simulation we performed for March 2015 (not shown) shows less spatial heterogeneity over regions with a diffuse spatial distribution of NO_x sources (e.g. Germany). These shortcomings can be resolved by averaging the signal over multiple grid cells, or by applying more formal inversion methods.

Our results demonstrate that surface NO_x emissions in our WRF-Chem configuration are increased substantially after applying an emission scaling approach. In a first-order budget calculation we derive that 43-69% of this total increase can be attributed to soil NO_x. This is diagnosed from the notably higher relative increase in emissions in
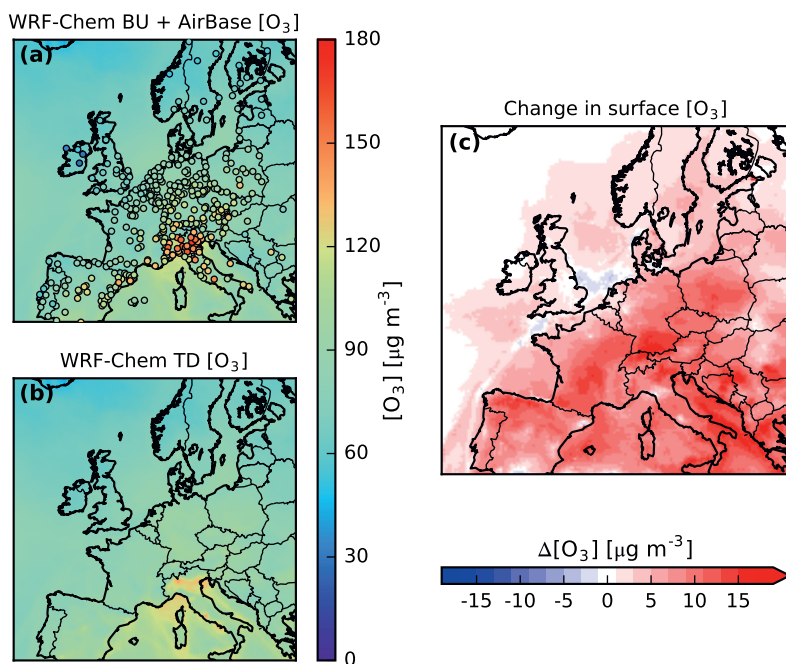
Figure 2.11: Monthly-averaged 12:00 h UTC surface O_3 concentration with bottom-up (BU, panel a) and top-down (TD, panel b) NO_x emissions. Panel c shows the difference between the two monthly averages (TD - BU).

regions with moderate anthropogenic emissions compared to regions with low and high anthropogenic emissions. We therefore conclude that the contribution of soil NO_x to total surface emissions is likely underestimated in our model set-up. Additionally, our top-down soil NO_x emission estimate, derived with a budget calculation, agrees well with previous estimates for European summer (Table 2.2). Our findings are in line with a previous study (Oikawa et al., 2015) that, using WRF-Chem with MEGAN soil NO_x emissions, found a strong underestimation of NO_x emissions in a high-temperature agricultural region.

Several studies previously investigated the relation between soil NO_x emissions and O_3 formation. For example, one study estimated that European soil NO_x emissions contribute 4 ppb to the daily maximum concentration (Stohl et al., 1996). A sensitivity study by Li et al. (2019) indicates that a strong up-scaling of soil NO_x emissions by a factor 5 indeed leads to a better representation of the peak ozone concentration. It has further been shown that an improved process-based representation of soil NO_x emissions leads to MDA8 O_3 changes by up to 6 ppb (Rasool et al., 2016), and a reduced mean bias for ozone concentrations, particularly in agricultural areas (Rasool et al., 2019). Together, these findings provide support for the hypothesis that underestimated soil NO_x emissions,

in particular those from agricultural areas, contribute to underestimated peak ozone concentrations.

The comparison against in situ NO$_2$ observations from the AirBase network may be hindered by interference of reactive N species for measurements with molybdenum converters. The type of converter is not reported in the database. Literature-reported estimates of measurement overestimations due to this interference are 22% (Dunlea et al., 2007) and 5-18% (Boersma et al., 2009) at urban sites, and 20-42% at a rural site (Steinbacher et al., 2007). A correction factor can be applied to obtain corrected NO$_2$ measurements from observations using a molybdenum converter, which is on average 0.4-0.6 in summer, but with a large spread (0.2-0.8) (Lamsal et al., 2008; Lamsal et al., 2010). The strongest corrections of molybdenum-based in situ NO$_2$ measurements are needed in remote environments, where NO$_x$ is a relatively smaller component of the total reactive nitrogen budget compared to areas closer to NO$_x$ sources (Lamsal et al., 2008). We hypothesize that this can partially explain the remaining model-observation mismatch for NO$_2$ after the use of top-down emissions.

Despite the demonstrated improvement in ozone simulations, our simulation with OMI-derived top-down NO$_x$ emissions still misrepresents the high tail of the ozone distribution. We believe that there is a potential explanatory role for local to regional meteorological processes. The representation of several mesoscale phenomena requires a higher model resolution than 20×20 km^2. For example, Millán et al. (1997) demonstrated that local re-circulation of residual air masses from higher aloft, containing elevated O$_3$ transported aloft during previous days, can be entrained in the boundary layer and contribute substantially to air pollution episodes in southern Europe. This is supported by an analysis of measured ozone (precursors) in northeast Spain by Querol et al. (2017), where this mesoscale circulation pattern was found to contribute to concentrations that exceed the information threshold value set by the European Union (180 µg m^{-3}), alongside contributions from locally emitted NO$_x$ and biogenic VOCs.

Simulations of surface ozone in AQ models are also impacted by the choice of chemical parameterization. Recently, several studies have investigated the influence of the chemical mechanism on simulated NO$_x$ and O$_3$ concentrations. Regarding ozone chemistry, chemical mechanisms differ predominantly in two aspects: 1) the grouping of VOC species in species categories ("lumping") according to their chemical structure or number of C-atoms, and 2) the inorganic rate coefficients involved in the catalytic cycling of NO$_x$, HO$_x$ and O$_x$. Especially the latter aspect has a strong influence on simulated NO$_2$ concentrations, and can therefore influence the derivation of top-down emission estimates using satellite observations (Stavrakou et al., 2013). Coates et al. (2016) investigated the maximum ozone formation potential in different chemical mechanisms and found that mechanisms with lumped VOC categories led to lower ozone mixing ratios compared to a mechanism with a near-explicit treatment of VOCs. Knote et al. (2015) found small differences in

inorganic rate constants among mechanisms and thus concluded that VOC representation was the dominating source of uncertainty among mechanisms. However, Mar et al. (2016) performed a WRF-Chem sensitivity study where MOZART inorganic rate constants were applied within RADM2, leading to mean O_3 concentration differences of 8 µg m^{-3} between those mechanisms.

In order to test the importance of inorganic NO_x-HO_x-O_x reaction rates for ozone formation, we implemented inorganic rate constants from three different mechanisms (CBM-Z, RADM2 and MOZART) in a mixed layer model with simplified chemistry (Janssen et al., 2012). Further details are given in Section A2. Our analysis shows that varying the temperature-dependent rate constant of HNO_3 formation ($k_{NO_2 + OH}$) can lead to a spread of 2 ppb for end-of-afternoon ozone values on a typical summer day in a polluted boundary layer. CBM-Z uses the lowest $k_{NO_2 + OH}$ among the considered mechanisms, and thus leads to a higher NO_2 lifetime and more O_3 formation than in other mechanisms. Therefore, we conclude that modification of inorganic reaction rate constants has a modest effect on simulated O_3, but is not likely to lead to increases in simulated O_3 in our WRF-Chem configuration. Nevertheless, the model representation of ozone chemistry should be carefully considered in NO_x and O_3 air quality studies, besides the representation of NO_x emissions.

Several studies have considered the resolution dependence of air quality simulations. This is especially relevant for NO_2, since NO_x emissions display strong variation on the 20×20 km^2 scale applied in this study. Increasing model resolution leads to better representation of these local gradients and therefore improves simulations of NO_2 concentrations (Schaap et al., 2015). Valin et al. (2011) found that an accurate representation of mid-day NO_2 columns from highly localized sources requires a high model resolution, but regions with more diffuse sources can be simulated at a coarser resolution of $\pm 10 \times 10$ km^2. Although ozone production regimes do not strongly depend on the model resolution in regional models, high resolution models perform better at simulating local O_3 titration in freshly emitted NO plumes (Cohan et al., 2006).

Besides the representation of meteorological processes, there is an additional uncertainty related to surface-atmosphere exchange of pollutants. Dry deposition constitutes 17% of the tropospheric sink of ozone, and is the second most important removal process after chemical removal (Hu et al., 2017). Several studies have recently investigated the role of meteorological drivers that determine ozone removal at the surface. However, these meteorological controls are oversimplified in deposition parameterizations. The vapour pressure deficit strongly controls stomatal uptake of ozone, thereby affecting surface ozone levels in spring to summer in the United States (Kavassalis and Murphy, 2017). Analysis of 10-year O_3 flux observations in the northeastern United States revealed that the removal of ozone by the land surface exhibits a strong inter-annual variability, which is not captured in dry deposition parameterizations (Clifton et al., 2017). Lastly, the role of soil moisture has been proposed as a regulator of surface ozone uptake (Tawfik and Steiner, 2013) and is

often neglected in parameterizations of dry deposition, even though a recent study found that it can significantly reduce simulated ozone uptake (Anav et al., 2018). Improving the biophysical representation of the dry deposition process in WRF-Chem will be one of our foci in the future.

Future studies that apply satellite-based constraints on surface NO_x emissions can benefit from observations from the recently launched TROPOMI instrument (Veefkind et al., 2012), which delivers NO_2 column data at an unprecedented resolution of 7×3.5 km^2. This has the potential to lead to important improvements in satellite-constrained NO_x emissions. Recent work (Lorente et al., 2019) has applied TROPOMI observations in a column model study to derive emissions from Paris. The resolution of the instrument additionally enables the focus on more local areas with one dominating source such as soils in agricultural or bare-soil regions.

2.8   Conclusions

We performed a WRF-Chem simulation of NO_x and ozone over Europe for July 2015 and assessed its performance with AirBase in situ observations and OMI NO_2 column measurements. We find that WRF-Chem underestimates high surface ozone concentrations in central and southern Europe, and overestimates lower ozone concentrations in northern Europe. The model also underestimates the spread. The monthly averaged mean bias error (MBE) is relatively small (-2.4 µg m^{-3}, 10%). WRF-Chem underestimates daytime increases in ozone concentrations, as evidenced by substantial negative MBE values for the mid-day (12 h UTC) O_3 concentration and MDA8 O_3 (-15.1 µg m^{-3} and -14.2 µg m^{-3}, respectively). We relate the low bias in surface ozone to biases in ozone precursor concentrations. Of particular relevance are nitrogen oxides, which drive ozone production in much of NO_x-limited summertime Europe.

For NO_2, we find that WRF-Chem underestimates surface and column NO_2 values for most of the domain, with exception of some high-emission regions. With respect to AirBase, WRF-Chem monthly averaged surface NO_2 is biased low by -2.5 µg m^{-3} (-73%). The spatial distribution of WRF-Chem column NO_2 agrees well with OMI (r^2 = 0.68), and a mean underestimation of 0.3×10^{15} molec. cm^{-2} (-23%). We attribute the low bias in WRF-Chem NO_2 concentrations to underestimations in surface NO_x emissions in WRF-Chem. We subsequently derive optimized NO_x emissions based on the WRF-Chem/OMI relative difference using a mass balance approach. Overall emissions increase from 0.32 to 0.50 Tg N, an increase of 0.18 Tg N (+56%), for July 2015. The updates indicate that NO_x emissions should be scaled up across the domain. The relative increase in emissions is largest for regions with moderate emission strength (up to 50 Mg N month^{-1} cell^{-1}) and coincides with regions where agricultural soil NO_x emissions are substantial. Our

optimized soil NO_x emissions amount to 0.1 Tg N, in much better agreement with values from the literature.

A WRF-Chem simulation with optimized NO_x emissions removes the model's systematic bias with respect to OMI NO_2, and leads to an improved spatial agreement (slope = 0.98, r^2 = 0.84). An evaluation against AirBase NO_2 reveals that the top-down simulation improves particularly in the monthly average, where the systematic mismatch is reduced (slope = 0.89 instead of 0.73) and the mean bias is reduced by 50%. For ozone, the model skill improves particularly for mid-day and MDA8 O_3, when local ozone formation occurs and the sensitivity of ozone formation to NO_x concentrations is highest. On average, surface O_3 concentrations increase by 6 µg m^{-3} (6%). Still, peak (mid-day) ozone values are underestimated after NO_x emission optimization.

Overall, our findings demonstrate that air quality model simulations combined with in situ and remote sensing observations can be used to infer missing sources of NO_x at the surface. By optimizing NO_x emissions with satellite observations, substantial improvements in simulated ozone can be achieved. Our work shows that this helps to reduce the persistent biases in O_3 that most air quality models are suffering from. Projected decreasing trends in anthropogenic NO_x emissions will mean that the contribution of soils to total European NO_x emissions will likely increase in the future, and thus deserves careful attention in (European) air quality assessments, along with detailed assessments of emissions of volatile organic compounds and wildfires, boundary layer mixing, and chemistry.

A2 Appendix

A2.1 WRF-Chem namelist

Table A2.1: Parameterization schemes used in the WRF-Chem setup.

WRF-Chem option	Parameterization scheme (reference)
Physics	
Microphysics	Morrison double-moment (Morrison et al., 2009)
Longwave radiation	CAM (Collins et al., 2004)
Shortwave radiation	CAM (Collins et al., 2004)
Surface layer	MYNN2 (Nakanishi and Niino, 2006)
Land surface physics	Noah land surface model (Tewari et al., 2004)
Boundary layer physics	MYNN2 (Nakanasi and Niino, 2009; Nakanishi and Niino, 2006)
Cumulus parameterization	Grell 3D Ensemble Scheme (Grell and Devenyi, 2002)
Lightning physics	PR92 neutral buoyancy (Price and Rind, 1993)
Chemistry	
Gas-phase chemistry	CBM-Z (Zaveri and Peters, 1999)
Photolysis parameterization	Madronich F-TUV (Tie et al., 2003)

A2.2 Meteorology evaluation

Meteorological reanalysis data

A European-wide meteorology evaluation performed by Mar et al. (2016) and numerous other studies demonstrated the skill of WRF-Chem to simulate several meteorological variables relevant to O$_3$ formation (radiation, temperature, wind speed and wind direction, boundary layer height). We further evaluated WRF-Chem's performance to simulate meteorology by comparing to the ERA-Interim reanalysis product (Dee et al., 2011), for five variables that are important for surface ozone: surface pressure, 2m temperature, relative humidity, wind speed and wind direction. This complements the comparison with meteorological station observations (e.g. Mar et al., 2016), and has the additional advantage that it is continuous in space.

Results

To evaluate the meteorology in WRF-Chem we perform a comparison with the state-of-the-art ECMWF operational reanalysis product (hereafter referred to as ECMWF reanalysis). Model performance metrics for the meteorological evaluation for the two simulated months are shown in Table A2.2, for which show the monthly average of single-day comparisons.

We only calculate performance metrics for land-based pixels, as the oceanic pixels generally contribute less to the overall bias. Overall, WRF-Chem shows good performance compared to ECMWF-reanalysis data, and WRF-Chem-ECMWF differences between March and July are consistent in sign.

WRF-Chem performs best at simulating surface temperature and pressure, but relative humidity and wind speed and -direction are simulated with less accuracy. Surface temperature is slightly underestimated, which agrees well with the cold bias generally found in WRF(-Chem) (e.g. Holtslag et al., 2013; Kleczek et al., 2014). Surface pressure is in general slightly underestimated, although we must note that this comparison is limited by terrain height differences in ECMWF reanalysis compared to WRF-Chem. Relative humidity is overestimated substantially in WRF-Chem, by approximately 10%. This potentially impacts simulated surface ozone in WRF-Chem, as there is an important role for surface atmospheric humidity, which governs the VPD in combination with temperature, in describing ozone removal at the surface (Kavassalis and Murphy, 2017).

We found an approximately linear increase in the model bias (defined in this section as WRF-Chem - ECMWF reanalysis) for RH in July, with a slope of 0.2% d^{-1}. This coincides with a linear decrease in the bias from 0.12 K to -0.98 K, which would suggest that the domain-averaged latent energy flux is overestimated, leading to an enhanced moisture flux to the atmosphere and underestimated temperatures. For all other variables we did not observe a clear change in domain-average model biases with time, indicating that model performance is robust over the simulation period. Overall, this evaluation, in combination with recent WRF-Chem meteorology evaluation studies (e.g. Mar et al., 2016) provides confidence in WRF-Chem's skill to reproduce domain-averaged surface meteorological conditions.

Table A2.2: Meteorological evaluation of two one-month WRF-Chem simulations with ECMWF operational reanalysis fields for five key surface meteorological variables. Only land-based pixels are used in the evaluation.

	March					July				
	μ_{ERA}	μ_{WRF}	r^2	MB	RMSE	μ_{ERA}	μ_{WRF}	r^2	MB	RMSE
T_{2m} [K]	281.51	280.52	0.77	-0.95	2.86	296.33	295.38	0.87	-0.95	2.69
P_{sfc} [hPa]	978.90	976.61	0.83	-2.29	18.56	972.94	972.28	0.96	-0.67	7.98
RH [%]	61.74	71.55	0.41	9.81	18.19	53.21	63.81	0.42	10.60	19.11
WS_{10m} [m s^{-1}]	4.78	5.45	0.56	0.68	2.08	3.34	4.51	0.50	1.17	1.95
WD_{10m} [°]	181.70	180.39	0.44	1.30	82.53	215.18	209.83	0.34	-5.35	85.71

A2.3   Emission speciation

Table A2.3: Distribution of TNO-MACC non-methane VOC emission categories over VOC species in CBM-Z.

CBM-Z	TNO-MACC-III
e_ch3oh	alcohols
e_c2h5oh	alcohols
e_hc3	propane, butanes, ethyne
e_hc5	pentanes
e_hc8	hexanes & higher alkanes
e_ol2	ethene
e_olt	propene
e_oli	other alk(adi)enes & alkynes
e_tol	benzene, toluene, other aROUatics
e_xyl	xylene, trimethylbenzenes
e_hcho	methanal
e_ald	other alkanals, ethers
e_ket	ketones
e_ora2	acids

A2.4   Spatial plots of emission scaling parameters
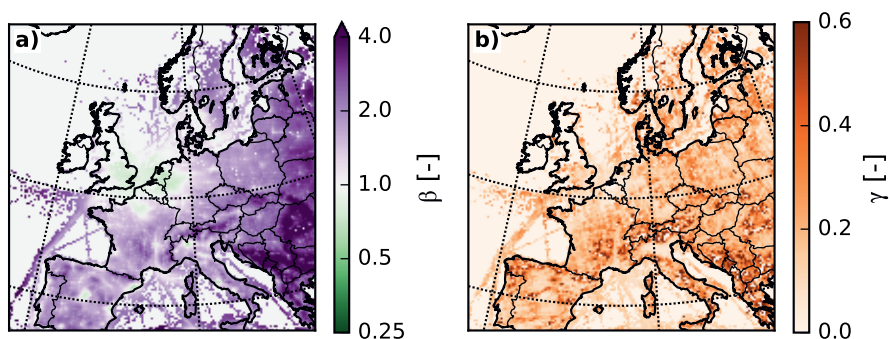
Figure A2.1: Spatial plots of monthly-averaged values of a) β and b) γ, calculated following Eqns. 3 and 4 (in main text), respectively.

A2   Sensitivity study on inorganic reaction rates

A recent study investigated the representation of inorganic rate constants for tropospheric O_3 formation in WRF-Chem, and found a strong impact on the monthly average of 8 µg m^{-3} when using MOZART inorganic rate constants in RADM2 (Mar et al., 2016). To evaluate the potential impact of this on our simulations, we apply the mixed-layer and chemistry model MXLCH (Janssen et al., 2012), which uses a simplified version of the MOZART mechanism. We set up this case as follows in order reproduce polluted conditions occurring in the Mediterranean, in order to determine the impact of inorganic reaction rates on the production of ozone in a well-mixed boundary layer: The location is set at 45.5°N/3.4°E (Southern France), initial O_3 concentrations in the mixed layer and the free troposphere are set to 62 ppbv and 78 ppbv, respectively, initial NO and NO_2 concentrations in the mixed layer are set to 1.6 ppb and 4.0 ppb, respectively, we apply NO and CO emission fluxes representative for relatively polluted conditions (0.15 ppb s^{-1} and 2.0 ppb s^{-1}, respectively), and we add two reactions to this mechanism representing HO_x cycling via reaction with O_3.

From a comparison of rate constants among the mechanisms CBM-Z, RADM2 and MOZART, we found the largest differences in rate constants for the reaction forming HNO_3 ($NO_2 + OH + M \longrightarrow HNO_3 + M$), while other inorganic rate constants are much more comparable. This is in line with the rate constant comparison by Knote et al. (2015). We modify the temperature-dependent rate constants of the reaction forming HNO_3 ($k_{NO_2 + OH}$) according to Fig. A2.2 (panel a), and subsequently we study the sensitivity of afternoon ozone concentrations to $k_{NO_2 + OH}$.

The NO_2 concentration and lifetime increase with decreasing rate constants, but the impact of $k_{NO_2 + OH}$ on NO_2 concentrations is rather small (Fig. A2.2c). The relative impact on OH is stronger (Fig. A2.2d): the NO_2 availability in combination with $k_{NO_2 + OH}$ drives OH loss, causing increasing OH concentrations for a decrease in k_{NO_2+OH}.

HNO_3 formation in CBM-Z has a somewhat lower rate constant compared to other mechanisms, and therefore leads to a longer NO_2 lifetime. This accelerates O_3 formation, and thus leads to higher afternoon O_3 concentrations. The upper right panel of Fig. A2.2 shows that the inter-mechanism spread is ±2 ppbv. From this sensitivity analysis with a simplified representation of atmospheric chemistry within the atmospheric boundary layer, we conclude that there is some sensitivity of afternoon O_3 concentrations to the representation of inorganic reactions, particularly HNO_3 formation, involved in O_3 chemistry.
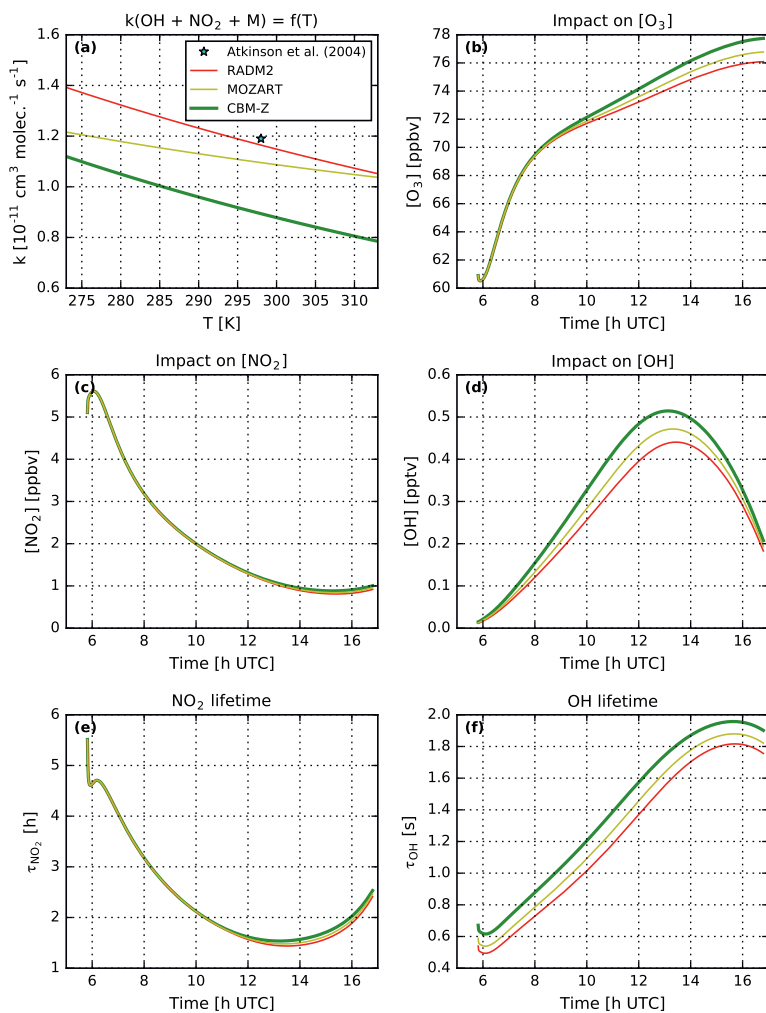
Figure A2.2: Temperature-dependence of rate constants for the reaction $NO_2 + OH + M \longrightarrow HNO_3 + M$ from three different mechanisms (panel a), and the resulting impacts on O_3 (pabel b), NO_2 (c) and OH (d). Panel a additionally gives the IUPAC-recommended value under standard conditions (P = 1 bar, T = 298 K) given by Atkinson et al. (2004). The lifetimes of NO_2 and OH are given in panels e and f, respectively.
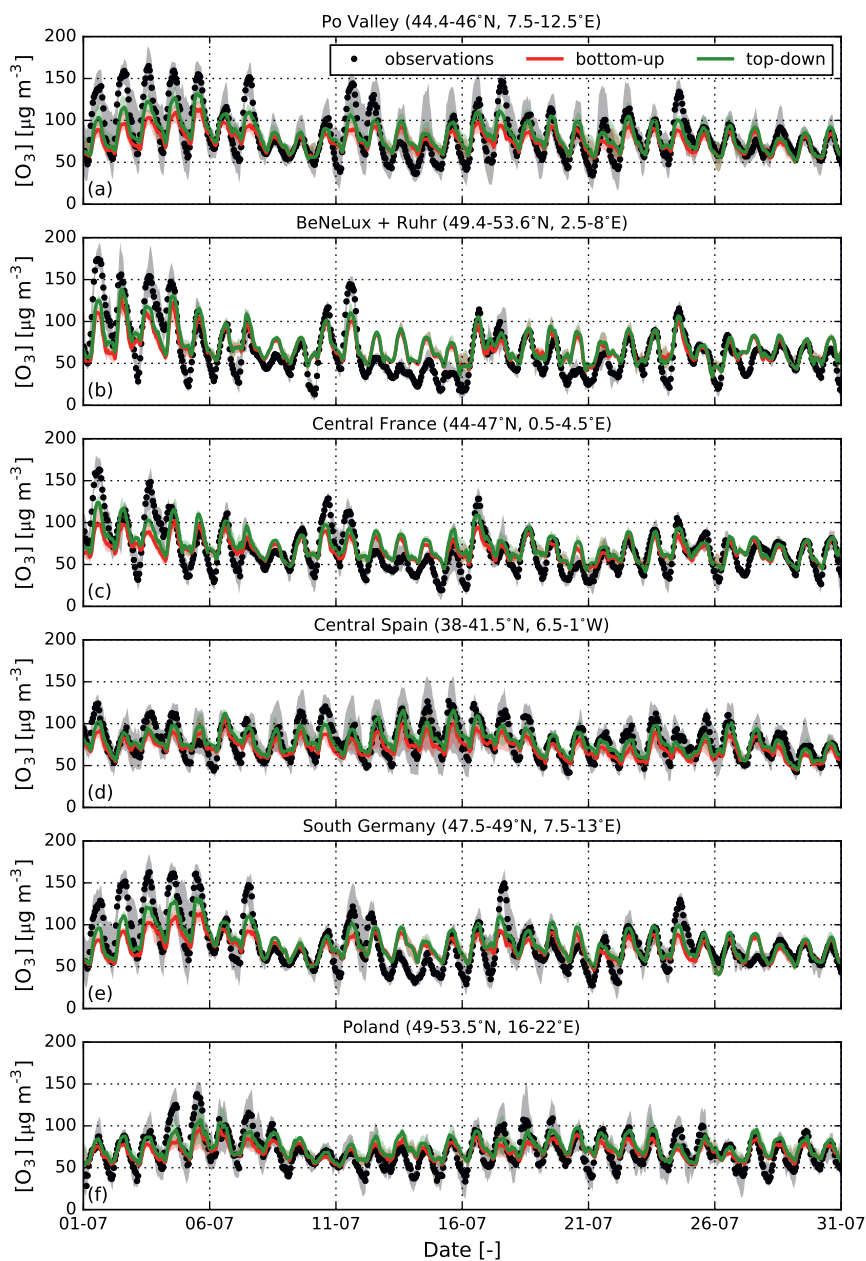
Figure A2.3: July 2015 time series of the median (shaded areas show inter-quartile range) O_3 concentrations as observed at AirBase stations (black dots), and as simulated by WRF-chem with bottom-up (red) and top-down emissions (green). Medians are calculated by including all stations (resp. co-sampled simulations) in the latitude/longitude range specified in the subplot titles.

Table A2.4: Model performance statistics for surface ozone concentration time series of the WRF-Chem simulation with bottom-up and top-down emissions for six European regions.

	Po Valley	BeNeLux + Ruhr	Central France	Central Spain	South Germany	Poland
n (stations)	59	32	29	24	39	18
			Bottom-up			
MBE	-20.14	16.82	3.35	-22.40	-11.15	1.74
RMSE	68.07	71.48	59.92	45.39	68.68	43.64
r	0.80	0.78	0.76	0.81	0.74	0.77
			Top-down			
MBE	-1.58	25.94	17.29	-1.33	5.02	16.10
RMSE	55.08	68.57	56.48	36.44	58.13	41.81
r	0.85	0.81	0.79	0.83	0.81	0.80

Chapter 3

Ozone deposition impact assessments for forest canopies require accurate ozone flux partitioning on diurnal timescales

Abstract

Dry deposition is an important sink of tropospheric ozone that affects surface concentrations, and impacts crop yields, the land carbon sink and the terrestrial water cycle. Dry deposition pathways include plant uptake via stomata and non-stomatal removal by soils, leaf surfaces and chemical reactions. Observational studies indicate that ozone deposition exhibits substantial temporal variability that is not reproduced by atmospheric chemistry models due to a simplified representation of vegetation uptake processes in these models. In this study, we explore the importance of stomatal and non-stomatal uptake processes in driving ozone dry deposition variability on diurnal to seasonal timescales. Specifically, we compare two land surface ozone uptake parameterizations - a commonly applied 'big leaf' parameterization (W89; Wesely, 1989) and a multi-layer model (MLC-CHEM) constrained with observations - to multi-year ozone flux observations at two European measurement sites (Ispra, Italy, and Hyytiälä, Finland). We find that W89 cannot reproduce the diurnal cycle in ozone deposition due to a mis-representation of stomatal and non-stomatal sinks at our two study sites, while MLC-CHEM accurately reproduces the different sink pathways. Evaluation of non-stomatal uptake further corroborates the previously found important roles of wet leaf uptake in the morning under humid conditions, and soil uptake during warm conditions. The misrepresentation of stomatal versus non-stomatal uptake in W89 results in an overestimation of growing-season cumulative ozone uptake (CUO), a metric for assessments of vegetation ozone damage, by 18% (Ispra) and 28% (Hyytiälä), while MLC-CHEM reproduces CUO within 7% of the observation-inferred values. Our results indicate the need to accurately describe the partitioning of the ozone atmosphere-biosphere flux over the in-canopy stomatal and non-stomatal loss pathways to provide more confidence in atmospheric chemistry model simulations of surface ozone mixing ratios and deposition fluxes for large-scale vegetation ozone impact assessments.

3.1 Introduction

Ozone (O_3) in the atmospheric surface layer is an air pollutant that is toxic to humans and plants. Ozone is removed by oceans, bare soil and vegetated areas, which together are called 'dry deposition' and account for $\pm$ 15-20% of the total tropospheric ozone sink (Bates and Jacob, 2020; Hu et al., 2017). In vegetation canopies, the dominant deposition pathway is stomatal uptake, which typically accounts for 40-60% of the total deposition to vegetation (Fowler et al., 2009). Stomatal ozone uptake reduces carbon assimilation in vegetation (Ainsworth et al., 2012; Sitch et al., 2007), affects the terrestrial water cycle (Arnold et al., 2018; Lombardozzi et al., 2015; Sadiq et al., 2017) and causes economic damage through reduced crop yield (e.g. Tai et al., 2014). Besides stomatal uptake, ozone removal occurs via a range of non-stomatal removal mechanisms such as uptake by the leaf exterior and soils, and in-canopy chemical removal involving nitrogen oxides (NO_x) or plant-emitted reactive carbon species. The contribution of these ozone removal processes to the total non-stomatal term is uncertain (Fowler et al., 2009), and displays temporal variability on diurnal to inter-annual timescales that is incompletely understood (Clifton et al., 2020c). Given that these non-stomatal removal processes act in parallel to the stomatal removal of ozone, characterization and quantification of non-stomatal sinks is important for quantification of total and stomatal ozone uptake.

The contribution of different ozone uptake pathways cannot be routinely measured at the plant canopy level due to the various non-stomatal uptake pathways. Most studies infer stomatal conductance (g_s) from canopy-top micro-meteorological and eddy covariance observations using an inverted form of the Penman-Monteith equation (e.g. Clifton et al., 2017; Clifton et al., 2019; Ducker et al., 2018; Fowler et al., 2001), although some studies apply alternative g_s estimation methods based on gross primary production (GPP; Clifton et al., 2017; El-Madany et al., 2017). In such observation-based studies, the non-stomatal ozone removal component (g_{ns}) is generally treated as the residual of the total uptake 'conductance' (g_c, inferred based on the ozone dry deposition velocity) and g_s. However, sites with long-term ozone flux measurements are scarce (Clifton et al., 2020c), which limits characterization of the seasonal to inter-annual temporal variability in the stomatal and non-stomatal components of ozone removal. Several campaign-based studies partitioned total canopy ozone fluxes by using ozone flux measurements along a vertical gradient, to study the in-canopy flux divergence and relate this to the vertical distribution of ozone sinks in the canopy (Fares et al., 2014; Finco et al., 2018), but these are limited to short timescales. Given the scarce availability of ozone deposition observations that span at least one year, and preferentially multiple years, quantifying temporal variability in stomatal and non-stomatal ozone deposition solely based on observations remains challenging.

Studies of ozone deposition (and its impacts) on regional to global scales rely on application of atmospheric chemistry models and their dry deposition parameterizations. Many models

treat deposition in a zero-dimensional manner and do not, or only implicitly, account for the variation of different in-canopy loss pathways as a function of environmental drivers and height within the canopy (the "big leaf" approach, Clifton et al., 2020c). Recent advances in the description of ozone deposition have been made by improving the simulation of stomatal conductance (Clifton et al., 2020a; Lin et al., 2019), improved representation of various non-stomatal removal terms (e.g. Potier et al., 2015; Stella et al., 2019; Stella et al., 2011; Zhang et al., 2003) and in-canopy turbulence and radiation extinction (Makar et al., 2017). Additionally, some models account for vegetation ozone damage via effects on photosynthesis and stomatal conductance (Arnold et al., 2018; Lombardozzi et al., 2015; Sadiq et al., 2017). Another class of models treats the canopy as a separate exchange regime with different biophysical and chemical conditions compared to the lowermost atmospheric layer, and explicitly resolves in-canopy vertical gradients of ozone deposition and its driving variables by using multiple in-canopy layers (e.g. Fares et al., 2014; Ganzeveld et al., 2010; Ganzeveld et al., 2002b; Otu-Larbi et al., 2020). Despite these advances in the representation of ozone deposition in atmospheric chemistry models, their application for ozone impact assessments remains a challenge. For example, the description of stomatal conductance is an important parameter for understanding year-to-year variability in impact metrics such as cumulative uptake of ozone (CUO; Clifton et al., 2020c), but stomatal versus non-stomatal ozone flux partitioning in these models is uncertain. Additionally, spatio-temporal controls of ozone deposition pathways remain incompletely understood (Clifton et al., 2017; Clifton et al., 2020c), in part owing to the scarcity of long-term ozone flux observations. Therefore, we here study temporal controls on stomatal and non-stomatal ozone deposition pathways, and their implications for simulations of CUO, using two multi-year ozone deposition datasets as well as a big leaf and multi-layer parameterization of land surface ozone uptake.

Specifically, we investigate the added value of an explicit multi-layer canopy representation of ozone deposition (MLC-CHEM: the Multi-Layer Canopy-CHemistry Exchange Model; Ganzeveld et al., 2002b) compared to a commonly applied big leaf parameterization (Wesely, 1989) in terms of simulating ozone deposition pathways and ozone impact metrics. We first study long-term (seasonal to annual) and short-term (diurnal) temporal variability in ozone dry deposition to forest canopies at a pristine boreal site (Hyytiälä) and a prealpine site that frequently experiences high ozone concentrations (Ispra). We then evaluate the performance of a big-leaf and a multi-layer representation of atmosphere-biosphere exchange in simulating ozone dry deposition pathways and their temporal variability. Subsequently, we characterize the relationship of non-stomatal conductance as a function of environmental drivers. Lastly, we aim to demonstrate how representations of the drivers of long- and short-term variability in ozone stomatal and non-stomatal removal in those different land surface parameterizations affect simulated CUO. To this end, we employ multi-year canopy-top observations of micro-meteorology, ozone mixing ratios, surface energy balance components and fluxes of ozone to derive the stomatal and

non-stomatal components of the total ozone flux, combined with observation-driven ozone dry deposition simulations using the two aforementioned representations.

3.2   Data and Methods

3.2.1   Site description

Our study makes use of half-hourly observations of micro-meteorology (net radiation, air pressure, air temperature, relative humidity, precipitation, wind speed, friction velocity) surface energy balance components and fluxes of CO_2 and ozone from two forested flux observation sites (Ispra and Hyytiälä), which are detailed below.

The Ispra Forest Flux station is situated in a deciduous forest in Northern Italy (45.81°N, 8.63°E) at the European Commission Joint Research Centre (EC-JRC) in a 10 hectare almost natural ecosystem mainly consisting of Quercus robur (80%), Alnus glutinosa (10%), Popolus alba (5%) and Carpinus betulus (3%). Leaf Area Index (LAI) shows an average value of 4.1 m^2m^{-2} during the growing season (Fumagalli et al., 2016). In our analysis we rely on continuous LAI measurements unavailable at this site, which we therefore take from a remote sensing product derived from MODIS (Xiao et al., 2014). The LAI range at Ispra in this product is 0.7-3.7 m^2m^{-2}, scaled up to a locally measured LAI maximum of 4.5 m^2m^{-2} in July 2015 (Fumagalli et al., 2016) using a seasonally varying sinusoidal scaling function. The turbulent flux measurements of surface energy balance components and ozone were performed in 2013-2015 at 36m above ground level, approximately 10m above the canopy height of 26m. More information regarding the measurement setup of this site can be found in Gruening et al. (2012).

The Hyytiälä SMEAR II (Station for Measuring Forest Ecosystem Atmosphere Relations) measurement station is located in a needleleaf forest in Southern Finland (61.85°N, 24.28°E) with a forest cover dominated by Pine trees. LAI was periodically measured at this site and varies between 2.3 and 4 m^2m^{-2}. Ozone flux measurements are available for 2002-2012, with a one-year data gap in 2006. Turbulent flux measurements are performed at 23m above ground level, 5-9m above the forest top of 14-18m. Ozone mixing ratios at this altitude are derived by linearly interpolating between observations at 16.8 and 33m. More information about the measurement setup of this site and eddy-covariance flux calculation can be found in Rannik et al. (2012) and Mammarella et al. (2016).

3.2.2   Observational approach

Our observational analysis, schematically depicted in Figure 3.1a, aims to derive bulk canopy stomatal and non-stomatal resistances from canopy-top eddy-covariance observa-

tions in order to estimate the magnitude of stomatal and non-stomatal ozone removal. We first derive the ozone canopy conductance (g_{c,O_3}) from the observed ozone dry deposition velocity ($V_d(O_3)$), measurement-inferred aerodynamic resistance r_a and bulk canopy quasi-laminar layer resistance r_b (see Supplement).

We use the inverted Penman-Monteith equation to derive bulk canopy stomatal conductance (g_s) from canopy-top eddy-covariance observations of the latent heat flux complemented with other observed variables (Knauer et al., 2018; Monteith, 1965):

$$g_s = \frac{\lambda E g_a \gamma}{\Delta(R_n - G) + \rho c_p g_a VPD - \lambda E(\Delta + \gamma)} \tag{3.1}$$

where g_a is the aerodynamic conductance to water vapor (Supplementary Information S1), λE is the latent heat flux, γ is the psychrometric constant, which relates the water vapor partial pressure to air temperature, Δ is the slope of the saturation vapor pressure curve, R_n is net radiation, G is the ground heat flux, ρ is the air density, c_p is the specific heat of air, and VPD is the vapour pressure deficit. Note that all components of Equation 3.1 are observed or derived from observations. g_s refers to stomatal conductance to H$_2$O. When we refer to the stomatal conductance for ozone, we scale g_s for the diffusivity (D) ratio of ozone and water vapour: $g_{s,O_3} = \frac{D_{O_3}}{D_{H_2O}} g_{s,H_2O} = 0.61 g_{s,H_2O}$. Non-stomatal conductance is derived as the residual of the bulk canopy conductance and the canopy stomatal conductance, assuming that stomatal and (bulk) non-stomatal uptake are two parallel pathways (see Fig. 3.1a).

3.2.3   Ozone uptake parameterizations

The 'big leaf' approach

The parameterization of gaseous dry deposition in many atmospheric chemistry models is based on the resistance in series framework introduced by Wesely (1989), hereafter referred to as W89. The discussion below considers the implementation of the big-leaf dry deposition approach in the coupled meteorology-chemistry model WRF-Chem (Grell et al., 2005). Other big leaf parameterizations are available with improved treatment of stomatal (e.g. Emberson et al., 2000; Lin et al., 2019; Val Martin et al., 2014) and non-stomatal uptake (e.g. Zhang et al., 2003). However, the common use of Wesely's (1989) parameterization in state-of-science 3D atmospheric chemistry and transport models (see e.g. Galmarini et al., 2021) motivates the choice for this scheme in our experiment setup.

Figure 3.1b depicts the resistance framework. Note that this dry deposition representation is zero-dimensional, i.e. no explicit in-canopy ozone mixing ratios are calculated. The aerodynamic resistance (r_a) is calculated following Monin-Obukhov Similarity Theory, and
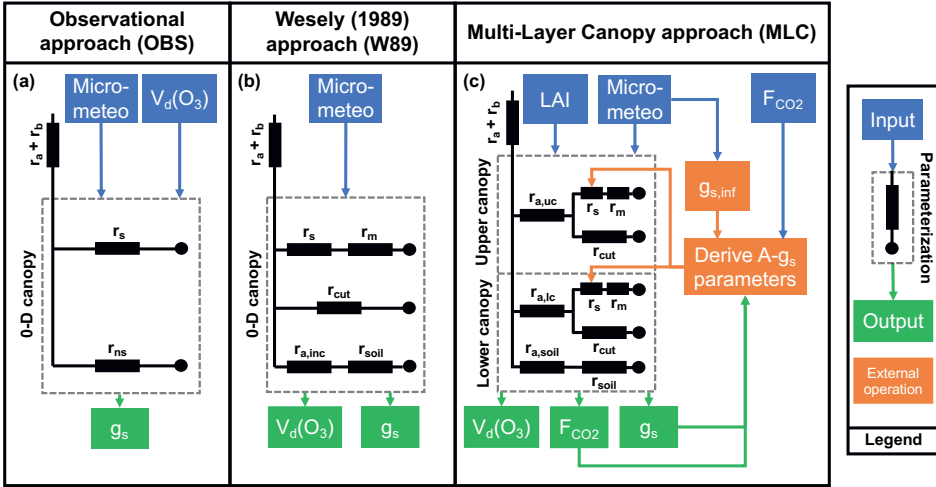
Figure 3.1: Schematic displaying the representation of the biophysical controls on surface ozone removal in plant canopies in the three different approaches in this study, and their input and output variables. The combination of uptake resistances (shown as black rectangles) inside the dashed grey rectangle yields the bulk canopy resistance (r_c). In- and output variables of the mechanisms are shown in blue and green, respectively. Orange rectangles in panel c display the derivation of photosynthesis parameters required in MLC-CHEM, this procedure is described in more detail in Appendix A3.1. Shown resistances are: stomatal resistance (r_s), bulk canopy non-stomatal resistance (r_{ns}), resistance to cuticular uptake (r_{cut}), the resistance to in-canopy transport ($r_{a,inc}$), resistance to soil uptake (r_{soil}), resistance to in-canopy transport in the upper canopy layer ($r_{a,uc}$), lower canopy layer ($r_{a,lc}$), and to the soil ($r_{a,soil}$).

the quasi-laminar layer resistance (r_b) is estimated following Hicks et al. (1987). Stomatal resistance is calculated as follows (Erisman et al., 1994; Wesely, 1989):

$$r_s = r_i \left(1 + \left(\frac{200}{R_n + 0.1} \right)^2 \right) \left(\frac{400}{T_s(40 - T_s)} \right) \qquad (3.2)$$

where r_i is a season- and land use-dependent scaling factor, R_n is net radiation and T_s is the surface temperature. r_s is corrected for the diffusivity difference between H_2O and ozone, as explained in Section 3.2.2. In this formulation, the resistance to stomatal uptake is lowest during high-radiation conditions and for an optimum temperature of 20°C, reflecting that stomatal aperture follows a diurnal cycle with a peak around mid-day. Note that this parameterization does not explicitly account for stomatal closure due to a vapour pressure deficit or soil moisture stress. We use the non-stomatal resistances

following Wesely (1989), which are all constant except the resistance to transport to the lower canopy that depends inversely on net radiation. For the soil uptake resistance, we use site-inferred values of 300 s m^{-1} for Ispra (Fumagalli et al., 2016) and 400 s m^{-1} for Hyytiälä (Zhou et al., 2017).

The Multi-Layer Canopy-CHemistry Exchange Model (MLC-CHEM)

We also apply the Multi-Layer Canopy-CHemistry Exchange Model (MLC-CHEM) to evaluate simulated long-term canopy-scale ozone deposition at the two sites. This one-dimensional model explicitly simulates canopy exchange and vertical profiles of ozone concentrations as a function of radiation, turbulent mixing, chemistry (using the Carbon Bond Mechanism version 4; CBM-4), biogenic emissions (following the Model for Emissions of Gases and Aerosols from Nature (MEGAN); Guenther et al., 2006; Guenther et al., 2012), soil NO emissions (Yienger and Levy, 1995) and (non-)stomatal uptake and their vertical gradients in the canopy. MLC-CHEM has been applied coupled to single-column and global chemistry-climate modelling studies (Ganzeveld et al., 2010; Ganzeveld et al., 2002b), as well as in an offline set-up for the interpretation of site-scale measurements (e.g. Yanez-Serrano et al., 2018).

In our set-up, the model consists of three layers, representing the understory and the crown layer, as well as one layer aloft representing a bulk surface layer. In-canopy exchange is represented by two canopy layers whose depth depends on the canopy height (h_c), each with a layer thickness of $0.5h_c$. This two-canopy layer set-up allows simulation of in-canopy concentration and flux profiles using a computationally efficient analytical solution, allowing for coupling MLC-CHEM to single-column and global chemistry-climate modelling studies (Ganzeveld et al., 2010; Ganzeveld et al., 2002b). Given the large gradients in radiation in the canopy, vertical profiles of radiation and radiation-dependent processes (photolysis, biogenic emissions) are calculated considering four canopy layers. The four-layer radiation profiles and biogenic emission rates are subsequently averaged over the two canopy layer for the exchange simulation. The model simulation time step is 30 minutes, but for processes requiring a higher temporal resolution a sub-timestep temporal resolution is applied, which depends on the removal rate (Ganzeveld et al., 2002b).

Micro-meteorological variables are provided as input to the model, and ozone concentrations in the upper layer are nudged to observed above-canopy ozone concentrations to represent entrainment and advection. We use a weighting factor of 0.5, which implies that we force simulated above-canopy ozone mixing ratios to observed mixing ratios with a timescale of ±2 h, based on the applied temporal resolution of 0.5 h. The specific procedure to incorporate observations in our model set-up is described in Section 3.2.4.

In-canopy aerodynamic resistance (r_a) is calculated as a function of canopy height, LAI and u_*. Leaf-level stomatal conductance is calculated using the assimilation-stomatal conductance model A-g$_s$ (Ronda et al., 2001):

$$g_{s,c,leaf} = g_{min,c} + \frac{a_1 A_g}{([CO_2] - \Gamma)\left(1 + \frac{D_s(a_1-1)}{D_0}\right)}$$ (3.3)

where $g_{min,c}$ (cuticular conductance), the constant a_1 and Γ (the CO_2 compensation point) depend on the vegetation type. A_g is gross assimilation, calculated as a function of photosynthetically active radiation (PAR), skin temperature, the internal CO_2 concentration and the soil water content (SWC). We refer the reader to Appendix A in Ronda et al. (2001) for more details on the calculation of A_g. D_s is the vapour pressure deficit (VPD) leaf level, and D_0 the VPD at which stomata close. $g_{s,c,leaf}$ is calculated at the leaf level and subsequently integrated to the specific layer as a function of layer-specific LAI and PAR (Ronda et al., 2001). This stomatal conductance representation accounts for observed increases in g_s for an increase in CO_2 assimilation (which responds to radiation), whereas g_s decreases as the external CO_2 concentration increases (a lower CO_2 uptake rate is needed to maintain the supply of CO_2 to the photosynthesis mechanism). g_s also decreases as the vapour pressure deficit increases in order to minimize plant water loss through transpiration. This is a more mechanistic description of stomatal conductance compared to the big leaf approach (Equation 3.2), where g_s is parameterized as a function of radiation and temperature.

The A-g$_s$ model has several degrees of freedom in determining the parameter settings. In order to derive physically appropriate settings, we tested the sensitivity of the MLC-CHEM-simulated canopy stomatal conductance (g_s) and the canopy CO_2 flux to A-g$_s$ parameter settings by comparison with observation-inferred g_s (using Eqn. 3.1) and canopy-top F_{CO_2} observations (see Fig. 3.1c). This procedure is described in Appendix A3.1, and the final, optimized A-g$_s$ parameters are shown in Table A3.1. With this approach, we effectively implement a realistic, observation-constrained representation canopy-top CO_2 flux and g_s in MLC-CHEM.

Non-stomatal removal in MLC-CHEM is represented using uptake resistances taken from Wesely (1989), Ganzeveld and Lelieveld (1995) and Ganzeveld et al. (1998). Analogous to W89, we adapt MLC-CHEM's default soil uptake resistance to site-inferred values of 300 s m^{-1} for Ispra (Fumagalli et al., 2016) and 400 s m^{-1} for Hyytiälä (Zhou et al., 2017). Experimental evidence suggests increased deposition to dew-wet leaves (Altimir et al., 2006; Zhang et al., 2002). MLC-CHEM accounts for this by using two distinct uptake resistances for deposition to leaf cuticles and uptake by water films on leaves of 10^5 s m^{-1} and 2000 s m^{-1}, respectively (Ganzeveld and Lelieveld, 1995). Canopy wetness is represented by inferring the fraction of wet vegetation (f_{wet}) as a function of RH (Lammel, 1999):

$$f_{wet} = \begin{cases} 1 & \text{RH} \geq 0.9 \\ \frac{RH - 0.55}{0.35} & 0.55 \leq \text{RH} < 0.9 \\ 0 & \text{RH} < 0.55 \end{cases} \tag{3.4}$$

3.2.4   Experimental setup

We apply the W89 big-leaf parameterization and the multi-layer ozone atmosphere-biosphere exchange parameterization to simulate total canopy ozone removal, and its partitioning into stomatal and non-stomatal removal, at two locations with contrasting climate and pollution regimes, for a total of 12 site-years. These simulations are compared against observation-inferred g_s and g_{ns}. We restrict this analysis to daytime values (8-20 h LT) during April-September, which approximately coincides with the growing season. The observational approach is known to be biased under high canopy wetness conditions due to dew formation or precipitation, and various approaches to correct for this have been reported in the literature (e.g. Clifton et al., 2017; Clifton et al., 2019; Launiainen et al., 2013; Rannik et al., 2012). We therefore only include data with RH < 90% and when the accumulated precipitation in the preceding 12 hours is less than 0.1 mm. This set of assumptions compromises between data quality and retention of data points.

3.3   Results

3.3.1   Temporal variability in ozone dry deposition velocity

Monthly and inter-annual variability

The observed ozone uptake at Ispra is generally highest in June-August, with little inter-annual variability (Fig. 3.2). W89 underestimates the observed dry deposition velocity ($V_d(O_3)$) by ± 0.1 cm s^{-1}, while MLC-CHEM reproduces the observed magnitude of $V_d(O_3)$ within 7% in May-September. On the basis of the statistical model performance metrics in Table 3.1, there is no parameterization that consistently outperforms the other on monthly timescales. MLC-CHEM systematically overestimates ozone deposition in April. To evaluate this bias further, we performed MLC-CHEM simulations with a deactivated sink to wet leaves, motivated by the considerable uncertainty in this ozone removal pathway (Clifton et al., 2020c). This simulation resulted in the strongest decrease in $V_d(O_3)$ in the relatively humid months of April (Fig. A3.3), ranging from 0.15 cm s^{-1} in April 2013 to 0.05 cm s^{-1} in April 2015. This modification results in an improved representation of seasonality in $V_d(O_3)$, suggesting seasonal variation in the ozone sink to wet leaves that

Table 3.1: Performance statistics for the monthly-averaged simulations of $V_d(O_3)$ with W89 and MLC-CHEM (MLC). The unit is cm s^{-1} for MBE, RMSE and intercept, and unitless for the other metrics. Shown are several conventionally applied performance metrics (MBE, RMSE, slope (s) and intercept (i) of a linear regression fit of simulations against observations, and r^2 from ordinarily least squares regression), as well as the index of agreement d (Willmott, 1982).

	MBE	RMSE	r^2	slope, intercept	d
	Ispra (n = 18 months)				
W89	-0.09	0.14	0.24	0.79, 0.19	0.60
MLC	0.08	0.13	0.28	1.18, -0.20	0.58
	Hyytiala (n = 45 months)				
W89	-0.01	0.15	0.11	0.32, 0.28	0.62
MLC	0.04	0.09	0.59	1.26, -0.16	0.78

might not be properly captured by the RH-dependent parameterization of wet leaf uptake (Eqn. 3.4).

The observed $V_d(O_3)$ at Hyytiälä is generally lower compared to Ispra, reflecting a lower leaf area and thus less stomatal uptake at the Finnish site. W89 and MLC-CHEM both capture the observed magnitude of $V_d(O_3)$ to within the interquartile range of observations (± 0.2 cm s^{-1}) in most years, although $V_d(O_3)$ in W89 peaks one month early compared to the observations. MLC-CHEM reproduces the seasonal cycle in $V_d(O_3)$ with a Pearson (temporal) correlation coefficient between simulations and observations which is markedly higher compared to the W89 approach (r^2=0.59 for MLC-CHEM; r^2=0.11 for W89, Table 3.1). These results suggest that MLC-CHEM better reproduces stomatal and non-stomatal removal processes, and we will investigate this further below.

The interannual variability in the ozone dry deposition velocity for Hyytiälä is 0.17 cm s^{-1}, and is slightly underestimated in both simulations (0.10-0.11 cm s^{-1}, not shown). We therefore calculated the contributions from stomatal conductance and non-stomatal conductance to the overall deposition velocity, as described in Section 3.2.2. Interannual variability in stomatal conductance is overestimated slightly by W89 and MLC-CHEM compared to the observation-derived g_s estimates, by 0.02 cm s^{-1} and 0.05 cm s^{-1}, respectively. Interannual variability in non-stomatal conductance is strongly underestimated in both simulations (0.04-0.07 cm s^{-1}) compared to the observed inter-annual variability in non-stomatal conductance (0.19 cm s^{-1}). The missing interannual variability in the non-stomatal deposition pathway may be due the chemical, wet leaf and soil uptake pathways.
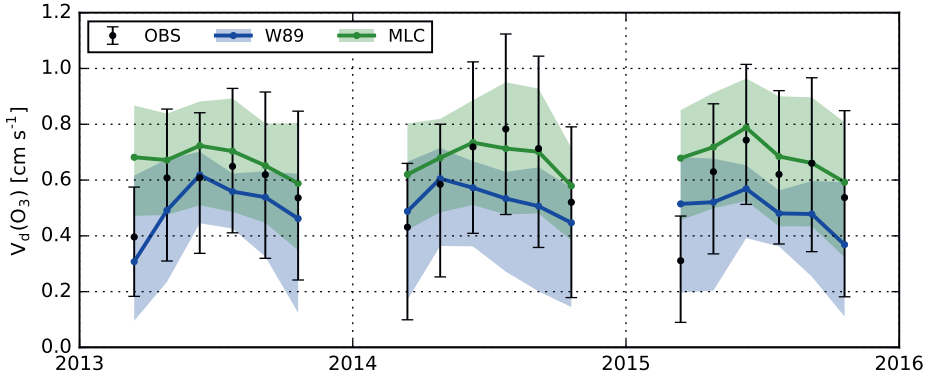
Figure 3.2: Time series of April-September monthly average daytime (8-20 h LT) ozone dry deposition velocity for Ispra, for W89 (blue), MLC-CHEM (green) and observations (black). Solid lines and points show monthly daytime medians for simulations and observations, respectively, and shaded areas and whiskers display the inter-quartile range.

Diurnal cycles

The observed diurnal cycle of $V_d(O_3)$ at Ispra (Fig. 3.4a) is characterized by an asymmetrical pattern, with a steep morning increase that plateaus around 0.8 cm s^{-1}, and a decrease in the afternoon that reflects stomatal closure and reduced non-stomatal uptake. W89 underestimates the observed median daytime $V_d(O_3)$ values by ±0.1 cm s^{-1} (20%), while MLC-CHEM reproduces the observations within 10%. The onset of the W89-simulated daytime $V_d(O_3)$ peak shows a one-hour time lag, with an underestimation by around -0.3 cm s^{-1} (52%) in the morning (6-10 h LT) and an overestimation of 0.1 cm s^{-1} (13%) in the afternoon (12-16 h LT). The contribution of stomatal and non-stomatal removal to this model-observation mismatch will be discussed in Section 3.3.2. MLC-CHEM reproduces the diurnal course of $V_d(O_3)$ within 0.1 cm s^{-1} throughout the day.

The observed $V_d(O_3)$ diurnal cycle at Hyytiälä (Fig. 3.4b) increases earlier during the day compared to Ispra and decreases later, due to the extended day length during the growing season at the Finnish site. $V_d(O_3)$ peaks at 0.5 cm s^{-1} between 9-12 h LT, and decreases in the early afternoon due to decreasing (non-)stomatal sink ozone removal. W89 overestimates the magnitude of $V_d(O_3)$ by 0.1 cm s^{-1} (22%) in the afternoon (12-16 h LT), and underestimates ozone uptake in the morning (3-10 h LT) and evening (after 19 h LT). Apart from a morning overestimation by up to 0.1 cm s^{-1}, MLC-CHEM reproduces the diurnal evolution of $V_d(O_3)$ well, apparently due to a more realistic representation of stomatal and non-stomatal removal processes.
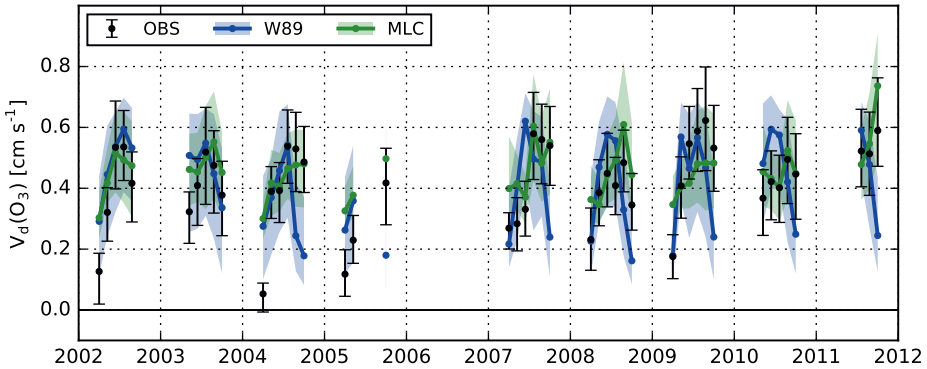
Figure 3.3: As Figure 3.2, but for Hyytiälä.

3.3.2 Diurnal variability in stomatal and non-stomatal uptake

Ispra

Next, we analyze the stomatal and non-stomatal components of ozone deposition to further understand the model-observation agreement on diurnal timescales. Figure 3.5 shows growing season median diurnal cyles of bulk canopy conductance (g_c), canopy stomatal conductance (g_s) and non-stomatal conductance (g_{ns}) for Ispra, in W89 and MLC-CHEM simulations and observational estimates. At Ispra, the observation-derived daytime median ozone canopy conductance is 0.87 cm s^{-1} (Fig. 3.5a). The inferred daytime median stomatal conductance is as small as 0.26 cm s^{-1} (grey points in Fig. 3.5b), corresponding to a daytime stomatal uptake fraction of 35% (Fig. 3.5d). However, we found a substantial gap (of 56%) in the energy balance closure (Q_{gap}), defined as the difference between net incoming radiation (R_n) and the surface energy balance components (Foken, 2008). This indicates underestimations in observed sensible and latent energy fluxes (H, LE), which affects our observation-derived stomatal conductance. The energy balance closure issues remain after filtering the observations based on quality flags and u_* thresholds (Fig. A3.2).

To resolve these energy balance closure issues, we applied a correction method that partitions Q_{gap} to H and LE via the evaporative fraction ($EF = \frac{LE}{H+LE}$) (Renner et al., 2019; Twine et al., 2000). This correction increases LE and H by 156 W m^{-2} and 25 W m^{-2}, respectively, corresponding to an evaporative fraction of 0.86. With these corrected surface energy balance components, we derive a substantially larger daytime median stomatal conductance to ozone of 0.49 cm s^{-1} (black points in Fig. 3.5b,d), an increase of nearly 90% with respect to the original observation-derived estimate. The Q_{gap} correction also leads to a better model-observation agreement for g_s. Ozone fluxes are also affected
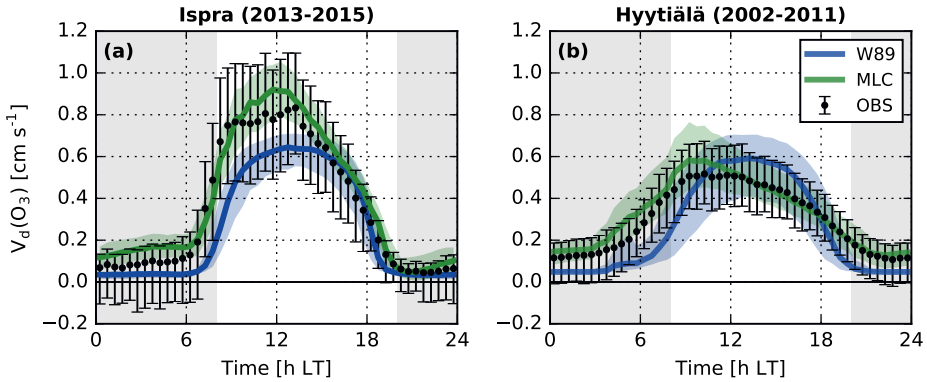
Figure 3.4: Diurnal cycles of April-September ozone dry deposition velocity at Ispra (panel a) and Hyytiälä (b), derived from observations (black), and simulations with the W89 parameterization (blue) and MLC-CHEM (green). Lines and points show median values, and shaded areas and whiskers display the inter-quartile range.

by the surface energy balance closure gap: additional data filtering based on u_* thresholds leads to increases in observed ozone fluxes, which exceeds 50% in the morning and evening when absolute fluxes are low, but the effect is smaller (<15%) during mid-day.

The observed diurnal cycle in canopy conductance at Ispra is better captured by MLC-CHEM compared to W89 (Fig. 3.5a). MLC-CHEM also better captures decreases in g_c observed in the afternoon. MLC-CHEM and W89 simulate a daytime median ozone stomatal conductance of 0.43 and 0.51 cm s^{-1}, respectively, and thus agree better with the Q_{gap}-corrected stomatal conductance estimate derived from observations (Fig. 3.5b). The observation-derived stomatal fraction during 8-20 h LT (0.62) is overestimated by W89 (0.72) and underestimated by MLC-CHEM (0.52). The observed stomatal uptake fraction increases throughout the day, from ± 0.4 at 8 h LT to ± 0.8 at 18 h LT, and this diurnal course is better reproduced by MLC-CHEM than by W89.

Observation-derived non-stomatal conductance peaks in the morning and levels off at ± 0.8 cm s^{-1} (Fig. 3.5c, grey points), and decreases in the afternoon before reaching a night-time value of 0.1 cm s^{-1}. The stomatal conductance increase following Q_{gap} correction leads to a reduction in the daytime average inferred non-stomatal conductance, from 0.57 to 0.35 cm s^{-1}. This correction does however not affect the shape of the diurnal cycle in g_{ns}, characterized by a sharp increase in the morning and a more gradual reduction in the afternoon. Daytime non-stomatal conductance is strongly underestimated by W89, and shows little diurnal variability since most in-canopy resistances are constant, and apparently too high. MLC-CHEM reproduces the observed diurnal evolution in non-stomatal conductance more accurately than W89 (Fig. 3.5c), apparently due to its
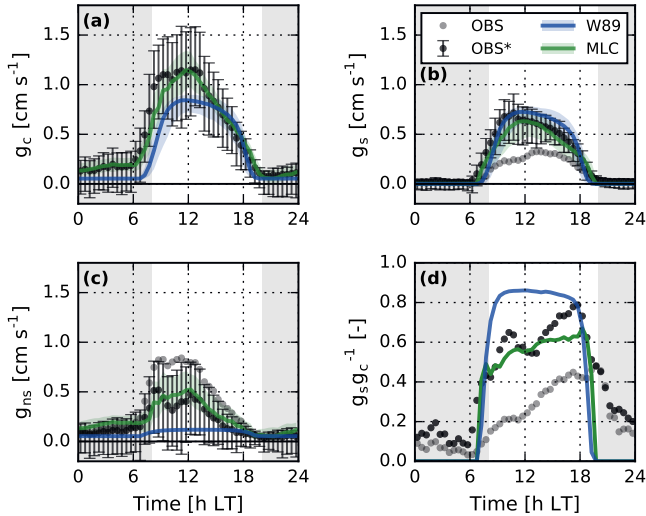
Figure 3.5: April-September median diurnal cycles of ozone bulk canopy conductance (panel a), canopy stomatal conductance (b), bulk non-stomatal conductance (c) and the stomatal fraction of total ozone removal ($g_s g_c^{-1}$, panel d) for Ispra. Observed medians and inter-quartile ranges after Q_{gap} correction (OBS*; see Text) are shown as black points and whiskers (the values prior to Q_{gap} correction, denoted as OBS, are shown in gray). The median and inter-quartile range of W89 and MLC-CHEM are shown in blue and green, respectively. The shaded area in panel d highlights the nighttime period (defined as 8-20 h LT) over which the stomatal flux is calculated.

representation of diurnal variability in processes involved in non-stomatal removal, wet leaf uptake and in-canopy turbulence. The contributions of different removal processes to total non-stomatal uptake will be discussed in Section 3.3.3.

Hyytiälä

At Hyytiälä, the observation-derived daytime median g_c is 0.53 cm s^{-1} (Fig. 3.6a), which is lower compared to Ispra due to lower non-stomatal ozone removal. W89 overestimates canopy conductance by up to 0.2 cm s^{-1} in the afternoon, while morning and evening g_c are underestimated. Similar to Ispra, MLC-CHEM captures the diurnal evolution in g_c better than W89, with a peak around 9 h LT as in the observations, but overestimates morning canopy conductance by 0.1 cm s^{-1}. We did not correct for surface energy balance closure gaps for the Hyytiälä observations, since this gap was considerably smaller ($\pm 20\%$ of R$_n$, without a distinct diurnal cycle), and in closer agreement to literature-reported values for tall vegetation (Foken, 2008).
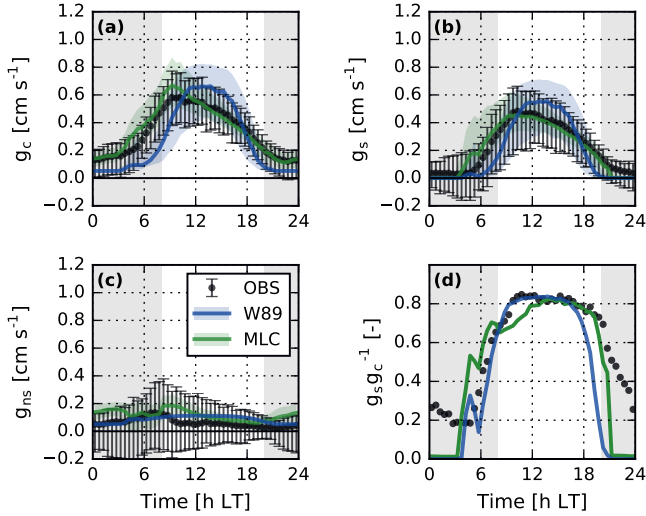
Figure 3.6: As Figure 3.5, but for Hyytiälä.

Observed stomatal conductance peaks at ± 0.5 cm s^{-1} at 10 h LT, followed by a decrease in the afternoon (Fig. 3.6b). W89 underestimates g_s in the morning (5-10 h LT), and overestimates afternoon values by 20-25%. MLC-CHEM overestimates morning stomatal conductance, but follows the observed diurnal cycle well throughout the rest of the day. The observed stomatal ozone uptake fraction is relatively constant at 0.8 (Fig. 3.6), comparable to the upper range of stomatal uptake fraction estimates by Rannik et al. (2012). The stomatal fraction is well reproduced by both parameterizations, although for BL this seems a coincidence given the mis-represented diurnal cycle in g_c and g_s.

Observation-derived non-stomatal conductance at Hyytiälä (Fig. 3.6c) is relatively constant at 0.1 cm s^{-1}, except for a morning peak of 0.2 cm s^{-1} around 8 h LT that likely reflects wet leaf ozone uptake (Altimir et al., 2006; Rannik et al., 2012). W89 reproduces the observed daytime magnitude of g_{ns}, but cannot reproduce its morning peak. MLC-CHEM overestimates the night-time non-stomatal ozone sink, in line with a study by Zhou et al. (2017) based on a one-month time series of ozone flux observations (August 2010) indicating that observed nighttime ozone deposition appear to reflect smaller nocturnal soil uptake efficiency than assumed. Except for an overestimation in the morning, MLC-CHEM captures the observation-inferred magnitude of non-stomatal ozone deposition well during daytime.

3.3.3   Dependence of non-stomatal deposition on driving variables

Non-stomatal ozone uptake, and its dependence on micro-meteorological and other environmental drivers, is incompletely understood. Previous studies employed statistical or process-oriented modelling (Clifton et al., 2019; Fares et al., 2014; El-Madany et al., 2017; Rannik et al., 2012) to determine the contribution of driving variables to this ozone sink. In this section, we study observed and simulated relationships between the non-stomatal ozone removal fraction ($g_{ns}g_c^{-1}$) and two variables (air temperature, T_a, and VPD) that we hypothesize to contribute to temporal variability in non-stomatal ozone removal. This section focuses on non-stomatal ozone removal at Ispra, since Rannik et al. (2012) previously characterized the non-stomatal ozone sink for Hyytiälä, and we compare our findings for Ispra to their results at the end of this section.

We first determine how W89 and MLC-CHEM can reproduce the observed relationship between non-stomatal ozone removal and T_a and VPD. We focus on the average daytime response (8-20 h LT) and subsequently on three different periods in the diurnal cycle (6-20 h LT, 10-14 h LT, 14-18 h LT). In this manner, we can disentangle processes affecting (non-)stomatal uptake that act during different periods of the diurnal cycle (wet leaf uptake in the morning, optimal stomatal functioning during mid-day, suppressed stomatal conductance during the afternoon).

The temperature response of the relative contribution of non-stomatal removal to total ozone deposition (expressed by the non-stomatal fraction, $g_{ns}g_c^{-1}$) during different periods of the diurnal cycle is shown in Figure 3.7 (panels a-d). Non-stomatal uptake decreases with temperature during the day (Fig. 3.7a). This decrease is largely driven by the morning temperature sensitivity of $g_{ns}g_c^{-1}$, which shows less sensitivity to temperature later during the day (Fig. 3.7b-d). W89 underestimates the observed temperature dependence of the non-stomatal fraction throughout the day by ± 0.2, although the morning non-stomatal fraction is higher for the lowest temperature bin (10-15 °C). MLC-CHEM reproduces the daytime response well, characterized by elevated morning non-stomatal uptake under low-temperature conditions. For most temperature bins, W89 strongly underestimates the observed variability in the non-stomatal fraction. The observed variability is also underestimated by MLC-CHEM, although to a smaller extent, and apparently indicates still missing or mis-represented deposition processes.

The observation-derived non-stomatal fraction increases with VPD during daytime (Fig. 3.7e-h), indicating that non-stomatal ozone removal decreases under dry conditions. This result contradicts an anticipated increase in the contribution by non-stomatal removal to overall canopy removal due to a VPD-induced decrease in stomatal uptake. However, the observed non-stomatal uptake also decreases in the afternoon (Fig. 3.5c), and therefore does not compensate for the decreasing stomatal sink with VPD. The non-stomatal fraction displays the strongest VPD sensitivity in the morning, which mainly reflects simulated

wet leaf uptake under humid (i.e., low-VPD) conditions. Non-stomatal removal in W89 is insensitive to VPD, and this parameterization particularly underestimates the non-stomatal fraction under humid conditions (Fig. 3.7a-b). MLC-CHEM reproduces the daytime slope between VPD and the non-stomatal fraction well.

We then perform a number of sensitivity experiments with MLC-CHEM with deactivated non-stomatal sinks, to identify the role of each sink in explaining temporal variability in non-stomatal ozone removal, and its dependence on T_a and VPD. In these experiments, we exclude the contribution by wet leaf uptake, soil uptake and in-canopy chemical removal, as well as an experiment with strongly enhanced turbulent exchange between the crown layer and the understory. Section A3.5 and Figure A3.5 display the results from the sensitivity analysis of non-stomatal removal at Ispra. We list the main outcomes of this section and the MLC-CHEM sensitivity analysis below:

- Soil deposition accounts for almost 40% of non-stomatal removal under high-temperature conditions, reflecting a simulated increase in in-canopy turbulent transport with air temperature.

- Non-stomatal uptake is elevated under cold and humid conditions in the morning. This is consistent with MLC-CHEM-simulated wet leaf uptake, which accounts for over 20% of the morning non-stomatal removal fraction.

- Enhanced turbulent transport from the crown layer to the understory reduces the non-stomatal uptake fraction in MLC-CHEM, as it leads to enhanced stomatal uptake in the understory.

- Chemical removal plays a minor role in the total canopy ozone sink at Ispra.

In their multivariate analysis of environmental drivers of non-stomatal ozone removal at Hyytiälä, Rannik et al. (2012) derived that air temperature and VPD are significantly associated with variations in non-stomatal ozone removal, similar to our findings for Ispra. However, Rannik et al. (2012) also found an explanatory role for monoterpene concentrations at Hyytiälä, while our results suggest a minor role of chemical removal at Ispra.

3.3.4   Cumulative Uptake of Ozone (CUO)

In the previous sections we have shown that the seasonal evolution of ozone deposition in W89 and MLC-CHEM is relatively similar. However, there are consistent differences in daytime ozone stomatal and non-stomatal sinks between the deposition representations. In this section, we evaluate the implications of these differences in representation of (non-)stomatal removal for determining the cumulative stomatal uptake of ozone over the growing season (CUO), which is often used for ozone impact assessments (Mills et al., 2011b; Musselman et al., 2006). We here use the term CUO_{st} to refer to cumulative
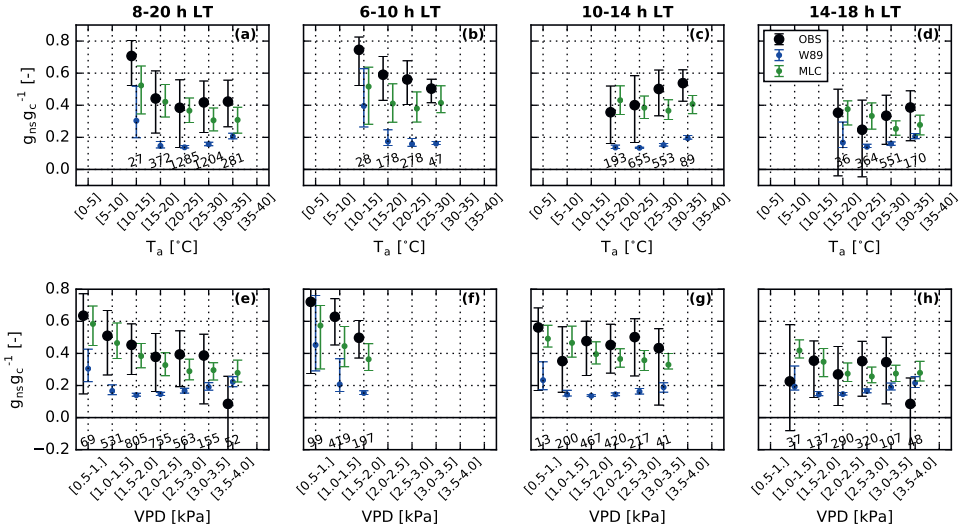
Figure 3.7: Non-stomatal ozone removal fraction $g_{ns}g_c^{-1}$ binned by air temperature (panels a-d) and vapour pressure deficit (panels e-h) during June-September, 2013-2015, at Ispra. Black dots and whiskers show $g_{ns}g_c^{-1}$ from observations, and simulations by W89 (blue points and whiskers) and MLC-CHEM (green points and whiskers). Dots and whiskers display the median and inter-quartile range per bin, respectively, and the number of observations in the bin is displayed at the bottom of the panels. Each column corresponds to a different time period in the diurnal cycle, namely all-day (8-20 h LT, panels a,e), morning (6-10 h LT, panels b,f), mid-day (10-14 h LT, panels c,g) and afternoon (14-18 h LT, panels d,h). Points and whiskers are only shown if the number of samples in the bin exceeds 10.

stomatal uptake, to distinguish this from cumulative non-stomatal ozone removal (CUO_{ns}). In Figure 3.8 we compare growing season-integrated stomatal and non-stomatal ozone fluxes from W89 and MLC-CHEM to observation-derived estimates of total seasonal ozone uptake for both sites (Fig. 3.8, panels a,c). Our observation-based derivation of stomatal conductance requires dry conditions (RH<90%, and no precipitation in the preceding 12 hours) to avoid overestimations in the observation-inferred stomatal conductance which lead to overestimations in CUO. However, application of these data selection criteria also lead to a reduction in data points that hinders the calculation of CUO_{st} based on observations. In order to derive a first-order CUO_{st} estimate, we divide the cumulative stomatal uptake inferred from valid observations by the fraction of valid observations. This method serves mainly to perform a site-to-site comparison of inferred CUO_{st}. Inferred CUO_{st} at Ispra varies between 61 and 72 mmol m^{-2} (Fig. 3.8b). The inferred CUO_{st} in 2014 was lower compared to 2013 and 2015 due to comparatively low ozone mixing ratios, while stomatal conductance displayed less year-to-year variability. At Hyytiälä, inferred CUO_{st} varies between 39 and 41 mmol m^{-2} (Fig. 3.8d), where the lower value in 2005 (29
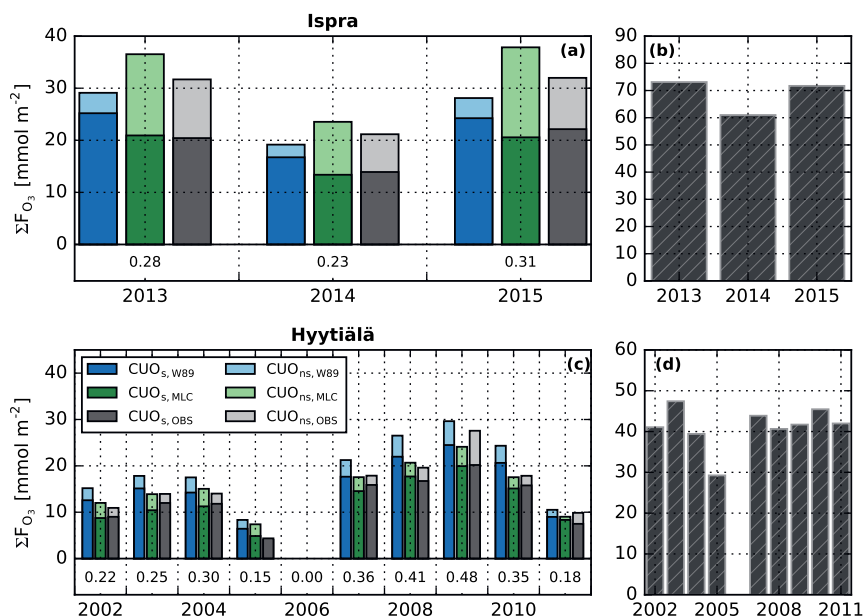
Figure 3.8: Panels a,c: growing season-integrated daytime (8-20 h LT) stomatal (CUO_{st}; dark colours) and non-stomatal (CUO_{ns}; light colours) ozone fluxes for the different years in the study period, for Ispra (panel a) and Hyytiälä (panel c) . Results from the W89 parameterization are shown in blue, from MLC-CHEM in green and from observations in grey. Only the data points with valid observation-inferred stomatal conductance estimates are selected for this comparison, the fraction of valid data points per growing season that remains is shown at the bottom of panels a and c. Panels b,d: inferred cumulative stomatal ozone uptake (CUO) estimate at both sites (hatched bars) after dividing the season-integrated daytime stomatal ozone flux (dark grey bars) by the fraction of valid data points. Note the different y axis ranges in the four panels.

mmol m^{-2}) is caused by missing data during June-August, when stomatal ozone uptake peaks. The higher inferred CUO_{st} values at Ispra compared to Hyytiälä reflect both higher stomatal conductance and ozone mixing ratios at the Italian site.

The differences between W89- and MLC-CHEM-simulated conductances are also manifested in the simulated growing-season cumulative (stomatal) uptake (Fig. 3.8a-c). The cumulative total ozone flux for Ispra is underestimated by W89 (-10%), while this parameterization overestimates cumulative stomatal uptake by 14-22%. MLC-CHEM accurately reproduces observation-derived CUO_{st} (within 7%), but overestimates the cumulative total flux by 15% (Fig. 3.8a). Therefore, the model-observation agreement of the two parameterizations for simulated cumulative total ozone removal largely reflects non-stomatal uptake differences, which deviates from observation-inferred values by -64% and 51%,

respectively. At Hyytiälä, the observed cumulative total ozone flux is 15.1 mmol m^{-2} and is overestimated by 34% by W89 reflecting overestimated stomatal uptake (Fig. 3.8c). The observation-derived CUO$_{st}$ is 12.6 mmol m^{-2}, compared to 15.8 mmol m^{-2} in W89 (+28%) and 12.3 mmol m^{-2} in MLC-CHEM (-2.4%). We conclude that the better representation of canopy stomatal conductance in MLC-CHEM compared to W89, particularly during the afternoon peak in ozone mixing ratios, may lead to a substantially reduced bias in the simulated growing-season integrated (stomatal) ozone flux.

3.4   Discussion

This study evaluates the potential added value of a multi-layer representation of vegetation canopies with respect to a commonly applied big leaf approach (W89; Wesely, 1989) for simulating ozone deposition and ozone impact metrics for forest canopies. We focus on short- to long-term temporal variability in $V_d(O_3)$ and its partitioning into stomatal and non-stomatal components, as well as the simulation of ozone impact metrics. We find that both parameterizations reasonably reproduce the observed seasonal cycle in $V_d(O_3)$, in agreement with previous chemistry transport model evaluations (e.g. Hardacre et al., 2015). Despite their comparable performance on seasonal timescales, the parameterizations deviate in their simulation of the diurnal cycle: the W89 parameterization particularly underestimates morning ozone removal by 52% (Ispra) and 37% (Hyytiälä) due to a combination of underestimated stomatal removal and a missing non-stomatal sink, likely wet leaf uptake. In the afternoon, W89 deviates less from observations at both sites (-13% at Ispra, +22% at Hyytiälä). Consequently, cumulative stomatal ozone uptake is overestimated by on average 18% (Ispra) and 28% (Hyytiälä) in W89 simulations, while cumulative total ozone removal deviates by -10% (Ispra) and 20% (Hyytiälä). Ozone mixing ratios typically peak in the afternoon and thus occur simultaneously with stomatal conductance misrepresentations, which may lead to simulated ozone fluxes overestimates using this mechanism. The multi-layer mechanism, constrained with latent energy and NEE observations to optimally represent stomatal exchange, displays a better agreement with the observed ozone deposition velocity (within 10%) and inferred cumulative stomatal and total uptake (within 15% and 9% for Ispra and Hyytiälä, respectively). Therefore, an accurate representation of diurnal variability in ozone uptake partitioned to stomatal and non-stomatal sinks is essential for reproducing cumulative (stomatal) ozone uptake at the land surface.

We applied a big leaf parameterization that is commonly used in (regional) atmospheric chemistry models, for example in WRF-Chem (Galmarini et al., 2021; Grell et al., 2005). Big leaf parameterizations advantageously depend on a limited number of routinely available meteorological variables and a simplified description of land use characteristics, and can be readily applied at any location without location-specific parameter derivations (Clifton

et al., 2020c). However, the empirical nature of these schemes leads to an oversimplification of in-canopy physical and chemical processes that affect atmosphere-biosphere exchange of ozone, e.g. by not accounting for stomatal closure based on the vapour pressure deficit (VPD) and soil moisture, or in-canopy chemical reactions. There are big leaf versions available with a more process-based description of ozone deposition processes, particularly stomatal conductance (e.g. Büker et al., 2012; Clifton et al., 2020a; Emberson et al., 2001; Lin et al., 2019) and non-stomatal ozone removal (Zhang et al., 2003).

To further explore the effect of model assumptions in big leaf parameterizations, we performed a comparison between W89 and another commonly used big leaf dry deposition scheme by Zhang et al., 2003, referred to as Z03 in Appendix A3.2. This parameterization includes a separate treatment of sunlit versus shaded leaves and explicit treatment of water stress in the stomatal conductance calculation, and includes variations in non-stomatal resistances as a function of LAI and u_*. We find that both parameterizations overestimate afternoon stomatal conductance compared to observations, while Z03 better reproduces morning g_s (Fig. A3.1). The differences between these parameterizations are therefore largely driven by differences in non-stomatal ozone removal (Fig. A3.1). The agreement with observation-inferred non-stomatal removal depends on site-specific conditions, particularly friction velocity. Our analyses highlight potential areas of improvement in process representation that can be considered in future larger-scale modelling studies to improve simulations of ozone deposition pathways and their temporal variability. This is particularly important for season-integrated (stomatal) ozone fluxes with big leaf parameterizations.

Our results suggest that A_{net}-g_s parameterizations, as applied in MLC-CHEM, simulate stomatal conductance in good agreement with observation-inferred values throughout the diurnal cycle. Such models are sensitive to parameters typically derived at leaf level that display spatio-temporal variability. Further observational constraints on these parameters, e.g. from leaf-level ecophysiological measurements, improve the representation of stomatal conductance and biosphere-atmosphere exchange (Vilà-Guerau De Arellano et al., 2020), benefitting simulations of CO_2 and ozone exchange as simulated by A_{net}-g_s within MLC-CHEM. Determining these parameters from canopy-top observations is an underdetermined problem in a mathematical sense, which we circumvented by deriving a realistic set of model parameters based on a comparison with canopy-top observed NEE and observation-derived stomatal conductance while remaining as close as possible to the original parameter set in Ronda et al. (2001). Choosing A_{net}-g_s parameters could be formalized by applying mathematical techniques such as data assimilation (Raoult et al., 2016).

MLC-CHEM can be driven by diagnostic variables available from CTM output (or their driving meteorological models), favoring its implementation to represent atmosphere-biosphere fluxes of reactive compounds (Ganzeveld et al., 2010; Ganzeveld et al., 2002b).

In such a coupled setup, MLC-CHEM would use simulated stomatal conductance from the driving model to represent atmosphere-biosphere exchange consistent with the model's representation of (micro-)meteorology. An implementation of A-g_s with CO_2 mixing ratios, calculated online or offline, can be tested if simulated stomatal conductance estimates are unavailable.

Our analysis did not include soil moisture as a predictor of stomatal conductance. Sensitivity simulations in MLC-CHEM with observation-constrained soil water content (SWC) at different depths resulted in strong reductions in simulated NEE and g_s during summer compared to observations, which suggests that these SWC observations are not indicative of root-zone soil moisture. Nonetheless, simulations of ozone deposition and mixing ratios at various spatial scales suggest a higher predictive skill when accounting for SWC (Anav et al., 2018; Clifton et al., 2020a; Lin et al., 2020; Lin et al., 2019; Otu-Larbi et al., 2020). Including this stress term is especially important in the context of projected drought risk and intensity increases in future climate scenarios (Cook et al., 2018), that may aggravate ozone smog episodes due to a decreased stomatal sink (Lin et al., 2020).

Our analysis of non-stomatal ozone removal as a function of micro-meteorological drivers (air temperature and VPD) for Ispra reveals that the non-stomatal sink is elevated under low-VPD (i.e., high-RH) morning conditions, likely indicating uptake at the leaf surface in water films formed by dew (Potier et al., 2015; Zhang et al., 2002). This sink is reproduced by MLC-CHEM by applying a wet canopy fraction dependent on RH and a constant wet skin uptake resistance. Observations suggest that this non-stomatal ozone sink is less important at Hyytiälä, which could be due to a lower RH threshold for development of wet canopy conditions in MLC-CHEM compared to previous work (Altimir et al., 2006; Zhou et al., 2017). Since wet leaf uptake may affect simulated diurnal cycles of ozone in chemistry transport models (Travis and Jacob, 2019), uptake parameterizations would benefit from better observation-based constraints on this removal process, both in terms of canopy wetness and wet leaf uptake efficiency.

Our sensitivity analysis also reveals an important role of soil deposition during the afternoon due to more active in-canopy transport. We applied a constant soil resistance to ozone uptake in our simulations, despite various environmental controls that have been identified, including air temperature, soil water content, near-surface air humidity and soil clay content (Fares et al., 2014; Fumagalli et al., 2016; Stella et al., 2019; Stella et al., 2011). Our results suggest a minor importance of chemical ozone removal at the two considered sites. However, we did not investigate the role of ozone scavenging by reactive sesquiterpenes (Hellén et al., 2018; Vermeuel et al., 2021; Zhou et al., 2017) nor soil-emitted nitric oxide (Finco et al., 2018). Since most (big leaf) parameterizations work with a poorly constrained resistance to transport from canopy-top to the soil (e.g. Makar et al., 2017), the importance of the chemical and soil ozone sinks for total canopy ozone

removal can be best explored with better-resolved in-canopy turbulent exchange in model simulations.

We have shown that stomatal and non-stomatal sinks are not accurately reproduced using the W89 big leaf parameterization compared to observations at two forested ozone flux sites, leading to structurally biased instantaneous and growing-season cumulated (stomatal) ozone flux simulations. Improved methods (e.g., the DO3SE mechanism, Büker et al., 2012; Emberson et al., 2001) do correct for soil moisture and VPD in the stomatal conductance calculation. Overestimated stomatal ozone fluxes also likely have implications for simulated ozone mixing ratios. Many models underestimate mid-day ozone mixing ratios in Europe (Im et al., 2015; Solazzo et al., 2012; Visser et al., 2019), and a mis-representation of land surface uptake may contribute to this bias. Therefore, an overestimated ozone deposition flux may also affect the simulation of concentration-based vegetation ozone impact metrics, such as AOT40, in the opposite direction compared to flux-based metrics. An improved model representation of the ozone deposition process will provide more confidence in the application of atmospheric chemistry models for surface air quality and vegetation ozone damage assessments.

To stimulate improvement of big leaf and multi-layer parameterizations, modelers may benefit from evaluations against existing long-term dry deposition observations in various ecosystems (e.g. forests and grassland), and for contrasting environmental conditions (e.g. during dry vs. wet seasons). Such an assessment is currently underway in Stage 4 of the Air Quality Model Evaluation International Initiative (AQMEII4; Galmarini et al., 2021). Additionally, evaluation against in- and above-canopy ozone flux measurements (Fares et al., 2014; Finco et al., 2018) can reveal information about non-stomatal sinks in these parameterizations, such as soil deposition and in-canopy chemical removal. Lastly, the application of proposed parameterizations for non-stomatal ozone sinks, such as for wet leaf uptake (Potier et al., 2015) and soil uptake (Stella et al., 2019) should be tested in 3D and single-point models of ozone deposition.

3.5   Conclusions

We compare ozone deposition simulations to multi-year observations at two European forested flux sites, with a focus on temporal variability, contributions from stomatal and non-stomatal sinks, and metrics for the damage incurred by ozone on vegetation. The widely used big leaf parameterization W89; Wesely, 1989 and the in-canopy process-resolving MLC-CHEM model both reproduce the seasonal cycle of daytime ozone deposition velocity reasonably well, but there are important differences in the skill of the two approaches to capture the diurnal changes in ozone deposition. Specifically, W89 consistently underestimates ozone deposition velocities in the morning (by 37-52%), while the afternoon model-observation is somewhat smaller (-13-22%). MLC-CHEM captures the diurnal cycle

much better with relatively small biases in the morning (-9% at Ispra, +17% at Hyytiälä), and good agreement (within 10%) in the afternoon. Accounting for stomatal closure, wet leaf removal and in-canopy turbulent transport followed by soil uptake turns out to be important for accurately simulating ozone deposition on diurnal timescales.

The structural errors in W89 are explained by a misrepresentation of the diurnal cycle in stomatal and non-stomatal conductance. Simulations with a more recent big leaf parameterization result in similar biases regarding stomatal and non-stomatal uptake. The MLC-CHEM model, constrained by local observations of diurnal CO_2 and latent energy fluxes, captures stomatal and non-stomatal ozone conductance better. As a result, W89 systematically overestimates cumulative ozone uptake by 20-30% in the growing season at Ispra and Hyytiälä, whereas MLC-CHEM reproduces cumulative ozone uptake within 3% at both sites. We conclude that MLC-CHEM, nudged with observation-inferred stomatal conductance, accurately describes non-stomatal uptake processes as well as vegetation ozone impact metrics.

Sensitivity tests with MLC-CHEM for Ispra point out that in relatively cold and humid conditions, ozone deposition on wet leaves appears to explain up to 20% of the non-stomatal ozone sink. During high-temperature conditions characterized by efficient in-canopy transport, enhanced uptake by soils accounts for up to 40% of non-stomatal ozone deposition. The tests suggest a minor role for chemical destruction of ozone at Ispra.

Our results indicate that current model representations of stomatal and non-stomatal ozone uptake by vegetation, often based on W89, should be thoroughly evaluated. This study provides a strategy for such evaluations, and shows how a more detailed, canopy-resolving model driven by ancillary measurements of CO_2 and energy fluxes, can provide more realistic estimates of ozone deposition and vegetation ozone impact metrics.

A3   Appendix

A3.1   A-g_s optimization

Prior to applying MLC-CHEM to analyze ozone fluxes at our study sites, we first paid attention to simulations of the canopy CO_2 flux (F_{CO_2}) and canopy stomatal conductance (g_s) to ensure that the photosynthesis parameterization (A-g_s) functions satisfactorily. An initial simulation with the default settings for the C3 vegetation class resulted in a strongly overestimated F_{CO_2} compared to observations at both sites (see Table A3.2). This is accompanied by strong overestimation of the canopy stomatal conductance at Ispra, while MLC-CHEM slightly underestimates stomatal conductance at Hyytiälä.

The default A-g_s settings were derived for low vegetation such as grassland and crops (Ronda et al., 2001) and are therefore not necessarily representative for forest canopies. We performed a sensitivity analysis of simulated F_{CO_2} and g_s to A-g_s model parameters in order to determine optimized parameter sets for our simulations. These settings are given in Table A3.1. We found that strongly overestimated F_{CO_2} is largely caused by a high presumed reference mesophyll conductance ($g_{m,298}$), leading to overestimated transport of CO_2 in the plant's chloroplast. Our reductions of $g_{m,298}$ are in better correspondence with previously reported estimates of 0.8-2.0 mm s^{-1} for different forest plant functional types (ECMWF, 2020; Steeneveld, 2002; Voogt et al., 2006). At Ispra, we additionally modified the mesophyll conductance temperature response curve, which differs between plant species (Caemmerer and Evans, 2015; Calvet et al., 1998), to improve the amplitude of the seasonal cycle in simulated F_{CO_2}. At Hyytiälä, the maximum internal CO_2 concentration (f_0, given as a fraction of the external CO_2 concentration) was increased to improve the correspondence with observation-derived g_s.

Our observational constraints to A-g_s lead to improved simulations of g_s and F_{CO_2} (Table A3.2). The parameter changes additionally affect the simulation of the ozone dry deposition velocity ($V_d(O_3)$), as shown in Table A3.3. At Ispra, the strong reduction in stomatal conductance leads to an underestimation in $V_d(O_3)$ (MBE = -0.12 cm s^{-1}), while the other statistical metrics indicate a modest model improvement. At Hyytiala, the growing-season model overestimation is slightly reduced from 0.04 cm s^{-1} to 0.02 cm s^{-1}. Our approach results in a reduced model bias at the two study sites, particularly for F_{CO_2}, while taking care to stay as close as possible to the original parameter set.

Table A3.1: A-g_s parameter settings used in MLC-CHEM simulations. The first column indicates the default C3 settings from Ronda et al. (2001), and the other two columns show the optimal settings from our analysis. A dash ("-") indicates that a parameter is unchanged with respect to the default C3 value.

	C3 (reference)	Ispra	Hyytiälä
$g_{m,298}$ [mm s^{-1}]	7.0	1.5	1.5
f_0 [-]	0.89	-	0.99
$g_{m,T1}$ [K]	278	283	-
$g_{m,T2}$ [K]	301	306	-
$A_{m,max,T1}$ [K]	281	286	-

Table A3.2: Model performance statistics of MLC-CHEM before and after A-gs optimization for canopy stomatal conductance and CO_2 flux. Shown are several conventionally applied performance metrics (MBE, RMSE, slope (s) and intercept (i) of a linear regression fit of simulations against observations, and r^2 from ordinarily least squares regression), as well as the index of agreement d Willmott (1982). The units are cm s^{-1} and μmol m^{-2} s^{-1}, respectively, unless indicated otherwise.

	Hyytiälä				Ispra			
	g_s [cm s^{-1}]		F_{CO_2} [μmol m^{-2} s^{-1}]		g_s [cm s^{-1}]		F_{CO_2} [μmol m^{-2} s^{-1}]	
	REF	OPT	REF	OPT	REF	OPT	REF	OPT
MBE	-0.04	-0.07	-20.1	-5.1	0.56	0.26	-45.8	-17.0
RMSE	0.43	0.41	21.1	6.1	0.89	0.66	50.3	18.4
r^2 [-]	0.12	0.22	0.64	0.46	0.16	0.16	0.57	0.61
s [-], i	0.77, 0.17	1.01, 0.07	0.36, 2.34	0.65, 0.62	0.42, 0.05	0.69, -0.02	0.25, 3.15	0.62, 6.50
d [-]	0.48	0.56	0.30	0.63	0.49	0.52	0.29	0.55

Table A3.3: As Table A3.2, but for $V_d(O_3)$ (unit: cm s^{-1}).

	Hyytiälä		Ispra	
	REF	MOD	REF	MOD
MBE	0.04	0.02	0.11	-0.01
RMSE	0.17	0.17	0.47	0.32
r^2 [-]	0.37	0.39	0.28	0.45
s [-], i	1.93, -0.01	0.86, 0.04	0.45, 0.32	0.89, 0.08
d [-]	0.73	0.76	0.69	0.80

A3.2   Comparison between two big leaf parameterizations

In order to derive more generic conclusions about big leaf parameterizations, we considered another commonly applied parameterization (Zhang et al., 2003), and recently extended to different gases by Wu et al. (2018). This big leaf formulation (hereafter Z03) differs compared to the Wesely (1989) parameterization (hereafter W89) in several aspects: (1) Z03 calculates stomatal condutance for sunlit and shaded leafs differently, (2) stomatal conductance is affected by VPD and soil moisture stress, (3) non-stomatal resistances contain seasonal and diurnal variability due to dependencies on leaf area index and friction velocity (u_*). This model version was derived from Zhang and Wu (2021), with two modifications. First, we adapted the soil resistance to locally derived values of 400 s m^{-1} (Hyytiälä) and 300 s m^{-1} (Ispra), similar to W89 and MLC-CHEM (see Methods). The implementation by Zhang and Wu (2021) relies on observed canopy wetness, which is not available for our two study sites. We therefore parameterize canopy wetness as a function of relative humidity, analogous to MLC-CHEM (Eqn. 3.4). In this section, we compare simulations by W89 and Z03 to observations of the ozone dry deposition velocity, and observation-inferred stomatal and non-stomatal conductance.

Figure A3.1 shows multi-year growing season median diurnal cycles of $V_d(O_3)$, g_s and g_{ns} for Ispra and Hyytiälä. From this analysis, we conclude that W89 and Z03 perform similarly for Ispra compared against observed $V_d(O_3)$ (panel a). Z03 better captures the early morning onset of $V_d(O_3)$ for Hyytiälä than W89, but more strongly overestimates mid-day and afternoon $V_d(O_3)$ compared to observations (panel b). Both parameterizations overestimate mid-day and afternoon g_s, while Z03 better captures the observed morning and afternoon g_s values than W89 (panels c,d). For g_{ns}, there is no parameterization that performs best for the two sites. Both parameterizations underestimate observation-inferred g_{ns} at Ispra (corrected for energy balance closure gaps, see Sect. 3.3.2), while W89 better captures the magnitude of observation-inferred g_{ns} (although Z03 better reproduces the shape of the diurnal cycle). This suggest that the g_{ns} dependence on u_* is less strong in the observations than is suggested in the Z03 parameterization: a sensitivity experiment with doubled u_* values for Ispra results in daytime g_{ns} values of 0.2-0.35 cm s^{-1}, an increase by a factor 2.3-2.8. Based on our findings, we conclude that the different representation of non-stomatal ozone removal drives the differences between W89 and Z03, but the magnitude of these differences depends on site-specific conditions.
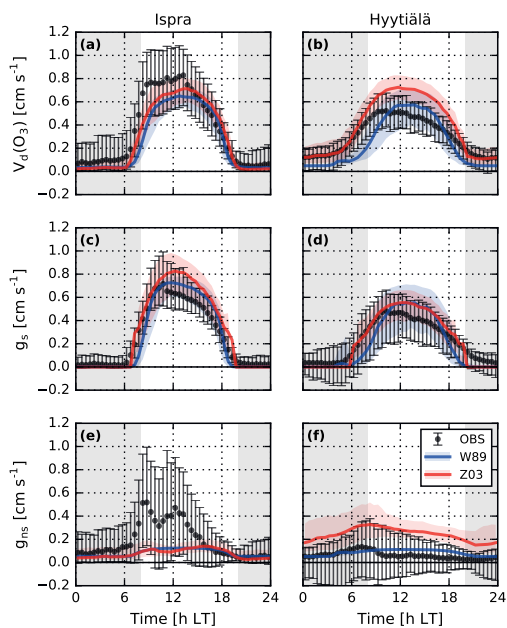
Figure A3.1: Comparison of the dry deposition parameterizations W89 (Wesely, 1989) and Z03 (Zhang et al., 2003) against the observed dry deposition velocity (panels a,b) and observation-inferred stomatal conductance (panels c,d) and non-stomatal conductance (panels e,f) for Ispra and Hyytiälä (left and right panels, respectively). Lines and shaded areas (points and whiskers) show April-September median and inter-quartile range of the simulations (observations).

A3.3   Supplementary figures
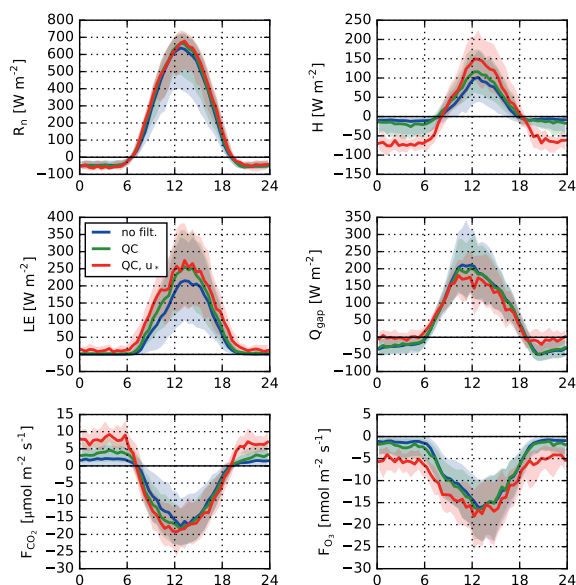
Figure A3.2: Median April-September 2013-2015 diurnal cycles of net radiation, sensible and latent heat fluxes, surface energy balance closure gap, CO_2 flux and ozone flux before and after gap correction. Blue lines depict unfiltered data, green lines show the data after quality-control (QC) filtering (discarding poor quality flux observations), and red lines show QC- and u_*-filtered data 9based on a u_* threshold of 0.35 m s^{-1}, determined using the REddyProcWeb tool (Wutzler et al., 2018).
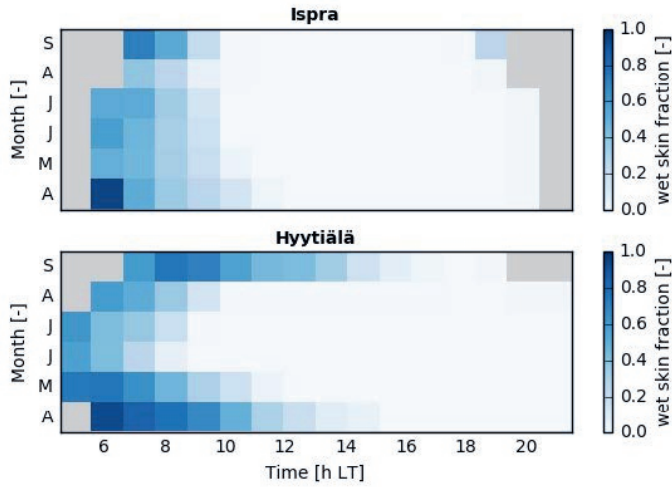
Figure A3.3: Mean values of the MLC-CHEM canopy wet skin fraction binned by month and hour for Ispra (2013-2015) and Hyytiälä (2002-2011) during April-September.
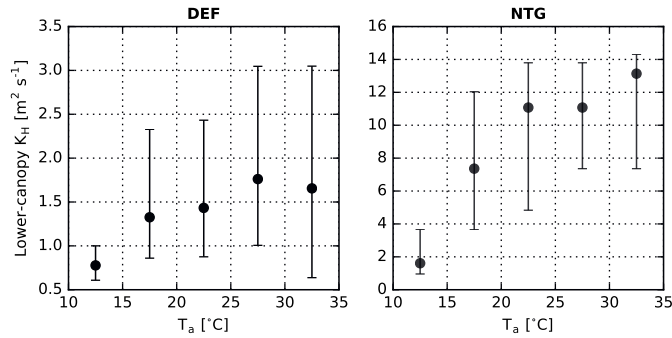
Figure A3.4: Lower-canopy eddy diffusivity (K_H) binned by air temperature (in steps of 5°C for the default simulation for Ispra in the default MLC-CHEM simulation (DEF) and the simulation with a deactivated gradient in turbulent mixing (NTG).

A3.4 Observational analysis: methodology

Derivation of the canopy resistance from the observation-derived deposition velocity requires knowledge on the aerodynamic resistance (r_a) and the quasi-laminar layer resistance (r_b). Above-canopy aerodynamic resistance is calculated as follows:

$$r_a = \frac{ln\left(\frac{z_r-d}{z_{0,m}}\right) - \Psi\left(\frac{z_r-d}{L}\right)}{ku_*} \tag{A3.1}$$

with k the Von Karman constant (0.40) [unitless], $u+*$ is friction velocity [m s^{-1}], z_r is the reference height (set to the canopy height), $z_{0,m}$ is the roughness length for momentum (set at a typical value for forests of 1.1 m), and d is the displacement height (set to 2/3 of the canopy height). L is the Obukhov Length, calculated as follows:

$$L = \frac{-u_*^3}{kg\frac{H}{T_v c_p \rho_a}} \tag{A3.2}$$

with g the gravitational acceleration [9.81 m s^{-2}], H is the sensible heat flux [W m^{-2}], T_v is the virtual temperature [K], c_p the specific heat capacity of air [1010 J K^{-1} kg^{-1}], and ρ_a the air density at 298K and 1013 hPa [1.225 kg m^{-3}]. Ψ is the stability correction function reflecting Monin-Obukhov Similarity Theory (Foken, 2006), as applied in Clifton et al. (2017):

$$\Psi = \begin{cases} 2ln\left(\frac{1+\left(0.95\left(1-11.6\frac{z_r-d}{L}\right)^{\frac{1}{2}}\right)}{2}\right), & \text{if } -2 \leq \frac{z_r-d}{L} < 0 \\ -7.8\frac{z_r-d}{L}, & \text{if } 0 \leq \frac{z_r-d}{L} < 1 \end{cases} \tag{A3.3}$$

r_b is the quasi-laminar layer resistance, calculated following Wesely and Hicks (1977):

$$r_b = \frac{2}{ku_*}\left(\frac{\kappa}{D_{O_3}}\right)^{\frac{2}{3}} \tag{A3.4}$$

with κ being the thermal diffusivity of air [0.2 cm^2 s^{-1}], and D_{O_3} the diffusivity of ozone [0.13 cm^2 s^{-1}] (Wesely, 1989).

A3.5   Dependence of non-stomatal deposition on driving variables: MLC-CHEM sensitivity experiments

With a range of MLC-CHEM sensitivity experiments (Table A3.4), we aim to further understand the observed temperature and VPD sensitivity of the non-stomatal ozone removal fraction ($g_{ns}g_c^{-1}$). With this analysis, we aim to assess the role of each process in explaining temporal variability in non-stomatal ozone removal. We focus this sensitivity analysis on the Ispra observations and simulations, since the non-stomatal ozone sink for Hyytiälä has been characterized before (Rannik et al., 2012).

Table A3.4: Setup of MLC-CHEM sensitivity experiments in Section 3.3.3, and hypotheses regarding the change in the non-stomatal ozone removal fraction ($g_{ns}g_c^{-1}$).

Experiment name	Code modification	Hypothesized effect on T_a/VPD sensitivity
DEF (Default)	MLC-CHEM setup as in paper	-
NWL (no wet leaf uptake	$f_{ws} = 0$	Reduced $g_{ns}g_c^{-1}$ under high-humidity conditions
NSL (no soil deposition)	$r_{soil} = 10^5$ s m^{-1}	Reduced $g_{ns}g_c^{-1}$ under high-temperature conditions
NCH (no in-canopy chemistry)	Chemical reactions turned off	Reduced $g_{ns}g_c^{-1}$ under high-temperature conditions
NTG (no vertical turbulence gradient)	Lower-canopy eddy diffusivity set to upper-canopy eddy diffusivity	Increased $g_{ns}g_c^{-1}$ due to more efficient transport to the soil

Figure A3.5 displays the MLC-CHEM-simulated temperature sensitivity of non-stomatal ozone removal after deactivating various non-stomatal removal processes. Deactivated wet leaf deposition (NWL) reduces $g_{ns}g_c^{-1}$ under low-temperature conditions by up to 21%, particularly during the morning when humid conditions prevail (Fig. A3.5b). This effect is even more pronounced under low-humidity conditions, when $g_{ns}g_c^{-1}$ is reduced by more than 0.2 during the morning (Fig. A3.5e). Deactivated soil uptake (NSL) most strongly reduces the non-stomatal fraction during high-temperature conditions in the afternoon, by up to 38% (Fig A3.5d). This reflects increasing atmospheric instability with temperature in MLC-CHEM, that results in simulated increases in turbulent transport in the canopy (Fig. A3.4). To further evaluate the sensitivity of the simulated non-stomatal ozone removal fraction to turbulent transport in the understory, we conducted an additional experiment in which the eddy diffusivity for transport between the crown layer and the understory laye was strongly enhanced (NTG). Conrary to our expectations, this experiment leads to a decreased non-stomatal fraction by 2-10%. this reflects enhanced stomatal uptake in the understory, which is more efficient than soil deposition. Deactivating temperature-dependent removal (NCH) leads to little change ($< 2\%$) in the non-stomatal ozone removal fraction.
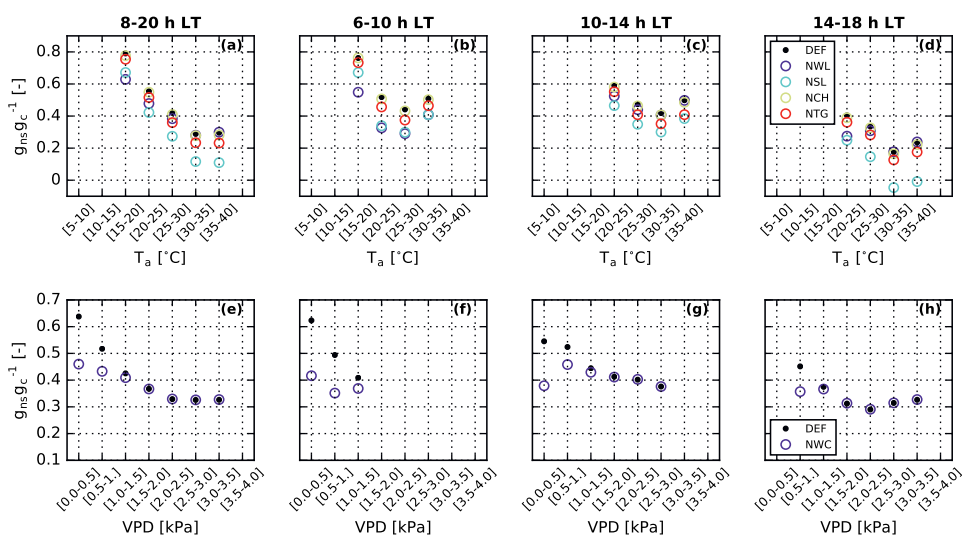
Figure A3.5: Non-stomatal ozone removal fraction ($g_{ns}g_c^{-1}$) binned by air temperature (panels a-d) and vapour pressure deficit (panels e-h) in the MLC-CHEM sensitivity experiments for Ispra (see Table A3.4 for experiment abbreviations).

Chapter 4

The combined impact of canopy stability and soil NO$_x$ exchange on ozone removal in a temperate deciduous forest

Abstract

Dry deposition is an important ozone sink that impacts ecosystem carbon and water cycling. Ozone dry deposition in forests is regulated by vertical transport, stomatal uptake, and non-stomatal processes including chemical removal. However, accurate descriptions of these processes in deposition parameterizations are hindered by sparse observational constraints on individual sink terms. Here we quantify the contribution of canopy-atmosphere turbulent exchange and chemical ozone removal by soil-emitted nitric oxide (NO) to ozone deposition in a North-Italian broadleaf deciduous forest. We apply a multi-layer canopy exchange model to interpret campaign observations of nitrogen oxides (NO$_x$=NO+NO$_2$) and ozone exchange above and inside the forest canopy. Two state-of-science parameterizations of in-canopy vertical diffusivity, based on above-canopy wind speed or stability, do not reproduce the observed exchange suppressed by canopy-top radiative heating, resulting in overestimated dry deposition velocities of 10-19% during daytime. Applying observation-derived vertical diffusivities in our simulations largely resolves this overestimation. Soil emissions are an important NO$_x$ source despite the observed high background NO$_x$ levels. Soil NO$_x$ emissions decrease the gradient between canopy and surface layer NO$_x$ mixing ratios, which suppresses simulated NO$_x$ deposition by 80% compared to a sensitivity simulation without soil emissions. However, a sensitivity analysis shows that the enhanced chemical ozone sink by reaction with soil-emitted NO is offset by increased vertical ozone transport from aloft and suppressed dry deposition. Our results highlight the need for targeted observations of non-stomatal ozone removal and turbulence-resolving deposition simulations to improve quantification and model representation of forest ozone deposition.

4.1   Introduction

Removal of ozone at the land surface (ozone dry deposition) is an important component of the tropospheric ozone budget, accounting for 15-20% of the total tropospheric ozone sink (Bates and Jacob, 2020; Hu et al., 2017; Young et al., 2018). Ozone dry deposition occurs when air masses, transported downward by turbulent motions in the atmospheric boundary layer, come in contact with the land surface. Forests are particularly efficient ozone sinks (e.g., Hardacre et al., 2015): removal processes include plant uptake through stomata and various non-stomatal sinks such as external leaf surfaces and soils, and chemical removal in the canopy airspace (Fowler et al., 2009). Upon stomatal uptake, ozone may impact stomatal conductance and photosynthesis, reducing ecosystem carbon assimilation on large spatial scales (Ainsworth et al., 2012). Better quantitative estimates of stomatal and non-stomatal ozone sinks can improve understanding and quantification of the total land surface ozone sink and impacts on ecosystem carbon uptake driven by stomatal ozone uptake.

Stomatal uptake typically accounts for 40-90% of forest ozone uptake during the growing season (Fowler et al., 2009), but the contribution by individual sink terms is poorly constrained by parameterizations of land-atmosphere exchange in global and regional atmospheric chemistry models (Clifton et al., 2020a). Multi-parameterization intercomparisons indicate that these uncertainties lead to a large spread in simulated ozone deposition (Visser et al., 2021; Wu et al., 2018). Likewise, Clifton et al. (2017) found that inter-annual variability in the ozone deposition velocity in a global atmospheric chemistry model was underestimated by a factor of two compared to an 11-year ozone flux dataset, and attributed this to year-to-year variability in non-stomatal removal. Global model simulations of ozone deposition carry considerable uncertainty (Hardacre et al., 2015; Young et al., 2018), and an effort to quantify inter-model spread of ozone deposition in regional air quality models is currently underway (Galmarini et al., 2021). Altogether, these findings highlight the need for improved process understanding of ozone deposition. In this study, we focus on two of these uncertain processes: in-canopy turbulent exchange and ozone scavenging by soil-emitted nitric oxide (NO). These processes are not explicitly considered in commonly applied "big leaf" representations of dry deposition. Additionally, the scarcity of observational constraints on these processes limit our understanding of their contribution to forest ozone deposition.

Vertical mixing conditions inside forests can be different compared to those above the canopy, leading to an inversion at the canopy top or inside the canopy, which are regulated by meteorological conditions and forest structure (Russell et al., 2018). This can lead to a (partial) decoupling between the canopy and the overlying air layers, with implications for canopy-atmosphere gas exchange (e.g., Foken et al., 2012). For example, in-canopy inversions can lead to a missing soil carbon respiration contribution to above-canopy

measurements of net ecosystem exchange of CO_2 (Jocher et al., 2018). For ozone, several studies suggest a dependence of ozone deposition on in-canopy turbulent mixing based on correlations between the deposition velocity and the friction velocity (e.g., Fares et al., 2014; El-Madany et al., 2017; Neirynck et al., 2012). Van Pul and Jacobs (1994) derived such a parameterization from measurements over maize crop, but its applicability to other land use categories remains uncertain. Multi-layer canopy-atmosphere exchange models typically simulate vertically resolved in-canopy and canopy-surface layer turbulent exchange based on K-theory (e.g., Ashworth et al., 2015; Ganzeveld et al., 2002b), which however has strong limitations when applied for rough surfaces such as forests (Bannister et al., 2022). Inferring in-canopy mixing conditions from observations requires vertical profile measurements of temperature and the sensible heat flux (e.g., Brown et al., 2020), which are not typically available at flux measurement sites. Therefore, the simplified representation of canopy-atmosphere exchange in current models and the sparse observational constraints limit our understanding of the role of turbulent mixing in canopy ozone removal.

Chemical ozone removal in plant canopies is another poorly constrained element of the ozone deposition sink. Compared to the surface layer, the canopy has a distinctly different photo-chemical regime, which is affected by radiation extinction, emissions of soil NO and biogenic volatile organic compounds (BVOCs), as well as deposition processes. In big leaf parameterizations, it is common practice to emit soil NO directly into the surface layer after the application of a canopy reduction factor, thereby only implicitly accounting for in-canopy NO$_x$ removal. Therefore, these parameterizations do not account for the different photo-chemical regime inside the canopy. Observation-based studies indicate a widely varying contribution of chemical ozone removal by soil NO and BVOCs, that largely depends on site-specific characteristics such as soil and vegetation type, temperature, soil moisture and vapour pressure deficit (Fares et al., 2012; Finco et al., 2018; Rannik et al., 2012; Vermeuel et al., 2021).

Due to decreasing anthropogenic emissions, agricultural and forest soils are becoming an increasingly important component of the European NO$_x$ emission budget (Skiba et al., 2021), that contribute to ozone formation particularly during NO$_x$-limited ozone formation conditions (Visser et al., 2019). Soil-emitted NO also act as an ozone sink inside forest canopies depending on the emission strength and canopy radiation extinction, leading to a locally NO$_x$-saturated ozone production regime. Commonly used parameterizations of soil-biogenic NO$_x$ emissions in chemical transport models assume that forest soil NO emissions are relatively small compared to anthropogenic emissions, but are an important source of NO$_x$ in pristine environments (Yienger and Levy, 1995). For example, Rummel et al. (2007) found that soil NO-ozone chemistry accelerates nighttime near-surface ozone loss in a tropical forest. In more polluted environments, nitrogen deposition accumulated over multiple years may substantially increase forest soil NO$_x$ emissions (Pilegaard et al., 2006). Under such circumstances, soil NO-ozone chemistry may explain a considerable

part of total ozone deposition even during daytime (Dorsey et al., 2004; Duyzer et al., 2004).

In this study, we aim to investigate the combined impact of canopy stability and soil NO emissions in the canopy airspace on ozone fluxes. We interpret field campaign observations of vertical gradients in ozone uptake in the North-Italian Bosco Fontana temperate midlatitude forest, which experiences substantial NO_x and ozone air pollution (Finco et al., 2018). This analysis of field observations is supported by observation-driven simulations with the Multi-Layer Canopy-CHemistry Exchange Model (Ganzeveld et al., 2002b; Visser et al., 2021). Specifically, we address the following research questions:

1. How does the representation of vertical exchange in a multi-layer canopy model affect simulated canopy ozone uptake?

2. What is the contribution of soil and canopy-top NO_x fluxes to observed NO_x mixing ratios inside and above the canopy?

3. What is the contribution of NO_x-ozone chemistry to in-canopy ozone removal under different model representations of vertical exchange?

4.2   Data and methods

4.2.1   Observations

We use atmosphere-biosphere exchange measurements obtained during an observational campaign in June-July 2012 at the Bosco Fontana temperate deciduous forest in northern Italy (45.20°N,10.74°E) (Finco et al., 2018). This campaign took place within the European project ECLAIRE (Effects of Climate Change on Air Pollution Impacts and Response Strategies for European Ecosystems). This forested site is situated in the Po Valley, in a 235 ha natural reserve composed primarily of *Carpinus betulus L.* and *Quercus robur L.*, and the average canopy height is 26 m above ground level (Gerosa et al., 2017).

The Po Valley is characterized by warm summers with high concentrations of ozone. Under such conditions, hydrological interactions leading to droughts might reduce the land surface ozone sink, which can exacerbate ozone air pollution (Lin et al., 2020). The summer of 2012 was characterized by slightly drier meteorological conditions ($\pm 1\sigma$) compared to the long-year average around Bosco Fontana, while the area south of the Po Valley experienced dry conditions (Fig. 4.1b, more details can be found in Appendix A4.1). The stomatal ozone flux does not exceed 3 nmol m^{-2} s^{-1} and is up to 50% lower compared to the multi-year summer average value (Fig. 4.1). This is likely caused by stomatal closure as a result of drought conditions. In the (pre-)alpine regions north of Bosco Fontana, conditions are slightly wetter than average, and stomatal ozone fluxes are higher (>4
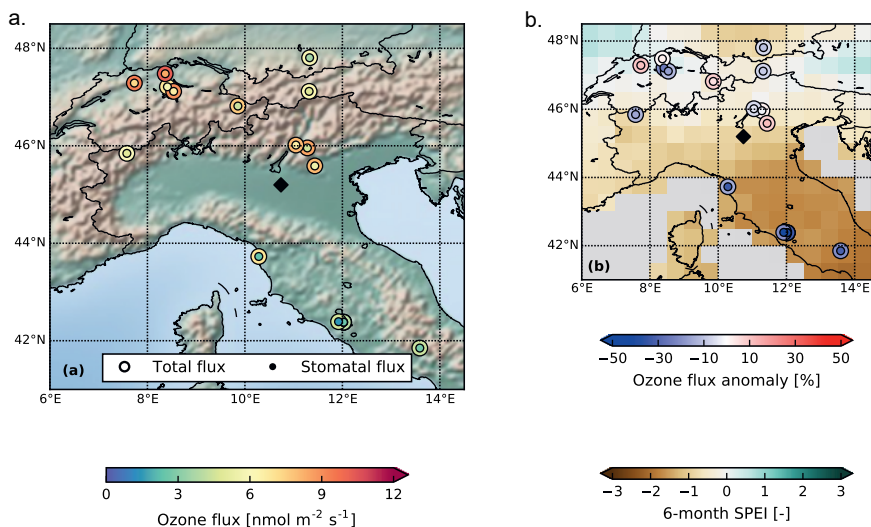
Figure 4.1: Summer 2012 ozone fluxes around northern Italy in a spatio-temporal context. Panel a: June-August average daytime total (outer circles) and stomatal (inner circles) ozone fluxes derived from observations at FLUXNET locations (data from Ducker et al., 2018). Panel b: July-August normalized 3-month SPEI anomaly (gridded data, derived from https://spei.csic.es/index.html, last access 24 March 2022), where negative (positive) values indicate drier (wetter) than average conditions, and the total and stomatal ozone flux relative anomaly compared to the observational record at the FLUXNET location. Bosco Fontana is indicated with a black diamond in both figures. See Appendix A4.1 for details on the SPEI and SynFlux data analysis.

nmol m^{-2} s^{-1}) compared to the south, with no clear indication of a regional anomaly (Fig. 4.1b). We therefore deem these observations representative for typical summer conditions in North Italy.

We here focus on the period of 24 June-11 July 2012, when temperature, wind speed, humidity, ozone and NO$_x$ concentrations as well as fluxes of sensible heat and ozone were measured along a vertical profile inside and above the canopy at the Bosco Fontana site. Specifically, measurements were performed at two heights above the canopy top (41m and 32m), at the interface layer between the canopy and the surface layer (24m) and at two heights inside the canopy (8m and 16m). More details on the observational setup and flux data processing can be found in Finco et al. (2018).

4.2.2 The Multi-Layer Canopy-CHemistry Exchange Model (MLC-CHEM)

We perform biosphere-atmosphere trace gas exchange simulations using the Multi-Layer Canopy-CHemistry Exchange Model (MLC-CHEM). This model simulates atmosphere-biosphere exchange fluxes and vertical profiles of trace gases, and includes a representation of biogenic volatile organic compounds (BVOC) emissions (Guenther et al., 2012) and soil NO emissions (Yienger and Levy, 1995), in-canopy vertical mixing, a complex chemistry scheme (CBM-IV) and dry deposition of atmospheric compounds (Ganzeveld and Lelieveld, 1995; Ganzeveld et al., 1998). Stomatal conductance is calculated using the assimilation-stomatal conductance model A-g_s (Ronda et al., 2001), with parameter settings based on the observation-driven values derived by Visser et al. (2021). In this study, we force MLC-CHEM with canopy-top observations of net shortwave radiation, temperature, relative humidity, wind speed, friction velocity and surface-layer NO, NO_2 and ozone mixing ratios. MLC-CHEM simulates in-canopy mixing ratios and fluxes of these species as affected by the aforementioned sources and sinks inside the canopy. We further highlight MLC-CHEM's representation of vertical exchange and soil NO emissions in the sections below.

In the set-up of MLC-CHEM in this study, the model consists of three layers: one bulk atmospheric surface layer, and a crown and understory layer that together represent the forest canopy. This set-up of the model has also been coupled to large-scale atmospheric chemistry models (Ganzeveld et al., 2010; Ganzeveld et al., 2002a). In-canopy radiation is expected to display large gradients between canopy-top and soil, and therefore processes affected by radiation (photolysis and biogenic emissions) are calculated in more vertical detail using four layers. Although MLC-CHEM can in principle be applied at a higher vertical resolution (i.e. with more than two canopy layers), we can only derive vertical transport from observations at two heights inside the canopy (see Section 4.2.3 and Figure 4.2). This motivates our use of the two-layer version in this study.

4.2.3 Vertical mixing in MLC-CHEM

We here test two methods of simulating turbulent exchange between atmosphere and the canopy, and compare these to exchange simulations with observation-derived vertical exchange. These representations will be introduced in this section, and are schematically visualised in Figure 4.2.

Reference parameterization of turbulent exchange (REF)

MLC-CHEM's default parameterization of turbulent exchange between canopy and the surface layer derives the surface-layer to upper-canopy eddy diffusivity (denoted as $K_{H,sl}$)
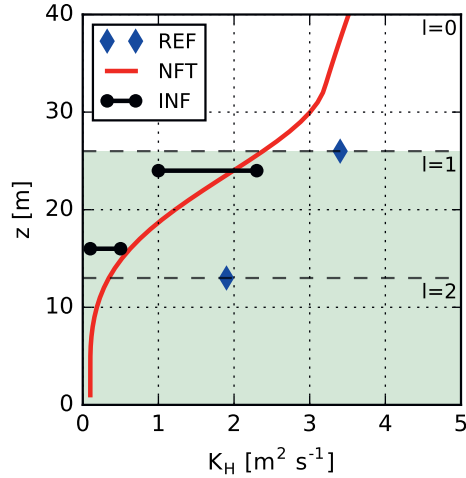
Figure 4.2: Schematic representation of typical afternoon vertical profiles of vertical diffusivity (K$_H$) in the Bosco Fontana forest (indicated by the green shaded area) in an unstable mixing regime. The reference MLC-CHEM vertical mixing parameterization (REF) is shown in blue diamonds and the near-field theory parameterization (NFT) is indicated by the red line. These profiles are calculated using u$_*$ = 0.5 m s^{-1}, u = 2 m s^{-1}, K$_H(z_{ref})$ = 4 m^2 s^{-1} (at a reference height of 50 m), r$_a$ = 20 s m^{-1}. Solid black lines and points show the mid-day (12-15 h LT) range of observation-inferred K$_H$ values at two different heights. Dashed black lines indicate the interface between model layers in MLC-CHEM. The index l (varying from 0-2) refers to the model layers in Equation 4.1.

by integrating the aerodynamic conductance over the difference in reference height between the surface layer and the upper canopy layer, following Monin-Obukhov Similarity Theory. The in-canopy eddy diffusivity ($K_{H,cl}$), used to calculate turbulent exchange between the crown layer and the understory layer, is then derived by scaling $K_{H,sl}$ with the in-canopy wind speed profile (Ganzeveld et al., 2002b):

$$K_{H,cl} = K_{H,sl} \frac{0.5(u(l) + u(l-1))}{0.5(u(1) + u(0))}.$$

(4.1)

where $u(l)$ is the horizontal wind speed at layer l (index values 0,1,2 represent the bulk surface layer, the upper canopy layer and the lower canopy layer, respectively, as shown in Fig. 4.2). The simulated in-canopy wind speed decreases exponentially as a function of canopy height and canopy-specific attenuation coefficients (Cionco, 1978). Figure 4.2 displays typical mid-day values of the vertical diffusivity as derived from MLC-CHEM. During typical summer afternoon conditions characterized by efficient vertical mixing

above the canopy, in-canopy K_H is typically a factor ± 7 lower than canopy-top K_H due to the scaling by the in-canopy wind speed.

Near-field theory (NFT)

We additionally apply a parameterization based on near-field theory (Raupach, 1989), which has resulted in improved surface ozone simulations with an online chemistry transport model (CTM) over forested regions in the United States (Makar et al., 2017). This formulation accounts for a decrease in the turbulent mixing intensity inside and above the forest with respect to the reference height of the lowermost model layer, resulting from obstruction of air flow due to the presence of trees. In this parameterization, $K_{H,sl}$ in the lowermost model layer of the CTM is scaled down towards the land surface as a function of canopy height, friction velocity and the Obukhov length. Figure 4.2 shows how the NFT vertical diffusivity decreases towards the surface in this formulation as a result of canopy influences on turbulence intensity. K_H at the canopy-top is particularly smaller in NFT compared to the reference parameterization (REF) in MLC-CHEM. In-canopy K_H is relatively similar in both formulations.

Observation-inferred turbulent exchange derivation (INF)

We also derive the turbulent exchange coefficient from observations following K-theory. This theory relates the observed sensible heat flux to the obseved vertical potential temperature gradient via the vertical diffusivity coefficient K_H:

$$H(z) = -K_H(z)\frac{\delta\theta(z)}{\delta z} \tag{4.2}$$

where $H(z)$ is the observed sensible heat flux at height z and $\frac{\delta\theta(z)}{\delta z}$ is the vertical potential temperature gradient at height z, inferred from temperature measurements above and below z. This slope is derived by fitting potential temperature to the curve $\theta = a + b \times ln(z) + c \times ln(z)^2$ (Brown et al., 2020; Mölder et al., 1999). We here apply the vertical diffusivity derived from observed vertical profiles of temperature and the sensible heat flux in our simulations of ozone and NO_x canopy-atmosphere exchange, assuming that exchange coefficients of these gases resemble the exchange coefficient of heat. We will revisit this assumption in the discussion, by a comparison with exchange coefficients derived from vertical gradients of ozone concentrations and fluxes.

We calculate $K_H(z)$ at two different heights within the canopy. K_H is calculated at the canopy-surface layer interface from 30-minute averages of sensible heat fluxes measured at 24m and temperature gradients between 16m and 32m. In-canopy K_H is derived from 30-minute averages of sensible heat fluxes measured at 16m and temperature gradients

between 8m and 24m. Figure 4.2 displays the typical mid-day K_H range as derived from observations. Note that we apply $K_{H,24m}$ for simulating exchange at the canopy-top, so these values are shown at z=26m. $K_{H,16m}$ is used for simulating vertical exchange between the crown and understory layers (z=13m). The observation-inferred K_H is lower than REF and NFT at the canopy-top, and the mid-canopy values of REF and NFT approximately coincide with the upper value of the observation-inferred K_H range.

4.2.4   Soil NO$_x$ exchange

We perform an initial evaluation of MLC-CHEM-simulated NO$_x$ mixing ratios in the understory to understand the role of soil NO$_x$ exchange on observed NO$_x$ mixing ratios at Bosco Fontana. A simulation with the default deciduous forest soil NO emission factor from Yienger and Levy (1995) results in an emission strength of 0.2-0.6 ng N m^{-2} s^{-1} (Supp. Fig. 2a). This is substantially lower than the site-derived emission flux of 20.8 ng N m^{-2} s^{-1}, based on enclosure chamber measurements directly above the Bosco Fontana forest floor (Finco et al., 2018). As a result, MLC-CHEM-simulated understory NO$_x$ mixing ratios using the default deciduous forest emission factor are underestimated by 2.1 ppb (27%) on average (Supplementary Fig. A4.2c).

However, imposing the observation-derived soil NO emission flux in MLC-CHEM leads to an overestimation of understory NO$_x$ mixing ratios by 3.1 ppb (37%) compared to observations, reflecting NO$_x$ accumulation (Supplementary Fig. A4.2c). These over-estimations in simulated lower-canopy [NO$_x$] result partly from an underestimated NO$_2$ deposition sink in MLC-CHEM (1-6 ng N m^{-2} s^{-1}) that is more than a factor two smaller compared to the observation-derived soil NO$_2$ deposition flux of ± 14 ng N m^{-2} s^{-1} (Finco et al., 2018). A sensitivity test assuming a strongly enhanced soil uptake efficiency of NO$_2$, by reducing MLC-CHEM's NO$_2$ soil uptake resistance from 600 to 100 s m^{-1}, does not strongly increase simulated soil NO$_2$ deposition. Additionally, there are strong observed vertical gradients in NO$_x$ mixing ratios near the soil, reflecting strongly stable conditions and NO$_x$ loss due to chemical removal and soil deposition, which are not represented in MLC-CHEM's understory layer with a thickness of 13 m. This indicates that a substantial part of the soil-emitted NO$_x$ does not escape the air layer directly above the soil.

In order to infer the contribution of soil NO$_x$ exchange to observed NO$_x$ mixing ratios at the reference height of MLC-CHEM's understory layer (z=6.5 m), we study the sensitivity of simulated understory NO$_x$ to the soil NO emission flux. By comparing with observed NO$_x$ mixing ratios in the understory, we find that application of a reduced soil NO emission strength of 8 ng N m^{-2} s^{-1} minimizes the mismatch between simulated and observed understory NO$_x$ (Supplementary Fig. A4.2c), and we therefore choose this value to represent the effect of soil NO$_x$ exchange on canopy ozone uptake for our simulations.

Table 4.1: Configuration of MLC-CHEM simulations.

Experiment	K_H method	$E_{NO,soil}$ [ng N m^{-2} s^{-1}]	$r_{soil}(NO_2)$ [s m^{-1}]
1	REF	0.2-0.6^a	600
2	REF	8	600
3	NFT	8	600
4	INF	8	600
5	REF	0	10^5
6	NFT	0	10^5
7	INF	0	10^5

^{a} Diurnal range, peaking in the afternoon

4.2.5 Setup of the numerical experiments

In order to answer our research questions, we modify the representation of in- and above-canopy vertical mixing, as well as soil NO_x exchange, in MLC-CHEM. The reference simulation (experiment 1) applies the model's reference vertical diffusivity formulation (REF), a default temperate forest soil NO emission factor (Yienger and Levy, 1995) and the standard soil NO_2 uptake resistance (Ganzeveld and Lelieveld, 1995). In experiments 2-4, we modify MLC-CHEM's vertical exchange formulation as explained in Section 4.2.3. We use the effective soil NO emission flux that best represents soil effects on lower-canopy NO_x mixing ratios and the default NO_2 uptake resistance (Section 4.2.4). In experiments 5-7, we deactivate soil NO emissions and soil NO_2 deposition to quantify the effect of soil NO_x exchange on in-canopy NO_x mixing ratios and ozone deposition.

4.3 Results

4.3.1 Vertical exchange

We start our analysis by examining temporal variability in the observation-derived vertical diffusivity (K_H) and its relation to in- and above-canopy stability. Figure 4.3 displays the stability regimes in the surface layer and the canopy. Stably stratified conditions occur frequently inside the canopy even during daytime (Fig. 4.3), resulting from radiative heating of the canopy-top and a closed canopy structure that prevent the warm above-canopy air from entering the canopy airspace (Finco et al., 2018). Observation-inferred K_H at the interface between the canopy and the overlying air layer (z=24 m) peaks at 2.4 m^2 s^{-1} at 15:30 LT (Fig. 4.4b), coinciding with prevailing unstable mixing conditions above the canopy (Fig. 4.3). The campaign-average diurnal cycle of the observation-derived K_H inside the canopy (z=13 m) is characterized by lower values throughout the day (up to 0.5 m^2 s^{-1}, Fig. 4.4d), reflecting the decrease in vertical mixing inside the forest canopy
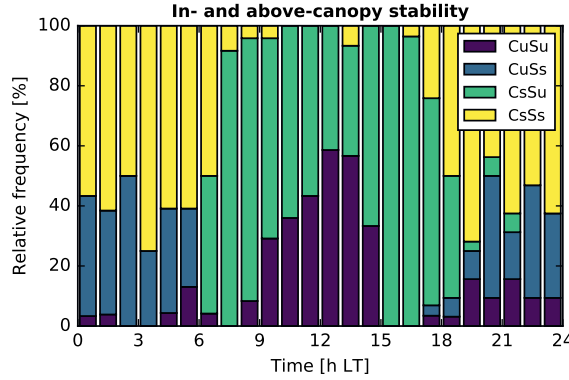
Figure 4.3: Occurrence of in- and above-canopy stability classes during the observational time period (24 June-12 July, 2012). Data were separated into four stability classes, based on stability parameter $\frac{z}{L}$ as unstable (lowercase u, $\frac{z}{L} < 0$) or stable (lowercase s, $\frac{z}{L} > 0$), as well as height of the observations, being representative of the surface layer (uppercase S, derived from observations at 32m) or inside the canopy (uppercase C, derived from observations at 16m).

(Fig. 4.2). Mid-canopy K_H derived from observations peaks at 11:30-12:00 LT (Fig. 4.4d), coinciding with predominantly unstable conditions inside and above the canopy.

Contrary to the observations, simulated K_H according to the REF approach in MLC-CHEM follows a symmetric diurnal profile peaking at 13:00 LT (Fig. 4.4b), which is substantially larger compared to the observation-inferred K_H during daytime. The K_H overestimation results from the simplified K_H derivation in this model setup (see Section 4.2.3). As a result, REF-simulated vertical exchange at the canopy-top is overestimated compared to observation-inferred K_H (Fig. 4.4b). The REF-simulated in-canopy K_H shows substantial day-to-day variation due to its dependence on above-canopy wind speed (Section 4.2.3), and strongly overestimates K_H inside the canopy leading to well-mixed conditions inside the canopy during daytime in this simulation. As a result, vertical exchange is strongly overestimated in the REF vertical exchange representation in MLC-CHEM compared to observation-inferred vertical mixing during the observational campaign.

Canopy-top K_H from a simulation based on near-field theory (NFT) follows a similar diurnal cycle compared to REF, since NFT is derived from scaling down the REF-simulated vertical diffusivity to include effects of the roughness sublayer (see Section 4.2.3). The NFT-simulated K_H above the canopy is up to 3 m^2 s^{-1} lower compared to the REF simulation during mid-day, and in closer agreement with observation-inferred K_H values. Inside the canopy, the NFT-simulated K_H is also substantially lower compared to the REF K_H, and in closer agreement with observation-inferred values. However, NFT does also not reproduce the observed low afternoon K_H values indicative of stably stratified conditions
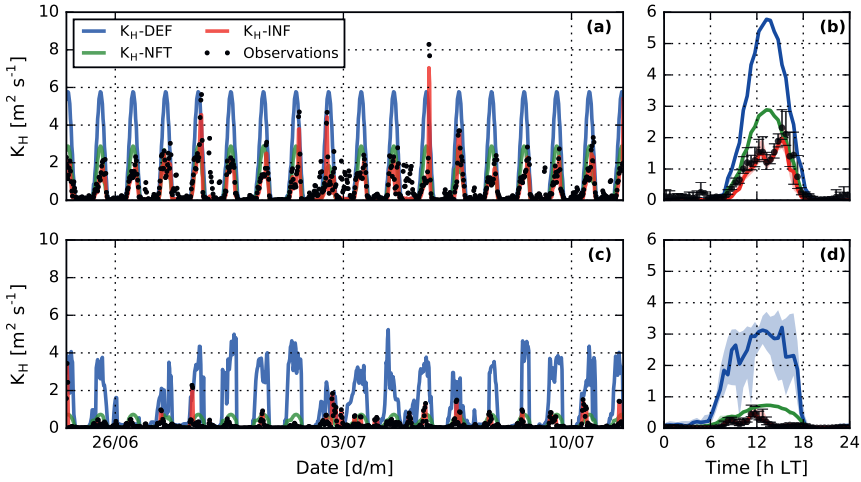
Figure 4.4: Time series (panels a,c) and campaign-average diurnal cycle (panels b,d) of vertical diffusivity at the canopy-surface layer interface (panels a,b) and 13 m, halfway the canopy (panels c,d), as derived from observations (black dots), and as calculated from three MLC-CHEM simulations (solid lines, see Section 4.2.3). Black lines and shaded areas indicate the inter-quartile range.

inside the canopy. In the next section, we will evaluate the effects of these different representations of vertical diffusivity on the simulated ozone and NO_x profiles.

4.3.2   Effects of turbulent mixing on canopy ozone uptake

We analyze the effect of vertical mixing on ozone deposition via the simulated deposition velocity. In MLC-CHEM, vertical mixing affects the canopy-atmosphere transport of ozone and thus the ozone flux. $V_d(O_3)$ is diagnostically calculated from the ozone flux at the canopy-atmosphere interface and canopy-top ozone mixing ratios simulated by MLC-CHEM. Figure 4.5 displays the campaign-median ozone dry deposition velocity ($V_d(O_3)$) diurnal cycle from observations and three MLC-CHEM simulations with different representations of vertical exchange. Observed $V_d(O_3)$ is characterized by nighttime values of 0.0-0.2 cm s^{-1}, followed by a sudden increase in the morning (± 8 h LT) to its peak value, and a subsequent decrease throughout the day. Notably, the REF and NFT simulations strongly overestimate $V_d(O_3)$ at 5-8 h LT, while a simulation with the observation-derived representation of vertical exchange (INF) agrees better with observations during this time period. This coincides with overestimated K_H values in REF and NFT, particularly at mid-canopy, during the early morning (Fig. 4.4d). Neither simulation reproduces the daytime peak value occurring at 8 h LT, which reflects a sudden change from stable to
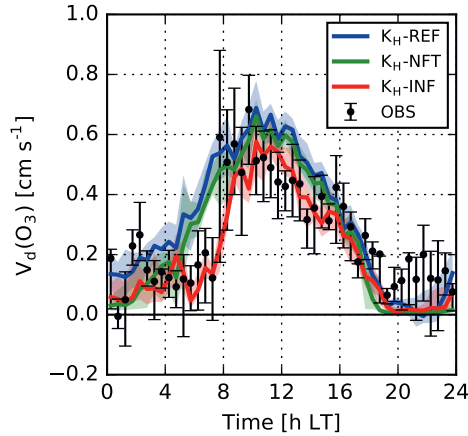
Figure 4.5: Campaign-median diurnal cycle of the ozone dry deposition velocity derived from observations (black points and whiskers), and simulated by MLC-CHEM with three different K_H derivations: MLC-CHEM's reference vertical diffusivity description (REF), near-field theory (NFT) and observation-inferred K_H (INF). The observation-inferred deposition velocity ($V_d(O_3) = \frac{F_{O_3}}{[O_3]}$) at the canopy-atmosphere interface (26 m) is derived by linear interpolation between observations at 24m and 32m.

unstable stratification in the upper canopy. The spread in observed $V_d(O_3)$ at this time is high, indicating that the timing of the change to unstable conditions varies from day to day, or a possible role of intermittent exchange. The REF and NFT simulations overestimate daytime $V_d(O_3)$ (9-16 h LT) by 19% and 10%, respectively. INF reproduces daytime $V_d(O_3)$ within 5% of the observations due to accounting for a (partial) decoupling between the canopy and the surface layer.

Despite distinct differences in the simulated diurnal cycle, effects of vertical exchange on MLC-CHEM's performance (shown in Table 4.2) are small. The similar model performance metrics reflect the compensating effects of model overestimations and underestimations during different stages in the diurnal cycle, as discussed above. The effect of constraining the simulations with observation-derived vertical exchange most strongly reduces overestimations in the simulated ozone flux, as INF reduces the model overestimations from 13-16% to 8% (Table 4.2). When analyzing skill scores for 9-15 h LT, when unstable conditions inside and above the canopy are more prevalent, the MBE is markedly lower in the INF simulation (0.7 nmol m^{-2} s^{-1}) compared to the REF and NFT simulations (4.3 and 3.2 nmol m^{-2} s^{-1}, respectively). Hence, vertical exchange only minimally affects canopy ozone uptake averaged over the entire day, but the effects are substantial during time periods characterized by (partial) decoupling between canopy and the overlying atmospheric layers.

Table 4.2: Model performance statistics of the simulated ozone flux in three MLC-CHEM simulations with different representations of vertical exchange. The table includes several common statistical model performance indicators (MBE, RMSE, r^2, slope and intercept of the linear regression fit through simulations and observations (s,i), as well as the index of agreement d (Willmott, 1982) and the fraction of simulated data points overestimated and underestimated by a factor larger than 2 (f>2× and f<2×), respectively. The unit is nmol m^{-2} s^{-1}, unless indicated otherwise.

	MBE	RMSE	r^2 [-]	s [-], i	d [-]	f>2× [-]	f<2× [-]
REF	1.61	5.5	0.45	0.69, 3.73	0.80	0.16	0.16
NFT	0.75	5.1	0.47	0.70, 2.86	0.82	0.13	0.22
INF	-0.18	4.9	0.45	0.60, 2.63	0.81	0.08	0.23

4.3.3 Effects of soil NO_x exchange on the canopy NO_x budget

Biosphere-atmosphere exchange of NO_x can be bi-directional (i.e. emission or deposition), depending on the difference between above- and below-canopy NO_x mixing ratios. Generally, the canopy-atmosphere NO_x flux is downward in (forested) regions with high background NO_x mixing ratios, regardless of the soil NO source strength (Ganzeveld et al., 2002a). Elevated NO_x mixing ratios observed at Bosco Fontana (up to 16 ppb in the morning and 4 ppb in the afternoon) therefore suggest that NO_x deposition to the forest canopy is expected to prevail at this site. The observed exchange of NO_x at the soil interface is bi-directional (NO emissions, NO_2 deposition), resulting in a substantial net upward NO_x flux (Finco et al., 2018, see also Sect. 4.2.4). We infer the contribution of soil NO_x exchange to in-canopy NO_x mixing ratios by comparing an MLC-CHEM simulation with observation-inferred vertical exchange (INF) to an experiment with deactivated soil NO_x exchange (experiments 4 and 7 in Table 4.1). Figure 4.6 displays observed and MLC-CHEM-simulated upper- and lower-canopy NO_x mixing ratios. As expected, the effect of soil NO_x exchange is largest in the understory, with simulated enhancements in NO_x mixing ratios of 0.6 ppb during daytime to 7.5 ppb at night due to soil NO_x exchange (Fig. 4.6b). Additionally, the simulation without soil NO_x exchange does not lead to nighttime NO_x accumulation in the canopy, and an underestimation of [NO_x] by >5 ppb during nighttime. Our sensitivity simulation suggests that the soil contributes on average 45% to observed mixing ratios in the understory. The net upward soil NO_x flux additionally affects the simulated diurnal course of lower-canopy NO_x mixing ratios, as the observed evening increase rate in NO_x mixing ratios is absent in the simulation without soil NO_x exchange.

Soil NO_x has a smaller effect on NO_x mixing ratios in the upper canopy layer compared to the understory. NO_x mixing ratios are lower by 0.1 ppb (daytime) up to 3.2 ppb (nighttime) in the simulation without soil NO_x exchange (Fig. 4.6a), and we infer that the soil contributes on average 21% to NO_x mixing ratios in this layer. The soil contribution
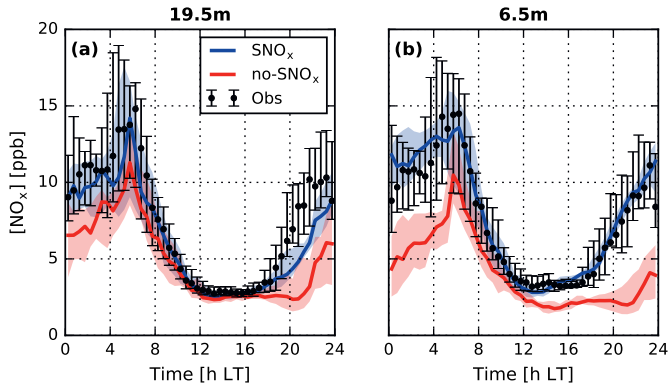
Figure 4.6: Campaign-median diurnal cycle of NO_x mixing ratios the reference heights of the two canopy layers, as simulated by MLC-CHEM (with observation-inferred vertical mixing) with (SNO_x, blue line) and without (no-SNO_x, red line) soil NO_x exchange. Observations at 19.5m are derived by vertical interpolation of measurements at 8 and 24m, while observations at 5m are directly compared to model output at 6.5m. Points and solid lines display the mean, and whiskers and shaded area display the inter-quartile range.

is lowest during mid-day, when vertical exchange between the upper canopy and the overlying air layer is intense while mixing between the two canopy layers is suppressed (Fig. 4.4b,d). Note here that the NO_x concentrations in MLC-CHEM's surface layer are nudged to observations at 32 m. The similarity in the shape of the simulated diurnal cycles suggests that diurnal variation in upper-canopy NO_x mixing ratios is largely driven by the canopy-top NO_x flux. The two simulations diverge after 16 h LT, when the upper canopy becomes stably stratified, which indicates a substantial contribution of the soil to upper-canopy NO_x levels even at this site with a large NO_x source from advection.

Canopy-atmosphere NO_x exchange is strongly affected by soil NO_x exchange. Figure 4.7 displays campaign-median diurnal cycles of simulated canopy-top NO_x fluxes with and without considering the contribution by soil NO emissions. The simulated daytime upward canopy-top NO flux is higher by up to 3 ng N m^{-2} s^{-1} due to soil NO_x exchange (Fig. 4.7a). In both simulations, the canopy remains a net sink of NO_2 due to the high background levels observed at this site. However, canopy uptake of NO_2 is reduced due to the effect of soil NO_x emissions (Fig. 4.7b), and even changes in sign at night, as mixing of soil-emitted NO_x into the canopy layers reduces the gradient between canopy and the overlying air layer. As a result of the changing vertical gradient in NO_x mixing ratios between the canopy layers and the surface layer, considering soil NO_x exchange in MLC-CHEM reduces the canopy-top NO_x fluxes by on average 4.5 ng N m^{-2} s^{-1} (-79.8%). This analysis highlights the importance of accounting for soil NO_x exchange for accurately simulating NO_x deposition in larger-scale models for relatively polluted regions.
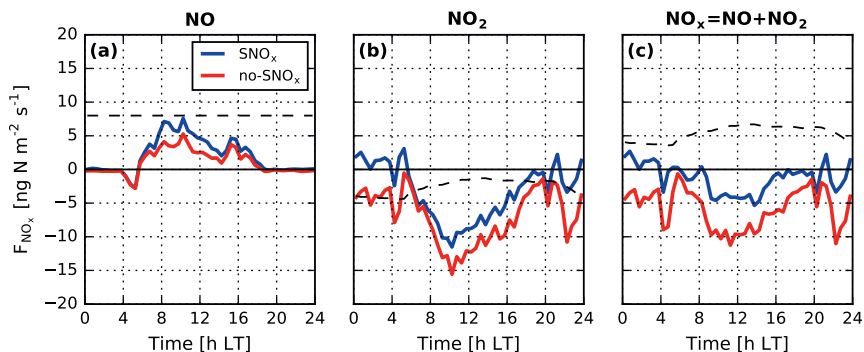
Figure 4.7: Canopy-top (26 m) fluxes of NO, NO_2 and NO_x simulated by MLC-CHEM with (SNO_x) and without (no-SNO_x) soil NO_x exchange, and using the observation-derived vertical diffusivity in both simulations (experiments 4 and 7 in Table 4.1). The black dashed lines indicate the soil fluxes for the SNO_x simulation.

4.3.4 Canopy reduction of NO_x

The simulated canopy-top NO flux is generally smaller than the soil NO flux at Bosco Fontana (Fig. 4.7), which reflects in-canopy NO_x loss. Many large-scale models do not explicitly represent canopy processes, and account for this decrease in the effective contribution by soil NO emissions to atmospheric NO_x mixing ratios by applying a canopy reduction factor (CRF) to account for in-canopy removal of the emitted NO_x by NO_2 deposition (Yienger and Levy, 1995). When above-canopy NO_x mixing ratios are smaller compared to the in-canopy NO_x mixing ratio, this CRF has a value between 0-1 (Yienger and Levy, 1995), e.g. ±0.75 for midlatitude deciduous forest (Vinken et al., 2014b). However, for high-NO_x regions such as northern Italy, an alternative definition of the CRF is more appropriate.

This alternative CRF is derived as the ratio between above-canopy and above-soil NO_x fluxes (Ganzeveld et al., 2002a), and reflects the role of in-canopy NO_2 deposition, chemical cycling, and the bi-directionality of canopy-atmosphere NO_x exchange. We derive a CRF of -0.24 (diurnal average), which indicates that the soil NO_x exchange flux is approximately 4 times higher than the simulated downward canopy-top NO_x flux. This negative estimate reflects that Bosco Fontana is a sink of NO_x, although much closer to zero compared to the CRFs of -10 to -1 found by Ganzeveld et al. (2002a) over high-NO_x regions in the northern midlatitudes. This relatively small CRF inferred from our canopy-exchange simulations can largely be explained by the large soil NO emission flux at Bosco Fontana: Ganzeveld et al. (2002a) used emission factors from Yienger and Levy (1995), which strongly underestimate soil NO emissions at Bosco Fontana (see Sect. 4.2.4). This study suggests caution for using large-scale soil NO emission algorithms (including canopy reduction factors) for
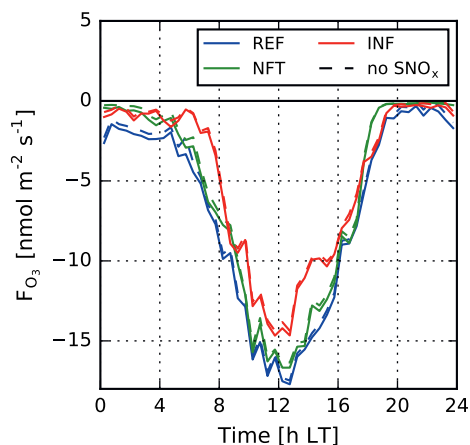
Figure 4.8: Campaign-median diurnal cycle of the total canopy ozone flux as simulated by MLC-CHEM using reference vertical exchange (REF), vertical exchange derived using near-field theory (NFT) and observation-inferred vertical exchange (INF). Solid lines indicate simulations with soil NO_x exchange, and dashed lines show simulations with deactivated soil NO_x exchange (i.e. soil NO emissions and soil NO_2 deposition).

interpreting the soil NO contribution to biosphere-atmosphere NO_x exchange in polluted environments.

4.3.5   Combined impact of vertical mixing and soil NO_x exchange on canopy ozone uptake

Figure 4.8 displays the campaign-median diurnal cycle of the total ozone flux as simulated by MLC-CHEM, using the three different representations of vertical exchange, with and without considering soil NO_x exchange. There is a decrease in the diurnal average ozone flux of 5-10% associated with the role of soil NO_x at this site, depending on the representation of vertical exchange. During daytime (5-20 h LT), the soil NO_x-induced decrease in ozone fluxes is smaller (3-4%), while the relative effect is largest during the night (>20%) due to low nighttime ozone fluxes. The in-canopy chemical ozone sink competes with other canopy ozone sinks, including stomatal uptake. However, the daytime stomatal ozone flux is reduced by only 1-3% due to the soil NO-ozone sink (not shown), suggesting that the substantial source of soil NO_x at Bosco Fontana is of minor importance for stomatal ozone uptake and flux-based metrics for ozone impacts on vegetation.

To further understand the weak sensitivity of the atmosphere-biosphere ozone flux to soil NO_x exchange, we analye differences in simulated ozone formation and removal tendencies with and without soil NO_x exchange. The tendencies (unit: ppb h^{-1}) are calculated as
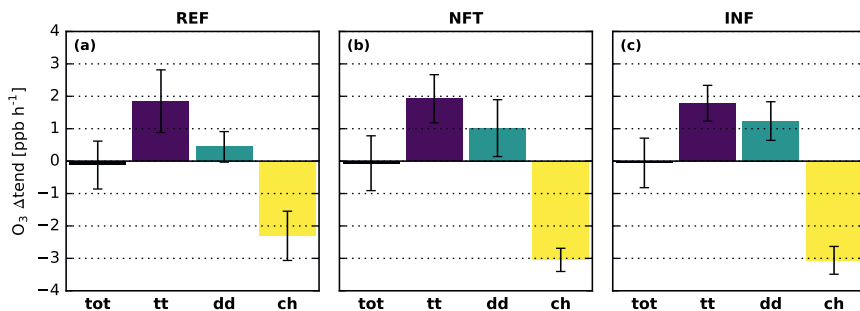
Figure 4.9: Change in lower-canopy ozone mean diurnal process tendencies as a result of soil NO_x exchange for three MLC-CHEM simulation pairs using REF-, NFT-, and INF-based vertical exchange (panels a,b,c, respectively). Displayed tendency differences (tendency with soil NO_x exchange minus tendency without soil NO_x exchange) are due to changes turbulent transport (tt), dry deposition (dd) and chemistry (ch), as well as the resulting total tendency change (tot). Error bars indicate the standard deviation of the mean diurnal process tendencies. Changes in simulated process tendencies due to soil NO_x exchange for the upper canopy are shown in Supplementary Figure A4.4.

the contribution of vertical exchange, deposition and chemical transformation to changes in ozone mixing ratios at each time step, following Ganzeveld et al. (2002b). Campaign-average diurnal cycles of these tendencies are shown in Supplementary Figure A4.3. The net upward soil NO_x exchange flux leads to changes in the diurnal variability in ozone tendencies, particularly in the lower canopy, but their diurnal variability remains similar. Therefore, we display diurnal averages of tendency changes due to soil NO_x exchange in Figure 4.9 for the three tested representations of vertical exchange, to explain the weak sensitivity of canopy-top ozone fluxes to soil NO_x exchange. Note that sinks result in negative ozone tendencies. As a result, an increased sink leads to a negative tendency change, while a decreased sink leads to a positive tendency change.

The chemical ozone sink is increased due to reaction with soil-emitted NO, reflected by a negative tendency change for ozone in the lower canopy (Fig. 4.9). This introduces two compensating effects that both result in positive tendency changes: reduced deposition and increased vertical transport. Lower-canopy ozone deposition is reduced, because chemical removal and deposition are two competing sinks, acting on the ozone reservoir in the lower canopy. However, the reduced deposition sink does not fully compensate for the enhanced chemical ozone destruction. An additional compensating effect results from the dependence of vertical transport on the ozone gradient between the upper and lower canopy. The soil NO_x-induced chemical sink results in a larger vertical ozone gradient between the upper and lower canopy, and this increases vertical ozone transport into the lower canopy. These results do not strongly depend on the representation of vertical

exchange (Figure 4.9). According to our analysis, reduced dry deposition and increased vertical transport together offset the enhanced lower-canopy ozone sink by reaction with soil NO.

4.4   Discussion

Our results show how vertical mixing conditions inside a forest differ from those in the atmospheric surface layer as a result of the presence of thermal inversions within the canopy. Accounting for these stability effects in the multi-layer canopy exchange model MLC-CHEM, by inferring the vertical diffusivity from observations (INF), leads to morning ozone deposition velocity decreases by up to 0.2-0.4 cm s^{-1} compared to two tested vertical exchange parameterizations in MLC-CHEM (REF and NFT), and in closer agreement with observations. In the afternoon, REF and NFT overestimate ozone deposition flux by on average 4.3 and 3.2 nmol m^{-2} s^{-1}, respectively, while INF agrees better with observations (MBE = 0.7 nmol m^{-2} s^{-1}). Given the dependence of in-canopy turbulence on stand density and vertical leaf area distribution (e.g., Banerjee and Linn, 2018; Russell et al., 2018), this effect may be generalizable to closed forest canopies receiving high solar radiation. For these conditions, 3D atmospheric chemistry models, with highly parameterized vertical mixing inside and above forest canopies, could potentially overestimate atmosphere-biosphere exchange of ozone and other trace gases.

In our observation-based characterization of canopy-atmosphere exchange, we derived the vertical diffusivity from 30-minute averages of temperature and the sensible heat flux. This is a common method to infer canopy-atmosphere exchange from observations (e.g., Brown et al., 2020) that incorporates effects of thermal stability on vertical exchange inside the canopy and between the canopy and the surface layer. This is an advancement compared to conventional methods that simulate in-canopy transport, used in deposition parameterizations applied in large-scale chemistry-transport models (e.g., Van Pul and Jacobs, 1994), which are based on above-canopy turbulence intensity (via the friction velocity) and canopy density (via LAI). However, the K-theory approach based on average fluxes and gradients does not account for non-local, intermittent sources of turbulence (Finnigan, 2000; Raupach, 1989). Previous work found variable effects of coherent structures to observed canopy-top fluxes: Thomas and Foken (2007) found a resulting 4% error in eddy-covariance fluxes, while Steiner et al. (2011) reported a 44-65% contribution by coherent structures to the observed sensible heat flux.

The availability of ozone flux and mixing ratio observations along a vertical profile enables us to explore the similarity between K_H and a vertical diffusivity derived from 30-minute averages of ozone flux and mixing ratio observations (K_{O_3}), shown in Supplementary Figure A4.4. In the morning, K_{O_3} exceeds MLC-CHEM-simulated and observation-inferred K_H in the upper canopy (Supplementary Fig. A4.4a). Finco et al. (2018) find an enhanced ozone

flux at the canopy-atmosphere interface, possibly resulting from a local enhancement in NO mixing ratios at the canopy-top transported to this height from the soil and the surface layer. During the morning, with a relatively large vertical transport timescale ($\tau_t \approx 10$ h, Fig. 4.10) compared to the smaller timescale of chemical ozone loss by reaction with NO ($\tau_c \approx 1$ h, Fig. 4.10), we suspect that this enhanced flux will not change the ozone gradient between the canopy and the atmosphere, leading to an elevated K_{O_3} compared to K_H. During the afternoon, observation-derived values of K_H and K_{O_3} agree well, suggesting that chemical alteration of the ozone flux in the upper canopy dominantly occurs in the morning. Lower-canopy K_{O_3} exceeds K_H throughout the day (Supplementary Fig. A4.4b), reflecting enhanced ozone removal due to the reaction between soil-emitted NO and ozone.

Our results highlight that canopy exchange of NO_x is driven by the vertical gradient in NO_x mixing ratios between the canopy and the surface layer. Soil NO emissions are high at our North-Italian study site, possibly due to high nitrogen deposition (Vries et al., 2021) leading to nitrogen accumulation in the soil. We estimate that these soil emissions offset the total NO_x deposition by 80%, and that soil-emitted NO is largely removed inside the forest. We conclude that information on canopy sources and sinks of NO_x, including soil NO emissions, is essential to understand the NO_x budget of forests, particularly in regions with high background levels of air pollution.

The campaign observations applied in this study indicate the presence of strong vertical gradients in NO_x and ozone mixing ratios in the lower canopy. Daytime NO_x mixing ratios measured directly above the soil are higher by up to 7 ppb compared to measurements at 5 m, while ozone mixing ratios above the soil (0.15 m) are $\pm$20-55 ppb lower (Finco et al., 2018). These differences are caused by soil exchange processes (emissions of NO, deposition of NO_2 and ozone) and chemical reactions, amplified by the very stable stratification at this height. This near-surface effect is important for evaluating the contribution of soil emissions to the canopy NO_x exchange budget, as our results show that the soil NO_x flux inferred from above-soil enclosure chamber measurements cannot be reconciled with the observed NO_x mixing ratios at 6.5 m (Supplementary Fig. A4.2), likely indicating NO_x loss near the forest floor. Resolving these gradients requires an increased vertical resolution in MLC-CHEM. Our choice for a model with two canopy layers is justified by the applicability of this model version in regional/global models (Ganzeveld et al., 2010; Ganzeveld et al., 2002b), and the availability of observational constraints at two heights in the canopy.

To further investigate potential sub-grid vertical gradients, we derive mid-canopy lifetimes against vertical transport, chemical loss and deposition (Figure 4.10). If the lifetime against vertical transport (τ_t) is of a similar magnitude as the lifetime of other processes, replenishment is not sufficiently fast to counter chemical loss or deposition, leading to sharp vertical ozone gradients that are challenging to resolve in multi-layer canopy models.
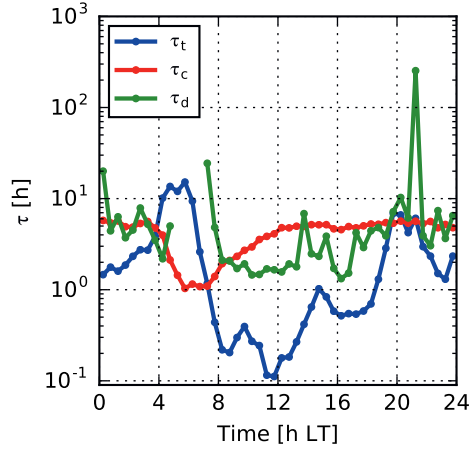
Figure 4.10: Campaign-averaged diurnal cycles of lifetimes against vertical transport (τ_t), chemical ozone loss by reaction with NO (τ_c) and deposition (τ_d) calculated from observations approximately at mid-canopy. Lifetimes are derived as follows: $\tau_t = \frac{1.1|h_c - z|^2}{K_H}$ (Gerken et al., 2017, with z=13m), $\tau_c = \frac{1}{k[NO]}$ (with $k = 1.9 \times 10^{14}$ s^{-1} and [NO] at 8 m), and $\tau_d = \frac{z}{V_d(O_3)}$ (with z=16m). Note that early-morning τ_d values are omitted as they display erratic behavior due to near-zero ozone flux observations.

During the early morning and evening, τ_t is indeed of a similar or higher magnitude compared to τ_c and τ_d. During daytime, however, vertical ozone transport is much faster than chemical loss and deposition, indicating that the mid-canopy is well-mixed. However, sharp ozone and NO$_x$ gradients occur directly above the soil (Finco et al., 2018), which occurs at the subgrid-scale in MLC-CHEM.

The aforementioned shortcomings could be addressed by application of a Large-Eddy Simulation (LES) model coupled to a multi-layer canopy model to study ozone deposition (hereafter LES-MLC). Recently, LES simulations of canopy turbulence have been performed under varying atmospheric stability (e.g., Patton et al., 2016), and Clifton and Patton (2021) have extended this approach with ozone uptake. These models advantageously resolve turbulent motions at a larger range of length scales, and have an in-canopy vertical resolution on the order of several meters. Therefore, LES models are an appropriate tool to investigate vertical gradients in turbulent exchange inside and directly above forest canopies, and how this affects canopy-atmosphere exchange of NO$_x$ and ozone. As a future line of research, we propose to apply coupled LES-MLC models to improve mechanistic understanding of the interaction between in-canopy turbulent mixing gradients and ozone removal processes. For example, LES-MLC models can be applied to investigate how vegetated canopies affect chemical ozone flux divergence (Vila-Guerau De Arellano et al., 1993), and to test how this affects the (dis)similarity between vertical diffusivities for

sensible heat and trace gases (Fig. A4.4). This would require performing LES-MLC simulations that closely mimic site conditions at selected observational sites with detailed observations of in-canopy turbulence and trace gas exchange fluxes, which is an area of ongoing research (Bannister et al., 2022). The proposed developments have large potential to improve the representation of turbulent exchange in multi-layer canopy exchange models (e.g. MLC-CHEM) that can be applied in coupled 3D atmospheric chemistry model experiments used for air quality assessments and chemistry-climate studies.

4.5 Conclusions

We quantified the impact of forest-atmosphere turbulent exchange and soil NO_x exchange on ozone deposition in a polluted Italian forest. To this end, we applied a multi-layer canopy exchange model (MLC-CHEM) to interpret campaign observations of NO_x and ozone mixing ratios, temperature, and fluxes of sensible heat and ozone. Vertical mixing conditions in the dense Bosco Fontana forest canopy are fully or partially decoupled from the overlying air layers during large parts of the campaign. This poses a challenge for simulating ozone uptake in multi-layer models of canopy-atmosphere exchange using traditional vertical exchange parameterizations based on K-theory.

We show how turbulent transport can be a limiting factor for ozone deposition to forest canopies. In land surface parameterizations applied in large-scale atmospheric chemistry and transport models, turbulent transport generally does not limit land surface ozone uptake. However, two parameterizations of canopy-atmosphere exchange cannot reproduce the vertical diffusivity derived from observed vertical temperature and sensible heat flux gradients, since they parameterize in-canopy vertical mixing based on above-canopy wind speed or friction velocity. Accounting for observed vertical exchange in our simulations decreases the simulated deposition velocity by 0.2-0.4 cm s^{-1} ($>$100%) in the morning when canopy-atmosphere exchange is weak, and a better agreement with observations (-5%) compared to the two tested parameterizations (+10-19%).

The soil contribution to observed in-canopy NO_x mixing ratios is substantial, particularly in the lower canopy layer (45% on average). This is remarkable, given the high background NO_x mixing ratios observed above the canopy (around 4 ppb during daytime). The canopy-atmosphere exchange flux of NO_x at this site, which is dominated by NO_x deposition, is decreased by up to 80% as a result of a significant soil NO_x emission source. However, a sensitivity study showed that the simulated canopy ozone deposition flux is hardly affected by the reaction between ozone and soil-emitted NO. This is partly because the increasing ozone sink posed by the soil NO-ozone reaction leads to reduced dry deposition to the soil and understory vegetation, partly due to enhanced downward ozone transport as the lower canopy becomes a stronger sink.

Our results highlight how the complex nature of vertical mixing in forests affects canopy-atmosphere exchange of reactive trace gases. Including a more physically accurate representation of canopy-atmosphere exchange in atmospheric chemistry modelling on larger spatial scales will help to better quantify the land surface ozone sink, as well as its impacts on surface ozone mixing ratios and ecosystem carbon uptake. In this context, we suggest to apply turbulence-resolving model experiments coupled to multi-layer canopy models of trace gas exchange to support analysis of field observations. This approach has potential to increase our understanding of the interaction between in-canopy turbulence and ozone sinks, and to improve the representation of this interaction in land surface parameterizations in larger-scale chemistry transport models.

A4   Appendix
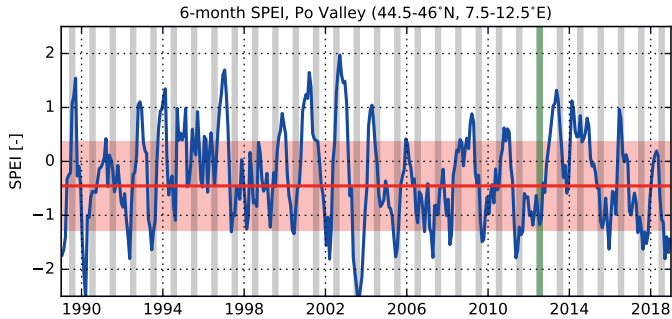
Figure A4.1: 30-year time series (1989-2018) of the Standardized Precipitation Evaporation Index (SPEI) integrated over the preceding 6 months for the Po Valley in North Italy. Red line and shaded area indicate the June-August mean 6-month SPEI value over the 30-year time series. The green shaded area indicates June-August 2012 when the Bosco Fontana intensive measurement campaign took place.

A4.1   Spatio-temporal context of ozone deposition

We analyze a synthetic ozone flux data set (SynFlux; Ducker et al., 2018), where the stomatal ozone flux is derived for flux tower eddy covariance measurements based on a combination of inferred stomatal conductance (by inverting the Penman-Monteith equation for flux tower measurements), a gridded dataset of surface ozone concentrations, and a parameterized non-stomatal ozone flux component. Figure 4.1a shows SynFlux-derived stomatal and total ozone fluxes for summer 2012 (June-August) near North Italy. To place this in a temporal context, we calculate stomatal and total ozone flux anomalies by subtracting the multi-year June-August flux from the June-August 2012 mean flux per site, depicted in Figure 4.1b.

The ozone flux anomalies in Figure 4.1b are overlaid on a Standardized Precipitation-Evaporation Index (SPEI) map for June-August 2012. SPEI is a drought index that is based on the difference between precipitation and potential evaporation (Vicente-Serrano et al., 2010). SPEI can be integrated over different timescales; we here use the 6-month SPEI to analyze water deficits occurring over a 6-month time period to capture effects from the onset of the growing season. A 6-month SPEI time series over 1989-2018 is shown in Figure A4.1. The negative SPEI values in Figure 4.1b (range: -1.17 to -0.95) indicate a water deficit in summer 2012, but this falls within the 1-σ range of North-Italian summer SPEI-values in the climatological time period. We therefore conclude that the
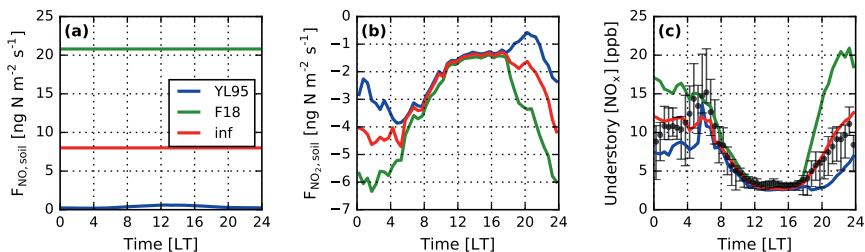
Figure A4.2: Diurnally averaged soil fluxes of NO (panel a) for different MLC-CHEM runs during July 2012 in Bosco Fontana, based on default MLC-CHEM emissions factors for deciduous forests (blue line; Yienger and Levy, 1995), the emission strength at Bosco Fontana derived from observations above the forest floor (green line; Finco et al., 2018) and the inferred "effective" soil NO flux representative for the soil impact on simulated mixing ratios at 6.5 m. Panels b and c show the resulting impacts in the diurnal averages of the soil NO_2 deposition flux and NO_x mixing ratios in the understory, respectively. Note that the three MLC-CHEM simulations presented in this figure have been performed with MLC-CHEM's reference parameterization of vertical exchange (REF).

Bosco Fontana observations in summer 2012 are likely representative for typical summer conditions in this region.
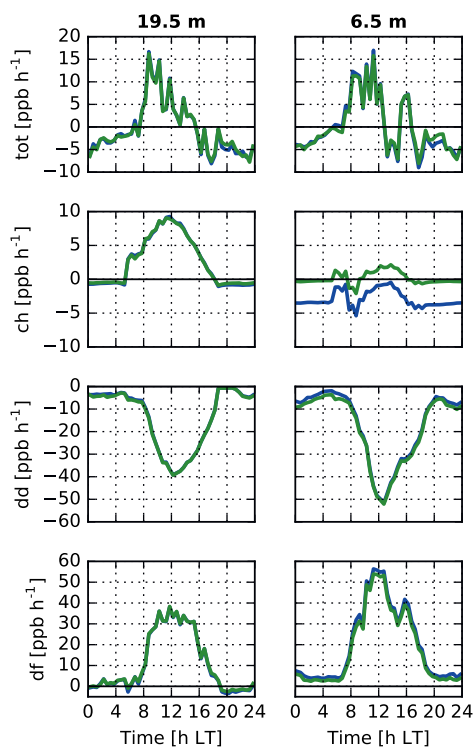
Figure A4.3: Mean diurnal variation in MLC-CHEM-simulated process tendencies in the upper canopy (19.5 m) and the lower canopy (6.5 m) for the simulations with and without soil NO_x exchange (simulations 4 and 7 in Table 1 in the main text). Tendencies from the following processes are shown: vertical exchange (df), dry deposition (dd), chemistry (ch), and total (tot, i.e., the sum of the previous three tendencies).
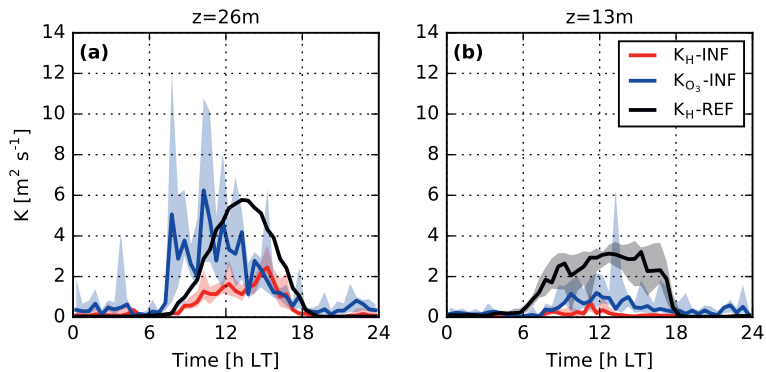
Figure A4.4: Diurnal variation in vertical diffusivity derived from MLC-CHEM's reference simulation (black line), inferred from sensible heat flux and potential temperature observations (red line), and from vertical profile measurements of the ozone flux and ozone mixing ratios (blue line; obtained by applying Eqn. 4.2 in the main text for the observed ozone flux and vertical gradient). Solid lines display the campaign median, and shaded areas indicate the inter-quartile range.

Chapter 5

Simulating the effect of land surface heterogeneity on ozone dry deposition in a Large Eddy Simulation model

Abstract

Heterogeneity in land surface properties influences atmospheric composition via its effects on turbulent mixing in the planetary boundary layer and deposition processes. These small-scale features are not resolved in atmospheric chemistry models with a spatial resolution on the order of several kilometers or coarser. In this study, we examine surface ozone concentration fluctuations caused by spatially heterogeneous ozone dry deposition rates, leading to covariance between concentrations and deposition velocities. This process is termed dry deposition flux covariance (flux $F = V_d \times C$). Coincident small-scale variations in the dry deposition velocity and surface ozone mixing ratios have the potential to affect the simulated domain-average ozone dry deposition flux. The simultaneous effect of land surface heterogeneity on turbulent mixing and dry deposition has previously not been quantified to our knowledge. We perform turbulence-resolving simulations with the Large Eddy Simulation (LES) model MicroHH, at a 100×100 m^2 resolution. MicroHH's explicit representation of chemistry and dry deposition (using a big leaf parameterization coupled to MicroHH's land surface model) enables us to quantify the covariance between concentration and deposition velocity. When turbulence, land cover and dry deposition velocities are explicitly resolved, ozone dry deposition is virtually similar (within 0.1%) compared to a simplified situation with parameterized, homogeneous turbulence and domain-average land cover. In a range of sensitivity experiments, we find that the magnitude of this covariance is affected by the dry deposition strength and variability, as well as by the imposed vertical ozone gradient. If the ozone gradient is positive, downward transport towards the surface compensates for the negative dry deposition flux covariance. When we investigate the covariance between concentration and deposition velocity in a simulation of a power plant plume, we find moderate effects. This leads to amplified dry deposition flux co-variances of +2% for ozone, since the ozone concentration increases with height since the high in-plume NO causes ozone titration. Inside the plume, NO$_x$ mixing ratios strongly peak at the surface, and this results in a stronger, negative flux covariance values (-9 to -22%). This work suggests that dry deposition flux covariance can be important, affecting domain-integrated deposition fluxes, particularly for species that display strong vertical concentration gradients in the boundary layer.

5.1   Introduction

Heterogeneity in land surface properties affects the composition of the overlying atmosphere at different spatial scales (Ganzeveld et al., 2010; Ouwersloot et al., 2011). A persistent challenge in atmospheric chemistry modelling is the scale at which to represent relevant processes. Large-scale atmospheric chemistry models typically have a grid size on the order of ± 5–100 km, and thus cannot explicitly represent processes on smaller spatial scales. Such subgrid-scale effects are typically parameterized or neglected. Resolution dependence of atmospheric chemistry modelling is widely documented, and for example affects the model-observation agreement for surface ozone mixing ratios (Im et al., 2015; Solazzo et al., 2012; Vinken et al., 2011). One common method to study scale issues is to vary model resolution in global or regional models. Generally, increasing model resolution leads to improved simulation of spatial emission variations important for simulating non-linear chemistry (Cohan et al., 2006; Schaap et al., 2015; Wild and Prather, 2006).

A downside of these large-scale models, even when being applied at a high spatial resolution (e.g., up to 5 km), is that they still parameterize turbulent motions, and therefore assume homogeneous mixing conditions within regions of ± 5–100 km, also known as "instant dilution". Large-Eddy Simulation (LES) models resolve a larger range of turbulence length scales and operate on sub-kilometer horizontal resolutions. Therefore, LES models are an appropriate tool to study heterogeneity on the subgrid-scale of regional/global models. For example, land surface heterogeneity affects the surface energy balance, which can induce organized boundary layer motions, depending on the spatial scale of the heterogeneity and the boundary layer height (Patton et al., 2005). Inhomogeneous mixing of the convective boundary layer is referred to as segregation.

As the name suggests, segregation leads to inhomogeneous mixing of chemical species. As a result, reactive species can be distributed in an (anti-)correlated manner, which affects their domain-average reaction rate (Vila-Guerau De Arellano et al., 1993). This has for example been shown in wind tunnel experiments for the NO-ozone reaction (Vilà-Guerau de Arellano et al., 1990), and using observations in a German deciduous forest, where the isoprene-OH reaction rate is reduced by inhomogeneous mixing of the two species (Dlugi et al., 2010). In addition, inhomogeneously distributed emissions of reacting species enhance chemical segregation. LES models can be used to assess how chemical reaction efficiencies are affected by heterogeneity in turbulent mixing and surface emissions (e.g., Auger and Legras, 2007; Krol et al., 2000; Ouwersloot et al., 2011; Vinuesa and Galmarini, 2009). Approaches to account for chemical segregation due to heterogeneous surface emissions are available in the literature (e.g., Vinken et al., 2011). However, the effect of spatial heterogeneity on surface deposition has thus far received little attention. Typically, such analyses are limited to parameterizing sub-grid variations in the dry deposition velocity on simulated domain-average values by large-scale models (Gao, 1995; Ma and

Daggupaty, 2000; Tetzlaff et al., 2002), without accounting for the effect of sub-grid land cover heterogeneity on simulated turbulence.

Typically, LES-based analyses of chemical segregation assume a constant dry deposition velocity, while in reality the dry deposition velocity may vary considerably as a function of land cover, radiation, temperature, vertical mixing, soil moisture and vapor pressure deficit. (Clifton and Patton, 2021) explicitly simulated leaf ozone uptake in a forest canopy, and found that the effect of segregated mixing in the boundary layer on leaf ozone uptake in a forest canopy is small. However, that study focused on in-canopy conditions and was limited to homogeneous land cover, representative for a midlatitude deciduous forest. In this study, we investigate the effect of spatial land cover heterogeneity on the deposition sink, and feedbacks on surface ozone mixing ratios.

To address this interaction, we apply a modular approach, in which we first study the effect of spatial variability in dry deposition associated with land surface heterogeneity in a simulation without chemistry (i.e., pollutant mixing ratios are only affected by lateral boundary in- and outflow, vertical mixing and deposition). Then, we study the effect of dry deposition heterogeneity in a simulation that also accounts for chemistry and strongly heterogeneous emissions. Specifically, we ask:

1. How does spatial heterogeneity in land cover affect the deposition patterns of NO_x and ozone on spatial scales relevant for interpreting observations?

2. How does resolving landscape heterogeneity affect the domain-integrated NO_x and ozone dry deposition budget?

5.2　Model description

We perform simulations with a Large Eddy Simulation model for a 25.6×25.6 km² domain in eastern Germany, which is displayed in Figure 5.1 (a further case study description is given in Section 5.3.1). The numerical simulations presented in this study are performed using MicroHH (Van Heerwaarden et al., 2017). This computational fluid dynamics model solves the energy, momentum and mass conservation equations, and can be applied for direct numerical simulations (DNS, spatial resolution of several meters) or large eddy simulations (LES, spatial resolution of 50–100 m). In the simulation set-up we use the Land Surface Model (LSM) HTESSEL (Balsamo et al., 2009), that is coupled to the atmosphere. To calculate the radiative fluxes, the model uses the RRTMGP radiation scheme (Pincus et al., 2019). Recently, MicroHH has been set up under realistic meteorological conditions by prescribing the geostrophic wind and large-scale advection terms based on ERA5 data (Hersbach et al., 2020), as described in Ražnjević et al. (2022). The model has been applied successfully to simulate the dynamics of the convective boundary layer (Bosman et al., 2019; Van Heerwaarden et al., 2014). Recently, the model has been extended

Figure 5.1: Left panel: map of Germany showing the approximate location of the case study region in red. Right panel: zoomed image of the approximate MicroHH model domain. The Jänschwalde power plant is indicated on the top right.

with transport of passive tracers (Ražnjević et al., 2022), and a version with an explicit representation of chemistry is currently under development.

The LSM is a tiled parameterization that represents components of the surface energy balance over varying land cover. The MicroHH configuration of HTESSEL is a tiled LSM where every surface grid cell is divided into four land cover categories: vegetation, bare soil, wet skin and open water. Land cover data is derived from the CORINE land use data set at a 100 m spatial resolution (European Environment Agency, 2021). The stomatal resistance (r_s) for the vegetation tile is calculated following the multiplicative approach by Jarvis (1976):

$$r_s(H_2O) = \frac{r_{s,veg,min}}{LAI} \times f_{VPD} \times f_{SWC} \times f_{rad} \tag{5.1}$$

This formulation accounts for the effects of radiation (rad), leaf area index (LAI), soil water content (SWC) and the vapour pressure deficit (VPD) on r_s (correction functions can be found in Van den Hurk et al., 2000).

The 21 land cover classes in CORINE are assigned vegetation properties (e.g. vegetation/soil fraction, LAI, roughness length, minimum stomatal resistance ($r_{s,veg,min}$), etc.) for use in the LSM following Van den Hurk et al. (2000). Parameter settings for some relevant land cover types are displayed in Table 5.1. The wet skin fraction is calculated per time step and accounts for precipitation interception and dew formation. The wet skin tile is a composite of vegetation and bare soil, following the pixel-specific vegetation and bare soil fractions.

Table 5.1: Parameter settings of the HTESSEL land surface model used in MicroHH (derived from Van den Hurk et al., 2000).

	crops	short grass	evergreen needleleaf	deciduous broadleaf	urban
$z_{0,m}$ [m]	0.25	0.2	2	2	1
LAI [m^2 m^{-2}]	3	2	5	5	2
$r_{s,veg,min}$ [s m^{-1}]	100	100	250	175	100
c_{veg} [-]	0.90	0.88	0.90	0.90	0.50

5.2.1   Chemistry representation

MicroHH has recently been extended to include a representation of gas-phase chemistry. The gas-phase chemical mechanism consists of 14 species and 33 reactions, and includes NO_x-ozone photochemistry and a simplified representation of carbon monoxide (CO) and hydrocarbon oxidation. The chemistry scheme is based on the chemical mechanism in the IFS operational system (Flemming et al., 2015), but with a reduced number of chemical species and reactions for computational efficiency. The representation of chemistry will be the subject of a forthcoming publication, and here we mainly focus on the representation of dry deposition.

5.2.2   Deposition parameterization

We implemented a big leaf parameterization to represent deposition of gaseous species in MicroHH. This parameterization calculates local, land use class-specific dry deposition velocities of seven gaseous species: ozone, NO, NO_2, nitric acid (HNO_3), hydrogen peroxide (H_2O_2), hydroperoxides (ROOH) and formaldehyde (HCHO). A schematic of the gaseous dry deposition velocity parameterization is shown in Figure 5.2. The dry deposition velocity of species X is calculated as follows:

$$V_{d,X} = (r_a + r_b + r_c)^{-1} \tag{5.2}$$

In this equation, r_a is the aerodynamic resistance, calculated following Monin-Obukhov similarity theory. r_b is the quasi-laminar layer resistance, derived from the formulation by Wesely and Hicks (1977). r_c is the surface uptake resistance, whose formulation depends on the land cover type (Fig. 5.2). For vegetation, r_c reflects removal pathways by stomatal uptake, external leaf surfaces (cuticula) and soils, and is calculated as follows:

$$r_c = \left(\frac{1}{r_s(X) + r_m} + \frac{1}{r_{cut}} + \frac{1}{r_{a,inc} + r_{soil}} \right)^{-1} \tag{5.3}$$
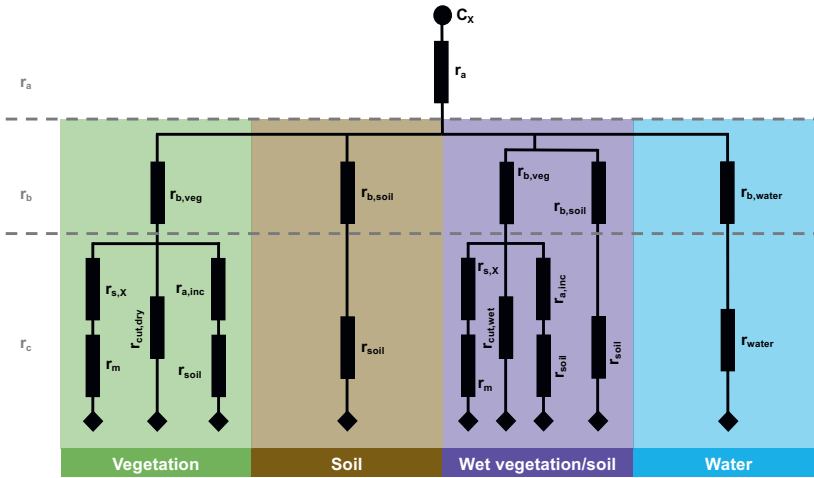
Figure 5.2: Schematic representation of the dry deposition parameterization implemented in MicroHH, based on Wesely, 1989 and Ganzeveld and Lelieveld, 1995. Separate dry deposition velocities are calculated for vegetation, soil, wet skin and water tiles. Shown resistance groups are: aerodynamic resistance (r_a), quasi-laminar layer resistance (r_b), calculated per tile, and the surface resistance (r_c). r_c is calculated using the stomatal resistance corrected for diffusivity ($r_{s,X}$, Equation 5.1), mesophyll resistance (r_m), cuticular resistance (r_{cut}, calculated differently for wet and dry vegetation), in-canopy aerodynamic resistance ($r_{a,inc}$), and resistances to removal by soils (r_{soil}) and open water bodies (r_{water}).

Table 5.2: Resistance values for ozone, NO and NO$_2$ used in the dry deposition parameterization in MicroHH.

Resistance	O$_3$	NO	NO$_2$	Reference
r_s	Equation 5.1			Jarvis (1976)
$r_{a,inc}$	$\frac{14 LAI h_c}{u_*}$			Van Pul and Jacobs (1994)
r_m	1	$5 \times r_s$	$0.5 \times r_s$	
$r_{cut,dry}$	10^5	10^5	10^5	
$r_{cut,wet}$	2000	10^5	10^5	Ganzeveld and Lelieveld (1995)
r_{soil}	400	10^5	600	
r_{water}	2000	10^5	10^5	

where $r_s(X)$ is the canopy stomatal resistance for species X (i.e., scaled from leaf-level to canopy-level using LAI), which is derived by correcting $r_s(H_2O)$ (calculated using Equation 5.1) for the different diffusivity of water vapour and X. The resistance values for the gases under consideration in this study (ozone, NO and NO_2) are presented in Table 5.2. Surface uptake resistances for HNO_3 are also taken from Ganzeveld and Lelieveld (1995), and for the other gases (H_2O_2, ROOH and HCHO) we use the values from Wesely (1989). The in-canopy aerodynamic resistance ($r_{a,inc}$) represents the resistance to transport from the canopy-top to the soil (Van Pul and Jacobs, 1994). Although originally derived for maize crop, this parameterization is widely used for all vegetation classes in dry deposition parameterizations (e.g., Erisman et al., 1994; Pleim and Ran, 2011; Visser et al., 2021; Zhang et al., 2002) in absence of observations for other land cover types.

For the soil and water tiles, r_c simply equates the soil and water resistance, respectively. For the wet skin tile, the surface resistance is separately calculated for the vegetation and bare soil components. Note that cuticular uptake is affected by water films on leaves, and is represented with a modified resistance value ($r_{cut,wet}$). The presence of water films on leaves is assumed to result in a reduced cuticular resistance of 2000 s m^{-1} (e.g., Altimir et al., 2006), but the cuticula resistance of NO and NO_2 is unaffected (Table 5.2). The dry deposition velocities calculated in this procedure are added as surface layer reaction rates in the chemistry parameterization:

$$\left[\frac{\partial C}{\partial t}\right]_{deposition} = -\frac{V_{d,C}}{dz}[C] \tag{5.4}$$

which expresses that the concentration change due to deposition ($\left[\frac{\partial C}{\partial t}\right]_{deposition}$) is the product of the dry deposition velocity ($V_{d,C}$) and the concentration of C, divided by the height of the grid box in contact with the surface.

5.3   Methods

5.3.1   Case study description

We perform MicroHH simulations in the context of the European Union's Horizon 2020 project CoCO2 (https://coco2-project.eu/). This project aims to develop a monitoring system for anthropogenic CO_2 emissions using high-resolution atmospheric modelling, with the aim to exploit remote sensing data of co-emitted species (e.g. carbon monoxide and nitrogen oxides). The model domain of 25.6×25.6 km^2 is situated in eastern Germany contains the fifth-largest coal-fired power plant in Europe (Jänschwalde), and the emitted plume serves as a test case for emission verification in CoCO2. The vertical extent of the model domain is 4 km above the land surface. Figure 5.3a-c shows the vegetation,
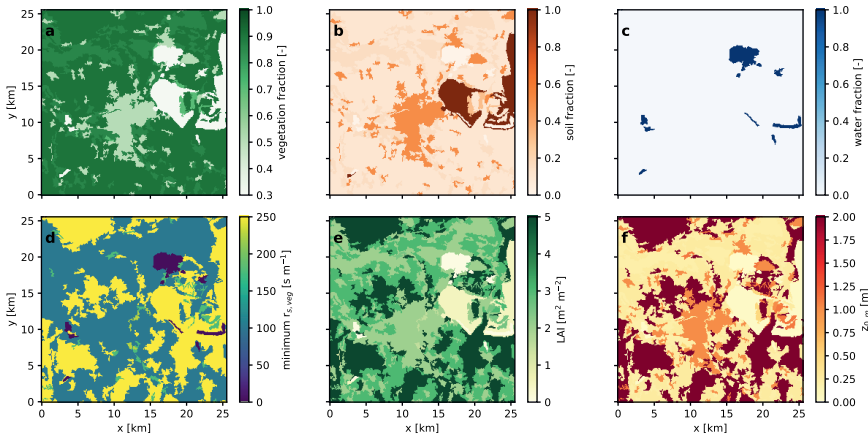
Figure 5.3: Land surface model parameters used for the high-resolution MicroHH simulation. Pixel fractions of the vegetation, soil and water tiles are shown in panels a-c, respectively. Panels d-f respectively show the minimum stomatal resistance for vegetation (as used in Equation 5.1), the leaf area index, and the roughness length for momentum.

soil and water tile fractions for the model domain. The domain is characterized by a heterogeneous land cover, including brown coal mines, a city approximately in the center of the domain (Cottbus), smaller urban agglomerations, forests, agricultural areas, and open water bodies. As such, this area serves as an interesting case study to investigate the impact of land cover heterogeneity on dry deposition.

The simulations are performed for May 22nd-23rd 2018, at a spatial resolution of 100×100 m^2 and a vertical resolution of 62.5 m. MicroHH is initialized on May 22nd at 21:00 h UTC, and the first three hours are used for model spin-up. The model is initialized and forced along the lateral boundaries with potential temperature, specific moisture content and u and v wind components from hourly meteorological reanalysis data from ERA5, interpolated to the model time steps. Figure 5.4a-c shows the initial and boundary conditions of the u- and v- components of the wind vector (panels a and b, respectively) and potential temperature (panel c). The meteorological conditions are characterized by predominantly negative u values indicating an easterly flow. The well-mixed potential temperature profiles in the afternoon (Figure 5.4c) indicate convective turbulent vertical mixing conditions. MicroHH is forced with chemical boundary conditions from the CAMS reanalysis product (Inness et al., 2019). Figure 5.4d-f displays hourly vertical profiles of NO, NO$_2$ and O$_3$ from CAMS-derived lateral boundary conditions. NO and NO$_2$ mixing ratios display a strong enhancement in lowermost model layers, and decrease strongly with altitude. In contrast, ozone mixing ratios are lowest towards the surface (42-45 ppb) and increase with altitude to values above 60 ppb in the upper model level. All
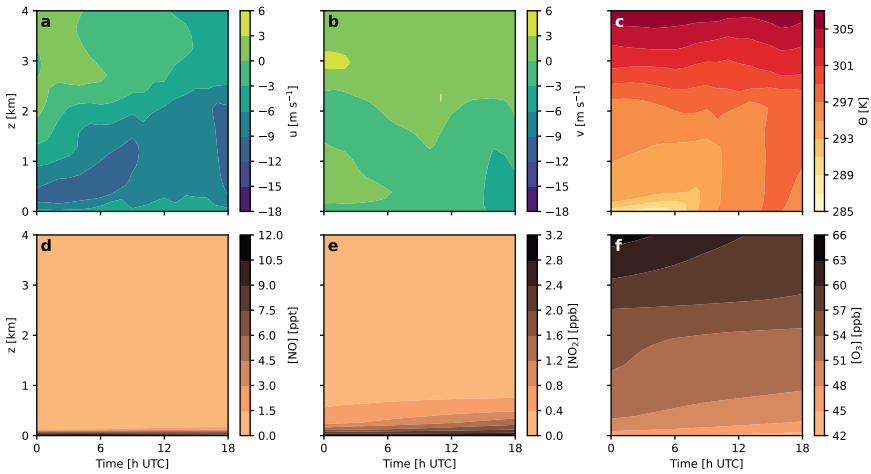
Figure 5.4: Hourly vertical profiles of large-scale model forcings of meteorological variables, NO_x and ozone. Displayed variables are the u- and v-components of the wind vector (panels a and b, respectively) and potential temperature (panel c), derived from the ERA5 reanalysis product (Hersbach et al., 2020), and mixing ratios of NO, NO_2 and ozone, derived from the CAMS reanalysis product (Inness et al., 2019).

boundary conditions are applied uniformly along the model boundaries in the x- and y-directions.

5.3.2   Dry deposition sensitivity to land surface parameters

Before we investigate the effect of land surface heterogeneity on dry deposition, we first examine the dependence of ozone deposition on land cover type in MicroHH. Figure 5.5 shows the simulated spatial and temporal variability of the ozone dry deposition velocity for the standard LSM setup and with two modified parameter settings. In the default LSM setup, the simulated noontime average dry deposition velocity shows distinct spatial variability, with low values over water bodies and soils (0.05 cm s^{-1} and 0.2 cm s^{-1}, respectively, see Fig 5.5a,d), and higher values over areas with a high vegetation fraction (see Fig. 5.3a). Within the pixels dominantly covered by vegetation, noontime V_{d,O_3} varies spatially between 0.4-0.7 cm s^{-1} (Fig. 5.5a). This simulated range reflects a lower V_{d,O_3} for forests compared to that of grassland, due to an assumed lower minimum stomatal resistance for grassland areas compared to forests in HTESSEL (Fig. 5.3d), resulting in higher model-simulated transpiration (and stomatal deposition) for grassland compared to forests (Fig. 5.5a). This contrasts common model outcomes that deposition velocities to (deciduous) forests are comparable or higher than to grassland (Hardacre et al., 2015).
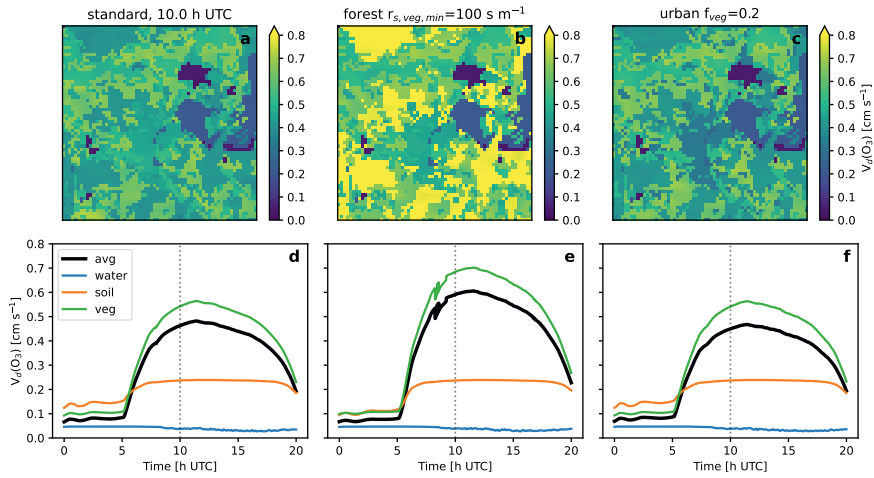
Figure 5.5: MicroHH-simulated ozone dry deposition velocity and its sensitivity to LSM surface properties. The top row panels (a-c) show the simulated instantaneous ozone dry deposition velocity (V_{d,O_3}) at 10:00 h UTC. The bottom row panels (d-f) show the domain-average diurnal cycle at the tile level (vegetation, soil and water), and at the pixel level (the weighted average of the tile-level V_{d,O_3} values) for the three simulations with different LSM parameter settings (left: standard LSM setup; center: modified $r_{s,veg,min}$ for forests; right: modified urban vegetation fraction). The dotted vertical lines in panels d-f indicate the time of the V_{d,O_3} maps in panels a-c. These sensitivity simulations have been performed with 21-hour MicroHH simulations at a spatial resolution of 400m×400m (the first three hours are treated as spin-up).

We performed a sensitivity simulation in which we lowered the minimum stomatal resistance for forests from 175-200 s m^{-1} (depending on the forest type, as shown in Table 5.1) to 100 s m^{-1}. The resulting spatio-temporal variability in V_{d,O_3} is shown in Figure 5.5 (panels b and e). The modification results in a strong increase in V_{d,O_3} over forests (by ±0.4 cm s^{-1}), and to a higher overall V_{d,O_3} by up to 0.13 cm s^{-1} in the afternoon. Additionally, we decreased the vegetation fraction of the urban tile from 0.5 to 0.2 to better represent urban morphology over Cottbus. This results in a lower dry deposition velocity by ±0.1 cm s^{-1} over the city (Fig. 5.5c). However, this modification has little effect on the domain-average diurnal cycle of V_{d,O_3} (Fig. 5.5f).

The aforementioned modifications in land surface properties also affect the surface energy balance, which impact turbulent mixing and also pollutant mixing ratios. Averaged over the entire domain, the resulting changes in NO_x and ozone associated with this decrease in the minimum stomatal resistance for forests are negligible. Still, accurate characterization of land surface properties can be important for model comparison against point observations.

5.3.3   Covariance of the dry deposition flux: formulation

We quantify the covariance between the concentration and the dry deposition velocity by means of the covariance of the dry deposition flux, termed $C_{F,dd}$. $C_{F,dd}$ expresses the spatial co-variability between the ozone dry deposition velocity and the ozone mixing ratio in the lowermost model layer, and follows from performing Reynolds averaging on the components of the horizontally averaged dry deposition flux ($\overline{F_{O_3,dd}}$) (Clifton and Patton, 2021):

$$\overline{F_{O_3,dd}} = \overline{-V_{d,O_3}[O_3]} = \overline{-V_{d,O_3}}\ \overline{[O_3]} + \overline{-V'_{d,O_3}[O_3]'} = \overline{-V_{d,O_3}}\ \overline{[O_3]}(1 + C_{F,dd}) \qquad (5.5)$$

where $\overline{V_{d,O_3}}$ and $\overline{[O_3]}$ are the horizontal averages of the dry deposition velocity and surface ozone mixing ratio, and $\overline{V'_{d,O_3}[O_3]'}$ expresses the covariance between the ozone dry deposition velocity and the surface ozone mixing ratio. $C_{F,dd}$ is defined by normalizing the covariance term in Equation 5.5 by the horizontally averaged dry deposition flux:

$$C_{F,dd} = \frac{\overline{-V'_{d,O_3}[O_3]'}}{\overline{-V_{d,O_3}}\ \overline{[O_3]}} \qquad (5.6)$$

In equation 5.6, $C_{F,dd}$ expresses the change in the horizontally averaged dry deposition flux after resolving the impact of land surface heterogeneity on turbulence and dry deposition, relative to the deposition flux under homogeneous land surface conditions. Since the denominator in Equation 5.6 is positive by definition, negative $C_{F,dd}$ value indicates that negative anomalies in the 2D dry deposition velocity field coincide with positive anomalies in the surface ozone mixing ratio or vice versa. If the dry deposition flux covariance is substantial, $C_{F,dd}$ can be used to parameterize the effect of subgrid-scale heterogeneity on dry deposition in coarser-scale atmospheric chemistry models where turbulence is not resolved.

Note that the derivation of $C_{F,dd}$ is similar to the intensity of segregation for second-order chemical reactions ($I_{s,c}$) derived elsewhere (e.g., Arellano and Duynkerke, 1993). $I_{s,c}$ accounts for a modified efficiency of chemical reactions due to non-homogeneous mixing conditions. For a generic reaction between species A and B with rate constant k, the average reaction rate ($\overline{R}$) that accounts for segregation can be derived as follows:

$$\overline{R} = k\overline{[A]}\ \overline{[B]}(1 + I_{s,c}) \qquad (5.7)$$

Table 5.3: Experimental setup of sensitivity study on dry deposition flux covariance in MicroHH. Changes with respect to the default simulation (simulation 1) are shown in **bold**.

Simulation	V_d strength	Initial and LBC mixing ratio [ppb]	Vertical gradient [ppb km^{-1}]
1 (default)	default	40	0
2a	**$V_d \times 0.5$**	40	0
2b	**$V_d \times 2$**	40	0
3a	default	**0.4**	0
3b	default	**4**	0
3c	default	**400**	0
4a	default	40	**-2**
4b	default	40	**-1**
4c	default	40	**1**
4d	default	40	**2**

5.3.4 Setup of the numerical experiments

We first study the drivers of covariance between concentrations and dry deposition velocities using coarse-resolution sensitivity simulations in section 5.4.1. These simulations are performed using 64×64 horizontal grid cells and 32 vertical model levels (at a horizontal resolution of 400m×400m), which is justified by the low sensitivity of $C_{F,dd}$ to model resolution (see Discussion section). Photochemical ozone production and destruction is deactivated in these sensitivity simulations to ensure that the simulated covariability is not affected by chemistry. To isolate the effect of deposition, we assume that ozone only enters the domain from time-invariant lateral model boundaries, and its only sink is removal at the land surface by dry deposition.

We perform a range of sensitivity experiments to better understand how $C_{F,dd}$ is controlled by the magnitude of the dry deposition velocity, surface ozone mixing ratios and the vertical ozone profile. The setup of the sensitivity experiments is shown in Table 5.3. In a first set of sensitivity simulations (simulations 2a-b), we modify the strength of the deposition sink by halving and doubling the dry deposition velocity, respectively. We expect that $C_{F,dd}$ scales with the magnitude of the dry deposition velocity, following Equation 5.6. In the second of experiments (simulations 3a-c) we impose uniform vertical ozone profiles of 0.4, 4 and 400 ppb in the initial and lateral boundary conditions. Here we expect that dry deposition has more potential to introduce a dry deposition flux covariance if the ozone mixing ratios are small. In the third set of sensitivity experiments (simulations 4a-d), we force our simulations with vertical ozone profiles with a linear vertical gradient, where the surface ozone mixing ratio is kept constant at 40 ppb. We expect that the shape of the vertical ozone profile affects the downward vertical transport of ozone towards the surface,

and also affects $C_{F,dd}$. In the results section, we present afternoon (12-17 h LT) average values of the dry deposition flux covariance ($C_{F,dd}$).

Next, in Section 5.4.2 we analyze how the covariance of the dry deposition flux of ozone and NO_x is potentially affected by a plume of NO_x transported over a heterogeneous land surface. These simulations are performed at a horizontal resolution of 100×100 m^2 using 160 vertical levels. We activate the chemistry parameterization to ensure that chemical ozone production and destruction can occur inside the domain as a function of radiation, temperature and ozone precursor abundance. For these simulations, we add emissions of NO_x, carbon monoxide and hydrocarbons from the Jänschwalde power plant, with respective emission strengths of 20300, 7984 and 122 ppm m s^{-1}. 97% of NO_x emissions are in the form of NO. We use Gaussian functions to describe the horizontal and vertical distribution of the emissions. The standard deviation of the Gaussian (σ) in x- and y-direction was set to 50 m, so that 97% of the emissions (i.e., 2σ on either side of the mean) fall within a circle with a 100×100 m^2 radius around the center point of the emission grid cell. A similar procedure was applied to distribute emissions vertically, with Gaussian emission variations around a mean height of 300 m, using σ=122 m. This corresponds with the dimensions and design of a large powerplant and smokestack.

5.4   Results

5.4.1   Controls on dry deposition covariance

We now analyze idealized sensitivity simulations to study the drivers of dry deposition covariance. Figure 5.6 shows the dry deposition flux covariance ($C_{F,dd}$), which can be interpreted as the change in the domain-average dry deposition flux due to resolving dry deposition and turbulence at a high spatial resolution, for the sensitivity simulations listed in Table 5.3. In the default simulation, we find a very small negative dry deposition flux covariance (-0.05%, Fig. 5.6a) for ozone, indicating that resolving dry deposition at a high spatial resolution hardly affects the domain-average ozone deposition flux. In this simulation, positive anomalies in the dry deposition velocity co-occur with negative anomalies in ozone mixing ratios, and vice versa. However, despite substantial spatial variability in the dry deposition velocity (with a normalized standard deviation of 30%), surface ozone mixing ratios display much less spatial variability (with a normalized standard deviation of 0.5%), which explains the small flux covariance.

In a first set of sensitivity experiments (simulations 2a-b in Table 5.3), we halved and doubled the dry deposition velocities uniformly over the model domain, thereby also affecting V_{d,O_3} spatial variability (Fig. 5.6b). In case of halving the dry deposition velocity, the spatial variability in V_{d,O_3} is reduced. As a result, spatial variability in surface ozone
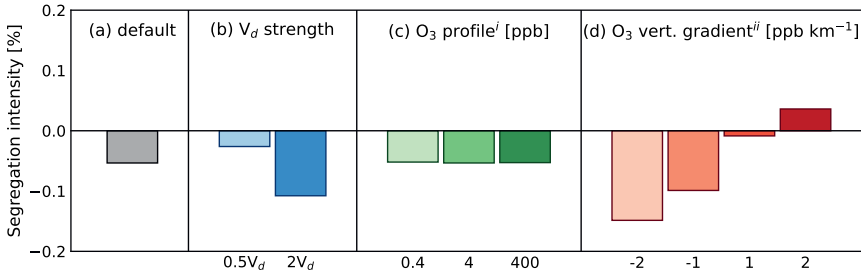
Figure 5.6: Afternoon (12-17 LT) averages of the covariance of the dry deposition flux ($C_{F,dd}$) for the different sensitivity experiments in Table 5.3. This averaging window was chosen since convective conditions prevail, and the $C_{F,dd}$ is relatively constant. [i]Uniform vertical ozone profiles are used for the experiments in panel c (i.e., the vertical gradient is 0 ppb km^{-1}). [ii]The surface ozone mixing ratio is set to 40 ppb for the experiments in panel d.

as a result of dry deposition is also inhibited. Combined, this leads to a reduced dry deposition flux covariance, which is conform our expectations (Fig. 5.6). When doubling V_{d,O_3}, the variability of the dry deposition velocity increases, leading to a stronger effect on surface ozone, and an increased $C_{F,dd}$.

In the second set of experiments (simulations 3a-c in Table 5.3), we impose uniform vertical ozone profiles of 0.4, 4 and 400 ppb in the initial and lateral boundary conditions (Fig. 5.6c). Contrary to our expectations, these perturbations have a minimal effect on $C_{F,dd}$, which is constant at -0.05% in these simulations, and equal to $C_{F,dd}$ in the default experiment. Apparently, turbulent mixing quickly counteracts segregation in ozone mixing ratios. In these simulations, the domain averages and fluctuations of surface ozone scale linearly with the imposed ozone mixing ratios, resulting in minimal changes in $C_{F,dd}$ compared to that of the reference simulation.

In the last set of sensitivity experiments (simulations 4a-d in Table 5.3), we force our simulations with vertical ozone profiles with a varying vertical gradient. These simulations, shown in Figure 5.6d, show a dependence of $C_{F,dd}$ on the vertical ozone gradient. In the case of a negative vertical gradient (i.e., higher ozone mixing ratios at the surface than aloft), downward transported air is depleted in ozone relative to surface mixing ratios, resulting in an upward ozone flux in large parts of the boundary layer despite the presence of an ozone sink at the surface by dry deposition. To illustrate how the sign of $C_{F,dd}$ depends on turbulent transport of air from aloft to the surface, we show pairwise covariances of aerodynamic resistance (r_a, a metric of above-canopy turbulent mixing), dry deposition velocity (V_{d,O_3}) and the surface ozone mixing ratio ([O_3]) in Figure 5.7. Efficient downward transport mixes air from higher above compared to a situation with less efficient transport, and simultaneously leads to a lower r_a. Because of the inverse
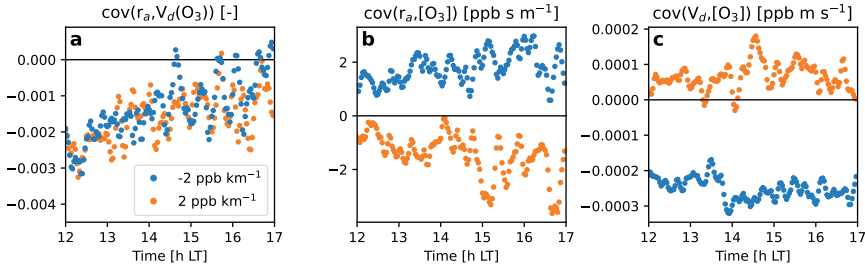
Figure 5.7: Spatial covariances between the aerodynamic resistance for vegetation (r_a) and the ozone dry deposition velocity (V_{d,O_3}) (panel a), between r_a and the surface ozone mixing ratio ($[O_3]$) (panel b), and between V_{d,O_3} and $[O_3]$ (panel c) for simulations with negative and positive ozone vertical gradients (-2 and 2 ppb km^{-1}, simulations 4a and 4d in Table 5.3, respectively).

dependence of V_{d,O_3} on r_a, this leads to a negative covariance between these two variables (Fig. 5.7a).

However, the covariance between the aerodynamic resistance and surface ozone changes sign depending on the sign of the vertical ozone gradient. In reality, the vertical ozone gradient is most often positive (lower ozone near the surface compared to higher aloft), but we varied the vertical ozone gradient to quantify the resulting effect on dry deposition flux covariance. In the case of a negative vertical ozone gradient, downward-moving eddies (with $r_a' < 0$) transport air masses with low ozone mixing ratios to the surface ($[O_3]' < 0$), thus resulting in a positive covariance between r_a and $[O_3]$ (Fig. 5.7b). This covariance changes sign when the vertical ozone gradient is positive (Fig. 5.7b), which counteracts the negative $C_{F,dd}$ by dry deposition. When the vertical ozone gradient is sufficiently large, this effect can overcome the negative effect of surface removal on $C_{F,dd}$, resulting in a positive covariance between surface ozone and the dry deposition velocity (Fig. 5.7c), and a positive $C_{F,dd}$ (Fig. 5.6d).

Overall, we conclude that covariance of the dry deposition flux only minimally affects the ozone dry deposition sink. Generally, the dry deposition flux covariance is negative, and depends on the magnitude of the dry deposition velocity. The background mixing ratios have a marginal effect on $C_{F,dd}$ in case of a uniform vertical profile. If the profile is not constant, $C_{F,dd}$ is affected by the vertical ozone gradient. Using our quantitative understanding of $C_{F,dd}$ gained in this section, we now analyze covariance of the dry deposition flux in a simulation with boundary conditions from ERA5 and CAMS, and with a point source of NO_x.
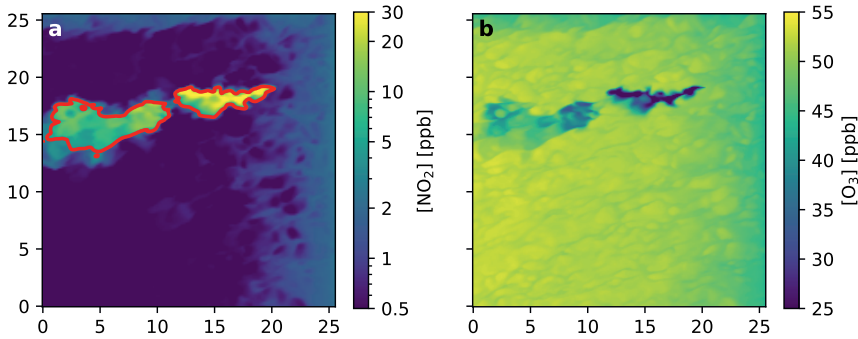
Figure 5.8: Horizontal cross-section of MicroHH-simulated surface-layer NO_2 (panel a, note the logarithmic colorbar) and ozone (panel b) at 12:00 LT on May 23rd, 2018. The red contour line indicates the extent of the NO_x plume. The plume extent is defined as the area where surface NO_2 mixing ratios are higher than 0.4σ, which visually corresponds well with the plume characterized by high NO_2 and low ozone mixing ratios.

5.4.2 Covariance of the dry deposition flux affected by a NO_x plume

Next, we analyze how the dry deposition flux covariance is affected by a plume freshly emitted nitrogen oxides transported over a heterogeneous land surface. The presence of a strong NO_x emission source modifies the ozone production regime downwind of the power plant. An example of this plume is shown in Figure 5.8, which displays horizontal cross-sections of simulated NO_2 and ozone mixing ratios at 12:00 h LT in the surface layer. NO_2 mixing ratios downwind of the power plant are higher by on average a factor 10 compared to the background NO_2 levels (8 ppb inside the plume and 0.75 ppb outside the plume) at this time. These elevated levels of NO_x lead to titration of ozone, which is on average 6 ppb lower inside the plume compared to outside the plume (a decrease from 51 to 46 ppb on average).

The presence of a NO_x plume also affects the vertical NO_x and ozone gradients within the domain. In the afternoon (12-17 LT), NO_2 increases by on average 0.5 ppb km^{-1} towards the surface in the lowermost 2 km, while ozone decreases by 2 ppb km^{-1} towards the surface. The NO_x plume introduces strong spatial variation in the vertical profile. We diagnose this by analyzing the domain-wide standard deviation of NO_2 and ozone mixing ratios as a function of altitude (σ_z). This standard deviation is approximately 3 ppb in the lowermost three model levels for NO_2 and ozone, and is indicative of large vertical gradients in NO_2 and ozone mixing ratios inside the plume.

We established in Section 5.4.1 that covariance of the dry deposition flux is partly controlled by the vertical profile of the depositing species through the mutual dependence of the dry deposition velocity and surface mixing ratios on the aerodynamic resistance (Fig. 5.7a,b).
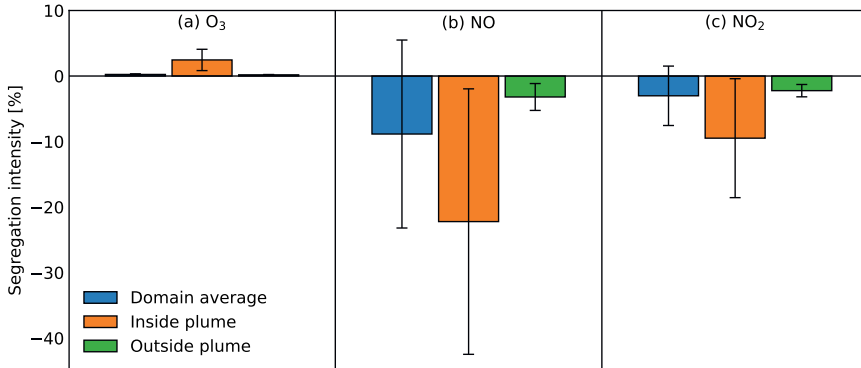
Figure 5.9: Afternoon (12-17 h LT) average values of the effects of the NO_x plume on dry deposition flux covariance, displayed for ozone (panel a), NO (panel b) and NO_2 (panel c), displayed as the domain average (blue), inside the plume (orange) and outside the plume (green). Error bars indicate the 1-σ range of the flux covariance calculated for each timestep in the analysis window (12-17 h LT).

In Figure 5.9, we display the afternoon (12-17 LT) average dry deposition flux covariance ($C_{F,dd}$) for ozone, NO and NO_2. On average, over the entire domain, covariance of the ozone dry deposition flux is unimportant (+0.2%), but the positive sign is remarkable. $C_{F,dd}$ is slightly stronger inside the plume (+2.4% on average), where the concentration increases more strongly with increasing altitude due to near-surface, in-plume ozone titration. However, the dry deposition flux covariance is small compared to the *chemical* segregation of NO and ozone inside the plume, which is strongly negative (-20% - -80% at the surface) and agrees well with the observed segregation-induced suppression of the NO-ozone reaction in a NO_x plume (Vilà-Guerau de Arellano et al., 1990; Vinken et al., 2011).

For NO and NO_2, the in-plume deposition flux is higher compared to outside the plume because of the high NO_x mixing ratios inside the plume. Compared to ozone, the effect of deposition flux covariance is reverse for NO and NO_2, which peak in the lowermost 500 m of the model domain, and efficient uptake coincides with transport of low-NO_x air from aloft (see the strongly negative vertical NO_x gradients in Fig. 5.4). Although this effect is visible outside the plume (with average $C_{F,dd}$ values of -3.2% for NO and -2.2% for NO_2), the domain-average signal is dominated by the effects of the NO_x plume. For the grid cells inside the plume, there is a stronger negative covariance between concentration and V_d. This is mostly driven by r_a and the NO and NO_2 profiles that strongly peak near the surface, acting to reduce in-plume deposition of NO and NO_2 by 22.2% and 9.5%, respectively. $C_{F,dd}$ is stronger for NO than for NO_2 because the vertical NO gradient is larger than that of NO_2. Coarser-scale models do not resolve these small-scale fluctuations

in concentrations and dry deposition velocities, and must therefore parameterize these effects.

5.5   Discussion and conclusions

We have described the implementation of a big leaf dry deposition parameterization in the high-resolution (100×100 m^2), turbulence-resolving MicroHH model, coupled to its land surface model. Using this coupled modelling setup, we investigate covariance of the ozone dry deposition flux, which causes domain-average changes in the dry deposition sink due to simultaneous fluctuations in the surface uptake rate and mixing ratios. In a range of sensitivity experiments under controlled conditions, we found that dry deposition leads to a minimal flux covariance. The dry deposition flux covariance is further sensitive to the efficiency of the dry deposition sink (the magnitude of the dry deposition velocity). Additionally, the vertical profile of the depositing scalar is an important explanatory variable for the deposition flux covariance. In case of a decreasing vertical scalar profile with height, downward vertical transport simultaneously reduces the aerodynamic resistance (an important component of the dry deposition velocity) and the surface layer mixing ratio, leading to a reduced dry deposition sink. If the vertical scalar profile is positive and sufficiently high, simultaneous fluctuations in dry deposition and vertical transport can lead to an enhancement in the domain-average flux.

Our sensitivity experiments agree with an earlier LES study showing that the flux covariance of ozone dry deposition due to non-homogeneous boundary layer turbulent mixing is small (Clifton and Patton, 2021). However, those simulations were performed for homogeneous, mid-latitude forest conditions, with little spatial variability in dry deposition velocity. The results of the sensitivity simulations presented here are quantitatively similar, even with substantial V_{d,O_3} spatial variability, suggesting that dry deposition flux covariance is largely driven by variability in surface ozone mixing ratios due to turbulent mixing. Since Clifton and Patton (2021) forced their simulations with constant vertical ozone profiles, their work likely underestimates the dry deposition flux covariance under realistic conditions.

We found stronger changes in domain-average dry deposition fluxes in our analysis of a NO_x plume traveling over a heterogeneous land surface and affected by chemistry. For NO_x, the dry deposition flux covariance ($C_{F,dd}$) of -9 – -3% indicates that land surface- and turbulence-induced heterogeneity in the dry deposition velocity leads to a decreased domain-average NO_x dry deposition flux compared to a situation with a homogeneous surface removal rate. Inside the plume, $C_{F,dd}$ for NO_x is even more strongly negative (-22 – -9%) as a result of the strong negative vertical NO_x gradients inside the plume. For ozone, the domain-average dry deposition flux covariance is small and positive (+0.2%), but $C_{F,dd}$ is higher inside the plume (+2.4%), where ozone is depleted at the surface due to titration leading to a positive vertical ozone gradient.

In coarser models without explicit turbulent mixing, covariance of the dry deposition flux can be parameterized based on the vertical profile of the depositing species, the intensity of turbulent mixing (e.g. based on vertical wind speed), and subgrid-scale information on surface characteristics important for deposition and boundary layer turbulence (e.g., land cover and roughness length). Additionally, parameterizations of subgrid-scale plume chemistry in coarser-scale models (Vinken et al., 2011) could include changes in downwind deposition.

In setting up these simulations, we simplified several processes which could affect our results. Firstly, we discard other sources of NO_x and hydrocarbons from anthropogenic activities, soils and vegetation, which could affect NO_x-ozone photochemistry. Second, our representation of the land surface simplifies the land surface effects on turbulence, such as locally enhanced vertical mixing as a result of sharp roughness transitions, e.g., between grasslands and forest (Bannister et al., 2021). Last, our sensitivity simulations (Section 5.4.1) were performed at a resolution where a relatively large part of turbulent transport is still parameterized. A comparison of the dry deposition flux covariance calculated from model output at different horizontal resolutions (Fig. A5.1) shows that the derived flux covariance is smaller in the high resolution simulation, but nevertheless qualitatively similar.

This work presents an initial exploration of the effects of resolving vertical transport and effects of heterogeneous land cover on dry deposition of ozone and NO_x. Our results suggest that the effect is generally small if the depositing scalar is vertically well-mixed, such as ozone. However, for species that display strong vertical gradients, such as NO and NO_2, the effect can be substantial. Future work could focus on consolidating these results under varying degrees of turbulent mixing and land cover heterogeneity to quantify the error in coarser-scale air quality models that do not resolve this heterogeneity. Such experiments could contribute to the development of a larger-scale model parameterization of sub-grid dry deposition flux covariance based on atmospheric properties (the degree of turbulent mixing, the vertical profile of the depositing species) and heterogeneity in land surface properties. Additionally, this approach can be extended to other species where deposition is of concern for ecosystem health, such as ammonia and other reactive nitrogen species.

A5   Appendix
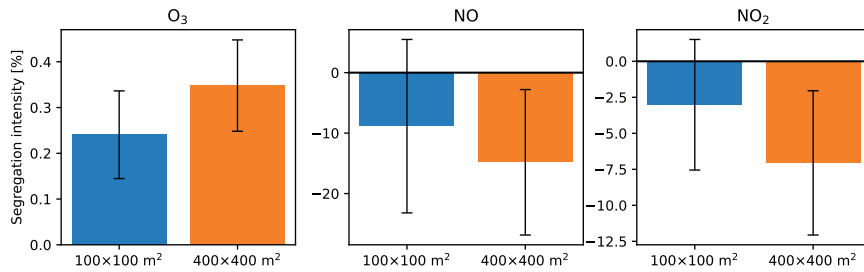
Figure A5.1: Segregation intensity of dry deposition for ozone, NO and NO$_2$ in the plume simulation performed at different horizontal resolutions. The displayed dry deposition flux covariance values are domain averages.

Chapter 6

General discussion and outlook

6.1   Findings of this thesis

The central aim of this thesis is to gain a better quantitative understanding of the ozone dry deposition sink to ecosystems using atmospheric chemistry models combined with in situ and remote sensing observations. An improved understanding would benefit the applicability of these models for simulations of ozone air pollution and assessments of the impact of ozone on the land carbon sink. In the introduction, we identified three key elements that currently hinder this applicability: (1) underestimated peak surface ozone, (2), an incomplete understanding of the spatio-temporal variability in ozone dry deposition processes, and (3) the impact of unresolved spatial heterogeneity in land cover on boundary layer mixing and surface deposition in air quality models.

In Chapter 2, we investigated the dependence of summertime surface ozone simulations on NO_x emissions using the regional meteorology-air quality model WRF-Chem and OMI tropospheric NO_2 column observations. We found that simulated NO_2 was underestimated with respect to surface and column measurements. To solve this mismatch, we applied a mass balance approach to derive updated surface NO_x emissions. Emissions had to be increased particularly in rural background areas, and we hypothesized this could be due to underestimated (agricultural) NO_x emissions. A simulation with these updated emissions resulted in a better model-observation agreement and an improved simulation of surface ozone (peaks). We concluded that a realistic representation of anthropogenic and biogenic NO_x sources is necessary for realistic simulations of ozone concentrations in regional air quality models.

In Chapters 3 and 4, we zoomed in on the deposition process. Our hypothesis was that a mis-representation of ozone dry deposition processes in air quality models, such as a strong decrease in dry deposition during warm and dry conditions, could contribute to the underestimated peak ozone concentrations simulated by WRF-Chem. In Chapter 3, we performed an offline comparison of ozone dry deposition flux simulations between WRF-Chem's big leaf parameterization and a multi-layer model for two European measurement sites with multi-year observations of ozone fluxes above forests. We found that both models satisfactorily reproduced seasonal variability in ozone dry deposition, but that these models differed in their simulations of the diurnal cycle of the ozone dry deposition velocity. The multi-layer canopy representation better reproduced the diurnal cycle in stomatal ozone uptake, and better captured the response of non-stomatal deposition to environmental drivers such as temperature and relative humidity. This resulted in a better agreement with instantaneous and growing season-accumulated ozone flux observations compared to the big leaf parameterization commonly applied in most air quality models.

In Chapter 4, we used the multi-layer canopy model and campaign observations under summertime high-ozone conditions in Italy to develop our understanding of two non-stomatal processes that are typically not represented in big leaf dry deposition parameterizations:

suppressed vertical exchange inside forest canopies and chemical ozone removal by soil-emitted NO in the lower canopy. We found that two commonly used parameterizations of canopy-atmosphere vertical transport overestimate canopy-atmosphere exchange derived from observations, since these parameterizations do not resolve the in-canopy stable stratification that was observed during large periods of the campaign. Multi-layer canopy model simulations indicated that removal by reaction with soil-emitted NO can potentially pose a substantial chemical sink of ozone in the lower canopy. However, the presence of a substantial chemical ozone sink does not seem to affect the magnitude of the ozone flux at the canopy-top: sensitivity simulations with a deactivated chemical sink result in a canopy-top ozone flux of a similar magnitude, since other lower-canopy removal processes (deposition to soils and lower-canopy vegetation) increase in response to the deactivated chemical ozone sink by reaction with soil NO.

In Chapter 5, we implemented a big leaf dry deposition parameterization in a turbulence-resolving model at high spatial resolution (100 m × 100 m). We used this model setup to investigate the potential significance of a dry deposition flux covariance, defined as a change in the efficiency of the dry deposition flux due to a co-occurrence of high concentrations and a low dry deposition velocity (or vice versa) associated with the effects of land cover heterogeneity on turbulent mixing and dry deposition. This process has the potential to affect the magnitude of dry deposition fluxes within a typical grid cell of a regional model. We found that the covariance between surface ozone and its dry deposition velocity is generally small ($< 0.1\%$) because concentration differences introduced by dry deposition are quickly counteracted by vertical mixing. However, the effect was stronger in a simulation with an emitted NO_x plume (with in-plume ozone titration) that leads to coinciding fluctuations of surface mixing ratios and the dry deposition velocity. We found that inside the plume, high-NO_x and low-ozone conditions lead to large vertical concentration gradients, affecting NO_x and ozone turbulent transport to the surface. Since efficient vertical transport coincides with low aerodynamic resistance (an important term term in the dry deposition calculation), significant co-variation between dry deposition velocities and atmospheric concentrations were induced. In the core of the power plant plume, NO and NO_2 concentrations are high and the ozone concentration is low due to titration. As a result, we found that the ozone deposition flux was increased by 2% due to quick resupply of ozone from aloft, while NO and NO_2 deposition was reduced by 22% and 9%, respectively, since vertical mixing transports low-NO_x air to the surface.

In this concluding discussion, the findings of this thesis are placed in context of the overall research objectives, and I provide perspectives on future research directions.

6.2   Surface ozone simulations in Europe

6.2.1   Status of current models

Regional air quality models are important tools to assess air pollution and to formulate abatement strategies. However, these simulations tend to underpredict surface ozone mixing ratios during summer (Mar et al. 2016), and particularly underestimate observed peak ozone levels (Im et al., 2015). The exact causes for this underestimation are not fully understood. Firstly, there is a mismatch in representativeness between surface observations (with a small measurement footprint) and model grids ($\pm 10 \times 10$ km^2). An avenue for model improvement is increasing the spatial resolution. At higher resolution, surface and column NO_2 is better simulated (Schaap et al., 2015; Valin et al., 2011), affecting the simulated ozone production regimes (Cohan et al., 2006). Additionally, the representation of atmospheric chemistry carries some uncertainty: there is considerable inter-mechanism spread in simulated surface ozone, which is thought to be due to the representation of inorganic reactivity (Mar et al., 2016) and the level of detail in the representation of reactivity of volatile organic compounds (VOCs Coates et al., 2016). The boundary conditions, often derived from global models or reanalysis products, is an additional source of uncertainty (Giordano et al., 2015). Additionally, incomplete understanding of NO_x and VOC emissions lead to mismatches between simulated and observed ozone concentrations (Chapter 2, Oikonomakis et al., 2018).

6.2.2   The contribution of soil NO_x to underestimated surface ozone

The hypothesis that soil NO_x emissions are underestimated in European air quality assessments has received support from recent studies. For example, Skiba et al. (2021) found that the share of (agricultural) soils in the European NO_x emission budget has increased in the past decades, because anthropogenic NO_x emissions have decreased at a faster rate than NO_x emissions from agricultural soils following (synthetic) fertilizer application. Additionally, Fortems-Cheiney et al. (2021) found that soil emissions can explain part of the observed tropospheric NO_2 column trends in rural regions. The increasing contribution by soil NO_x emissions to the tropospheric NO_2 column is most likely the explanation for an observed smaller decrease in NO_2 columns than the decreasing trend in anthropogenic NO_x emissions would suggest. Also in non-European regions, the importance of soil-biogenic NO_x emissions has received considerable attention. For example, unaccounted soil NO_x emissions are deemed to be partly responsible for a stagnating decrease in NO_2 column trends over the United States (Silvern et al., 2019; Wang et al., 2021).

A logical next step would be to improve the process representation of soil NO_x emissions in air quality models. One potential reason for the NO_x emission underestimations found in Chapter 2 is that the parameterization of Yienger and Levy (1995) applied in WRF-Chem does not simulate a contribution by agricultural soil NO_x emissions due to manure and synthetic fertilizer application. To our knowledge, this omission has not been detected in previous studies with the commonly applied WRF-Chem model. More recent assessments of soil-biogenic emissions (e.g., Hudman et al., 2012; Simpson and Darras, 2021; Steinkamp and Lawrence, 2011; Vinken et al., 2014b) indeed result in a higher global soil NO_x source (11-13 Tg N yr^{-1}) than the soil NO_x source of 5 Tg N yr^{-1} suggested by Yienger and Levy (1995). Recent developments in soil NO_x emission modelling now account for the availability of nitrogen compounds in non-agricultural soils and improved seasonal cycles of fertilizer application (Rasool et al., 2019; Rasool et al., 2016), and apply an improved temperature dependence of soil NO_x emissions (Wang et al., 2021). It must be noted that these developments have focused on other regions (particularly the United States), and better constraints on European soil NO_x emissions need to be developed. In this thesis, we have shown that an improved quantitative understanding of soil NO_x emissions may help to understand ozone production and peak ozone concentrations near the surface (Chapter 2) and chemical ozone loss inside vegetation canopies (Chapter 4).

The conditions favoring ozone formation in Europe have become increasingly NO_x limited (Jin et al., 2017). The contribution of soil emissions to underestimated peak ozone in Europe has not been explicitly evaluated, but analyses for other regions are promising. Rasool et al. (2019) reported on a reduced mean bias for simulated ozone concentrations in agricultural regions in the United States after implementing an improved representation of soil NO_x emissions. Lu et al. (2021) investigated the dependence of ozone formation on soil NO_x emissions around Beijing, China. Even under the high-NO_x conditions in this region due to the high anthropogenic emissions, soils are still an important source of NO_x, contributing to ozone formation. They concluded that targeting anthropogenic NO_x emissions to control ozone pollution is less effective as a result of high soil NO_x emissions near the urban region. This so-called "soil penalty" has also been quantified in other regions (Oikawa et al., 2015; Sha et al., 2021).

A combination of the modelling tools used in Chapters 2–5 can be used to gain understanding of the NO_x exchange processes between vegetation canopies and the surface layer. Many large-scale atmospheric chemistry models apply canopy reduction factor (CRF) to determine the effective release of soil-emitted NO in vegetation canopies to the surface layer. CRFs are applied to account for loss of NO_2, formed from soil-emitted NO, by deposition inside vegetation canopies (Yienger and Levy, 1995). This approach assumes that soil NO emissions exceed NO_2 deposition, i.e., that the effective NO_x flux is upward. However, in regions with high background NO_2 concentrations, NO_2 deposition exceeds soil NO emissions, which warrants an alternative CRF definition that accounts for the bi-directional nature of canopy-atmosphere NO_x exchange (Chapter 4, Ganzeveld et al.,

2002a). As demonstrated in Chapter 4, the use of multi-layer canopy exchange models can lead to improved process-understanding of biosphere-atmosphere NO_x exchange. This approach can be improved by using high-resolution LES models that resolve turbulent transport and other canopy processes (soil and vegetation emissions, chemistry, deposition processes) in order to better quantify the effective flux of soil NO_x into the surface layer by vertical transport inside the canopy layer.

6.2.3 Deriving NO_x emissions from remote sensing observations

In Chapter 2, we derived updated NO_x emissions using a mass balance approach applied to simulated and satellite-observed NO_2 columns. The advantages of this approach are its simplicity (no formal model inversion approach is needed) and its traceability (emissions are updated based on the model-observation mismatch). The mass balance approach works best when the chemical lifetime of NO_2 is small compared to the lifetime against transport. In Chapter 2, we worked with $\pm 20 \times 20$ km^2 OMI observations, where summer NO_2 could be related to underlying NO_x sources. However, this poses a challenge for application of mass balance approaches at high spatial resolution, for example by leveraging TROPOMI observations at 5x5 km^2 (Veefkind et al., 2012). There are promising case studies where TROPOMI NO_2 column observations are applied to estimate NO_x emissions from cities (Lorente et al., 2019), point sources (Beirle et al., 2011), biomass burning (Griffin et al., 2021) and open-sea shipping (Riess et al., 2022).

In comparison to urban or industrial sources, NO_x emissions from soils do not have an isolated source and have a lower magnitude, which complicates the use of satellite data alone to estimate soil NO_x emissions. Vinken et al. (2014b) showed the potential of deriving soil NO_x emissions in regions where the soil source dominates. However, as in Chapter 2, their mass balance approach relied on the combination of an atmospheric chemistry model (with prior estimates of soil emissions) and satellite observations. Soil NO_x emission pulses after rain events can be detected using satellite instruments (Bertram et al., 2005; Huber et al., 2020). Additionally, the availability of high-resolution TROPOMI NO_2 column observations enables quantification of soil NO_x emissions in geographically more confined areas, unaffected by other NO_x sources. As an alternative to improved monitoring of soil NO_x emissions with labor-intensive and costly surface measurements, as suggested by Skiba et al. (2021), the use of remote sensing NO_2 column observations to infer (agricultural) soil NO_x emissions should be further investigated. Potential case study regions for TROPOMI-based soil NO_x emissions are highlighted in Figure 6.1, and include Friesland (the Netherlands), Brittany (France) and parts of Germany.

An important uncertainty in using remote sensing NO_2 to estimate surface NO_x emissions is the use of a priori NO_2 vertical profiles used in the retrieval (Lorente et al., 2017). The a priori profile in standard global observational products (e.g., QA4ECV, Boersma et al.,
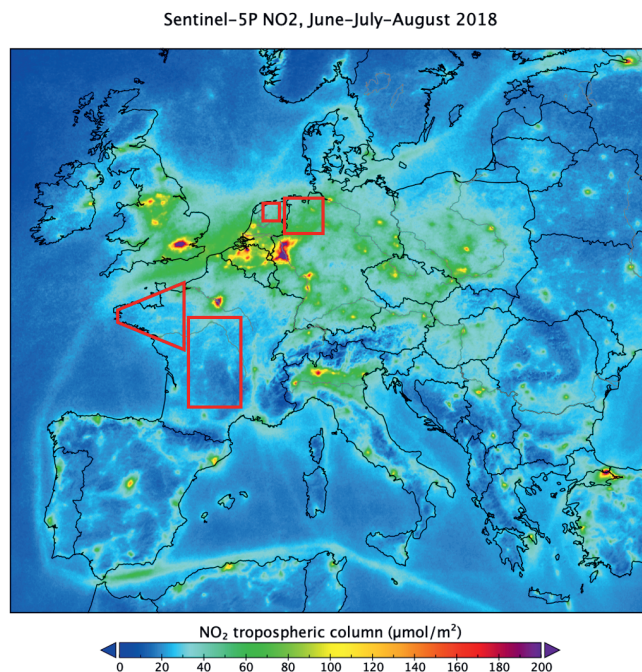
Figure 6.1: June-August 2018 average tropospheric NO_2 vertical column density from TROPOMI observations (dataset: S5P-PAL version 2.3.1, with a-priori NO_2 profiles replaced by CAMS-Europe NO_2 profiles). Red highlight areas show several potential areas of interest to derive soil NO_x emissions based on TROPOMI NO_2 column observations (source: Henk Eskes/KNMI, modified by adding red highlight areas).

2018a) comes from relatively coarse global atmospheric chemistry models (e.g., TM5) that do not resolve regional emission heterogeneity. This is becoming increasingly problematic as the spatial resolution of the NO_2 remote sensing data increases in the future (e.g., with the planned Nitrosat mission aiming to deliver NO_2 column data at a sub-kilometer spatial resolution). In Chapter 2, we corrected for this uncertainty by updating the retrieval based on WRF-Chem-simulated NO_2 columns at a 20×20 km^2 spatial resolution, which led to a structural increase in observed NO_2 columns of up to 20% in polluted regions. However, point source emission sources such as the one studied in Chapter 5 are still not resolved at this resolution. The use of high-resolution LES models is a promising way forward to quantify and reduce the uncertainty associated with the a priori profile, and to minimize the retrieval error associated with too coarse a priori NO_2 vertical profiles. However, the current computational cost of LES models does not allow their use at large spatial scales and on timescales beyond several days. Under these constraints, the best application of LES models in NO_2 retrievals is to apply simulations under a set of controlled conditions

(e.g., emissions, vertical NO_2 profiles, etc.) to derive retrieval corrections. At the same time, LES-based NO_2 profiles should be verified against measurements for optimal applicability in retrieval algorithms. This can be aided by ground-based remote sensing (MAX-DOAS sensors) and improved (balloon-based) airborne measurement infrastructure in different relevant locations across Europe.

6.3   The representation of dry deposition processes in air quality models

6.3.1   Big leaf versus multi-layer canopy models

In this thesis, different modelling approaches have been used to estimate ozone dry deposition to vegetation. Big leaf models were applied in Chapter 3 (in a model intercomparison with a multi-layer parameterization) and Chapter 5 (to simulate ozone dry deposition in a LES model). This type of model is conceptually simple and computationally efficient, and therefore it is most commonly applied in atmospheric chemistry models. However, big leaf parameterizations oversimplify ozone deposition processes inside plant canopies, which display vertical gradients as a function of vegetation properties (e.g., LAI, shading by the overlying leaf column). Multi-layer models advantageously contain several in-canopy model layers, which enables resolving the ozone budget equation within vegetation canopies (Eqn. 1.1). The downside class of models is their complexity and their computational cost. There is currently no community agreement on the need to account for detailed in-canopy processes in deposition parameterizations with multi-layer models in regional and global atmospheric chemistry models (Pfister et al., 2020). Nonetheless, multi-layer canopy models have already been successfully applied in large-scale atmospheric chemistry models (Ganzeveld et al., 2010; Ganzeveld et al., 2002a). Especially for trace gases of which canopy-atmosphere exchange is bi-directional (e.g., NO_x), adopting multi-layer parameterizations can affect the magnitude and direction of the flux (Chapter 4 Ganzeveld et al., 2002a). Additionally, multi-layer canopy models to represent atmosphere-biosphere exchange of momentum, energy, water and carbon dioxide are increasingly being applied in land surface models (Bonan et al., 2021), which facilitates adopting a multi-layer framework for canopy-atmosphere parameterizations of reactive trace gases as well.

Regional air quality models such as WRF-Chem could benefit from a multi-layer canopy representation of biosphere-atmosphere exchange, depending on the purpose. On the one hand, if the goal is to improve ozone deposition estimates in WRF-Chem (e.g., to quantify stomatal ozone fluxes as a function of moisture status), modellers may benefit from improved constraints on stomatal ozone uptake by coupling the deposition representation to the land surface model and validating against available measurements (e.g., forest H_2O

and CO_2 fluxes). Additionally, the representation of non-stomatal deposition estimates may be improved by applying recent parameterizations of soil and leaf uptake (Clifton et al., 2020b; Potier et al., 2015; Stella et al., 2019). However, if the goal is to gain an improved understanding of biosphere-atmosphere exchange of other species (e.g., NO_x and biogenic VOCs) or of in-canopy ozone loss, modelers should adopt a multi-layer parameterization. This requires robust knowledge about in-canopy meteorological drivers of non-stomatal deposition (e.g., temperature, relative humidity). Another venue that should therefore be explored is the use of high-resolution modeling with resolutions of $\pm 1 \times 1 \times 1$ m^3 (Pedruzo-Bagazgoitia et al., 2022, in review). In these models, the exchange between the canopy and the overlying turbulent atmosphere is explicitly resolved. However, these models require substantial (computational) efforts to account for chemical, biological and physical processes in the canopy, such as the distribution between sunlit and shaded leaves, in-canopy radiative transfer, and in-canopy chemistry.

6.3.2   Stomatal uptake

The representation of stomatal conductance in deposition parameterizations carries substantial uncertainty. Currently, modelling groups use different representations of stomatal conductance for simulating stomatal ozone deposition, such as the multiplicative Jarvis scheme (Chapter 5 Büker et al., 2012; Emberson et al., 2001), and assimilation-stomatal conductance (A-g_s) models (Chapters 3, 4; Lin et al., 2019; Val Martin et al., 2014). The representation of stomatal deposition in the original Wesely-scheme (Wesely, 1989), commonly applied in many regional and global atmospheric chemistry models, omits important environmental controls on stomatal uptake (vapour pressure deficit, soil moisture and LAI) and there is community agreement that this representation must be revisited. Nonetheless, this scheme remains used in some models, including the community model WRF-Chem (see an intercomparison of dry deposition schemes in Galmarini et al., 2021). Jarvis-based stomatal conductance representations are successfully applied in ozone impact assessments, but model parameters carry substantial uncertainty (Büker et al., 2012). As a result, Jarvis-based stomatal schemes are typically outperformed by other schemes in model intercomparisons (Otu-Larbi et al., 2021; Wu et al., 2018). A-g_s models were developed to represent leaf-level gas exchange, but its implementation in models requires knowledge on a set of uncertain input parameters. We resolved this in Chapter 3 by deriving a set of A-g_s parameters that optimally reproduce canopy-top CO_2 and water vapor flux measurements. Such an approach has potential to improve the robustness of estimates of the stomatal component of canopy ozone deposition. These A-g_s parameters can also be estimated from leaf-level eco-physiology measurements performed on a campaign basis (e.g., Vilà-Guerau De Arellano et al., 2020).

There is potential to constrain stomatal ozone uptake in atmospheric chemistry models using independent observations. For example, the use of remotely-sensed sun-induced fluorescence

(SIF, a proxy of stomatal conductance and photosynthesis) from TROPOMI observations has recently been applied in combination with an observation-driven model of canopy stomatal conductance to derive high-resolution estimates of stomatal NO_2 deposition over the United States (Delaria et al., 2021). These observations offer constraints on afternoon (the TROPOMI overpass time is approximately 13:30 LT) stomatal conductance at a high spatial resolution. Additionally, the use of satellite soil moisture observations has shown potential to constrain stomatal conductance in atmospheric chemistry models, benefiting assessments of ozone deposition (Huang et al., 2021).

Currently, policy-relevant assessments of ozone-induced damage to crops and vegetation apply metrics based on exposure to ambient ozone (i.e., exposure-based metrics). However, this metric is not indicative of stomatal ozone fluxes. Flux-based metrics combine the exposure to ozone with an estimate of stomatal uptake, and a species-specific detoxification threshold above which plants are no longer able to counteract the negative effect of ozone (Mills et al., 2011b; Musselman et al., 2006). Current assessments of ozone damage with flux-based metrics generally apply Jarvis-based stomatal conductance estimates (e.g., Büker et al., 2012; Emberson et al., 2000). This stomatal conductance parameterization is sensitive to uncertain input parameters, limiting their application in impact assessments (Chapter 3 Otu-Larbi et al., 2021). Stomatal conductance estimates that include a more mechanistic description of plant eco-physiology contain a more realistic stomatal response to external stimuli and therefore have potential for vegetation ozone impact assessments. Additionally, these parameterizations can simulate the separate effects of ozone on stomatal conductance and photosynthesis (Lombardozzi et al., 2013). The uncertainty associated with the detoxification level, the level below which plants can mitigate ozone's harmful impacts on the plant's interior, is also considerable (Musselman et al., 2006). Substantial progress towards the establishment of robust flux-based ozone impact metrics may be made by improved observational constraints on stomatal ozone uptake, by performing intercomparisons of different (stomatal) deposition parameterizations (currently underway in the AQMEII4 project, Galmarini et al., 2021), by investigating the use of model ensembles (Wu et al., 2018) and by investigating possibilities of inverse methods for parameter optimization in stomatal conductance models (Bosman and Krol, 2022).

6.3.3 Non-stomatal deposition

Non-stomatal removal processes in vegetation canopies are incompletely understood, which limits their inclusion in dry deposition parameterizations. Most big leaf and multi-layer parameterizations still rely on application of the first-order, often constant estimates of non-stomatal uptake resistances (Wesely, 1989). However, accumulating observational evidence suggests substantially different non-stomatal removal and with large temporal variability, such as for wet leaf deposition (e.g., Chapter 3; Altimir et al., 2006) and soil uptake (e.g., Fumagalli et al., 2016; Stella et al., 2019; Stella et al., 2011). Some parameterizations

include variable resistances as a function of LAI or friction velocity (Zhang et al., 2002), but such schemes do not necessarily reproduce non-stomatal conductance substantially better compared to constant-resistance approaches (Chapter 3).

Other non-stomatal processes are even more poorly constrained. For example, turbulent mixing between canopy and surface layer and within the canopy is a crucial first step in delivering the reactive compound to the surface where (non-)stomatal removal occurs. Yet, big leaf parameterizations only take into account in-canopy transport for soil deposition. Often-applied parameterizations of in-canopy turbulence suggest enhanced in-canopy vertical mixing with increasing above-canopy turbulent mixing intensity (Van Pul and Jacobs, 1994). However, as shown in Chapter 4, there can be distinct differences between in-canopy and above-canopy vertical mixing conditions. Multi-layer chemistry models need to resolve reduced in-canopy vertical transport towards the soil, but they might not always realistically represent specific features that control in-canopy turbulent transport, such as effects of in-canopy stability (Chapter 4). Additionally, the contribution of in-canopy chemical reactions to in-canopy ozone removal is uncertain (Clifton et al., 2020b). Not taking into account the drivers of non-stomatal ozone deposition leads to underestimated temporal variability in dry deposition in model simulations (Clifton et al., 2017).

Several avenues can be identified to improve process understanding and modelling of non-stomatal ozone deposition. Firstly, a meta-analysis of available long-term data records of ozone flux measurements may help to better understand the drivers of non-stomatal deposition across sites (e.g., temperature, vapour pressure deficit, soil moisture content). Secondly, model intercomparison projects focused on dry deposition help to quantify and reduce the uncertainty of dry deposition estimates. This effort is already in progress in the AQMEII4 project (Galmarini et al., 2021). Thirdly, targeted campaign-based observations of non-stomatal deposition processes can help to develop process understanding. This can be supported by process-based modelling of non-stomatal removal in turbulence-resolving models that resolve canopy processes (Clifton and Patton, 2021; Patton et al., 2016; Pedruzo-Bagazgoitia et al., 2022, in review).

6.4   Perspectives on bridging spatial and temporal scales

The analyses of aspects relevant to understanding ozone deposition in this thesis consider a range of spatial and temporal scales. For example, in Chapters 3 and 4, we used flux measurements with a footprint of typically less than 1×1 km^2 in forests that do not all span the size of a grid cell in the regional air quality model used in Chapter 2 (20×20 km^2). These simulations do not necessarily represent the local conditions that affect surface ozone and the micro-meteorological variables relevant for ozone deposition. The LES model
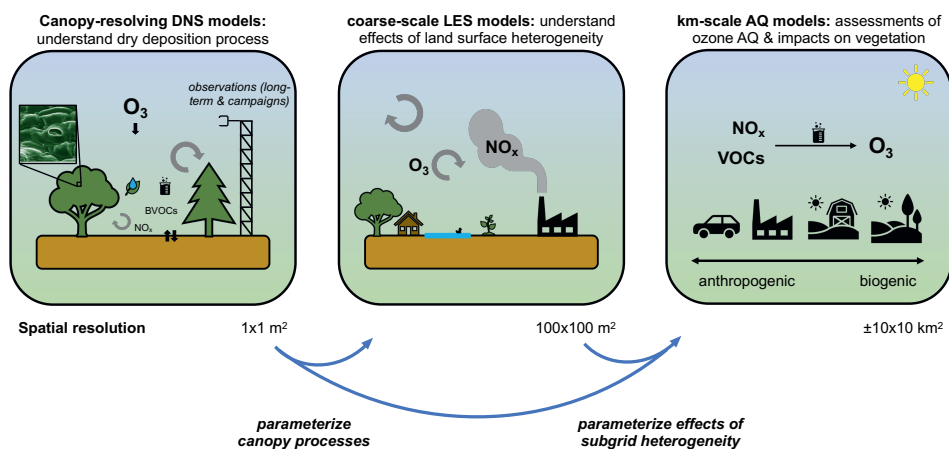
Figure 6.2: Visualization of a model hierarchy approach to bridge the gap in spatial scales between canopy processes and larger-scale air quality modelling. Arrows indicate processes that can be parameterized in coarser models based on higher-resolution models (image showing a stomate retrieved from: `https://en.wikipedia.org/wiki/Stoma#/media/File:Tomato_leaf_stomate_1-color.jpg`).

applied in Chapter 5 bridges the gap in spatial scales between the regional air quality model applied in Chapter 2 and the point-scale field observations and canopy-atmosphere exchange model used in Chapters 3 and 4. However, this LES model is currently only equipped with a big leaf parameterization of dry deposition.

The regional air quality model in Chapter 2 used information on land cover properties at the resolution of the model, i.e., the surface-atmosphere exchange processes of each grid cell were resolved based on one single value for land cover properties such as LAI and aerodynamic roughness length. The effects of subgrid-scale heterogeneity in land cover on surface deposition was not resolved in Chapter 2. Additionally, Chapter 5 gives an initial estimate of the effect of jointly resolving land surface heterogeneity and turbulence on domain-integrated dry deposition totals. The results suggest that this phenomenon is potentially important in the vicinity of strong emission sources that affect vertical gradients of the depositing tracers.

Figure 6.2 presents a model hierarchy approach to bridge the gap in spatial scales between detailed canopy processes and regional to global air quality models. We recommend the use of high-resolution LES or DNS models that explicitly resolve canopy-atmosphere exchange processes (Fig. 6.2, left panel). The setup of these models has horizontal and vertical resolutions on the order of several meters. Initial developments focus on exchange of carbon dioxide (Pedruzo-Bagazgoitia et al., 2022, in review) or include ozone as a passive tracer only subject to loss by dry deposition (Clifton and Patton, 2021). A development

of the canopy exchange representation in these models requires the representation of drag elements in the canopy and a description of the exchange processes per layer (affected by vertical profiles of LAI, radiation, temperature, humidity, etc.). This will enable the explicit simulation of all in-canopy ozone sinks and how they interact with in-canopy turbulence, with a large potential to advance process understanding of ozone deposition. An initial application of high-resolution LES models would be to derive updated formulations of in-canopy aerodynamic resistance for use in big leaf or multi-layer canopy dry deposition parameterizations used in coarser-scale models, and to investigate how the presence of in-canopy decoupled conditions may affect canopy-atmosphere exchange under more generalized circumstances compared to the observations in Chapter 4.

The currently applied high-resolution LES models assume horizontal heterogeneity in forest properties. In reality, land surface properties display spatial heterogeneity (as studied in Chapter 5). Even within forests, this assumed homogeneity is an oversimplification of reality (Bannister et al., 2022). This heterogeneity affects the air flow and the properties of turbulent mixing, and therefore also forest-atmosphere exchange. Quantifying these effects is important to understand canopy-atmosphere exchange and its effect on dry deposition. Therefore, the high-resolution, canopy-resolving LES models should be complemented by analyses on slightly coarser spatial resolutions (e.g., 100×100 m^2, center panel in Fig. 6.2) focused on the effects of land surface heterogeneity. High-resolution canopy-resolving models can serve for parameterization development of canopy-atmosphere exchange in coarser-scale LES simulations, which in turn can be used to parameterize effects of land surface heterogeneity (and associated processes such as turbulent mixing and deposition) in coarser kilometer-scale air quality models used for assessments of ozone air pollution and its harmful effect on ecosystems (Fig. 6.2, right panel).

The development of canopy-resolving modelling capacity can best be supported by advancements in observational infrastructure aiding the understanding of ozone deposition. In this respect, the addition of above-canopy (and ideally also in-canopy) fast ozone sensors to flux measurement towers is a good opportunity. One particular example is the recently renovated Loobos flux tower operated by the Meteorology and Air Quality group at Wageningen University. The Loobos site is already equipped with measurements of CO_2 and water vapour fluxes and ancillary (micro-)meteorological variables. Additionally, long-term ozone flux datasets are essential to understand the drivers of temporal variability in ozone deposition and its response to climatic extreme events such as droughts. To make optimal use of long-term measurement records, these developments should be supported by short-term intensive field campaigns that aim to collect more detailed measurements regarding the behavior of plant stomata and its link with plant eco-physiology from leaf-level observations, various non-stomatal ozone sinks (e.g., leaf uptake and chemical removal by NO and BVOCs), and meteorological measurements to understand how deposition links to boundary layer dynamics. Additionally, the availability of ozone flux measurements

may contribute to understanding how ecosystem carbon uptake is affected by stomatal ozone uptake.

References

Aidaoui, L., A. Maurizi, and A. Azzi (2015). "Modelled NO2 tropospheric columns at different resolutions versus OMI satellite data: analysis of a 1-year BOLCHEM simulation over Europe". *Air Quality, Atmosphere and Health* 8.2, 163–174. DOI: 10.1007/s11869-015-0315-x.

Ainsworth, E. E. a., C. R. Yendrek, S. Sitch, W. J. Collins, and L. D. Emberson (2012). "The effects of tropospheric ozone on net primary productivity and implications for climate change." *Annual review of plant biology* 63.March, 637–61. DOI: 10.1146/annurev-arplant-042110-103829.

Altimir, N., P. Kolari, J.-P. Tuovinen, T. Vesala, J. Bäck, T. Suni, M. Kulmala, and P. Hari (2006). "Foliage surface ozone deposition: a role for surface moisture?" *Biogeosciences* 3, 209–228.

Anav, A., A. De Marco, C. Proietti, A. Alessandri, A. Dell'Aquila, I. Cionni, P. Friedling-stein, D. Khvorostyanov, L. Menut, E. Paoletti, P. Sicard, S. Sitch, and M. Vitale (2016). "Comparing concentration-based (AOT40) and stomatal uptake (PODY) metrics for ozone risk assessment to European forests". *Global Change Biology* 22.4, 1608–1627. DOI: 10.1111/gcb.13138.

Anav, A., C. Proietti, L. Menut, S. Carnicelli, A. De Marco, and E. Paoletti (2018). "Sensitivity of stomatal conductance to soil moisture: implications for tropospheric ozone". *Atmospheric Chemistry and Physics* 18, 5747–5763. DOI: 10.5194/acp-18-5747-2018.

Andreae, M. (2019). "Emission of trace gases and aerosols from biomass burning. Global Biogeochemical". *Atomospheric Chemistry and Physics* 15 (4).April, 955–966.

Archer-Nicholls, S., D. Lowe, S. Utembe, J. Allan, R. A. Zaveri, J. D. Fast, O. Hodnebrog, H. Denier Van Der Gon, and G. McFiggans (2014). "Gaseous chemistry and aerosol mechanism developments for version 3.5.1 of the online regional model, WRF-Chem". *Geoscientific Model Development* 7.6, 2557–2579. DOI: 10.5194/gmd-7-2557-2014.

Arellano, J. V.-G. de and P. G. Duynkerke (1993). "Second-order closure study of the covariance between chemically reactive species in the surface layer". *Journal of Atmospheric Chemistry* 2, 145–155.

Arnold, S. R., D. Lombardozzi, J. F. Lamarque, T. Richardson, L. K. Emmons, S. Tilmes, S. A. Sitch, G. Folberth, M. J. Hollaway, and M. Val Martin (2018). "Simulated Global Climate Response to Tropospheric Ozone-Induced Changes in Plant Transpiration". *Geophysical Research Letters* 45.23, 070–13. DOI: `10.1029/2018GL079938`.

Ashworth, K., S. H. Chung, R. J. Griffin, J. Chen, R. Forkel, A. M. Bryan, and A. L. Steiner (2015). "FORest Canopy Atmosphere Transfer (FORCAsT) 1.0: A 1-D model of biosphere-atmosphere chemical exchange". *Geoscientific Model Development* 8.11, 3765–3784. DOI: `10.5194/gmd-8-3765-2015`.

Atkinson, R., D. L. Baulch, R. A. Cox, J. N. Crowley, R. F. Hampson, R. G. Hynes, M. E. Jenkin, M. J. Rossi, and J. Troe (2004). "Evaluated kinetic and photochemical data for atmospheric chemistry: Volume I - gas phase reactions of Ox, HOx, NOx and SOx species". *Atmospheric Chemistry and Physics* 4.6, 1461–1738. DOI: `10.5194/acp-4-1461-2004`.

Aubinet, M., T. Vesala, and D. Papale (2012). *Eddy covariance: A practical guide to measurement and data analysis*. Ed. by M. Aubinet, T. Vesala, and D. Papale. Dordrecht, NL: Springer Netherlands, 438. DOI: `10.1007/978-94-007-2351-1`.

Auger, L. and B. Legras (2007). "Chemical segregation by heterogeneous emissions". *Atmospheric Environment* 41.11, 2303–2318. DOI: `10.1016/j.atmosenv.2006.11.032`.

Avnery, S., D. L. Mauzerall, J. Liu, and L. W. Horowitz (2011). "Global crop yield reductions due to surface ozone exposure: 1. Year 2000 crop production losses and economic damage". *Atmospheric Environment* 45.13, 2284–2296. DOI: `10.1016/j.atmosenv.2010.11.045`.

Baklanov, A., K. Schlünzen, P. Suppan, J. Baldasano, D. Brunner, S. Aksoyoglu, G. Carmichael, J. Douros, J. Flemming, R. Forkel, S. Galmarini, M. Gauss, G. Grell, M. Hirtl, S. Joffre, O. Jorba, E. Kaas, M. Kaasik, G. Kallos, X. Kong, U. Korsholm, A. Kurganskiy, J. Kushta, U. Lohmann, A. Mahura, A. Manders-Groot, A. Maurizi, N. Moussiopoulos, S. T. Rao, N. Savage, C. Seigneur, R. S. Sokhi, E. Solazzo, S. Solomos, B. Sorensen, G. Tsegas, E. Vignati, B. Vogel, and Y. Zhang (2014). "Online coupled regional meteorology chemistry models in Europe: Current status and prospects". *Atmospheric Chemistry and Physics* 14, 317–398. DOI: `10.5194/acp-14-317-2014`.

Balsamo, G., P. Viterbo, A. Beijaars, B. van den Hurk, M. Hirschi, A. K. Betts, and K. Scipal (2009). "A revised hydrology for the ECMWF model: Verification from field site to terrestrial water storage and impact in the integrated forecast system". *Journal of Hydrometeorology* 10.3, 623–643. DOI: `10.1175/2008JHM1068.1`.

Banerjee, T. and R. Linn (2018). "Effect of vertical canopy architecture on transpiration, Thermoregulation and carbon assimilation". *Forests* 9.4. DOI: `10.3390/f9040198`.

Bannister, E. J., A. R. Mackenzie, and X. Cai (2021). "Realistic forests and the modeling of forest – atmosphere exchange", 1–65.

Bannister, E. J., A. R. MacKenzie, and X.-M. Cai (2022). "Realistic Forests and the Modeling of Forest-Atmosphere Exchange". *Reviews of Geophysics* 60.1, 1–47. DOI: `10.1029/2021rg000746`.

Bates, K. H. and D. J. Jacob (2020). "An Expanded Definition of the Odd Oxygen Family for Tropospheric Ozone Budgets: Implications for Ozone Lifetime and Stratospheric Influence". *Geophysical Research Letters* 47.4, 1–9. DOI: `10.1029/2019GL084486`.

Bauwens, M., T. Stavrakou, J. F. Müller, I. De Smedt, M. Van Roozendael, G. R. Van Der Werf, C. Wiedinmyer, J. W. Kaiser, K. Sindelarova, and A. Guenther (2016). "Nine years of global hydrocarbon emissions based on source inversion of OMI formaldehyde observations". *Atmospheric Chemistry and Physics* 16.15, 10133–10158. DOI: `10.5194/acp-16-10133-2016`.

Beekmann, M. and R. Vautard (2010). "A modelling study of photochemical regimes over Europe: Robustness and variability". *Atmospheric Chemistry and Physics* 10.20, 10067–10084. DOI: `10.5194/acp-10-10067-2010`.

Beirle, S., K. F. Boersma, U. Platt, M. G. Lawrence, and T. Wagner (2011). "Megacity emissions and lifetimes of nitrogen oxides probed from space". *Science* 333.6050, 1737–1739. DOI: `10.1126/science.1207824`.

Bertram, T. H., A. Heckel, A. Richter, J. P. Burrows, and R. C. Cohen (2005). "Satellite measurements of daily variations in soil NOxemissions". *Geophysical Research Letters* 32.24, 1–4. DOI: `10.1029/2005GL024640`.

Bieser, J., A. Aulinger, V. Matthias, M. Quante, and H. A. C. Denier Van Der Gon (2011). "Vertical emission profiles for Europe based on plume rise calculations". *Environmental Pollution* 159.10, 2935–2946. DOI: `10.1016/j.envpol.2011.04.030`.

Boersma, K. F., H. J. Eskes, A. Richter, I. D. Smedt, A. Lorente, S. Beirle, J. D. Maasakkers, R. J. V. D. A, J. Nightingale, A. D. Rudder, H. Irie, G. Pinardi, J.-c. Lambert, and S. C. Compernolle (2018a). "Improving algorithms and uncertainty estimates for satellite NO2 retrievals : results from the quality assurance for the essential climate variables (QA4ECV) project". *Atmos. Meas. Tech.* 11, 6651–6678.

Boersma, K. F., H. J. Eskes, A. Richter, I. D. Smedt, A. Lorente, S. Beirle, J. H. G. M. Van Geffen, M. Zara, E. Peters, M. Van Roozendael, T. Wagner, J. D. Maasakkers, R. J. Van der A, J. Nightingale, A. De Rudder, H. Irie, G. Pinardi, J.-C. Lambert, and S. C. Compernolle (2018b). "Improving algorithms and uncertainty estimates for satellite NO 2 retrievals : Results from the Quality Assurance for Essential Climate Variables (QA4ECV) project". *Atmos. Meas. Tech. Discuss.* DOI: `https://doi.org/10.5194/amt-2018-200`.

Boersma, K. F., H. J. Eskes, R. J. Dirksen, R. J. van der A, J. P. Veefkind, P. Stammes, V. Huijnen, Q. L. Kleipool, M. Sneep, J. Claas, J. Leitão, A. Richter, Y. Zhou, and D. Brunner (2011). "An improved tropospheric NO2 column retrieval algorithm for the

Ozone Monitoring Instrument". *Atmospheric Measurement Techniques* 4.9, 1905–1928. DOI: 10.5194/amt-4-1905-2011.

Boersma, K. F., H. J. Eskes, E. W. Meijer, and H. M. Kelder (2005). "Estimates of lightning NOx production from GOME satellite observations". *Atmospheric Chemistry and Physics* 5.9, 2311–2331. DOI: 10.5194/acp-5-2311-2005.

Boersma, K. F., H. J. Eskes, J. P. Veefkind, E. J. Brinksma, R. J. van der A, M. Sneep, G. H. J. van der Oord, P. F. Levelt, P. Stammes, J. F. Gleason, and E. J. Bucsela (2007). "Near-real time retrieval of tropospheric NO2 from OMI". *Atmospheric Chemistry and Physics* 7, 2103–2118. DOI: 10.5194/acp-7-2103-2007.

Boersma, K. F., D. J. Jacob, M. Trainic, Y. Rudich, I. De Smedt, R. Dirksen, and H. Eskes (2009). "Validation of urban NO2 concentrations and their diurnal and seasonal variations observed from the SCIAMACHY and OMI sensors using in situ surface measurements in Israeli cities". *Atmospheric Chemistry and Physics* 9, 3867–3879. DOI: 10.5194/acp-9-3867-2009.

Boersma, K. F., J. Van Geffen, H. J. Eskes, R. J. van der A, I. De Smedt, M. van Roozendael, H. Yu, A. Richter, E. Peters, S. Beirle, T. Wagner, A. Lorente, T. Scanlon, S. Compernolle, and J. Lambert (2017a). *Product specification document for the QA4ECV NO2 ECV precursor product*. Tech. rep. D4.6. De Bilt, the Netherlands: KNMI, 1–32.

Boersma, K. F., G. C. M. Vinken, and H. J. Eskes (2016). "Representativeness errors in comparing chemistry transport and chemistry climate models with satellite UV–Vis tropospheric column retrievals". *Geoscientific Model Development* 9.2, 875–898. DOI: 10.5194/gmd-9-875-2016.

Boersma, K., H. J. Eskes, A. Richter, I. De Smedt, A. Lorente, S. Beirle, J. Van Geffen, E. Peters, M. Van Roozendael, and T. Wagner (2017b). *QA4ECV NO2 tropospheric and stratospheric vertical column data from OMI (Version 1.1) [Data set]*. DOI: http://doi.org/10.21944/qa4ecv-no2-omi-v1.1.

Bonan, G. B., E. G. Patton, J. J. Finnigan, D. D. Baldocchi, and I. N. Harman (2021). "Moving beyond the incorrect but useful paradigm: reevaluating big-leaf and multilayer plant canopies to model biosphere-atmosphere fluxes – a review". *Agricultural and Forest Meteorology* 306.April. DOI: 10.1016/j.agrformet.2021.108435.

Bosman, P. J. M. and M. C. Krol (2022). "ICLASS 1 . 0: a variational Inverse modelling framework for the Chemistry Land-surface Atmosphere Soil Slab model: description , validation and application". *Geoscientific Model Development Discussions*, 1–37.

Bosman, P. J., C. C. van Heerwaarden, and A. J. Teuling (2019). "Sensible heating as a potential mechanism for enhanced cloud formation over temperate forest". *Quarterly Journal of the Royal Meteorological Society* 145.719, 450–468. DOI: 10.1002/qj.3441.

Bou-Zeid, E., W. Anderson, G. G. Katul, and L. Mahrt (2020). "The Persistent Challenge of Surface Heterogeneity in Boundary-Layer Meteorology: A Review". *Boundary-Layer Meteorology* 177.2-3, 227–245. DOI: 10.1007/s10546-020-00551-8.

Brown, J. S., M. M. Shapkalijevski, M. C. Krol, T. Karl, H. G. Ouwersloot, A. F. Moene, E. G. Patton, and J. Vilà-Guerau de Arellano (2020). "Ozone exchange within and above an irrigated Californian orchard". *Tellus, Series B: Chemical and Physical Meteorology* 72.1, 1–17. DOI: 10.1080/16000889.2020.1723346.

Bryan, A. M., S. B. Bertman, M. A. Carroll, S. Dusanter, G. D. Edwards, R. Forkel, S. Griffith, A. B. Guenther, R. F. Hansen, D. Helmig, B. T. Jobson, F. N. Keutsch, B. L. Lefer, S. N. Pressley, P. B. Shepson, P. S. Stevens, and A. L. Steiner (2012). "In-canopy gas-phase chemistry during CABINEX 2009: Sensitivity of a 1-D canopy model to vertical mixing and isoprene chemistry". *Atmospheric Chemistry and Physics* 12.18, 8829–8849. DOI: 10.5194/acp-12-8829-2012.

Büker, P., T. Morrissey, A. Briolat, R. Falk, D. Simpson, J. P. Tuovinen, R. Alonso, S. Barth, M. Baumgarten, N. Grulke, P. E. Karlsson, J. King, F. Lagergren, R. Matyssek, A. Nunn, R. Ogaya, J. Peñuelas, L. Rhea, M. Schaub, J. Uddling, W. Werner, and L. D. Emberson (2012). "DO3SE modelling of soil moisture to determine ozone flux to forest trees". *Atmospheric Chemistry and Physics* 12.12, 5537–5562. DOI: 10.5194/acp-12-5537-2012.

Caemmerer, S. von and J. R. Evans (2015). "Temperature responses of mesophyll conductance differ greatly between species". *Plant, Cell and Environment* 38.4, 629–637. DOI: 10.1111/pce.12449.

Calvet, J. C., J. Noilhan, J. L. Roujean, P. Bessemoulin, M. Cabelguenne, A. Olioso, and J. P. Wigneron (1998). "An interactive vegetation SVAT model tested against data from six contrasting sites". *Agricultural and Forest Meteorology* 92.2, 73–95. DOI: 10.1016/S0168-1923(98)00091-4.

Castellanos, P. and K. F. Boersma (2012). "Reductions in nitrogen oxides over Europe driven by environmental policy and economic recession." *Scientific reports* 2.2, 265. DOI: 10.1038/srep00265.

Chang, K.-L., I. Petropavlovskikh, O. R. Cooper, M. G. Schultz, and T. Wang (2017). "Regional trend analysis of surface ozone observations from monitoring networks in eastern North America, Europe and East Asia". *Elementa Science of the Anthropocene* 5.50, 22. DOI: 10.1525/elementa.243.

Cionco, R. M. (1978). "Analysis of canopy index values for various canopy densities". *Boundary-Layer Meteorology* 15, 81–93. DOI: 10.1007/BF00165507.

Clifton, O. E., A. M. Fiore, J. W. Munger, S. Malyshev, L. W. Horowitz, E. Shevliakova, F. Paulot, L. T. Murray, and K. L. Griffin (2017). "Interannual variability in ozone removal by a temperate deciduous forest". *Geophysical Research Letters* 44, 542–552. DOI: 10.1002/2016GL070923.

Clifton, O. E., A. M. Fiore, J. W. Munger, and R. Wehr (2019). "Spatiotemporal Controls on Observed Daytime Ozone Deposition Velocity Over Northeastern U.S. Forests During

Summer". *Journal of Geophysical Research: Atmospheres* 124.10, 5612–5628. DOI: 10.1029/2018JD029073.

Clifton, O. E., F. Paulot, A. M. Fiore, L. W. Horowitz, G. Correa, C. B. Baublitz, S. Fares, I. Goded, A. H. Goldstein, C. Gruening, A. J. Hogg, B. Loubet, I. Mammarella, J. W. Munger, L. Neil, P. Stella, J. Uddling, T. Vesala, and E. Weng (2020a). "Influence of Dynamic Ozone Dry Deposition on Ozone Pollution". *Journal of Geophysical Research: Atmospheres* 125.8, 1–21. DOI: 10.1029/2020JD032398.

Clifton, O. E., A. M. Fiore, W. J. Massman, C. B. Baublitz, M. Coyle, L. Emberson, S. Fares, D. K. Farmer, P. Gentine, G. Gerosa, A. B. Guenther, D. Helmig, D. L. Lombardozzi, J. W. Munger, E. G. Patton, S. E. Pusede, D. B. Schwede, S. J. Silva, M. Sörgel, A. L. Steiner, and A. P. Tai (2020b). "Dry Deposition of Ozone Over Land: Processes, Measurement, and Modeling". *Reviews of Geophysics* 58.1. DOI: 10.1029/2019RG000670.

Clifton, O. E., D. L. Lombardozzi, A. M. Fiore, F. Paulot, and L. W. Horowitz (2020c). "Stomatal conductance influences interannual variability and long-term changes in regional cumulative plant uptake of ozone". *Environmental Research Letters* 15.11. DOI: 10.1088/1748-9326/abc3f1.

Clifton, O. E. and E. G. Patton (2021). "Does Organization in Turbulence Influence Ozone Removal by Deciduous Forests?" *Journal of Geophysical Research: Biogeosciences* 126.6, 1–20. DOI: 10.1029/2021JG006362.

Coates, J., K. A. Mar, N. Ojha, and T. M. Butler (2016). "The influence of temperature on ozone production under varying NOx conditions – a modelling study". *Atmospheric Chemistry and Physics* 16.18, 11601–11615. DOI: 10.5194/acp-16-11601-2016.

Cohan, D. S., Y. Hu, and A. G. Russell (2006). "Dependence of ozone sensitivity analysis on grid resolution". *Atmospheric Environment* 40, 126–135. DOI: 10.1016/j.atmosenv.2005.09.031.

Collins, W. D., P. J. Rasch, B. Boville, J. J. Hack, J. R. McCaa, D. L. Williamson, J. T. Kiehl, B. Briegleb, C. Bitz, S. Lin, M. Zhang, and Y. Dai (2004). *Description of the NCAR community atmosphere model (CAM 3.0)*. Tech. rep. Boulder, CO: National Center for Atmospheric Research, 214.

Cook, B. I., J. S. Mankin, and K. J. Anchukaitis (2018). "Climate Change and Drought: From Past to Future". *Current Climate Change Reports* 4.2, 164–179. DOI: 10.1007/s40641-018-0093-2.

Crippa, M., D. Guizzardi, M. Muntean, E. Schaaf, F. Dentener, J. A. Van Aardenne, S. Monni, U. Doering, J. G. Olivier, V. Pagliari, and G. Janssens-Maenhout (2018). "Gridded emissions of air pollutants for the period 1970-2012 within EDGAR v4.3.2". *Earth System Science Data* 10.4, 1987–2013. DOI: 10.5194/essd-10-1987-2018.

Curci, G., P. I. Palmer, T. P. Kurosu, K. Chance, and G. Visconti (2010). "Estimating European volatile organic compound emissions using satellite observations of formaldehyde

from the Ozone Monitoring Instrument". *Atmospheric Chemistry and Physics* 10.23, 11501–11517. DOI: `10.5194/acp-10-11501-2010`.

Dammers, E. (2013). *Assessment of soil nitrogen oxides emissions and implementation in LOTOS-EUROS (MSc thesis)*. Eindhoven (NL), 63.

Dee, D. P., S. M. Uppala, A. J. Simmons, P. Berrisford, P. Poli, S. Kobayashi, U. Andrae, M. A. Balmaseda, G. Balsamo, P. Bauer, P. Bechtold, A. C. M. Beljaars, L. van de Berg, J. Bidlot, N. Bormann, C. Delsol, R. Dragani, M. Fuentes, A. J. Geer, L. Haimberger, S. B. Healy, H. Hersbach, E. V. Hólm, L. Isaksen, P. Kållberg, M. Köhler, M. Matricardi, A. P. Mcnally, B. M. Monge-Sanz, J. J. Morcrette, B. K. Park, C. Peubey, P. de Rosnay, C. Tavolato, J. N. Thépaut, and F. Vitart (2011). "The ERA-Interim reanalysis: Configuration and performance of the data assimilation system". *Quarterly Journal of the Royal Meteorological Society* 137.656, 553–597. DOI: `10.1002/qj.828`.

Delaria, E. R., B. K. Place, A. J. Turner, Q. Zhu, X. Jin, and R. C. Cohen (2021). "Development of a Solar-Induced Fluorescence-Canopy Conductance Model and Its Application to Stomatal Reactive Nitrogen Deposition". *ACS Earth and Space Chemistry*. DOI: `10.1021/acsearthspacechem.1c00260`.

Dirksen, R. J., K. F. Boersma, H. J. Eskes, D. V. Ionov, E. J. Bucsela, P. F. Levelt, and H. M. Kelder (2011). "Evaluation of stratospheric NO2 retrieved from the Ozone Monitoring Instrument: Intercomparison, diurnal cycle, and trending". *Journal of Geophysical Research Atmospheres* 116.8, 1–22. DOI: `10.1029/2010JD014943`.

Dlugi, R., M. Berger, M. Zelger, A. Hofzumahaus, M. Siese, F. Holland, A. Wisthaler, W. Grabmer, A. Hansel, R. Koppmann, G. Kramm, M. Möllmann-Coers, and A. Knaps (2010). "Turbulent exchange and segregation of HOx radicals and volatile organic compounds above a deciduous forest". *Atmospheric Chemistry and Physics* 10.13, 6215–6235. DOI: `10.5194/acp-10-6215-2010`.

Dorsey, J. R., J. H. Duyzer, M. W. Gallagher, H. Coe, K. Pilegaard, J. H. Weststrate, N. O. Jensen, and S. Walton (2004). "Oxidized nitrogen and ozone interaction with forests. I : Experimental observations and analysis of exchange with Douglas fir". *Quarterly Journal of the Royal Meteorological Society* 130.600 PART A, 1941–1955. DOI: `10.1256/qj.03.124`.

Ducker, J. A., C. D. Holmes, T. F. Keenan, S. Fares, A. H. Goldstein, I. Mammarella, J. W. Munger, and J. Schnell (2018). "Synthetic ozone deposition and stomatal uptake at flux tower sites". *Biogeosciences* 15, 5395–5413. DOI: `10.5194/bg-15-5395-2018`.

Dunlea, E., S. Herndon, D. Nelson, R. Volkamer, F. San Martini, P. Sheehy, M. Zahniser, J. Shorter, J. Wormhoudt, B. Lamb, E. Allwine, J. Gaffney, N. Marley, M. Grutter, C. Marquez, S. Blanco, B. Cardenas, A. Retama, C. Ramos Villegas, C. Kolb, L. Molina, and M. Molina (2007). "Evaluation of nitrogen dioxide chemiluminescence monitors in a polluted urban environment". *Atmos. Chem. Phys* 7, 2691–2704. DOI: `10.5194/acp-7-2691-2007`.

Duyzer, J. H., J. R. Dorsey, M. W. Gallagher, K. Pilegaard, and S. Walton (2004). "Oxidized nitrogen and ozone interaction with forests. II : Multi-layer process-oriented modelling results and a sensitivity study for Douglas fir". *Quarterly Journal of the Royal Meteorological Society* 130.600 PART A, 1957–1971. DOI: 10.1256/qj.03.125.

ECMWF (2020). "Part IV: Physical Processes". In: *IFS Documentation CY47R1*. June. Reading, United Kingdom: ECMWF, 228.

EEA (2017). *Air quality in Europe — 2017 report*. Tech. rep. 13. Copenhagen, Denmark: European Environment Agency, 80. DOI: 10.2800/22775.

– (2018). *Air Quality e-Reporting [Data Set]*.

– (2020). *Air quality in Europe — 2020 report, EEA Report No 09/2020, European Environment Agency*. 09. Copenhagen, Denmark: European Environment Agency.

Emberson, L. D., G. Wieser, and M. R. Ashmore (2000). "Modelling of stomatal conductance and ozone flux of Norway spruce: comparison with field data". *Environmental Pollution* 109, 393–402.

Emberson, L., M. Ashmore, D. Simpson, J.-P. Tuovinen, and H. Cambridge (2001). "Modelling and mapping ozone deposition in Europe". *Water, Air, and Soil Pollution* 130, 577–582. DOI: 10.1023/A:1013851116524.

Emberson, L. D., H. Pleijel, E. A. Ainsworth, M. van den Berg, W. Ren, S. Osborne, G. Mills, D. Pandey, F. Dentener, P. Büker, F. Ewert, R. Koeble, and R. Van Dingenen (2018). "Ozone effects on crops and consideration in crop models". *European Journal of Agronomy* 100.December 2016, 19–34. DOI: 10.1016/j.eja.2018.06.002.

EMEP/CCC (2016). *Air pollution trends in the EMEP region between 1990 and 2012*. Tech. rep. 1/2016. Kjeller, NO: EMEP, 107.

Erisman, J. W., A. Van Pul, and P. Wyers (1994). "Parametrization of surface resistance for the quantification of atmospheric deposition of acidifying pollutants and ozone". *Atmospheric Environment* 28.16, 2595–2607. DOI: 10.1016/1352-2310(94)90433-2.

Eskes, H. J. and K. F. Boersma (2003). "Averaging kernels for DOAS total-column satellite retrievals". *Atmospheric Chemistry and Physics* 3.5, 1285–1291. DOI: 10.5194/acp-3-1285-2003.

ETC/ACM (2016). *Long term air quality trends in Europe: contribution of meteorological variability, natural factors and emissions*. Tech. rep. 2016/7. Bilthoven, NL: European Topic Centre on Air Pollution and Climate Change Mitigation, 97.

European Environment Agency (2020). *European Union emission inventory report 1990-2018 under the UNECE Convention on Long-range Transboundary Air Pollution (LRTAP)*. 05. Copenhagen, Denmark, 160. DOI: 10.2800/233574.

– (2021). *CORINE Land Cover - User Manual*. Tech. rep. Copenhagen, Denmark: European Environment Agency, 128.

Fares, S., F. Savi, J. Muller, G. Matteucci, and E. Paoletti (2014). "Simultaneous measurements of above and below canopy ozone fluxes help partitioning ozone deposition between its various sinks in a Mediterranean Oak Forest". *Agricultural and Forest Meteorology* 198, 181–191. DOI: 10.1016/j.agrformet.2014.08.014.

Fares, S., A. Alivernini, A. Conte, and F. Maggi (2019). "Ozone and particle fluxes in a Mediterranean forest predicted by the AIRTREE model". *Science of the Total Environment* 682, 494–504. DOI: 10.1016/j.scitotenv.2019.05.109.

Fares, S., M. McKay, R. Holzinger, and A. H. Goldstein (2010). "Ozone fluxes in a Pinus ponderosa ecosystem are dominated by non-stomatal processes: Evidence from long-term continuous measurements". *Agricultural and Forest Meteorology* 150.3, 420–431. DOI: 10.1016/j.agrformet.2010.01.007.

Fares, S., R. Weber, J. H. Park, D. Gentner, J. Karlik, and A. H. Goldstein (2012). "Ozone deposition to an orange orchard: Partitioning between stomatal and non-stomatal sinks". *Environmental Pollution* 169, 258–266. DOI: 10.1016/j.envpol.2012.01.030.

Finco, A., M. Coyle, E. Nemitz, R. Marzuoli, M. Chiesa, B. Loubet, S. Fares, E. Diaz-Pines, R. Gasche, and G. Gerosa (2018). "Characterization of ozone deposition to a mixed oak-hornbeam forest - Flux measurements at five levels above and inside the canopy and their interactions with nitric oxide". *Atmospheric Chemistry and Physics* 18.24, 17945–17961. DOI: 10.5194/acp-18-17945-2018.

Finnigan, J. J. (2000). "Turbulence in plant canopies". *Annual Review of Fluid Mechanics* 32, 519–571.

Flemming, J., V. Huijnen, J. Arteta, P. Bechtold, A. Beljaars, A. M. Blechschmidt, M. Diamantakis, R. J. Engelen, A. Gaudel, A. Inness, L. Jones, B. Josse, E. Katragkou, V. Marecal, V. H. Peuch, A. Richter, M. G. Schultz, O. Stein, and A. Tsikerdekis (2015). "Tropospheric chemistry in the integrated forecasting system of ECMWF". *Geoscientific Model Development* 8.4, 975–1003. DOI: 10.5194/gmd-8-975-2015.

Foken, T., F. X. Meixner, E. Falge, C. Zetzsch, A. Serafimovich, A. Bargsten, T. Behrendt, T. Biermann, C. Breuninger, S. Dix, T. Gerken, M. Hunner, L. Lehmann-Pape, K. Hens, G. Jocher, J. Kesselmeier, J. Lüers, A. Moravek, D. Plake, M. Riederer, F. Rütz, M. Scheibe, L. Siebicke, M. Sörgel, K. Staudt, I. Trebs, A. Tsokankunku, M. Welling, V. Wolff, and Z. Zhu (2012). "Coupling processes and exchange of energy and reactive and non-reactive trace gases at a forest site - Results of the EGER experiment". *Atmospheric Chemistry and Physics* 12.4, 1923–1950. DOI: 10.5194/acp-12-1923-2012.

Foken, T. (2006). "50 years of the Monin-Obukhov similarity theory". *Boundary-Layer Meteorology* 119.3, 431–447. DOI: 10.1007/s10546-006-9048-6.

– (2008). "The energy balance closure problem: An overview". *Ecological Applications* 18.6, 1351–1367. DOI: 10.1890/06-0922.1.

Fortems-Cheiney, A., G. Broquet, I. Pison, M. Saunois, E. Potier, A. Berchet, G. Dufour, G. Siour, H. Denier van der Gon, S. Dellaert, and K. F. Boersma (2021). " Analysis

of the anthropogenic and biogenic NO x emissions over 2008-2017: assessment of the trends in the 30 most populated urban areas in Europe ". *Geophysical Research Letters.* DOI: 10.1029/2020gl092206.

Fowler, D., M. Amann, R. Anderson, M. Ashmore, P. Cox, M. Depledge, D. Derwent, P. Grennfelt, N. Hewitt, O. Hov, M. Jenkin, F. Kelly, P. Liss, M. Pilling, J. Pyle, J. Slingo, and D. Stevenson (2008). *Ground-level ozone in the 21st century: future trends, impacts and policy implications.* Tech. rep. London: The Royal Society, 134.

Fowler, D., C. Flechard, J. Neil Cape, R. Storeton-West, and M. Coyle (2001). "Measurements of ozone deposition to vegetation quantifying the flux, the stomatal and non-stomatal components". *Water, Air and Soil Pollution* 130.1, 63–74. DOI: 10.1023/A: 1012243317471.

Fowler, D., K. Pilegaard, M. A. Sutton, P. Ambus, M. Raivonen, J. Duyzer, D. Simpson, H. Fagerli, S. Fuzzi, J. K. Schjoerring, C. Granier, A. Neftel, I. S. A. Isaksen, P. Laj, M. Maione, P. S. Monks, J. Burkhardt, U. Daemmgen, J. Neirynck, E. Personne, R. Wichink-Kruit, K. Butterbach-Bahl, C. Flechard, J. P. Tuovinen, M. Coyle, G. Gerosa, B. Loubet, N. Altimir, L. Gruenhage, C. Ammann, S. Cieslik, E. Paoletti, T. N. Mikkelsen, H. Ro-Poulsen, P. Cellier, J. N. Cape, L. Horváth, F. Loreto, Ü. Niinemets, P. I. Palmer, J. Rinne, P. Misztal, E. Nemitz, D. Nilsson, S. Pryor, M. W. Gallagher, T. Vesala, U. Skiba, N. Brüggemann, S. Zechmeister-Boltenstern, J. Williams, C. O'Dowd, M. C. Facchini, G. de Leeuw, A. Flossman, N. Chaumerliac, and J. W. Erisman (2009). "Atmospheric composition change: Ecosystems-Atmosphere interactions". *Atmospheric Environment* 43.33, 5193–5267. DOI: 10.1016/j.atmosenv.2009.07.068.

Fumagalli, I., C. Gruening, R. Marzuoli, S. Cieslik, and G. Gerosa (2016). "Long-term measurements of NOx and O3 soil fluxes in a temperate deciduous forest". *Agricultural and Forest Meteorology* 228-229.x, 205–216. DOI: 10.1016/j.agrformet.2016.07.011.

Galmarini, S., P. Makar, O. E. Clifton, C. Hogrefe, J. Bash, R. Bellasio, R. Bianconi, J. Bieser, T. Butler, J. Ducker, J. Flemming, A. Hodzic, C. Holmes, I. Kioutsioukis, R. Kranenburg, A. Lupascu, J. Perez-Camanyo, J. Pleim, Y.-H. Ryu, R. San Jose, D. Schwede, S. Silva, M. Garcia Vivanco, and R. Wolke (2021). "Technical Note - AQMEII4 Activity 1: evaluation of wet and dry deposition schemes as an integral part of regional-scale air quality models". *Atmos. Chem. Phys. Discuss.* DOI: 10.5194/acp-2021-313.

Ganzeveld, L. N., L. Bouwman, E. Stehfest, D. van Vuuren, B. Eickhout, and J. Lelieveld (2010). "Impacts of future land cover changes on atmospheric chemistry-climate interactions". *Journal of Geophysical Research* 115. DOI: 10.1029/2010JD014041.

Ganzeveld, L. N. and J. Lelieveld (1995). "Dry deposition parameterization in a chemistry general circulation model and its influence on the distribution of reactive trace gases". *Journal of Geophysical Research* 100.D10. DOI: 10.1029/95jd02266.

Ganzeveld, L. N., J. Lelieveld, F. J. Dentener, M. C. Krol, A. J. Bouwman, and G. J. Roelofs (2002a). "Global soil-biogenic NOX emissions and the role of canopy processes". *Journal of Geophysical Research Atmospheres* 107.16, 1–17. DOI: 10.1029/2001JD001289.

Ganzeveld, L. N., J. Lelieveld, F. J. Dentener, M. C. Krol, and G. J. Roelofs (2002b). "Atmosphere-biosphere trace gas exchanges simulated with a single-column model". *Journal of Geophysical Research Atmospheres* 107.16, 1–21. DOI: 10.1029/2001JD000684.

Ganzeveld, L. N., J. Lelieveld, and G. J. Roelofs (1998). "A dry deposition parameterization for sulfur oxides in a chemistry and general circulation model". *Journal of Geophysical Research Atmospheres* 103.D5, 5679–5694. DOI: 10.1029/97JD03077.

Gao, W. (1995). "Parameterization of subgrid-scale land surface fluxes with emphasis on distributing mean atmospheric forcing and using satellite-derived vegetation index". *Journal of Geophysical Research* 100.D7, 305–317. DOI: 10.1029/95jd01464.

Gerken, T., M. Chamecki, and J. D. Fuentes (2017). "Air-Parcel Residence Times Within Forest Canopies". *Boundary-Layer Meteorology* 165.1, 29–54. DOI: 10.1007/s10546-017-0269-7.

Gerosa, G., R. Marzuoli, B. Monteleone, M. Chiesa, and A. Finco (2017). "Vertical ozone gradients above forests. Comparison of different calculation options with direct ozone measurements above a mature forest and consequences for ozone risk assessment". *Forests* 8.9. DOI: 10.3390/f8090337.

Ghude, S. D., G. G. Pfister, C. K. Jena, R. J. van der A, L. K. Emmons, and R. Kumar (2013). "Satellite constraints of Nitrogen Oxide (NOX) emissions from India based on OMI observations and WRF-Chem simulations". *Geophysical Research Letters* 40, 1–6. DOI: 10.1029/2012GL053926.

Giordano, L., D. Brunner, J. Flemming, C. Hogrefe, U. Im, R. Bianconi, A. Badia, A. Balzarini, R. Baró, C. Chemel, G. Curci, R. Forkel, P. Jiménez-Guerrero, M. Hirtl, A. Hodzic, L. Honzak, O. Jorba, C. Knote, J. J. Kuenen, P. A. Makar, A. Manders-Groot, L. Neal, J. L. Pérez, G. Pirovano, G. Pouliot, R. San José, N. Savage, W. Schröder, R. S. Sokhi, D. Syrakov, A. Torian, P. Tuccella, J. Werhahn, R. Wolke, K. Yahya, R. Žabkar, Y. Zhang, and S. Galmarini (2015). "Assessment of the MACC reanalysis and its influence as chemical boundary conditions for regional air quality modeling in AQMEII-2". *Atmospheric Environment* 115, 371–388. DOI: 10.1016/j.atmosenv.2015.02.034.

Goldstein, A. H., M. McKay, M. R. Kurpius, G. W. Schade, A. Lee, R. Holzinger, and R. A. Rasmussen (2004). "Forest thinning experiment confirms ozone deposition to forest canopy is dominated by reaction with biogenic VOCs". *Geophysical Research Letters* 31.22, 1–4. DOI: 10.1029/2004GL021259.

Grell, G. A., S. E. Peckham, R. Schmitz, S. A. Mckeen, G. Frost, W. C. Skamarock, and B. Eder (2005). "Fully coupled "online" chemistry within the WRF model". *Atmos. Env.* 39, 6957–6975. DOI: 10.1016/j.atmosenv.2005.04.027.

Grell, G. A. and D. Devenyi (2002). "A generalized approach to parameterizing convection combining ensemble and data assimilation techniques". *Geophysical Research Letters* 29.14, 10–13. DOI: 10.1029/2002GL015311.

Griffin, D., C. A. McLinden, E. Dammers, C. Adams, C. E. Stockwell, C. Warneke, I. Bourgeois, J. Peischl, T. B. Ryerson, K. J. Zarzana, J. P. Rowe, R. Volkamer, C. Knote, N. Kille, T. K. Koenig, C. F. Lee, D. Rollins, P. S. Rickly, J. Chen, L. Fehr, A. Bourassa, D. Degenstein, K. Hayden, C. Mihele, S. N. Wren, J. Liggio, A. Akingunola, and P. Makar (2021). "Biomass burning nitrogen dioxide emissions derived from space with TROPOMI: Methodology and validation". *Atmospheric Measurement Techniques* 14.12, 7929–7957. DOI: 10.5194/amt-14-7929-2021.

Gruening, C., I. Goded, A. Cescatti, D. Fachinetti, I. Fumagalli, and M. Duerr (2012). *ABC-IS Forest Flux Station Report on Instrumentation , Operational Testing and First Months of Measurements*. Tech. rep. Ispra: Joint Research Centre, 19. DOI: 10.2788/7774.

Guenther, A., T. Karl, P. Harley, C. Wiedinmyer, P. I. Palmer, and C. Geron (2006). "Estimates of global terrestrial isoprene emissions using MEGAN (Model of Emissions of Gases and Aerosols from Nature)". *Atmospheric Chemistry and Physics* 6, 3181–3210. DOI: 10.5194/acp-6-3181-2006.

Guenther, A. B., X. Jiang, C. L. Heald, T. Sakulyanontvittaya, T. Duhl, L. K. Emmons, and X. Wang (2012). "The model of emissions of gases and aerosols from nature version 2.1 (MEGAN2.1): An extended and updated framework for modeling biogenic emissions". *Geoscientific Model Development* 5.6, 1471–1492. DOI: 10.5194/gmd-5-1471-2012.

Hardacre, C., O. Wild, and L. Emberson (2015). "An evaluation of ozone dry deposition in global scale chemistry climate models". *Atmospheric Chemistry and Physics* 15, 6419–6436. DOI: 10.5194/acpd-14-22793-2014.

Heckel, A., S.-W. Kim, G. Frost, A. Richter, M. Trainer, and J. Burrows (2011). "Influence of low spatial resolution a priori data on tropospheric NO2 satellite retrievals". *Atmos. Meas. Tech.* 4, 1805–1820. DOI: 10.5194/amt-4-1805-2011.

Hellén, H., A. P. Praplan, T. Tykkä, I. Ylivinkka, V. Vakkari, J. Bäck, T. Petäjä, M. Kulmala, and H. Hakola (2018). "Long-term measurements of volatile organic compounds highlight the importance of sesquiterpenes for the atmospheric chemistry of a boreal forest". *Atmospheric Chemistry and Physics* 18.19, 13839–13863. DOI: 10.5194/acp-18-13839-2018.

Hersbach, H., B. Bell, P. Berrisford, S. Hirahara, A. Horányi, J. Muñoz-Sabater, J. Nicolas, C. Peubey, R. Radu, D. Schepers, A. Simmons, C. Soci, S. Abdalla, X. Abellan, G. Balsamo, P. Bechtold, G. Biavati, J. Bidlot, M. Bonavita, G. De Chiara, P. Dahlgren, D. Dee, M. Diamantakis, R. Dragani, J. Flemming, R. Forbes, M. Fuentes, A. Geer, L. Haimberger, S. Healy, R. J. Hogan, E. Hólm, M. Janisková, S. Keeley, P. Laloyaux, P. Lopez, C. Lupu, G. Radnoti, P. de Rosnay, I. Rozum, F. Vamborg, S. Villaume, and

J. N. Thépaut (2020). "The ERA5 global reanalysis". *Quarterly Journal of the Royal Meteorological Society* 146.730, 1999–2049. DOI: `10.1002/qj.3803`.

Heus, T., C. C. Van Heerwaarden, H. J. Jonker, A. Pier Siebesma, S. Axelsen, K. Van Den Dries, O. Geoffroy, A. F. Moene, D. Pino, S. R. De Roode, and J. V. G. De Arellano (2010). "Formulation of the Dutch Atmospheric Large-Eddy Simulation (DALES) and overview of its applications". *Geoscientific Model Development* 3.2, 415–444. DOI: `10.5194/gmd-3-415-2010`.

Hicks, B. B., D. D. Baldocchi, T. P. Meyers, R. P. Hosker, and D. R. Matt (1987). "A preliminary multiple resistance routine for deriving dry deposition velocities from measured quantities". *Water, Air, and Soil Pollution* 36.3-4, 311–330. DOI: `10.1007/BF00229675`.

Holtslag, A. A., G. Svensson, P. Baas, S. Basu, B. Beare, A. C. Beljaars, F. C. Bosveld, J. Cuxart, J. Lindvall, G. J. Steeneveld, M. Tjernström, and B. J. Van De Wiel (2013). "Stable atmospheric boundary layers and diurnal cycles: Challenges for weather and climate models". *Bulletin of the American Meteorological Society* 94.11, 1691–1706. DOI: `10.1175/BAMS-D-11-00187.1`.

Hu, L., D. J. Jacob, X. Liu, Y. Zhang, L. Zhang, P. S. Kim, M. P. Sulprizio, and R. M. Yantosca (2017). "Global budget of tropospheric ozone: Evaluating recent model advances with satellite (OMI), aircraft (IAGOS), and ozonesonde observations". *Atmospheric Environment* 167, 323–334. DOI: `10.1016/j.atmosenv.2017.08.036`.

Huang, M., J. H. Crawford, J. P. Digangi, G. R. Carmichael, K. W. Bowman, S. V. Kumar, and X. Zhan (2021). "Satellite soil moisture data assimilation impacts on modeling weather variables and ozone in the southeastern US - Part 1: An overview". *Atmospheric Chemistry and Physics* 21.14, 11013–11040. DOI: `10.5194/acp-21-11013-2021`.

Huber, D. E., A. L. Steiner, and E. A. Kort (2020). "Daily Cropland Soil NOx Emissions Identified by TROPOMI and SMAP". *Geophysical Research Letters* 47.22. DOI: `10.1029/2020GL089949`.

Hudman, R. C., N. E. Moore, A. K. Mebust, R. V. Martin, A. R. Russell, L. C. Valin, and R. C. Cohen (2012). "Steps towards a mechanistic model of global soil nitric oxide emissions: Implementation and space based-constraints". *Atmospheric Chemistry and Physics* 12.16, 7779–7795. DOI: `10.5194/acp-12-7779-2012`.

Huijnen, V., H. J. Eskes, A. Poupkou, H. Elbern, K. F. Boersma, G. Foret, M. Sofiev, A. Valdebenito, J. Flemming, and O. Stein (2010). "Comparison of OMI NO2 tropospheric columns with an ensemble of global and European regional air quality models". *Atmospheric Chemistry and Physics* 10.7, 3273–3296. DOI: `10.5194/acp-10-3273-2010`.

Im, U., R. Bianconi, I. Kioutsioukis, A. Badia, R. Bellasio, D. Brunner, A. Balzarini, R. Bar, C. Chemel, G. Curci, J. Flemming, R. Forkel, L. Giordano, M. Hirtl, A. Hodzic, L. Honzak, O. Jorba, P. Jim, C. Knote, J. J. P. Kuenen, P. A. Makar, A. Mandersgroot, G. Pirovano, G. Pouliot, R. San, L. Neal, L. P. Juan, N. Savage, W. Schroder,

R. S. Sokhi, D. Syrakov, A. Torian, P. Tuccella, J. Werhahn, R. Wolke, K. Yahya, R. Zabkar, Y. Zhang, J. Zhang, and C. Hogrefe (2015). "Evaluation of operational on-line-coupled regional air quality models over Europe and North America in the context of AQMEII phase 2 . Part I : Ozone". *Atmospheric Environment* 115, 404–420. DOI: `10.1016/j.atmosenv.2014.09.042`.

Inness, A., A. M. Blechschmidt, I. Bouarar, S. Chabrillat, M. Crepulja, R. J. Engelen, H. Eskes, J. Flemming, A. Gaudel, F. Hendrick, V. Huijnen, L. Jones, J. Kapsomenakis, E. Katragkou, A. Keppens, B. Langerock, M. De Mazière, D. Melas, M. Parrington, V. H. Peuch, M. Razinger, A. Richter, M. G. Schultz, M. Suttie, V. Thouret, M. Vrekoussis, A. Wagner, and C. Zerefos (2015). "Data assimilation of satellite-retrieved ozone, carbon monoxide and nitrogen dioxide with ECMWF's Composition-IFS". *Atmospheric Chemistry and Physics* 15.9, 5275–5303. DOI: `10.5194/acp-15-5275-2015`.

Inness, A., M. Ades, A. Agustí-Panareda, J. Barr, A. Benedictow, A. M. Blechschmidt, J. Jose Dominguez, R. Engelen, H. Eskes, J. Flemming, V. Huijnen, L. Jones, Z. Kipling, S. Massart, M. Parrington, V. H. Peuch, M. Razinger, S. Remy, M. Schulz, and M. Suttie (2019). "The CAMS reanalysis of atmospheric composition". *Atmospheric Chemistry and Physics* 19.6, 3515–3556. DOI: `10.5194/acp-19-3515-2019`.

IPCC (2013). *Climate Change 2013, the Physical Science Basis. Working Group I contribution to the fifth assessment report of the Intergovernmental Panel on Climate Change.* Cambridge University Press.

– (2021). *Climate Change 2021: The physical science basis. Contributions of Working Group I to the Sixth Assessment Report of the Intergovernmental Panel on Climate Change.* Tech. rep. Cambridge, United Kingdom: IPCC. DOI: `10.1017/9781009157896`.

Jacob, D. (1999). *Introduction to Atmospheric Chemistry.* Vol. 82. 42. Princeton, New Jersey: Princeton University Press, 490–490. DOI: `10.1029/01EO00292`.

Jaeglé, L., L. Steinberger, R. V. Martin, and K. Chance (2005). "Global partitioning of NOx sources using satellite observations: Relative roles of fossil fuel combustion, biomass burning and soil emissions". *Faraday Discussions* 130, 407. DOI: `10.1039/b502128f`.

Janssen, R. H., J. Vilà-Guerau De Arellano, L. N. Ganzeveld, P. Kabat, J. L. Jimenez, D. K. Farmer, C. C. Van Heerwaarden, and I. Mammarella (2012). "Combined effects of surface conditions, boundary layer dynamics and chemistry on diurnal SOA evolution". *Atmospheric Chemistry and Physics* 12.15, 6827–6843. DOI: `10.5194/acp-12-6827-2012`.

Jarvis, P. (1976). "The interpretation of the variations in leaf water potential and stomatal conductance found in canopies in the field". *Philosophical Transactions of the Royal Society of London. B, Biological Sciences* 273.927, 593–610. DOI: `10.1098/rstb.1976.0035`.

Jin, X., A. M. Fiore, L. T. Murray, L. C. Valin, L. N. Lamsal, B. Duncan, K. Folkert Boersma, I. De Smedt, G. G. Abad, K. Chance, and G. S. Tonnesen (2017). "Evaluating

a Space-Based Indicator of Surface Ozone-NOx-VOC Sensitivity Over Midlatitude Source Regions and Application to Decadal Trends". *Journal of Geophysical Research: Atmospheres* 122.19, 10439–10461. DOI: 10.1002/2017JD026720.

Jocher, G., J. Marshall, M. B. Nilsson, S. Linder, G. De Simon, T. Hörnlund, T. Lundmark, T. Näsholm, M. Ottosson Löfvenius, L. Tarvainen, G. Wallin, and M. Peichl (2018). "Impact of Canopy Decoupling and Subcanopy Advection on the Annual Carbon Balance of a Boreal Scots Pine Forest as Derived From Eddy Covariance". *Journal of Geophysical Research: Biogeosciences* 123.2, 303–325. DOI: 10.1002/2017JG003988.

Kavassalis, S. C. and J. G. Murphy (2017). "Understanding ozone-meteorology correlations: A role for dry deposition". *Geophysical Research Letters* 44.6, 2922–2931. DOI: 10.1002/2016GL071791.

Kleczek, M. A., G. J. Steeneveld, and A. A. Holtslag (2014). "Evaluation of the Weather Research and Forecasting Mesoscale Model for GABLS3: Impact of Boundary-Layer Schemes, Boundary Conditions and Spin-Up". *Boundary-Layer Meteorology* 152.2, 213–243. DOI: 10.1007/s10546-014-9925-3.

Kleipool, Q. L., M. R. Dobber, J. F. de Haan, and P. F. Levelt (2008). "Earth surface reflectance climatology from 3 years of OMI data". *Journal of Geophysical Research Atmospheres* 113.18, 1–22. DOI: 10.1029/2008JD010290.

Knauer, J., T. S. El-Madany, S. Zaehle, and M. Migliavacca (2018). "Bigleaf—An R package for the calculation of physical and physiological ecosystem properties from eddy covariance data". *PLoS ONE* 13.8, 1–26. DOI: 10.1371/journal.pone.0201114.

Knote, C., P. Tuccella, G. Curci, L. Emmons, J. J. Orlando, S. Madronich, R. Baró, P. Jiménez-Guerrero, D. Luecken, C. Hogrefe, R. Forkel, J. Werhahn, M. Hirtl, J. L. Pérez, R. San José, L. Giordano, D. Brunner, K. Yahya, and Y. Zhang (2015). "Influence of the choice of gas-phase mechanism on predictions of key gaseous pollutants during the AQMEII phase-2 intercomparison". *Atmospheric Environment* 115, 553–568. DOI: 10.1016/j.atmosenv.2014.11.066.

Krol, M., M. Molemaker, and J. Vilà-Guerau De Arellano (2000). "Effects of turbulence and heterogeneous emissions on photochemically active species in the convective boundary layer". 105.D5, 6871–6884. DOI: 10.1029/1999JD900958.

Kuenen, J. J. P., A. J. H. Visschedijk, M. Jozwicka, and H. a. C. Denier van der Gon (2014). "TNO-MACC_II emission inventory: a multi-year (2003-2009) consistent high-resolution European emission inventory for air quality modelling". *Atmos. Chem. Phys.* 14.2013, 10963–10976. DOI: 10.5194/acp-14-10963-2014.

Kuenen, J., S. Dellaert, A. Visschedijk, J. P. Jalkanen, I. Super, and H. Denier Van Der Gon (2022). "CAMS-REG-v4: a state-of-the-art high-resolution European emission inventory for air quality modelling". *Earth System Science Data* 14.2, 491–515. DOI: 10.5194/essd-14-491-2022.

Lammel, G. (1999). *Formation of nitrous acid: parameterisation and comparison with observations*. Tech. rep. 286. Hamburg, DE: Max-Planck-Institut für Meteorologie, 39.

Lamsal, L. N., R. V. Martin, A. van Donkelaar, M. Steinbacher, E. A. Celarier, E. Bucsela, E. J. Dunlea, and J. P. Pinto (2008). "Ground-level nitrogen dioxide concentrations inferred from the satellite-borne Ozone Monitoring Instrument". *Journal of Geophysical Research* 113.D16, D16308. DOI: 10.1029/2007JD009235.

Lamsal, L. N., R. V. Martin, A. Padmanabhan, A. van Donkelaar, Q. Zhang, C. E. Sioris, K. Chance, T. P. Kurosu, and M. J. Newchurch (2011). "Application of satellite observations for timely updates to global anthropogenic NOx emission inventories". *Geophysical Research Letters* 38.5, 1–5. DOI: 10.1029/2010GL046476.

Lamsal, L. N., R. V. Martin, A. Van Donkelaar, E. A. Celarier, E. J. Bucsela, K. F. Boersma, R. Dirksen, C. Luo, and Y. Wang (2010). "Indirect validation of tropospheric nitrogen dioxide retrieved from the OMI satellite instrument: Insight into the seasonal variation of nitrogen oxides at northern midlatitudes". *Journal of Geophysical Research Atmospheres* 115.5, 1–15. DOI: 10.1029/2009JD013351.

Lathière, J., D. A. Hauglustaine, N. De Noblet-Ducoudré, G. Krinner, and G. A. Folberth (2005). "Past and future changes in biogenic volatile organic compound emissions simulated with a global dynamic vegetation model". *Geophysical Research Letters* 32.20, 1–4. DOI: 10.1029/2005GL024164.

Launiainen, S., G. G. Katul, T. Grönholm, and T. Vesala (2013). "Partitioning ozone fluxes between canopy and forest floor by measurements and a multi-layer model". *Agricultural and Forest Meteorology* 173, 85–99. DOI: dx.doi.org/10.1016/j.agrformet.2012.12.009.

Lelieveld, J., J. S. Evans, M. Fnais, D. Giannadaki, and A. Pozzer (2015). "The contribution of outdoor air pollution sources to premature mortality on a global scale". *Nature* 525.7569, 367–371. DOI: 10.1038/nature15371.

Lelieveld, J. and F. J. Dentener (2000). "What controls tropospheric ozone?" *Journal of Geophysical Research Atmospheres* 105.D3, 3531–3551. DOI: 10.1029/1999JD901011.

Levelt, P. F., G. H. J. den Oord, M. R. Dobber, A. Malkki, H. Visser, J. de Vries, P. Stammes, J. O. V. Lundell, and H. Saari (2006). "The Ozone Monitoring Instrument". *IEEE Transactions on Geoscience and Remote Sensing* 44.5, 1093–1101. DOI: 10.1109/Tgrs.2006.872333.

Li, J. and Y. Wang (2019). "Inferring the anthropogenic NOx emission trend over the United States during 2003-2017 from satellite observations: Was there a flattening of the emission tend after the Great Recession?" *Atmospheric Chemistry and Physics Discussions* July, 1–35. DOI: 10.5194/acp-2019-472.

Li, J., Y. Wang, and H. Qu (2019). "Dependence of Summertime Surface Ozone on NOx and VOC Emissions Over the United States: Peak Time and Value". *Geophysical Research Letters* 46.6, 3540–3550. DOI: 10.1029/2018GL081823.

Lin, M., L. W. Horowitz, Y. Xie, F. Paulot, S. Malyshev, E. Shevliakova, A. Finco, G. Gerosa, D. Kubistin, and K. Pilegaard (2020). "Vegetation feedbacks during drought exacerbate ozone air pollution extremes in Europe". *Nature Climate Change* 10.May. DOI: `10.1038/s41558-020-0743-y`.

Lin, M., S. Malyshev, E. Shevliakova, F. Paulot, L. W. Horowitz, S. Fares, T. N. Mikkelsen, and L. Zhang (2019). "Sensitivity of Ozone Dry Deposition to Ecosystem-Atmosphere Interactions: A Critical Appraisal of Observations and Simulations". *Global Biogeochemical Cycles* 33.10, 1264–1288. DOI: `10.1029/2018GB006157`.

Lombardozzi, D., J. P. Sparks, and G. B. Bonan (2013). "Integrating O3 influences on terrestrial processes: photosynthetic and stomatal response data available for regional and global modeling". *Biogeosciences* 10.11, 6815–6831. DOI: `10.5194/bg-10-6815-2013`.

Lombardozzi, D., S. Levis, G. Bonan, P. G. Hess, and J. P. Sparks (2015). "The influence of chronic ozone exposure on global carbon and water cycles". *Journal of Climate* 28.1, 292–305. DOI: `10.1175/JCLI-D-14-00223.1`.

Lorente, A., K. F. Boersma, H. J. Eskes, J. P. Veefkind, J. H. van Geffen, M. B. de Zeeuw, H. A. Denier van der Gon, S. Beirle, and M. C. Krol (2019). "Quantification of nitrogen oxides emissions from build-up of pollution over Paris with TROPOMI". *Scientific Reports* 9.1, 1–10. DOI: `10.1038/s41598-019-56428-5`.

Lorente, A., K. Folkert Boersma, H. Yu, S. Dörner, A. Hilboll, A. Richter, M. Liu, L. N. Lamsal, M. Barkley, I. De Smedt, M. Van Roozendael, Y. Wang, T. Wagner, S. Beirle, J. T. Lin, N. Krotkov, P. Stammes, P. Wang, H. J. Eskes, and M. Krol (2017). "Structural uncertainty in air mass factor calculation for NO2 and HCHO satellite retrievals". *Atmospheric Measurement Techniques* 10.3, 759–782. DOI: `10.5194/amt-10-759-2017`.

Lu, X., X. Ye, M. Zhou, Y. Zhao, H. Weng, H. Kong, K. Li, M. Gao, B. Zheng, J. Lin, F. Zhou, Q. Zhang, D. Wu, L. Zhang, and Y. Zhang (2021). "The underappreciated role of agricultural soil nitrogen oxide emissions in ozone pollution regulation in North China". *Nature Communications* 12.1. DOI: `10.1038/s41467-021-25147-9`.

Ma, J. and S. M. Daggupaty (2000). "Effective dry deposition velocities for gases and particles over heterogeneous terrain". *Journal of Applied Meteorology* 39.8, 1379–1390. DOI: `10.1175/1520-0450(2000)039<1379:EDDVFG>2.0.CO;2`.

Maasakkers, J. D. (2013). *Vital improvements to the retrieval of tropospheric NO 2 columns from the Ozone Monitoring Instrument (MSc thesis)*. Eindhoven (NL), 67.

El-Madany, T. S., K. Niklasch, and O. Klemm (2017). "Stomatal and non-stomatal turbulent deposition flux of ozone to a managed peatland". *Atmosphere* 8.9, 1–16. DOI: `10.3390/atmos8090175`.

Makar, P. A., R. M. Staebler, A. Akingunola, J. Zhang, C. McLinden, S. K. Kharol, B. Pabla, P. Cheung, and Q. Zheng (2017). "The effects of forest canopy shading and turbulence on boundary layer ozone". *Nature Communications* 8.May, 1–14. DOI: `10.1038/ncomms15243`.

Mammarella, I., O. Peltola, A. Nordbo, and L. Järvi (2016). "Quantifying the uncertainty of eddy covariance fluxes due to the use of different software packages and combinations of processing steps in two contrasting ecosystems". *Atmospheric Measurement Techniques* 9.10, 4915–4933. DOI: 10.5194/amt-9-4915-2016.

Mar, K. A., N. Ojha, A. Pozzer, and T. M. Butler (2016). "Ozone air quality simulations with WRF-Chem (v3.5.1) over Europe : model evaluation and chemical mechanism comparison". *Geoscientific Model Development* 9, 3699–3728. DOI: 10.5194/gmd-9-3699-2016.

Marécal, V., V. H. Peuch, C. Andersson, S. Andersson, J. Arteta, M. Beekmann, A. Benedictow, R. Bergström, B. Bessagnet, A. Cansado, F. Chéroux, A. Colette, A. Coman, R. L. Curier, H. A. Van Der Gon, A. Drouin, H. Elbern, E. Emili, R. J. Engelen, H. J. Eskes, G. Foret, E. Friese, M. Gauss, C. Giannaros, J. Guth, M. Joly, E. Jaumouillé, B. Josse, N. Kadygrov, J. W. Kaiser, K. Krajsek, J. Kuenen, U. Kumar, N. Liora, E. Lopez, L. Malherbe, I. Martinez, D. Melas, F. Meleux, L. Menut, P. Moinat, T. Morales, J. Parmentier, A. Piacentini, M. Plu, A. Poupkou, S. Queguiner, L. Robertson, L. Rouïl, M. Schaap, A. Segers, M. Sofiev, L. Tarasson, M. Thomas, R. Timmermans, Valdebenito, P. Van Velthoven, R. Van Versendaal, J. Vira, and A. Ung (2015). "A regional air quality forecasting system over Europe: The MACC-II daily ensemble production". *Geoscientific Model Development* 8.9, 2777–2813. DOI: 10.5194/gmd-8-2777-2015.

Martin, R., D. Jacob, K. Chance, T. P. Kurosu, P. I. Palmer, and M. J. Evans (2003). "Global inventory of nitrogen oxide emissions constrained by space-based observations of NO2 columns". *Journal of Geophysical Research* 108.D17, 1–12. DOI: 10.1029/2003JD003453.

Matyssek, R., G. Wieser, A. J. Nunn, A. R. Kozovits, I. M. Reiter, C. Heerdt, J. B. Winkler, M. Baumgarten, K. H. Häberle, T. E. Grams, H. Werner, P. Fabian, and W. M. Havranek (2004). "Comparison between AOT40 and ozone uptake in forest trees of different species, age and site conditions". *Atmospheric Environment* 38.15, 2271–2281. DOI: 10.1016/j.atmosenv.2003.09.078.

Millán, M. M., R. Salvador, E. Mantilla, and G. Kallos (1997). "Photooxidant dynamics in the Mediterranean basin in summer: Results from European research projects". *Journal of Geophysical Research: Atmospheres* 102.D7, 8811–8823. DOI: 10.1029/96JD03610.

Mills, G., F. Hayes, D. Simpson, L. Emberson, D. Norris, H. Harmens, and P. Büker (2011a). "Evidence of widespread effects of ozone on crops and (semi-)natural vegetation in Europe (1990-2006) in relation to AOT40- and flux-based risk maps". *Global Change Biology* 17.1, 592–613. DOI: 10.1111/j.1365-2486.2010.02217.x.

Mills, G., H. Pleijel, S. Braun, P. Büker, V. Bermejo, E. Calvo, H. Danielsson, L. Emberson, I. G. Fernández, L. Grünhage, H. Harmens, F. Hayes, P. E. Karlsson, and D. Simpson (2011b). "New stomatal flux-based critical levels for ozone effects on vegetation". *Atmospheric Environment* 45.28, 5064–5068. DOI: 10.1016/j.atmosenv.2011.06.009.

Mills, G., H. Pleijel, C. S. Malley, B. Sinha, O. R. Cooper, M. G. Schultz, H. S. Neufeld, D. Simpson, K. Sharps, Z. Feng, G. Gerosa, H. Harmens, K. Kobayashi, P. Saxena, E. Paoletti, V. Sinha, and X. Xu (2018). "Tropospheric Ozone Assessment Report: Present-day tropospheric ozone distribution and trends relevant to vegetation". *Elementa Science of the Anthropocene* 6.1, 47. DOI: 10.1525/elementa.302.

Miyazaki, K., H. J. Eskes, K. Sudo, and C. Zhang (2014). "Global lightning NOx production estimated by an assimilation of multiple satellite data sets". *Atmospheric Chemistry and Physics* 14.7, 3277–3305. DOI: 10.5194/acp-14-3277-2014.

Miyazaki, K., H. Eskes, K. Sudo, K. Folkert Boersma, K. Bowman, and Y. Kanaya (2017). "Decadal changes in global surface NOx emissions from multi-constituent satellite data assimilation". *Atmospheric Chemistry and Physics* 17.2, 807–837. DOI: 10.5194/acp-17-807-2017.

Mölder, M., A. Grelle, A. Lindroth, and S. Halldin (1999). "Flux-profile relationships over a boreal forest - Roughness sublayer corrections". *Agricultural and Forest Meteorology* 98-99, 645–658. DOI: 10.1016/S0168-1923(99)00131-8.

Monteith, J. (1965). "Evaporation and Environment". *Symposia of the Society for Experimental Biology* 19, 205–234.

Morrison, H., G. Thompson, and V. Tatarskii (2009). "Impact of Cloud Microphysics on the Development of Trailing Stratiform Precipitation in a Simulated Squall Line: Comparison of One- and Two-Moment Schemes". *Monthly Weather Review* 137.3, 991–1007. DOI: 10.1175/2008MWR2556.1.

Musselman, R. C., A. S. Lefohn, W. J. Massman, and R. L. Heath (2006). "A critical review and analysis of the use of exposure- and flux-based ozone indices for predicting vegetation effects". *Atmospheric Environment* 40.10, 1869–1888. DOI: 10.1016/j.atmosenv.2005.10.064.

Nakanasi, M. and H. Niino (2009). "Development of an improved turbulence closure model for the atmospheric boundary layer". *Journal of the Meteorological Society of Japan* 87.5, 895–912. DOI: 10.2151/jmsj.87.895.

Nakanishi, M. and H. Niino (2006). "An improved Mellor-Yamada Level-3 model: Its numerical stability and application to a regional prediction of advection fog". *Boundary-Layer Meteorology* 119.2, 397–407. DOI: 10.1007/s10546-005-9030-8.

Neirynck, J., B. Gielen, I. a. Janssens, and R. Ceulemans (2012). "Insights into ozone deposition patterns from decade-long ozone flux measurements over a mixed temperate forest." *Journal of Environmental Monitoring* 14.6, 1684–95. DOI: 10.1039/c2em10937a.

Nuvolone, D., D. Petri, and F. Voller (2018). "The effects of ozone on human health". *Environmental Science and Pollution Research* 25.9, 8074–8088. DOI: 10.1007/s11356-017-9239-3.

Oikawa, P. Y., C. Ge, J. Wang, J. R. Eberwein, L. L. Liang, L. A. Allsman, D. A. Grantz, and G. D. Jenerette (2015). "Unusually high soil nitrogen oxide emissions influence air quality in a high-temperature agricultural region". *Nature Communications* 6. DOI: 10.1038/ncomms9753.

Oikonomakis, E., S. Aksoyoglu, G. Ciarelli, U. Baltensperger, and A. S. H. Prévôt (2018). "Low modeled ozone production suggests underestimation of precursor emissions (especially NOx) in Europe". *Atmospheric Chemistry and Physics* 18.3, 2175–2198. DOI: 10.5194/acp-18-2175-2018.

Oliver, R. J., L. M. Mercado, S. Sitch, D. Simpson, B. E. Medlyn, Y. S. Lin, and G. A. Folberth (2018). "Large but decreasing effect of ozone on the European carbon sink". *Biogeosciences* 15.13, 4245–4269. DOI: 10.5194/bg-15-4245-2018.

Ott, L. E., K. E. Pickering, G. L. Stenchikov, D. J. Allen, A. J. DeCaria, B. Ridley, R.-F. Lin, S. Lang, and W.-K. Tao (2010). "Production of lightning NOx and its vertical distribution calculated from three-dimensional cloud-scale chemical transport model simulations". *Journal of Geophysical Research* 115.D4, D04301. DOI: 10.1029/2009JD011880.

Otu-Larbi, F., A. Conte, S. Fares, O. Wild, and K. Ashworth (2020). "Current and future impacts of drought and ozone stress on Northern Hemisphere forests". *Global Change Biology* 26.11, 6218–6234. DOI: 10.1111/gcb.15339.

– (2021). "FORCAsT-gs: Importance of Stomatal Conductance Parameterization to Estimated Ozone Deposition Velocity". *Journal of Advances in Modeling Earth Systems* 13.9, 1–23. DOI: 10.1029/2021MS002581.

Ouwersloot, H. G., J. Vilà-Guerau De Arellano, C. C. Van Heerwaarden, L. N. Ganzeveld, M. C. Krol, and J. Lelieveld (2011). "On the segregation of chemical species in a clear boundary layer over heterogeneous land surfaces". *Atmospheric Chemistry and Physics* 11.20, 10681–10704. DOI: 10.5194/acp-11-10681-2011.

Patton, E. G., P. P. Sullivan, and C. H. Moeng (2005). "The influence of idealized heterogeneity on wet and dry planetary boundary layers coupled to the land surface". *Journal of the Atmospheric Sciences* 62.7, 2078–2097. DOI: 10.1175/JAS3465.1.

Patton, E. G., P. P. Sullivan, R. H. Shaw, J. J. Finnigan, and J. C. Weil (2016). "Atmospheric stability influences on coupled boundary layer and canopy turbulence". *Journal of the Atmospheric Sciences* 73.4, 1621–1647. DOI: 10.1175/JAS-D-15-0068.1.

Pedruzo-Bagazgoitia, X., E. G. Patton, A. F. Moene, H. G. Ouwersloot, T. Gerken, L. Machado, S. Martin, M. Sörgel, P. Stoy, M. Yamsoe, and J. Vila-Guerau De Arellano (2022). "Investigating the diurnal radiative, turbulent and biophyiscal processes in the Amazonian canopy-atmosphere interface by combining LES simulations and observations". *Under review*.

Pfister, G. G., S. D. Eastham, A. F. Arellano, B. Aumont, K. C. Barsanti, M. C. Barth, A. Conley, N. A. Davis, L. K. Emmons, J. D. Fast, A. M. Fiore, B. Gaubert, S. Goldhaber, C. Granier, G. A. Grell, M. Guevara, D. K. Henze, A. Hodzic, X. Liu, D. R. Marsh,

J. J. Orlando, J. M. Plane, L. M. Polvani, K. H. Rosenlof, A. L. Steiner, D. J. Jacob, and G. P. Brasseur (2020). "The multi-scale infrastructure for chemistry and aerosols (MUSICA)". *Bulletin of the American Meteorological Society* 101.10, E1743–E1760. DOI: `10.1175/BAMS-D-19-0331.1`.

Pickering, K. E., E. Bucsela, D. Allen, A. Ring, R. Holzworth, and N. Krotkov (2016). "Estimates of lightning NOx production based on OMI NO2 observations over the Gulf of Mexico". *Journal of Geophysical Research* 121.14, 8668–8691. DOI: `10.1002/2015JD024179`.

Pilegaard, K., U. Skiba, P. Ambus, C. Beier, N. Brüggemann, K. Butterbach-Bahl, J. Dick, J. Dorsey, J. Duyzer, M. Gallagher, R. Gasche, L. Horvath, B. Kitzler, A. Leip, M. K. Pihlatie, P. Rosenkranz, G. Seufert, T. Vesala, H. Westrate, and S. Zechmeister-Boltenstern (2006). "Factors controlling regional differences in forest soil emission of nitrogen oxides (NO and N2O)". *Biogeosciences* 3.4, 651–661. DOI: `10.5194/bg-3-651-2006`.

Pincus, R., E. J. Mlawer, and J. S. Delamere (2019). "Balancing Accuracy, Efficiency, and Flexibility in Radiation Calculations for Dynamical Models". *Journal of Advances in Modeling Earth Systems* 11.10, 3074–3089. DOI: `10.1029/2019MS001621`.

Pleim, J. and L. Ran (2011). "Surface flux modeling for air quality applications". *Atmosphere* 2.3, 271–302. DOI: `10.3390/atmos2030271`.

Pope, R. J., M. P. Chipperfield, N. H. Savage, C. Ordóñez, L. S. Neal, L. A. Lee, S. S. Dhomse, and N. A. D. Richards (2015). "Evaluation of a regional air quality model using satellite column NO2: treatment of observation errors and model boundary conditions and emissions". *Atmospheric Chemistry and Physics* 15, 5611–5626. DOI: `10.5194/acp-15-5611-2015`.

Potier, E., J. Ogée, J. Jouanguy, E. Lamaud, P. Stella, E. Personne, B. Durand, N. Mascher, and B. Loubet (2015). "Multilayer modelling of ozone fluxes on winter wheat reveals large deposition on wet senescing leaves". *Agricultural and Forest Meteorology* 211-212, 58–71. DOI: `10.1016/j.agrformet.2015.05.006`.

Pouliot, G., H. A. Denier van der Gon, J. Kuenen, J. Zhang, M. D. Moran, and P. A. Makar (2015). "Analysis of the emission inventories and model-ready emission datasets of Europe and North America for phase 2 of the AQMEII project". *Atmospheric Environment* 115, 345–360. DOI: `10.1016/j.atmosenv.2014.10.061`.

Price, C. and D. Rind (1993). "What determines the cloud-to-ground lightning fraction in thunderstorms?" *Geophysical Research Letters* 20.6, 463–466. DOI: `https://doi.org/10.1029/93GL00226`.

Pusede, S. E., A. L. Steiner, and R. C. Cohen (2015). "Temperature and Recent Trends in the Chemistry of Continental Surface Ozone". *Chemical Reviews* 115.10, 3898–3918. DOI: `10.1021/cr5006815`.

Querol, X., G. Gangoiti, E. Mantilla, A. Alastuey, M. C. Minguillón, F. Amato, C. Reche, M. Viana, T. Moreno, A. Karanasiou, I. Rivas, N. Pérez, A. Ripoll, M. Brines, M. Ealo, M. Pandolfi, H. K. Lee, H. R. Eun, Y. H. Park, M. Escudero, D. Beddows, R. M. Harrison, A. Bertrand, N. Marchand, A. Lyasota, B. Codina, M. Olid, M. Udina, B. Jiménez-Esteve, B. B. Jiménez-Esteve, L. Alonso, M. Millán, and K. H. Ahn (2017). "Phenomenology of high-ozone episodes in NE Spain". *Atmospheric Chemistry and Physics* 17.4, 2817–2838. DOI: `10.5194/acp-17-2817-2017`.

Rannik, Ü., N. Altimir, I. Mammarella, J. Bäck, J. Rinne, T. M. Ruuskanen, P. Hari, T. Vesala, and M. Kulmala (2012). "Ozone deposition into a boreal forest over a decade of observations: Evaluating deposition partitioning and driving variables". *Atmospheric Chemistry and Physics* 12.24, 12165–12182. DOI: `10.5194/acp-12-12165-2012`.

Raoult, N. M., T. E. Jupp, P. M. Cox, and C. M. Luke (2016). "Land-surface parameter optimisation using data assimilation techniques: The adJULES system V1.0". *Geoscientific Model Development* 9.8, 2833–2852. DOI: `10.5194/gmd-9-2833-2016`.

Rasool, Q. Z., J. O. Bash, and D. S. Cohan (2019). "Mechanistic representation of soil nitrogen emissions in the Community Multiscale Air Quality (CMAQ) model v 5.1". *Geoscientific Model Development* 12.2, 849–878. DOI: `10.5194/gmd-12-849-2019`.

Rasool, Q. Z., R. Zhang, B. Lash, D. S. Cohan, E. J. Cooter, J. O. Bash, and L. N. Lamsal (2016). "Enhanced representation of soil NO emissions in the Community Multiscale Air Quality (CMAQ) model version 5.0.2". *Geoscientific Model Development* 9.9, 3177–3197. DOI: `10.5194/gmd-9-3177-2016`.

Raupach, M. R. (1989). "A practical Lagrangian method for relating scalar concentrations to source distributions in vegetation canopies". *Quarterly Journal of the Royal Meteorological Society* 115.487, 609–632. DOI: `10.1002/qj.49711548710`.

Ražnjević, A., C. van Heerwaarden, B. van Stratum, A. Hensen, I. Velzeboer, P. van den Bulk, and M. Krol (2022). "Technical note: Interpretation of field observations of point-source methane plume using observation-driven large-eddy simulations". *Atmospheric Chemistry and Physics* 22, 6489–6505. DOI: `10.5194/acp-22-6489-2022`.

Renner, M., C. Brenner, K. Mallick, H. D. Wizemann, L. Conte, I. Trebs, J. Wei, V. Wulfmeyer, K. Schulz, and A. Kleidon (2019). "Using phase lags to evaluate model biases in simulating the diurnal cycle of evapotranspiration: A case study in Luxembourg". *Hydrology and Earth System Sciences* 23.1, 515–535. DOI: `10.5194/hess-23-515-2019`.

Riess, T. C. V. W., K. F. Boersma, J. Van Vliet, W. Peters, M. Sneep, H. Eskes, and J. Van Geffen (2022). "Improved monitoring of shipping NO2 with TROPOMI: Decreasing NOx emissions in European seas during the COVID-19 pandemic". *Atmospheric Measurement Techniques* 15.5, 1415–1438. DOI: `10.5194/amt-15-1415-2022`.

Ronda, R., H. De Bruin, and A. Holtslag (2001). "Representation of the canopy conductance in modeling the surface energy budget for low vegetation". *Journal of Applied Meteorology*

40, 1431–1444. DOI: `https://doi.org/10.1175/1520-0450(2001)040<1431:ROTCCI>2.0.CO;2`.

Rouïl, L. and F. Meleux (2018). *Annual Air Quality Assessment Report 2015*. Tech. rep. Copernicus Atmospheric Monitoring Service, 42.

Rummel, U., C. Ammann, G. A. Kirkman, M. A. Moura, T. Foken, M. O. Andreae, and F. X. Meixner (2007). "Seasonal variation of ozone deposition to a tropical rain forest in southwest Amazonia". *Atmospheric Chemistry and Physics* 7.20, 5415–5435. DOI: `10.5194/acp-7-5415-2007`.

Russell, A. R., A. E. Perring, L. C. Valin, E. J. Bucsela, E. C. Browne, P. J. Wooldridge, and R. C. Cohen (2011). "A high spatial resolution retrieval of NO2 column densities from OMI: Method and evaluation". *Atmospheric Chemistry and Physics* 11.16, 8543–8554. DOI: `10.5194/acp-11-8543-2011`.

Russell, E. S., H. Liu, H. Thistle, B. Strom, M. Greer, and B. Lamb (2018). "Effects of thinning a forest stand on sub-canopy turbulence". *Agricultural and Forest Meteorology* 248.January 2017, 295–305. DOI: `10.1016/j.agrformet.2017.10.019`.

Sadiq, M., A. P. K. Tai, D. Lombardozzi, and M. Val Martin (2017). "Effects of ozone-vegetation coupling on surface ozone air quality via biogeochemical and meteorological feedbacks". *Atmospheric Chemistry and Physics* 17, 3055–3066. DOI: `10.5194/acp-2016-642`.

Schaap, M., C. Cuvelier, C. Hendriks, B. Bessagnet, J. Baldasano, A. Colette, P. Thunis, D. Karam, H. Fagerli, A. Graff, R. Kranenburg, A. Nyiri, M. Pay, L. Rouïl, M. Schulz, D. Simpson, R. Stern, E. Terrenoire, and P. Wind (2015). "Performance of European chemistry transport models as function of horizontal resolution". *Atmospheric Environment* 112, 90–105. DOI: `10.1016/j.atmosenv.2015.04.003`.

Schumann, U. and H. Huntrieser (2007). "The global lightning-induced nitrogen oxides source". *Atmospheric Chemistry and Physics* 7.14, 3823–3907. DOI: `10.5194/acp-7-3823-2007`.

Sha, T., X. Ma, H. Zhang, N. Janechek, Y. Wang, Y. Wang, L. Castro García, G. D. Jenerette, and J. Wang (2021). "Impacts of Soil NOx Emission on O3 Air Quality in Rural California". *Environmental Science and Technology* 55.10, 7113–7122. DOI: `10.1021/acs.est.0c06834`.

Sillman, S., J. Logan, and S. Wofsy (1990). "The sensitivity of ozone to nitrogen oxides and hydrocarbons in regional ozone episodes". *Journal of Geophysical Research* 95.D2, 1837–1851. DOI: `10.1029/JD095iD02p01837`.

Sillman, S. (1999). "The relation between ozone, NOx and hydrocarbons in urban and polluted rural environments". *Atmospheric Environment* 33, 1821–1845. DOI: `10.1016/S1474-8177(02)80015-8`.

Silvern, R. F., D. J. Jacob, L. J. Mickley, M. P. Sulprizio, K. R. Travis, E. A. Marais, R. C. Cohen, J. L. Laughner, S. Choi, J. Joiner, and L. N. Lamsal (2019). "Using satellite observations of tropospheric NO 2 columns to infer long-term trends in US NO x emissions: the importance of accounting for the free tropospheric NO 2 background". *Atmos. Chem. Phys. Discuss.* 2. DOI: `10.5194/acp-2019-168`.

Simpson, D. and S. Darras (2021). "Global soil NO emissions for Atmospheric Chemical Transport Modelling: CAMS-GLOB-SOIL v2.2". *Earth System Science Data Discussions*, 1–35. DOI: `10.5194/essd-2021-221`.

Sindelarova, K., C. Granier, I. Bouarar, A. Guenther, S. Tilmes, T. Stavrakou, J.-F. Müller, U. Kuhn, P. Stefani, and W. Knorr (2014). "Global data set of biogenic VOC emissions calculated by the MEGAN model over the last 30 years". *Atmospheric Chemistry and Physics* 14.17, 9317–9341. DOI: `10.5194/acp-14-9317-2014`.

Sindelarova, K., J. Markova, D. Simpson, P. Huszar, J. Karlicky, S. Darras, and C. Granier (2022). "High-resolution biogenic global emission inventory for the time period 2000-2019 for air quality modelling". *Earth System Science Data* 14.1, 251–270. DOI: `10.5194/essd-14-251-2022`.

Sitch, S., P. M. Cox, W. J. Collins, and C. Huntingford (2007). "Indirect radiative forcing of climate change through ozone effects on the land-carbon sink." *Nature* 448.August, 791–794. DOI: `10.1038/nature06059`.

Skiba, U., S. Medinets, L. M. Cardenas, E. J. Carnell, N. J. Hutchings, and B. Amon (2021). "Assessing the contribution of soil NOxemissions to European atmospheric pollution". *Environmental Research Letters* 16.2. DOI: `10.1088/1748-9326/abd2f2`.

Solazzo, E., R. Bianconi, R. Vautard, K. W. Appel, M. Moran, C. Hogrefe, B. Bessagnet, J. Brandt, J. H. Christensen, C. Chemel, I. Coll, H. Denier van der Gon, J. Ferreira, R. Forkel, X. V. Francis, G. Grell, P. Grossi, A. B. Hansen, A. Jeričević, L. Kraljević, A. I. Miranda, U. Nopmongcol, G. Pirovano, M. Prank, A. Riccio, K. N. Sartelet, M. Schaap, J. D. Silver, R. S. Sokhi, J. Vira, J. Werhahn, R. Wolke, G. Yarwood, J. Zhang, T. S. Rao, and S. Galmarini (2012). "Model evaluation and ensemble modelling of surface-level ozone in Europe and North America in the context of AQMEII". *Atmospheric Environment* 53, 60–74. DOI: `10.1016/j.atmosenv.2012.01.003`.

Stavrakou, T., K. F. Boersma, R. J. van der A, Q. Zhang, T. Ohara, J. Kurokawa, and J.-F. Müller (2013). "Key chemical NOx sink uncertainties and how they influence top-down emissions of nitrogen oxides". *Atmospheric Chemistry and Physics* 13.17, 9057–9082. DOI: `10.5194/acp-13-9057-2013`.

Steeneveld, G. (2002). "On photosynthesis parameters for the A-gs surface scheme for high vegetation". March, 1–79.

Steinbacher, M., C. Zellweger, B. Schwarzenbach, S. Bugmann, B. Buchmann, C. Ordóñez, A. S. Prevot, and C. Hueglin (2007). "Nitrogen oxide measurements at rural sites in

Switzerland: Bias of conventional measurement techniques". *Journal of Geophysical Research Atmospheres* 112.11, 1–13. DOI: 10.1029/2006JD007971.

Steiner, A. L., S. N. Pressley, A. Botros, E. Jones, S. H. Chung, and S. L. Edburg (2011). "Analysis of coherent structures and atmosphere-canopy coupling strength during the CABINEX field campaign". *Atmospheric Chemistry and Physics* 11.23, 11921–11936. DOI: 10.5194/acp-11-11921-2011.

Steinkamp, J. and M. G. Lawrence (2011). "Improvement and evaluation of simulated global biogenic soil NO emissions in an AC-GCM". *Atmospheric Chemistry and Physics* 11.12, 6063–6082. DOI: 10.5194/acp-11-6063-2011.

Stella, P., B. Loubet, C. de Berranger, X. Charrier, E. Ceschia, G. Gerosa, A. Finco, E. Lamaud, D. Serça, C. George, and R. Ciuraru (2019). "Soil ozone deposition: Dependence of soil resistance to soil texture". *Atmospheric Environment* 199.July 2018, 202–209. DOI: 10.1016/j.atmosenv.2018.11.036.

Stella, P., B. Loubet, E. Lamaud, P. Laville, and P. Cellier (2011). "Ozone deposition onto bare soil: A new parameterisation". *Agricultural and Forest Meteorology* 151.6, 669–681. DOI: 10.1016/j.agrformet.2011.01.015.

Stohl, A., E. Williams, G. Wotawa, and H. Kromp-Kolb (1996). "A European inventory of soil nitric oxide emissions and the effect of these emissions on the photochemical formation of ozone". *Atmospheric Environment* 30.22, 3741–3755. DOI: 10.1016/1352-2310(96)00104-5.

Tai, A. P. K., M. V. Martin, and C. L. Heald (2014). "Threat to future global food security from climate change and ozone air pollution". *Nature Climate Change* 4.September, 817–821. DOI: 10.1038/nclimate2317.

Tarasick, D., I. E. Galbally, O. R. Cooper, M. G. Schultz, G. Ancellet, T. Leblanc, T. J. Wallington, J. Ziemke, X. Liu, M. Steinbacher, J. Staehelin, C. Vigouroux, J. W. Hannigan, O. García, G. Foret, P. Zanis, E. Weatherhead, I. Petropavlovskikh, H. Worden, M. Osman, J. Liu, K. L. Chang, A. Gaudel, M. Lin, M. Granados-Muñoz, A. M. Thompson, S. J. Oltmans, J. Cuesta, G. Dufour, V. Thouret, B. Hassler, T. Trickl, and J. L. Neu (2019). "Tropospheric ozone assessment report: Tropospheric ozone from 1877 to 2016, observed levels, trends and uncertainties". *Elementa: Science of the Anthropocene* 7. DOI: 10.1525/elementa.376.

Tawfik, A. B. and A. L. Steiner (2013). "A proposed physical mechanism for ozone-meteorology correlations using land-atmosphere coupling regimes". *Atmospheric Environment* 72, 50–59. DOI: 10.1016/j.atmosenv.2013.03.002.

Terrenoire, E., B. Bessagnet, L. Rouïl, F. Tognet, G. Pirovano, L. Létinois, M. Beauchamp, A. Colette, and P. T. Alata (2015). "High-resolution air quality simulation over Europe with the chemistry transport model CHIMERE". *Geoscientific Model Development* 8, 21–42. DOI: 10.5194/gmd-8-21-2015.

Tetzlaff, G., R. Dlugi, K. Friedrich, G. Gross, D. Hinneburg, U. Pahl, M. Zelger, and N. Mölders (2002). "On modeling dry deposition of long-lived and chemically reactive species over heterogeneous terrain". *Journal of Atmospheric Chemistry* 42.1, 123–155. DOI: 10.1023/A:1015740203204.

Tewari, M., F. Chen, W. Wang, J. Dudhia, M. A. Lemone, K. Mitchell, M. Ek, G. Gayno, J. Wegiel, and R. H. Cuenca (2004). "Implementation and verification of the Unified Noah Land Surface model in the WRF model". In: *20th conference on weather analysis and forecasting/16th conference on numerical weather prediction*, 11–15. DOI: 10.1007/s11269-013-0452-7.

Thomas, C. and T. Foken (2007). "Flux contribution of coherent structures and its implications for the exchange of energy and matter in a tall spruce canopy". *Boundary-Layer Meteorology* 123.2, 317–337. DOI: 10.1007/s10546-006-9144-7.

Tie, X., S. Madronich, S. Walters, R. Zhang, P. J. Rasch, and W. J. Collins (2003). "Effect of clouds on photolysis and oxidants in the troposphere". *Journal of Geophysical Research* 108.D20. DOI: 10.1029/2003JD003659.

Travis, K. R. and D. J. Jacob (2019). "Systematic bias in evaluating chemical transport models with maximum daily 8-hour average (MDA8) surface ozone for air quality applications". *Geoscientific Model Development* 12, 3641–3648. DOI: 10.5194/gmd-12-3641-2019.

Tuccella, P., G. Curci, G. Visconti, B. Bessagnet, L. Menut, and R. J. Park (2012). "Modeling of gas and aerosol with WRF/Chem over Europe: Evaluation and sensitivity study". *Journal of Geophysical Research Atmospheres* 117.3, 1–15. DOI: 10.1029/2011JD016302.

Twine, T. E., W. P. Kustas, J. M. Norman, D. R. Cook, P. R. Houser, T. P. Meyers, J. H. Prueger, P. J. Starks, and M. L. Wesely (2000). "Correcting eddy-covariance flux underestimates over a grassland". *Agricultural and Forest Meteorology* 103.3, 279–300. DOI: 10.1016/S0168-1923(00)00123-4.

Val Martin, M., C. L. Heald, and S. R. Arnold (2014). "Coupling dry deposition to vegetation phenology in the Community Earth System Model: Implications for the simulation of surface O3". *Geophysical Research Letters* 41.8, 2988–2996. DOI: 10.1002/2014GL059651.

Valin, L. C., A. R. Russell, R. C. Hudman, and R. C. Cohen (2011). "Effects of model resolution on the interpretation of satellite NO2 observations". *Atmospheric Chemistry and Physics* 11.22, 11647–11655. DOI: 10.5194/acp-11-11647-2011.

Van den Hurk, B., P. Viterbo, A. C. Beljaars, and A. Betts (2000). *Offline validation of the ERA40 surface scheme*. Tech. rep. Reading, United Kingdom: European Centre for Medium-Range Weather Forecasts, 42. DOI: 10.21957/9aoaspz8.

Van Dingenen, R., F. J. Dentener, F. Raes, M. C. Krol, L. Emberson, and J. Cofala (2009). "The global impact of ozone on agricultural crop yields under current and future

air quality legislation". *Atmospheric Environment* 43.3, 604–618. DOI: `10.1016/j.atmosenv.2008.10.033`.

Van Heerwaarden, C. C., J. P. Mellado, and A. de Lozar (2014). "Scaling laws for the heterogeneously heated free convective boundary layer". *Journal of the Atmospheric Sciences* 71.11, 3975–4000. DOI: `10.1175/JAS-D-13-0383.1`.

Van Heerwaarden, C. C., B. J. Van Stratum, T. Heus, J. A. Gibbs, E. Fedorovich, and J. P. Mellado (2017). "MicroHH 1.0: A computational fluid dynamics code for direct numerical simulation and large-eddy simulation of atmospheric boundary layer flows". *Geoscientific Model Development* 10.8, 3145–3165. DOI: `10.5194/gmd-10-3145-2017`.

Van Pul, W. and A. Jacobs (1994). "The conductance of a maize crop and the underlying soil to ozone under various environmental conditions". *Boundary-Layer Meteorology* 69, 83–99.

Veefkind, J. P., I. Aben, K. McMullan, H. Förster, J. de Vries, G. Otter, J. Claas, H. J. Eskes, J. F. de Haan, Q. Kleipool, M. van Weele, O. Hasekamp, R. Hoogeveen, J. Landgraf, R. Snel, P. Tol, P. Ingmann, R. Voors, B. Kruizinga, R. Vink, H. Visser, and P. F. Levelt (2012). "TROPOMI on the ESA Sentinel-5 Precursor: A GMES mission for global observations of the atmospheric composition for climate, air quality and ozone layer applications". *Remote Sensing of Environment* 120.2012, 70–83. DOI: `10.1016/j.rse.2011.09.027`.

Veefkind, J. P., J. F. De Haan, M. Sneep, and P. F. Levelt (2016). "Improvements to the OMI O2-O2 operational cloud algorithm and comparisons with ground-based radar-lidar observations". *Atmospheric Measurement Techniques* 9.12, 6035–6049. DOI: `10.5194/amt-9-6035-2016`.

Vermeuel, M. P., P. A. Cleary, A. R. Desai, and T. H. Bertram (2021). "Simultaneous Measurements of O3 and HCOOH Vertical Fluxes Indicate Rapid In-Canopy Terpene Chemistry Enhances O3 Removal Over Mixed Temperate Forests". *Geophysical Research Letters* 48.3, 1–15. DOI: `10.1029/2020GL090996`.

Verstraeten, W. W., J. L. Neu, J. E. Williams, K. W. Bowman, J. R. Worden, and K. F. Boersma (2015). "Rapid increases in tropospheric ozone production and export from China". *Nature Geoscience* 8, 690–695. DOI: `10.1038/ngeo2493`.

Vicente-Serrano, S. M., S. Beguería, and J. I. López-Moreno (2010). "A multiscalar drought index sensitive to global warming: The standardized precipitation evapotranspiration index". *Journal of Climate* 23.7, 1696–1718. DOI: `10.1175/2009JCLI2909.1`.

Vila-Guerau De Arellano, J., P. G. Duynkerke, and P. J. Builtjes (1993). "The divergence of the turbulent diffusion flux in the surface layer due to chemical reactions: the NO-O3-NO2 system". *Tellus, Series B* 45 B.1, 23–33. DOI: `10.3402/tellusb.v45i1.15576`.

Vilà-Guerau De Arellano, J., P. Ney, O. Hartogensis, H. De Boer, K. Van Diepen, D. Emin, G. De Groot, A. Klosterhalfen, M. Langensiepen, M. Matveeva, G. Miranda-García, A. F. Moene, U. Rascher, T. Röckmann, G. Adnew, N. Brüggemann, Y. Rothfuss,

and A. Graf (2020). "CloudRoots: Integration of advanced instrumental techniques and process modelling of sub-hourly and sub-kilometre land-Atmosphere interactions". *Biogeosciences* 17.17, 4375–4404. DOI: 10.5194/bg-17-4375-2020.

Vilà-Guerau de Arellano, J., A. Talmon, and P. J. H. Builtjes (1990). *A chemically reactive plume model for the NO-NO2-O3 system*. DOI: 10.1016/0960-1686(90)90255-L.

Vinken, G. C. M., K. F. Boersma, A. van Donkelaar, and L. Zhang (2014a). "Constraints on ship NOx emissions in Europe using GEOS-Chem and OMI satellite NO2 observations". *Atmospheric Chemistry and Physics* 14, 1353–1369. DOI: 10.5194/acp-14-1353-2014.

Vinken, G. C. M., K. F. Boersma, J. D. Maasakkers, M. Adon, and R. V. Martin (2014b). "Worldwide biogenic soil NOx emissions inferred from OMI NO2 observations". *Atmospheric Chemistry and Physics* 14, 10363–10381. DOI: 10.5194/acp-14-10363-2014.

Vinken, G. C., K. F. Boersma, D. J. Jacob, and E. W. Meijer (2011). "Accounting for non-linear chemistry of ship plumes in the GEOS-Chem global chemistry transport model". *Atmospheric Chemistry and Physics* 11.22, 11707–11722. DOI: 10.5194/acp-11-11707-2011.

Vinuesa, J. F. and S. Galmarini (2009). "Turbulent dispersion of non-uniformly emitted passive tracers in the convective boundary layer". *Boundary-Layer Meteorology* 133.1, 1–16. DOI: 10.1007/s10546-009-9416-0.

Visser, A. J., K. F. Boersma, L. N. Ganzeveld, and M. C. Krol (2019). "European NOx emissions in WRF-Chem derived from OMI: impacts on summertime surface ozone". *Atmospheric Chemistry and Physics* 19.18, 11821–11841. DOI: 10.5194/acp-2019-295.

Visser, A. J., L. N. Ganzeveld, I. Goded, M. C. Krol, I. Mammarella, G. Manca, and K. F. Boersma (2021). "Ozone deposition impact assessments for forest canopies require accurate ozone flux partitioning on diurnal timescales". *Atmospheric Chemistry and Physics* 21.24, 18393–18411. DOI: 10.5194/acp-21-18393-2021.

Voogt, M., B. Van den Hurk, and C. Jacobs (2006). "The ECMWF land surface scheme extended with a photosynthesis and LAI module tested for a coniferous site". De Bilt, the Netherlands.

Vries, W. de, L. Schulte-Uebbing, H. Kros, J. C. Voogd, and G. Louwagie (2021). "Spatially explicit boundaries for agricultural nitrogen inputs in the European Union to meet air and water quality targets". *Science of the Total Environment* 786, 147283. DOI: 10.1016/j.scitotenv.2021.147283.

Wang, Y., C. Ge, L. Castro Garcia, G. D. Jenerette, P. Y. Oikawa, and J. Wang (2021). "Improved modelling of soil NO xemissions in a high temperature agricultural region: Role of background emissions on NO2trend over the US". *Environmental Research Letters* 16.8. DOI: 10.1088/1748-9326/ac16a3.

Wesely, M. L. (1989). "Parameterization of surface resistances to gaseous dry deposition in regional-scale numerical models". *Atmospheric Environment* 23.6, 1293–1304. DOI: `10.1016/j.atmosenv.2007.10.058`.

Wesely, M. L. and B. B. Hicks (1977). "Some factors that affect the deposition rates of sulfur dioxide and similar gases on vegetation". *Journal of the Air Pollution Control Association* 27.11, 1110–1116. DOI: `10.1080/00022470.1977.10470534`.

Wild, O. and M. J. Prather (2006). "Global tropospheric ozone modeling: Quantifying errors due to grid resolution". *Journal of Geophysical Research Atmospheres* 111.11, 1–14. DOI: `10.1029/2005JD006605`.

Williams, J. E., K. Folkert Boersma, P. Le Sager, and W. W. Verstraeten (2017). "The high-resolution version of TM5-MP for optimized satellite retrievals: Description and validation". *Geoscientific Model Development* 10.2, 721–750. DOI: `10.5194/gmd-10-721-2017`.

Willmott, C. (1982). "Some comments on the evaluation of model performance". *Bulletin of the American Meteorological Society* 63.11, 1309–1313. DOI: `10.1175/1520-0477(1982)063<1309:SCOTEO>2.0.CO;2`.

Wittig, V. E., E. A. Ainsworth, S. L. Naidu, D. F. Karnosky, and S. P. Long (2009). "Quantifying the impact of current and future tropospheric ozone on tree biomass, growth, physiology and biochemistry: A quantitative meta-analysis". *Global Change Biology* 15.2, 396–424. DOI: `10.1111/j.1365-2486.2008.01774.x`.

Wolfe, G. M., J. A. Thornton, M. McKay, and A. H. Goldstein (2011). "Forest-atmosphere exchange of ozone: Sensitivity to very reactive biogenic VOC emissions and implications for in-canopy photochemistry". *Atmospheric Chemistry and Physics* 11.15, 7875–7891. DOI: `10.5194/acp-11-7875-2011`.

Wong, A. Y., J. A. Geddes, J. A. Ducker, C. D. Holmes, S. Fares, A. H. Goldstein, I. Mammarella, and J. W. Munger (2022). "New Evidence for the Importance of Non-Stomatal Pathways in Ozone Deposition During Extreme Heat and Dry Anomalies". *Geophysical Research Letters* 49.8, 1–12. DOI: `10.1029/2021GL095717`.

Wong, J., M. C. Barth, and D. Noone (2013). "Evaluating a lightning parameterization based on cloud-top height for mesoscale numerical model simulations". *Geoscientific Model Development* 6.2, 429–443. DOI: `10.5194/gmd-6-429-2013`.

Wu, Z., D. B. Schwede, R. Vet, J. T. Walker, M. Shaw, R. Staebler, and L. Zhang (2018). "Evaluation and Intercomparison of Five North American Dry Deposition Algorithms at a Mixed Forest Site". *Journal of Advances in Modeling Earth Systems* 10.7, 1571–1586. DOI: `10.1029/2017MS001231`.

Wutzler, T., A. Lucas-Moffat, M. Migliavacca, J. Knauer, K. Sickel, L. Šigut, O. Menzer, and M. Reichstein (2018). "Basic and extensible post-processing of eddy covariance flux data with REddyProc". *Biogeosciences* 15.16, 5015–5030. DOI: `10.5194/bg-15-5015-2018`.

Xiao, Z., S. Liang, J. Wang, P. Chen, X. Yin, L. Zhang, and J. Song (2014). "Use of general regression neural networks for generating the GLASS leaf area index product from time-series MODIS surface reflectance". *IEEE Transactions on Geoscience and Remote Sensing* 52.1, 209–223. DOI: `10.1109/TGRS.2013.2237780`.

Yan, Y., A. Pozzer, N. Ojha, J. Lin, and J. Lelieveld (2018). "Analysis of European ozone trends in the period 1995-2014". *Atmospheric Chemistry and Physics* 18.8, 5589–5605. DOI: `10.5194/acp-18-5589-2018`.

Yanez-Serrano, A. M., A. Christine Nölscher, E. Bourtsoukidis, E. Gomes Alves, L. Ganzeveld, B. Bonn, S. Wolff, M. Sa, M. Yamasoe, J. Williams, and M. O. Andreae (2018). "Monoterpene chemical speciation in a tropical rainforest:variation with season, height, and time of dayat the Amazon Tall Tower Observatory (ATTO)". *Atmospheric Chemistry and Physics* 18.5, 3403–3418. DOI: `10.5194/acp-18-3403-2018`.

Yienger, J. and H. Levy (1995). "Empirical model of global soil-biogenic NOx emissions". *Journal of Geophysical Research* 100.D6, 447–458. DOI: `10.1029/95JD00370`.

Young, P. J., V. Naik, A. M. Fiore, A. Gaudel, J. Guo, M. Y. Lin, J. L. Neu, D. D. Parrish, H. E. Rieder, J. L. Schnell, S. Tilmes, O. Wild, L. Zhang, J. Ziemke, J. Brandt, A. Delcloo, R. M. Doherty, C. Geels, M. I. Hegglin, L. Hu, U. Im, R. Kumar, A. Luhar, L. Murray, D. Plummer, J. Rodriguez, A. Saiz-Lopez, M. G. Schultz, M. T. Woodhouse, and G. Zeng (2018). "Tropospheric ozone assessment report: Assessment of global-scale model performance for global and regional ozone distributions, variability, and trends". *Elementa: Science of the Anthropocene* 6. DOI: `10.1525/elementa.265`.

Zara, M., K. F. Boersma, I. De Smedt, A. Richter, E. Peters, J. H. Van Geffen, S. Beirle, T. Wagner, M. Van Roozendael, S. Marchenko, L. N. Lamsal, and H. J. Eskes (2018). "Improved slant column density retrieval of nitrogen dioxide and formaldehyde for OMI and GOME-2A from QA4ECV: Intercomparison, uncertainty characterisation, and trends". *Atmospheric Measurement Techniques* 11.7, 4033–4058. DOI: `10.5194/amt-11-4033-2018`.

Zara, M., K. F. Boersma, H. Eskes, H. Denier van der Gon, J. Vilà-Guerau de Arellano, M. Krol, E. van der Swaluw, W. Schuch, and G. J. Velders (2021). "Reductions in nitrogen oxides over the Netherlands between 2005 and 2018 observed from space and on the ground: Decreasing emissions and increasing O3 indicate changing NOx chemistry". *Atmospheric Environment: X* 9. DOI: `10.1016/j.aeaoa.2021.100104`.

Zaveri, R. and L. Peters (1999). "A new lumped structure photochemical mechanism for large-scale applications". eng. *Journal of Geophysical Research: Atmospheres* 104.D23, 30387–30415. DOI: `10.1029/1999JD900876`.

Zhang, L., J. R. Brook, and R. Vet (2003). "A revised parameterization for gaseous dry deposition in air-quality models". *Atmospheric Chemistry and Physics* 3.6, 2067–2082. DOI: `10.5194/acp-3-2067-2003`.

Zhang, L. and Z. Wu (2021). *A computer code for calculating dry deposition velocities for 45 gaseous species.* DOI: `https://doi.org/10.5281/zenodo.4697426`.

Zhang, L., J. R. Brook, and R. Vet (2002). "On ozone dry deposition - With emphasis on non-stomatal uptake and wet canopies". *Atmospheric Environment* 36.30, 4787–4799. DOI: `10.1016/S1352-2310(02)00567-8`.

Zhou, P., L. Ganzeveld, Ü. Rannik, L. Zhou, R. Gierens, D. Taipale, I. Mammarella, and M. Boy (2017). "Simulating ozone dry deposition at a boreal forest with a multi-layer canopy deposition model". *Atmospheric Chemistry and Physics* 17, 1361–1379. DOI: `10.5194/acp-2016-155`.

Zhou, Y., D. Brunner, C. Hueglin, S. Henne, and J. Staehelin (2012). "Changes in OMI tropospheric NO 2 columns over Europe from 2004 to 2009 and the in fl uence of meteorological variability". *Atmospheric Environment* 46.2, 482–495. DOI: `10.1016/j.atmosenv.2011.09.024`.

Acknowledgements

You have made it to the chapter of my PhD thesis that I looked forward to writing the most over the past years. A PhD project may seem like an individual journey, but it has rarely felt this way thanks to the amazing help of a support network consisting of supervisors, colleagues, friends and family. I would like to thank these people below.

Laurens, bedankt voor je geweldige steun tijdens mijn PhD. Je stond altijd open voor mijn goede ideeën en leverde geduldig feedback op mijn minder goede ideeën. Naast al je inhoudelijke ondersteuning verloor je ook nooit de menselijke kant van het onderzoek doen uit het oog. Op maandagochtend spraken we altijd eerst het weekend door en pas later de wetenschap (als daar überhaupt nog tijd voor over was). Als ik in een dipje zat, zoals tijdens het thuiswerken in de lockdowns, wist je me altijd weer te motiveren! Dat heeft me geweldig geholpen en daar ben ik je erg dankbaar voor.

Folkert, heel erg bedankt voor je hulp in de afgelopen jaren. Jouw wetenschappelijke drive en enthousiasme waren erg aanstekelijk. Je bent altijd op zoek naar een duidelijke boodschap om te communiceren in teksten, en van deze benadering van wetenschap heb ik veel geleerd. Ook heeft deze mentaliteit, samen met je scherpe tekstuele commentaar, de hoofdstukken in dit proefschrift sterk verbeterd. Ik vond het ook erg leuk hoe je me hebt betrokken als onderwijsassistent bij het Atmospheric Composition-vak. Daarnaast heb ik ook genoten van je oraties bij de koffieautomaat over de prestaties van Ajax, vooral in het geweldige Champions League-seizoen van 2018-2019.

Maarten, in het begin van mijn PhD was je meer op de achtergrond betrokken bij mijn onderzoek. Later kreeg je een prominentere rol in mijn promotietraject doordat je me vroeg om de stikstof-adviescommissie te ondersteunen. Bedankt voor deze kans! In de laatste maanden van mijn PhD hebben we samengewerkt aan het laatste inhoudelijke hoofdstuk van mijn proefschrift. Ondanks je drukke agenda was je altijd beschikbaar voor discussies over mijn resultaten en voor ondersteuning bij het LES-modelleren. Bedankt daarvoor!

Jordi, you were not directly involved in my PhD project but from the sideline you had a considerable influence on the contents of this thesis. I greatly enjoyed our discussions on turbulence and chemistry inside forest canopies, which sometimes felt more like private

lectures. Chapter 4 of this thesis strongly benefitted from these meetings. It was always a pleasure to discuss about other things as well, including the Dutch eating culture. I hope you're not too offended by my last proposition!

Tijdens het stikstofproject was het heel interessant en geweldig leerzaam om een kijkje in de keuken te kunnen nemen op het snijvlak van wetenschappelijk onderzoek en milieubeleid. Het was heel inspirerend om samen te werken met alle leden en het secretariaat van het Adviescollege Meten en Berekenen Stikstof, en in het bijzonder met Leen, Henk en Jelle. Veel dank daarvoor!

Aris and Lennart, you were some of the first friends I knew in Wageningen when I moved here at the start of my PhD, and I am very happy that you agreed to be my paranymphs. Aris, thanks for all the amazing discussions on our research and many other topics. I am very happy that we continue to meet up regularly for dinners and game nights even though you left MAQ some time ago. Lennart, thanks to your adventurous attitude towards life we went on many great trips together, from skiing in Austria to mountain biking on Tenerife. And thanks also for dragging me away from my computer in the final stages of my PhD to sample some obscure sour ales!

Doing a PhD at the MAQ group has been a great experience, because of the excellent science, diverse research topics within the group and above all the amazing social atmosphere. I greatly enjoyed the long lunch breaks, social gatherings and sports tournaments. Keep up the good work! Sandra and Reinder, thank you for the administrative and technical support. Oscar, thanks for asking me to join the field training course, the trips to Spain were a highlight of my PhD. Wouter, thank you for organizing many nice social gatherings in your house and garden. Bert, thank you for putting my mountain biking skills to the test.

The interaction with fellow PhDs at MAQ was one of the nicest part of my PhD. Thanks to Arjan, Alba, Imme and Stijn for being such nice colleagues in the first years of my PhD. Xabi, I have fond memories of organizing the hiring process for a new PFQ professor together. Ruben and Anja, thanks for being able to talk about the hardship of the final PhD stages: shared sorrow is halved! Sjoerd and Chris, it has been nice to be able to discuss more in-depth on ozone deposition and NO_2 remote sensing with you. Martin, it has always been a joy to talk about football, geoengineering and everything in between. Anne-Wil, Auke (hee Auke!), Kim, Mary Rose, Menno and Wouter, thanks for organizing the volleyball sessions in the past months, they were a very welcome distraction from thesis writing!

Naast alle collega's heb ik me ook geweldig gesteund gevoeld door mijn vriendengroep. Allereerst een shout-out naar Elwin, Jesper, Luuc, Maarten en Tom (en eigenlijk iedereen die een scooter had toentertijd): ik vind het heel leuk hoe onze vriendschap zich heeft ontwikkeld over de jaren, vanaf de eerste roeitochten en donderdagavondborrels tot aan onze recente wandelvakantie in Schotland. Liza, David en John, bedankt voor de Risk-

avondjes, zeiluitjes en weekendtrips. Owen, Pim en Siebren, thanks voor alle filosofische gesprekken. CJ, even though we don't get to meet up very often, it's always a pleasure to catch up virtually and discuss life on either side of the pond. Arnout, Cees, Jonas, Lisa en Niek, ik had me geen betere huisgenoten kunnen wensen op de Dijkstraat! Aan de 'limited edition'-squashgroep, bedankt voor alle sportieve en gezellige dinsdagavonden. En aan de mountainbikers, onze jaarlijkse fietsweekenden (pre-corona) zijn altijd een hoogtepunt, laten we gauw een nieuw weekend plannen!

Gracias a todos los amigos latinos, Lobos, Eka, Diego y Elena, Nati, Jan y Lea, Alejo, Cristina y Flora, Marcos, Katia y Zaraí, por los momentos felices y también por ayudarme a mejorar mi español! Y además, gracias a los Requena Suarez por recibirme en su familia y por toda la alegría durante nuestro visito a Peru!

Ten laatste wil ik graag mijn familie bedanken. Nienke, Yorrick, Toon, papa en mama, bedankt voor alle gezellige momenten samen in Onnen, Utrecht en Wageningen. Papa en mama, jullie hebben me altijd gestimuleerd om mijn interesses te volgen en om mijn talenten te ontplooien. Bedankt daarvoor! And finally, Daniela, your love and care during the last years have been incredible. Doing a PhD comes with many ups and downs. I am happy that we could share the positive moments and I am grateful for your support during the difficult times. Muchísimas gracias!

About the author

Auke Visser was born on September 1st, 1993, in Schiedam. He spent most of his youth in Haren, Groningen, where he moved with his parents at the age of 8.

At high school, Auke developed a broad interest in the natural sciences. This led him to apply for a Liberal Arts and Sciences Bachelor program at Amsterdam University College. Here, he combined a major in environmental and earth sciences with courses in computer programming and mathematics. After graduating, Auke started a Master program in Climate Studies at Wageningen University, originally thinking about focusing on hydrology and water management. His interest in atmospheric chemistry was sparked by the course 'Atmospheric Composition and Air Quality' taught by Folkert Boersma and Maarten Krol. After a year of courses in Wageningen, he went on a six-month Erasmus exchange to ETH Zürich to develop a more solid background in atmospheric and climate science. In Zürich, he followed courses in stratospheric chemistry, land-climate interactions and Fortran programming.

Back in Wageningen, Auke wrote a Master thesis on comparing atmospheric chemistry model simulations with satellite observations, supervised by Folkert Boersma. This project laid the foundation for the work presented in Chapter 2 of this thesis. He then went back to ETH Zürich for a four-month internship to investigate the effect of irrigation on climate extremes, under supervision of Wim Thiery and Sonia Seneviratne. Upon completion of his studies, he got the opportunity to start on a PhD project on ozone deposition in the Meteorology and Air Quality department at Wageningen University, supervised by Laurens Ganzeveld, Folkert Boersma and Maarten Krol. This project combined his research interests in atmospheric chemistry and land-atmosphere interactions, and resulted in the PhD thesis you are currently reading.

List of peer-reviewed publications

Barten, J.G.M., Ganzeveld, L.N., **Visser, A.J.**, Jiménez, R., and Krol, M.C. (2020). "Evaluation of nitrogen oxides (NO_x) sources and sinks and ozone production in Colombia and surrounding areas". *Atmospheric Chemistry and Physics*, 20, 9441-9458. DOI: 10.5194/acp-20-9441-2020.

Thiery, W., **Visser, A.J.**, Fischer, E.M., Hauser, M., Hirsch, A., Lawrence, D.M., Lejeune, Q., Davin, E.L., and Seneviratne, S.I. (2020). "Warming of hot extremes alleviated by expanding irrigation". *Nature Communications*, 11, art. no. 290. DOI: 10.1038/s41467-019-14075-4.

Visser, A.J., Boersma, K.F., Ganzeveld, L.N., and Krol, M.C. (2019). "European NO_x emissions in WRF-Chem derived from OMI: impacts on summertime surface ozone". *Atmospheric Chemistry and Physics*, 19, 11821-11841. DOI: 10.5194/acp-2019-295.

Visser, A.J., Ganzeveld, L.N., Goded, I., Krol, M.C., Mammarella, I., Manca, G., and Boersma, K.F. (2021). "Ozone deposition impact assessments for forest canopies require accurate ozone flux partitioning on diurnal timescales". *Atmospheric Chemistry and Physics*, 21, 18393-18411. DOI: 10.5194/acp-21-18393-2021.

Visser, A.J., Ganzeveld, L.N., Finco, A., Krol, M.C., Marzuoli, R., and Boersma, K.F. (2022). "The combined impact of canopy stability and soil NO_x exchange on ozone removal in a temperate deciduous forest". *Journal of Geophysical Research: Biogeosciences, in press.* DOI: 10.1029/2022JG006997

Other scientific publications

Hordijk, L., Erisman, J.-W., Eskes, H., Hanekamp, J.C., Krol, M.C., Levelt, P.F., Schaap, M., Vries, W. de, **Visser, A.J.**, Massink, H.F., Stronks, J. (2020). "Meer meten, robuuster rekenen: Eindrapport van het Adviescollege Meten en Berekenen Stikstof". https://www.rijksoverheid.nl/documenten/rapporten/2020/06/15/meer-meten-robuuster-rekenen.

Hordijk, L., Erisman, J.-W., Eskes, H., Hanekamp, J.C., Krol, M.C., Levelt, P.F., Schaap, M., Vries, W. de, **Visser, A.J.** (2020). "Niet uit de lucht gegrepen: Eerste rapport van het Adviescollege Meten en Berekenen Stikstof". https://www.rijksoverheid.nl/documenten/rapporten/2020/03/05/bijlage-niet-uit-de-lucht-gegrepen.

SENSE

Netherlands Research School for the
Socio-Economic and Natural Sciences of the Environment

D I P L O M A

for specialised PhD training

The Netherlands research school for the
Socio-Economic and Natural Sciences of the Environment
(SENSE) declares that

Auke Jacobus Visser

born on 1 September 1993 in Schiedam, the Netherlands

has successfully fulfilled all requirements of the
educational PhD programme of SENSE.

Wageningen, 31 October 2022

Chair of the SENSE board

Prof. dr. Martin Wassen

The SENSE Director

Prof. Philipp Pattberg

The SENSE Research School has been accredited by the Royal Netherlands Academy of Arts and Sciences (KNAW)

K O N I N K L I J K E   N E D E R L A N D S E
A K A D E M I E   V A N   W E T E N S C H A P P E N

The SENSE Research School declares that **Auke Jacobus Visser** has successfully fulfilled all requirements of the educational PhD programme of SENSE with a work load of 37.9 EC, including the following activities:

SENSE PhD Courses

- o   Environmental research in context (2017)
- o   Research in context activity: 'The fitness-for-purpose of the Dutch nitrogen assessment methodologies' (2022)

Other PhD and Advanced MSc Courses

- o   Machine Learning for Spatial data, PE&RC and WIMEK (2018)
- o   IGAC early career workshop (2021)
- o   Reviewing a scientific Manuscript, Wageningen Graduate Schools (2017)
- o   Career Orientation, Wageningen Graduate Schools (2019)
- o   Supervising BSc & MSc thesis students, Wageningen University (2019)
- o   Writing Grant Proposals, Wageningen Graduate Schools (2020-2021)

Management and Didactic Skills Training

- o   PhD representative chair group 'Meteorology and Air Quality' (2019-2021)
- o   Co-supervising two MSc students with theses entitled 'Assessment of air quality over Colombia using a mesoscale model, in-situ and remote sensing data' (2018) and 'Assessing ozone deposition impacts on ecosystem scale vegetation productivity using ozone deposition flux estimates and MODIS data' (2020)
- o   Teaching in the MSc courses 'Field course in soil-vegetation-atmosphere interactions' (2017-2018) and 'Atmospheric Composition and Air Quality' (2018- 2019)

Oral Presentations

- o   *Multi-scale monitoring and modelling of ozone deposition to Ecosystems*. 2nd Ozone and Plants Conference, 21-25 May 2018, Florence, Italy
- o   *Changes in summertime peak ozone after implementing OMI-derived NO$_x$ emissions in WRF-Chem*. Buys Ballot Graduate School Annual PhD Symposium, 25-26 October 2018, Soest
- o   *OMI-derived European NO$_x$ emissions in WRF-Chem: impacts on summertime surface ozone*. European Geophysical Union General Assembly, 7-12 April 2019, Vienna, Austria
- o   *OMI-derived European NO$_x$ emissions in WRF-Chem: impacts on summertime surface ozone*. WRF-Chem European Users Workshop, 7-8 May 2019, Munich, Germany

SENSE coordinator PhD education

Dr. ir. Peter Vermeulen